Preface

This special issue collects works presented at the 11th International Symposium on Electrochemical Impedance Analysis (EIA11), held in Camogli (Italy) from the 6th to the 10th of November 2017.

The 2017 event was a valuable opportunity to widen the EIA community, traditionally located in Eastern-Europe, with new contributions from Italy, Germany, France, Spain, Portugal, Greece, Ireland, Israel, Denmark, United Kingdom and Japan. The richness of the topics presented at the Conference as well as the attention to next generation of experts being formed are well resumed in the "*Welcome Letter by the Chairs of EIA11*" following these lines.

Published papers represent some of the most interesting and advanced reports in the field of electrochemical analysis, with special attention to sustainable energy applications like fuel cells, biofuels and batteries. The bouquet is enriched by valuable contributions about electrochemical phenomena in organic systems like coatings, dyes and microbial cells.

This issue gathers the most recent developments of the Differential Resistance Analysis, a new tool for the analysis of degradation in electrochemical systems, firstly proposed by Prof. Zdravko Stoynov, and his last manuscript, entitled "Rotating Fourier Transform - engine for Non-stationary Impedance Spectroscopy".

Both are brilliant demonstrations of Zdravko's constant search for innovation out of consolidated schemes, which characterized all his successful carrier and gave him perpetual fame.

We would like to thank the authors that contributed with their valuable work to this special issue and all the referees that contributed to keep high the scientific level of publications. Special thanks go to the journal staff, the Editor in Chief and Dr. Gergana Raikova for their precious support.

Finally, we wish this issue will be appealing and source of inspiration for future research.

Genova, November 21, 2018

Guest Editors

Antonio Barbucci, Maria Paola Carpanese
University of Genova
Department of Chemical, Civil and Environmental Engineering

Sabrina Presto, Massimo Viviani
National Research Council of Italy
Institute of Condensed Matter Chemistry and Energy Technologies

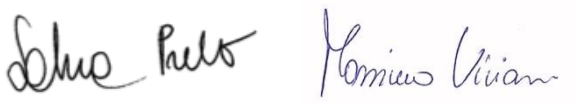

Welcome Letter by the Chairs of EIA11

The 11th International Symposium on Electrochemical Impedance Analysis (EIA11) is a new link in the well – established chain of EIA conferences held every three years. The present edition of EIA is held in the small fishermen village of Camogli, on the Ligurian coast of Italy. This event intends to bring together experts on the most recent advances and applications of Electrochemical Impedance Analysis to share knowledge, ideas, and achievements, as well as to create a friendly environment for fruitful discussions.

Maintaining the tradition of previous conferences, EIA11 aims at providing a common platform for scientists and experts from international research and industrial institutions. In addition, EIA11 encourages and educates the next generation of experts in the field of impedance analysis and more in general in its application in electrochemistry.

The symposium is enriched by a session dedicated to the Joint Programs “Fuel Cells and Hydrogen Technologies”, "Energy Storage” and “Advanced Materials and Processes for Energy Application” of the European Energy Research Alliance.

We wish to express our gratitude to the members of the Scientific Committee for their expertise and professional support, to all participants for their eager interest and valuable scientific contributions, as well as to the members of the Organizing Committee. Our gratitude is extended to the International Society of Electrochemistry, the Electrochemical division of the Italian Society of Chemistry, the Institute of Condensed Matter Chemistry and Technologies for Energy of the National Research Council and the Department of Civil Chemical and Environmental Engineering of the Genoa University. We also wish to thank Companies for sponsoring the event and supporting the participation of younger colleagues. Help from all contributors was essential for the organization of EIA11.

The Symposium is dedicated to Professor Zdravko Stoynov, who was expected to join us here and to ensure the success of EIA 11th edition with his knowledge and humor. We all lost a great scientist and friend.

His career was so successful thanks to a continuous desire to make rigorous science also enjoying like a child with a toy. We would like to remember him with a prize that will be awarded to one of the young scientists attending the symposium that is demonstrating to follow Zdravko’s path.

It is our great pleasure to welcome all of you in Camogli and wish you a pleasant and fruitful stay.

Antonio Barbucci

DICCA-University of Genoa

Massimo Viviani

ICMATE-National Research Council

Bulgarian Chemical Communications, Volume 50 Special Issue D (pp. 7 – 20) 2018

Professor Zdravko Stoynov- The Scientist Who Created New Horizons (16.05.1936 – 09.09.2017)

D. Vladikova

Acad. E. Budevski Institute of Electrochemistry and Energy Systems- Bulgarian Academy of Sciences, 10 Acad. G. Bonchev Str., Sofia1113, Bulgaria

Received August 18, 2018 Revised August 28, 2018

Prof. Zdravko Stoynov left our world abruptly – engulfed in the ebullience of his latest series of advanced inventions. However, he left us an abundant heritage – his spirit, his interminable wonder and inquisitiveness, his developments and inventions – all that he has taught us and brought us up with. It has no dimension, but rather a unique value and it is our duty to preserve, cherish, and augment it.

An original and non-standard personality with the spirit of a gentleman, he turned all that he touched into a masterpiece. His innovative thinking often made him feel as a scientific hermit. Some of his developments were highly evaluated only 10-15 years after their invention, while others are still waiting to be accepted and implemented.

At the age of 24, Zdravko Stoynov built the first in Bulgaria analog computer to calculate differential equations to the 12^{th} order after the decimal point. For over half a century right until his passing, he continued to create and develop algorithms & solutions, which he integrated into his nonstandard equipment, so he could unveil new key phenomena in the electrochemical power sources – the primary zone of his professional interest.

Prof. Stoynov's scientific achievements are not only numerous and significant, but also cross between different disciplines to redefine problems outside normal boundaries and reach solutions based on a new understanding of complex processes - a novel approach in modern science which usually involves different teams of scientists from diverse backgrounds and fields. Zdravko Stoynov's research married electrochemistry with engineering, mathematics, computer sciences… he suited the equipment he created to his experimental goals – from the development of unique hardware and software to original methods for data analysis. For example, he measured the underpotential pre-nucleation of Ag on dislocation free surface of single crystal face by constructing an ultra-sensitive potentiostat with a voltage range of 10 mV and sensitive current measurements. His precision equipment and methodology registered impedance on a single dislocation. His extensive inter-disciplinary knowledge and skills reflected in his academic degrees: Ph.D. in engineering (automatization of the experiment) from the Bulgarian Academy of Sciences (BAS), Doctor of Technical Sciences (technical cybernetics) from Zurich Polytechnical University, and Doctor of Chemical Sciences from BAS.

I have been wondering for many years about the source of Prof. Stoynov's limitless scientific curiosity and inexhaustible constructive energy to define new topics and undertake seemingly insoluble problems, transforming them into fertile and attractive research fields. Finally, I believe I have found the answer in the words of the renowned physical chemist Ivan Stransky: "*A scientist must possess the capability to wonder. He has to see voids where others see nothing*." It is as if those words are especially said for Zdravko Stoynov who managed to preserve and develop this childish curiosity and disregard for limits and taboos which, combined with exceptional intelligence and multidisciplinary knowledge accumulated during the years, made him an extraordinary scientist.

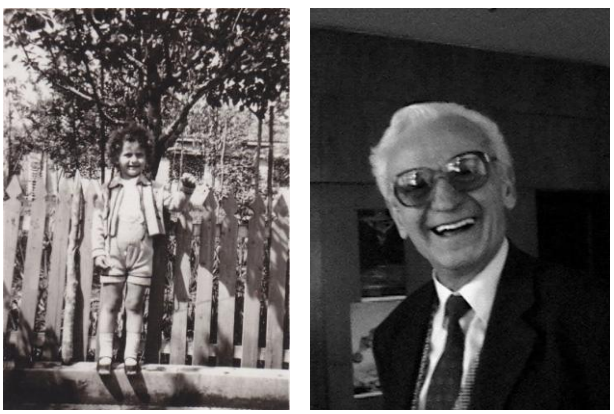

Fig. 1. Zdravko Stoynov in: early 1940's (left); 2010's (right).

To whom all correspondence should be sent:
E-mail: d.vladikova@bas.bg

In 1960, Zdravko Stoynov graduates from the Technical University of Sofia by constructing the first analog computer in Bulgaria. In the next 2 years, he establishes the "Computing and Modeling Laboratory" at the Technical University and constructs a larger analog computer to calculate non-linear differential equations up to the 120th order [1]. At the same time, he is developing non-standard equipment for researchers at the Bulgarian Academy of Sciences. As a result, in 1963 he is introduced to Evgeni Budevski, who is feverishly working with his team on growing a dislocation-free crystal. If successful, they will create the first "perfect crystal" in the world and confirm the Stransky-Kaischew theory of two-dimensional nucleation.

Thus, in 1963 Zdravko Stoynov becomes part of a talented world-renowned research team on the verge of a significant discovery. In a matter of months, he considerably increases the sensitivity, precision, and stability of the measuring equipment and albeit coming from a completely different scientific field, starts to participate actively in the scientific work of the department. Zdravko Stoynov himself enthusiastically describes the atmosphere, emotions, and dedication of the entire team during those exiting times in a contribution for Academician Evgeni Budevski [2]. In 1965, thirty-three years after the publication of the Stransky-Kaischew theory, comes its experimental proof – the Budevski team successfully grows the first in the world dislocation-free single crystal. This accomplishment sparks extensive research of electrochemical performance in a new, experimentally unexplored system with completely different behavior from systems with dislocations in the crystal lattice. Zdravko Stoynov is in the heart of this research, developing models for surface diffusion and monoatomic layer growth [3,4].

With such a strong scientific beginning, what to do next?! His exceptional engineering and mathematical background gives him the unique independence to develop targeted task-specific equipment. From then on, he has freedom to choose what scientific peak to overcome next. He selects a difficult and little exploited at the time, yet exciting field full of potential and enormous opportunities – electrochemical impedance spectroscopy (EIS). In parallel, he continues to work in a pure engineering field, automation of the scientific experiment, developing a series of automated battery testing equipment for the newly established Central Laboratory of Electrochemical Power Sources with Director Evgeni Budevski, founded in 1967 (Figs. 2,3).

Fig. 2. The Electrochemical Methods Department, founded by Zdravko Stoynov: 1986 (up); 2016 (middle and and down).

That equipment is implemented in the Bulgarian lead acid battery plants in Dobrich, Targovishte, and Pazardjik. Prof. Stoynov's power potentiostats are introduced in the laboratories of the German and Czech Academies of Sciences. During his specialization in Case Western Reserve University in Cleveland, he develops a new generation ultra-fast power potentiostat (BC 6000), which is put into production in Stonehard Ass. (USA) – the company owned by the inventor of the fuel cell for the American lunar rover.

Zdravko Stoynov never ceases to develop unique non-standard equipment (Figs. 3-5), but it serves as a means to a greater end as the focus of his work shifts to experimental methodologies.

Despite his interest and work in various scientific fields, his greatest and undying love remains electrochemical impedance. He is irresistibly drawn to this method by its exceptional informative capabilities and numerous exciting challenges. Electrochemical impedance has the unique advantage of separating the kinetics of the different steps describing the phenomenon or process under investigation. However, there are serious hurdles in the analysis of the experimental data, which need a statistical approach. The challenge is two-fold as both the method and the system under investigation must be considered… and Zdravko Stoynov has been "digging" in both directions… for more than 50 years.

Nowadays, measuring electrochemical impedance with frequency response analyzers is a mainstream method used by all. However, few know that Zdravko Stoynov implements this equipment into electrochemical measurements after a visit to the Solartron company in 1968. The same year the first two frequency response analyzers are bought and introduced by Prof. Epelboin in his laboratory in Paris (CNRS-UPMC, Université Pierre et Marie Curie) and by Zdravko Stoynov in CLEPS (Bulgarian Academy of Sciences).

Working in a "battery institute", Zdravko Stoynov decides to investigate the impedance of batteries – an object whose impedance is considered impossible to measure at the time. Under these circumstances, he starts to systematically chisel away at the scientific taboos… and continues to do so till his last day.

Fig. 3. Zdravko Stoynov's computerized testing laboratory in CLEPS (1975).

Fig. 4. Zdravko Stoynov's "Hydrogen Laboratory" in IEES (2015).

Fig. 5. Zdravko Stoynov and Massimo Schiavetti in front of Stoynov's equipment for impedance testing of large batteries for accumulation of energy from solar cells (ENEL- Pisa, 2014).

For a start, he introduces measurements outside the point of chemical equilibrium. Today, this is customary. However, it is completely unheard of nearly 40 years ago. Prof. Stoynov develops specialized equipment and with his colleagues at CNRS in Paris measures, for the first time in the world, impedance of batteries – galvanostatically and quasistrationary [5] (Fig. 6). A year later, he measures the impedance of large-scale batteries and promotes the introduction of this method in laboratories and practices of the European Space Agency, the Soviet space program, as well as in the Lewis Center at NASA.

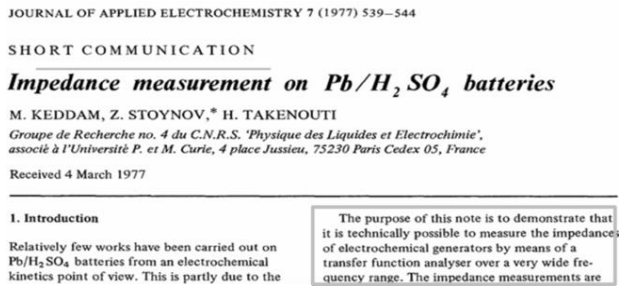

JOURNAL OF APPLIED ELECTROCHEMISTRY 7 (1977) 539–544

SHORT COMMUNICATION

Impedance measurement on Pb/H_2SO_4 batteries

M. KEDDAM, Z. STOYNOV,* H. TAKENOUTI

Groupe de Recherche no. 4 du C.N.R.S. 'Physique des Liquides et Electrochimie', associé à l'Université P. et M. Curie, 4 place Jussieu, 75230 Paris Cedex 05, France

Received 4 March 1977

1. Introduction

Relatively few works have been carried out on Pb/H_2SO_4 batteries from an electrochemical kinetics point of view. This is partly due to the

The purpose of this note is to demonstrate that it is technically possible to measure the impedance of electrochemical generators by means of a transfer function analyser over a very wide frequency range. The impedance measurements are

Fig. 6. The first publication for impedance on batteries.

Delving deeper into the subject, Prof. Stoynov focuses on the non-steady state of batteries during the impedance measurement process.

Non-stationary (4-D) impedance analysis

Based on the classical method of the Transfer Function (TF), Electrochemical Impedance Spectroscopy gives a local, linearized and full (in a frequency aspect) description of the investigated electrochemical system, which is assumed to be a steady-state one. However, batteries behave as big statistical systems with distributed parameters on a macro and micro scale. During cycling, processes of mass and energy transfer take place. They change the object's structure and parameters. Thus, batteries show non-steady state behavior, which is a restriction for correct impedance studies. For further development of the impedance of batteries, a liberation from the restriction of steady state conditions is needed and thus Zdravko Stoynov develops non-stationary (4-D) impedance analysis – a procedure which eliminates delay errors [6-9].

This approach is based on the assumption that the state and the parameter space of the system is a continuum. It corrects the errors arising from the measurement delay during the frequency sweep. In contrast to classical electrochemical impedance spectroscopy, which works with a 3-dimensional (3D) set of data, Zdravko Stoynov formulates a 4-dimensional initial set of experimental data, including the time of measurement. He approximates every iso-frequency dependence with a formal model and applies two orthogonal iso-frequency cubic splines respectively for the real and the imaginary components. The interpolation (and extrapolation) for a given time t_j and a set of frequencies ω_i gives the corresponding estimates of the real and imaginary parts. Thus, the data of each evolving diagram are reconstructed and the corresponding impedance diagrams already represent the impedances measured virtually at the same time for all frequencies. This, in practice, corrects the deformations due to the non-steady state evolution (Fig. 7).

Stoynov's innovative 4-D approach improves significantly the impedance studies of batteries [10-13]. It is no wonder this method has been introduced in the battery testing software of Zahner Elektrik GmbH & Co. KG and successfully applied by Mitsubishi in Li-ion battery research [14, 15], as well as for studies of other time-evolving systems [16, 17].

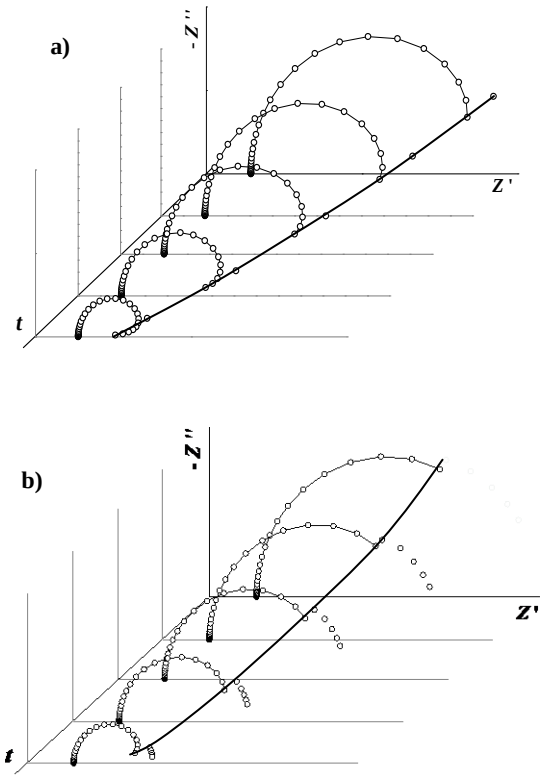

Fig. 7. Simulated impedance diagrams of an evolving simple Faradaic reaction deformed by measurement delay errors: a) iso-frequency dependence for the lowest frequency; b) fifth iso-frequency dependence (starting from the lowest frequency). *Reproduced with permission from D. Vladikova (2006) Nonstationary differential impedance spectroscopy in energy sources. In: Stoynov Z. and Vladikova D. (eds.) Portable and Emergency Energy Sources, pp. 411–436. Sofia: Marin Drinov Academic Publishing House.*

Rotating Fourier Transform (RFT)

The non-steady state conditions of the electrochemical system during impedance measurements penetrate deeper, affecting the Fourier Transform (FT), which is the mathematical kernel of every impedance analyzer of our days. The FT is the best estimator of sinusoidal signals in steady-state conditions. However, out of those conditions, the FT produces specific errors dependent on the frequency. After a profound analysis of those errors, Zdravko Stoynov succeeds to develop theoretically an advanced generalized form of this transform – the Rotating Fourier Transform. This is the subject of his doctoral dissertation in the Federal Institute of Technology – Zurich [18, 19]. The implementation of the RFT in impedance spectroscopy provides for precise measurements of time-evolving systems out of steady-state conditions. It opens a new horizon for studies of batteries and fuel cells, corrosion and numerous other systems.

During the last year of his life, Zdravko Stoynov refocuses on further theoretical and experimental development of his advanced mathematical RFT tool, introduced 30 years ago. He describes it as a "powerful engine for non-stationary impedance spectroscopy which opens up the exploration of the low and infra-low frequencies where many important and interesting phenomena, still hidden, can be measured precisely". Expecting the development of new "4th Generation" marketable impedance analyzers through the application RFT and MRFT (Multiple RFT) in the near future, he labors over both the mathematical tool and his experimental verification (Fig. 8) in order to accelerate the coming of this "near future" and to be able to see it (Fig. 9). An unedited version of his last unpublished work on this topic, written months before his passing, is presented in this issue in "Letters to the Editor" [20].

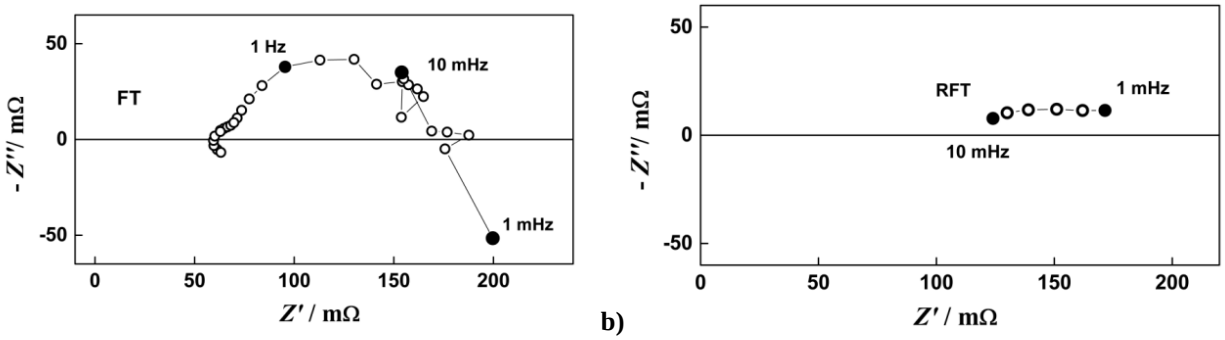

Fig. 8. Impedance diagrams of Li-ion battery 2000 mAh during charge with 100 mA: (a) produced by conventional Impedance Analyzer (Solartron 1260) using Fourier Transform. Frequency range 1 kHz – 1 mHz, 5 points/decade, A.C. current amplitude 11 mA; (b) produced by Rotating Fourier Transform of the data from Fig. 8a. Frequency range 10 mHz to 1 mHz, 5 points/decade [20].

Fig. 9. Bio-logic Science Instruments (Grenoble 2017): Zdravko Stoynov is explaining visually his Rotating Fourier Transforms.

Differential Coulometry Spectroscopy

Battery testing is an important application-oriented tool for evaluation of their operational capability and performance as sources of energy and power. The typical testing results give general information that represents the overall behavior and thus does not support the analytical understanding of the processes taking place. To fill this gap, Zdravko Stoynov develops Differential Coulometry Spectroscopy (DCS), which extracts valuable information about the batteries' internal kinetics, electrochemical design, and life degradation. This technique requires measurements of the voltage changes in time followed by precise aperiodic function Spectral Transform Analysis [21]. In order to separate the thermodynamic kinetics from the

masking dynamic effect of the intrinsically connected transport limitations, very slow-rate galvanostatic testing (charge/discharge) is required. In principle, the galvanostatic mode of testing is a sweep coulometry and provides for the evaluation of the quantity of electricity necessary for the propagation of the investigated process or its steps. DCS has been found to be a useful tool for investigating the electrochemical behavior and performance of rechargeable batteries based on intercalation materials (Fig. 10). Recently, it has been included in the analysis package of BioLogic Science Instruments' EC-Lab software version V11.01 [22].

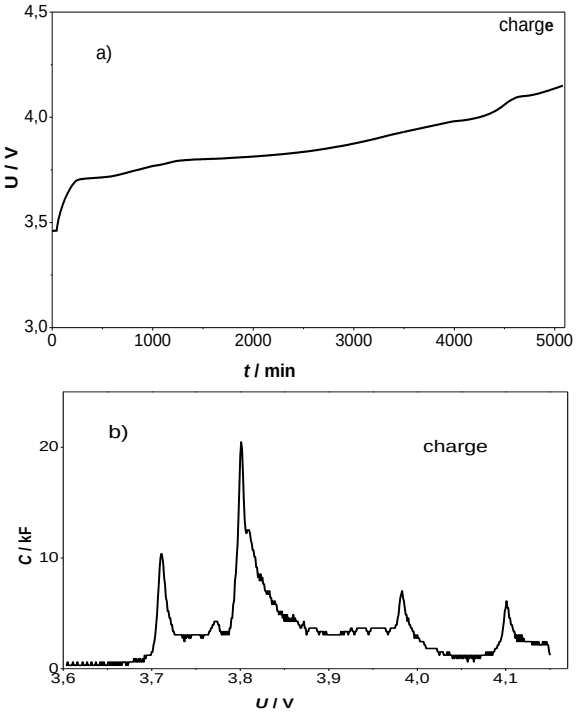

Fig. 10. Four volts Li-ion sample with nominal capacity of 2200 mAh: (a) Slow sweep voltage–time charge curve (h = 100 hours); (b) Capacity spectrum of the slow sweep voltage–time charge and discharge curves (h = 100 hours). *Reproduced with permission from D. Vladikova (2006) Differential Coulometry spectroscopy in: Stoynov Z. and Vladikova D. (eds.) Portable and Emergency Energy Sources, pp. 437–449. Sofia: Marin Drinov Academic Publishing House.*

Differential Impedance Analysis (DIA)

Although electrochemical impedance as a TF gives a local, linear, and full description of the system under study, this information must be extracted from the experimental data, since impedance does not directly measure the processes caused by the perturbation signal, i.e. it is not a physical reality, but an information property of the object. The commonly applied approach for the interpretation of the experimental data is the construction and confirmation of a preliminarily derived hypothetical model. The model structure is chosen *a priori*, and thus the identification procedure is only parametric.

The main efforts towards the improvement of the impedance data analysis are focused on the advancement of the identification procedure. In this direction, Zdravko Stoynov's achievements start with the development of the original Model Reduction Method [23]. However, the data analysis advancements by improvements in the parametric identification do not satisfy him because of the principle discrepancy between the power of the impedance measurement technique, which ensures a large volume of precise data, and their analysis, based on the formulation of hypotheses, often built on subjective or oversimplified assumptions.

In Technical Cybernetics, the Structural Identification Approach is applied for data analysis. It does not require an initial working hypothesis and provides both structural and parametric identification. However, the application of this procedure to electrochemistry creates a multitude of problems for a long time accepted as insoluble. This challenge attracts Zdravko Stoynov and to overcome it, he develops the technique of Differential Impedance Analysis (DIA), introducing the Structural Identification approach in the frequency domain [24-30] – one of his biggest breakthroughs and a monument to out-of-the-box thinking.

The DIA procedure starts with the initial set of experimental data (angular frequency, real and imaginary components of the impedance), and thus can be applied to previously measured data. The kernel is the local scanning analysis, performed with the so-called local operating model (LOM) with a simple structure consisting of a resistance R_1 in series with a parallel connection of capacitance C and a second resistance R_2. The effective time-constant $T = RC$ is also introduced as a LOM parameter. In contrast to the classical parametric identification performed over the entire frequency range, which estimates the parameters' vector as a preliminary chosen model structure, the identification of the LOM parameters' vector by local analysis is carried out within a narrow frequency range, regarded as an operating window. When the window width is a single frequency point, the solution is purely deterministic. The following steps describe the procedure of the structural and parametric identification:

- Scanning with the LOM throughout the whole frequency range with a scanning window of a single frequency point;
- Parametric identification of the LOM at every

working frequency. Since the number of the independent data available inside the observation window is smaller than the number of the unknown parameters, the initial set of impedance data is extended with two additional terms – the derivatives of the real and imaginary components of the impedance with respect to the frequency. Thus, the set of equations determining the LOM parameters estimation becomes solvable;

• Frequency analysis of the LOM parameters' estimates. The results are presented in the so-called temporal plots, which give the frequency dependence of the LOM parameters' estimates (Fig.11). If the LOM parameters' estimates are frequency-independent in a given frequency region, the sub-model corresponding to this frequency segment follows the LOM structure, i.e. it is described with a parallel combination of capacitance and resistance, which determine a time-constant. Thus, the number of the plateaus gives the number of the time-constants in the model (Fig. 11b). The results can be transformed in spectra, where the plateaus are depicted as spectral lines (Fig. 11c, d) [27-30].

The presence of frequency dependence in the temporal plots marks either the regions of mixing between two phenomena, or frequency-dependent behavior. Those segments are additionally examined by Secondary DIA [27, 29, 30]. The procedure, known as differential temporal analysis, includes the differentiation of the LOM parameters' estimates with respect to the log frequency. It recognizes frequency-dependent elements (CPE, Warburg, Bounded Warburg etc.) as well as their presence in more complicated models. DIA opens new horizons for EIS by increasing its information capability. It is successfully applied in electrochemical power source studies and other systems [30-40].

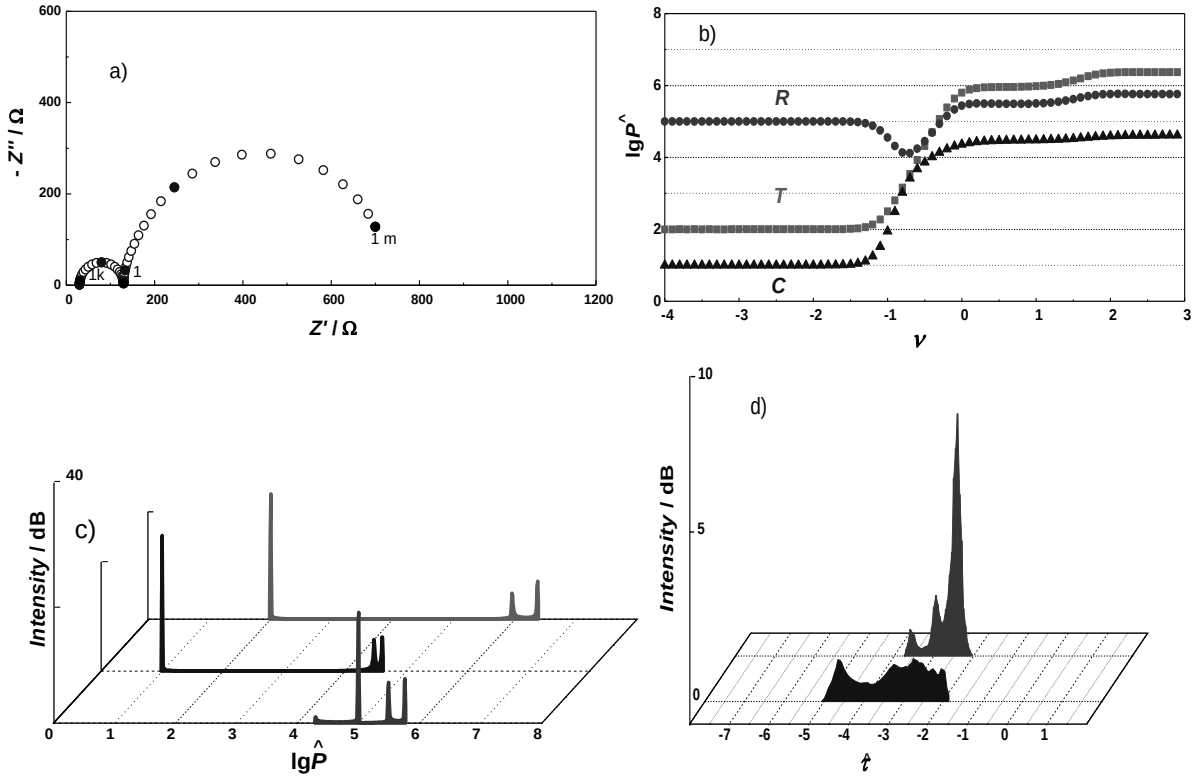

Fig. 11. DIA of a three-step reaction: (a) equivalent circuit and complex-plane impedance diagram; (b) temporal plots (c) spectral plots; d) time-constant spectra of motor oil Mobil Delvac MX 15W40: new (■); after 10000 km. (■). *Reproduced with permission from D. Vladikova (2005) Differential Impedance Analysis. Sofia: Marin Drinov Academic Publishing House.*

Differential Resistance Analysis

Zdravko Stoynov's final invention, developed in the last months of his life, is related to the most severe hurdles facing the deployment of batteries and fuel cells – lifetime and durability, and more precisely – their reliable evaluation. The SoA degradation already requires long-term testing, which can take several years – a huge deterrent to market deployment. For the moment, the problem-solving approach consists in the development of accelerated stress test (AST) procedures and protocols, which should shorten the testing time in conditions activating the same aging mechanisms

as non-accelerated testing. This is a critical moment, since the measured degradation should be transferred to the real-life behavior of the tested system. Thus, the selection of the acceleration parameters and the level of acceleration are of critical importance and may differ significantly between systems and applications.

The latest invention of Zdravko Stoynov offers a new and original approach that decreases the testing time by increasing the sensitivity and accuracy of the standard monitoring and diagnostic tools, providing reliable quantitative information. The new Differential Analysis of the current-voltage characteristics (DIVA) surprises with its simplicity and originality [41-43]. It works with Differential Resistance (dR), i.e. with the derivative of the voltage with respect to the current, which is more sensitive to small deviations and thus ensures increased sensitivity (Fig. 12). The introduction of a spectral transformation procedure additionally increases the noise immunity and sensitivity of the method (Fig. 13) [41-43].

The Differential Resistance Analysis (DRA) introduces new performance indicators and can give information about the origin of the degrading phenomena via a combination with impedance measurements in selected characteristic working points. The analysis is about 10 times more sensitive than the classical evaluation of degradation based on voltage decrease measurements at constant current.

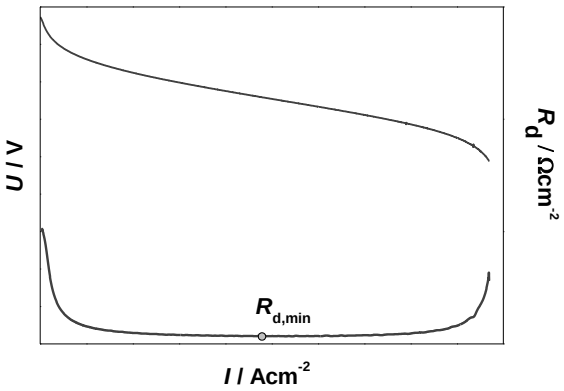

Fig. 12. DiVA procedure: i-V curve and R_d/I dependence.

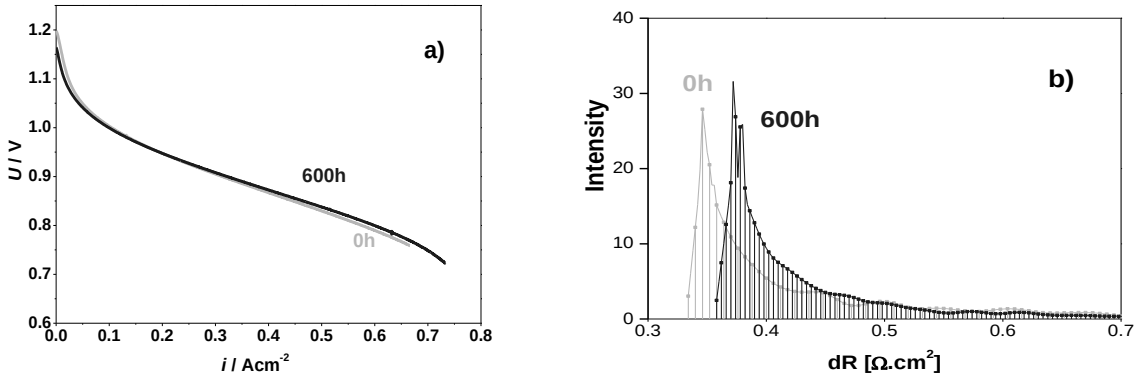

Fig. 13. DIVA of SOFC: (a) *I-V* curves measured during 600 hours testing; (b) spectral transform of the Differential Resistance dR = d*U*/d*I*).

International Activities

Although engulfed in practical and applied research, Zdravko Stoynov is no less valued as a "social scientist" with an acute sense of establishment, with excellent teaching skills, and with an unwithering enthusiasm to educate and pass on his knowledge and skills. He is one of founders of the international impedance society, a similarly minded enthusiastic group of colleagues fascinated by the potential of electrochemical impedance. For over 30 years, it has been gathering within the framework of two international conference chains:

• The International Electrochemical Impedance Spectroscopy Symposia (EIS), dating from 1989 (Fig. 14);

• The International Electrochemical Impedance Analysis Symposia (EIA), dating from 1988 (organized in Bulgaria in 1991, 1994, 2014) (Fig. 15).

On a regional level, he is one of the driving forces behind the establishment of the Regional Symposium of Electrochemistry – South-East Europe (RSE-SEE) and acts as its co-organizer in 2015 (Fig. 16). Starting in 1996, Zdravko Stoynov also establishes the national electrochemical event with international participation "Sofia Electro chemical Days" (Fig. 17).

Till his last day, Prof. Stoynov continued to invigorate these scientific forums with his innovative and avant-garde ideas.

Taking full advantage of and further developing the opportunities of virtual communication and dissemination tools, in 2002 he establishes the European Internet Center for Impedance Spectroscopy with its e-school, e-seminars and free-access e-journal (Impedance Contributions Online) – an extremely avant-garde idea for the first years of the 21st Century. For the past 16 years, the Proceedings of the EIA Symposium have been published in Impedance Contributions Online. In fact, Zdravko Stoynov was preparing to give the introductory speech for EIA11, dedicated to the 30th Anniversary of the Symposium, which, fate would have it, he would not attend.

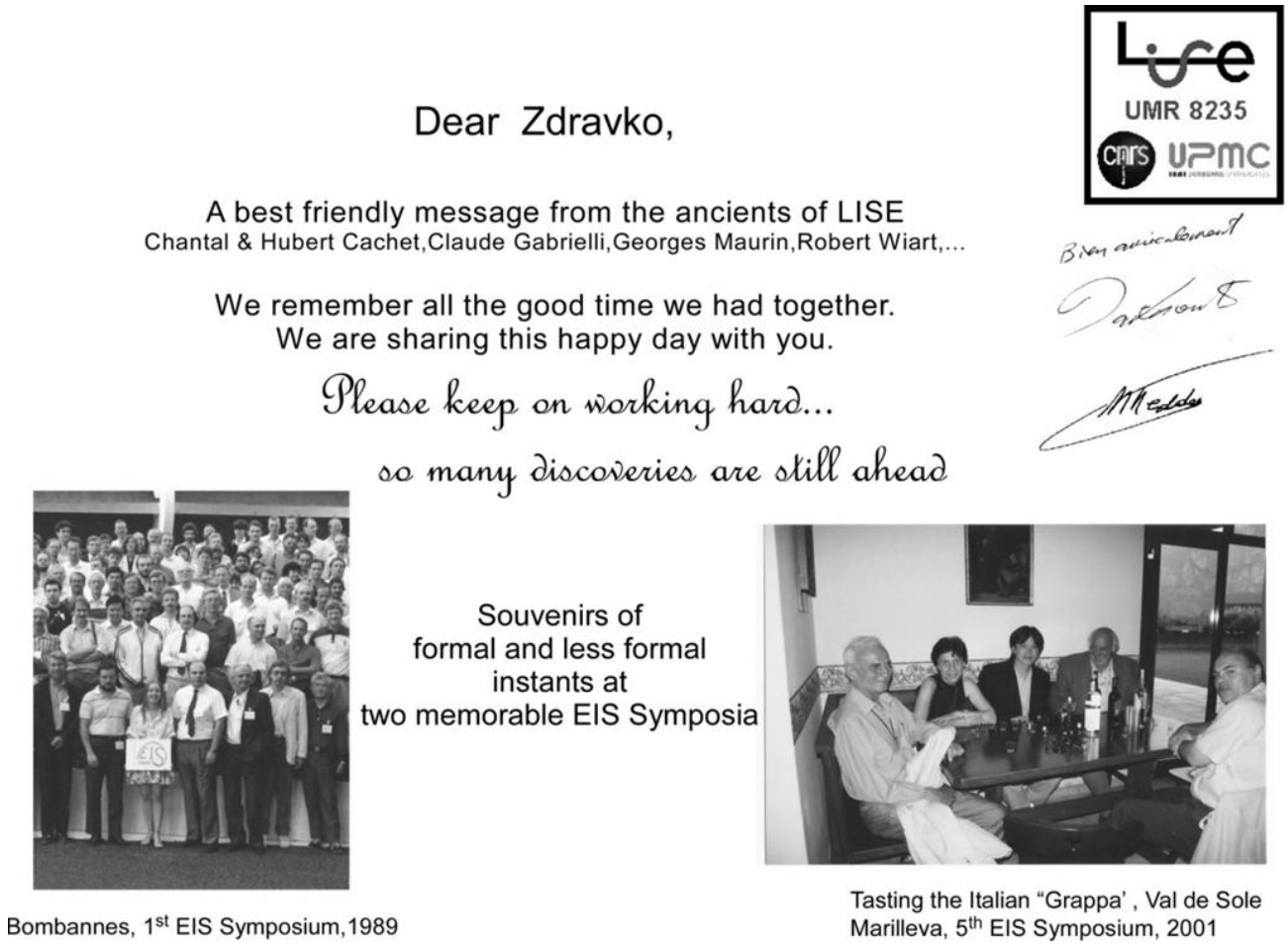

Fig. 14. (a) International Symposium on Electrochemical Impedance Spectroscopy; (b) Official Dinner, Algarve, Portugal, 8th EIS Symposium, 2010; (c) Lecture, A Toxa, Galicia, Spain,,10th EIS Symposium, 2016..

Fig. 15. International Symposium on Electrochemical Impedance Analysis (EIA): (a) Castle Trest, Moravia, Czech Republic, 5th EIA Symposium, 2008; (b) Welcome party, Red Island, Croatia 9th EIA Symposium, 2011; (c) Opening session, Borovetz, Bulgaria, 10th EIA Symposium, 2014.

Fig. 16. 5th Regional Symposium on Electro chemistry - South East Europe (RSE-SEE5), Pravets, Bulgaria, 2015.

Fig. 17. Opening of Sofia Electrochemical Days, 2012.

In the first difficult years after the fall of the iron curtain and the changes in Bulgaria, the Central Laboratory of Electrochemical Power Sources, as well as the Bulgarian Academy of Sciences as a whole, are functioning under the impending doom of being closed down and a great number of researchers leave the country to seek professional realization in Western Europe and the USA. However, during those troubling times, Prof. Stoynov's sense of duty towards Bulgarian science and his remaining colleagues does not permit him to emigrate. Instead of packing his suitcases for California, where he is expected to join the staff at Stanford University, he undertakes the responsibility to preserve and develop the scientific legacy of his greatest teachers Rostislaw Kaischew and Evgeni Budevski, accepting the position of Director of CLEPS in 1992. Four years later, he is elected as Chairman of the General Assembly (GA) of the Bulgarian Academy of Sciences - the executive body expected to reform the Academy in order to preserve its existence.

Prof. Stoynov once again unites seemingly disparate fields such as electrochemistry, management, economics, and policy-making. He applies to management his rich experience from impedance studies of energy systems, which behave as large statistical systems with distributed parameters on a micro and macro scale. He discerns that scientific infrastructure can be viewed as a large statistical system and can thus be analyzed and optimized in a similar way. The tool he offers for this system on a small and large scale (IEES and BAS) is a new type of scientific management based on: (i) microeconomic reforms; (ii) stable project financing; (iii) global scientific market participation; (iv) high-quality and high-level scientific products with a new positive emphasis on applied research, adequately balanced with fundamental studies.

Now, 25 years later, this socio-economic experiment which Prof. Stoynov takes an active leading role in has proven to be successful (Figs. 18,19). Not only has the Central Laboratory of Electrochemical Power Sources grown into the Institute of Electrochemistry and Energy Systems, one of the most successful BAS institutes with strong participation in the European Research Area, but also the Bulgarian Academy of Sciences has withstood the turmoil of the post-communist transition period and strengthened its position as a national research center with a 150-year history and a bright future ahead.

Zdravko Stoynov establishes the Innovation Centre at BAS, which has grown to be a long-term partner in the Enterprise Europe Network. He initializes the establishment of BAS Education Center, through which the Bulgarian Academy of Sciences obtains its accreditation for training and education.

Fig. 18. Celebration of Zdravko Stoynov's 80th Anniversary (16.05.2016): Prof. Stoynov receives the President of BAS Medal (16.05.2016) (1,2); together with the Electrochemical Methods Department team (3); flowers for „The Boss" at the birthday party (4).

Fig. 19. The "Zdravko Stoynov" Award (left) and the awarding ceremony for its first recipient, Antonio Bertei of Pisa University (Italy), during the 11th International Electrochemical Impedance Analysis Symposium (November 2017)

Noting the weakening of the BAS institutes in terms of the most valuable resource of any effective scientific infrastructure - the expert human resource, Prof. Stoynov implements proactive policies for career advancement and maintenance of the scientific staff above critical levels. While such policies sound trivial today, they are almost unheard of in Bulgaria during the 1990's and the beginning of the 21st century.

His advanced thinking gives birth to the original idea for a portable hydrogen refueling station, which with his inherent sense of humor, he calls "the bogie". It is introduced in 2013 in the National infrastructure proposal for "Energy Storage and Hydrogen Energetics", coordinated by IEES and accepted as part of the National Roadmap. It is in 2018 that we see for the first time in Bulgaria one of the new portable refueling stations, built by Air Liquide, fueling the demonstration hydrogen vehicles during the Summit for Hydrogen Applications organized for the 10^{th} anniversary of the Fuel Cells and Hydrogen Joint Undertaking. Had the national infrastructure project started in 2014, Prof. Stoynov's idea would have probably led to Bulgaria demonstrating its own portable refueling station in the event.

It is a quite rewarding experience to be able to reap what you have sown. Zdravko Stoynov could reap the respect and appreciation of his friends and colleagues from IEES, BAS, and all over the world, who joined together physically and virtually to celebrate his 80's birthday, turning it into a joyous and heartwarming event (Figs. 14-18).

The Bulgarian Academy of Sciences honored his exceptional service with the special medal of the President of BAS (Fig. 18), crowning and completing his BAS honors collection. On his anniversary, the international electrochemical community and Bulgarian colleagues expressed their gratitude to Prof. Stoynov for his insightful avant-garde contributions to the development of electrochemical science and its applications with a special issue of Bulgarian Chemical Communications, which included 30 publications by scientists from 13 countries.

As an age-old adage claims, scientists can only see further by standing on the shoulders of Giants. Professor Zdravko Stoynov will be remembered by his contemporaries and the generations that follow him as his colleague and comrade Digby Macdonald from UC Berkley describes him – "a Giant in electrochemical impedance spectroscopy".

Philosophers say that a man dies only when the memory of him is gone. The memory of Zdravko Stoynov will not fade. It will not be gone. It remains strong within the large international family of his students, colleagues, and friends from all over the world who honor, respect, and appreciate him. They named the Internet Center for Impedance Spectroscopy after him as it he who for 15 years developed and helped it grow into a powerful open platform for both beginners and experts in the field of impedance research. The "Zdravko Stoynov" prize in his honor will be awarded at each meeting of the International Electrochemical Impedance Analysis Symposium to foster and promote creative out-of-the-box thinking in young researchers (Fig. 19). The memory of Zdravko Stoynov is persistent, as are his deeds. All that he has sown and nurtured will continue to bear fruit into the future.

REFERENCES

1. P. Lazarova, First Steps in Analog Electronic Computing in Bulgaria, Yearbook of the National Polytechnic Museum, **10**, 149 (1980). (in Bulgarian) П. Лазарова, Първи стъпки в аналоговата електронно-изчислителна техника в България,Годишник на Националния политехнически музей, **10,** 149 (1980).
2. Z. Stoynov, W. Obretenov, Avademisian Evgeni Budevski, *Bulg. Chem. Communic*, **49 C**, 42 (2017).
3. E. Budevski, W. Bostanov, T. Vitanov, Z. Stoynov, A. Kotzewa, R. Kaischew, Keimbildungserscheinigung an versetzungsfreien (100) Flachen von Silbereinkristallen, *Electrochimica Acta*, **11**, 1697 (1966).
4. E. Budevski, W. Bostanov, Z. Stoynov, A. Kotzewa, R. Kaischew, Zweidimensionale Keimbildung und Ausbreitung von monoatomaren Silbereinkristallen, *Phys. Stat. Sol*., **13**, 577 (1966).
5. M. Keddam, Z. Stoynov, H. Takenouti, Impedance Measurement on PB-H_2SO_4 Batteries, *Journal of Applied Electrochemistry*, **7(6)**, 539 (1977).
6. Z. Stoynov, B. Savova Stoynov, Impedance Study of Non-Stationary Systems - 4-Dimensional Analysis, *Journal of Electroanalytical Chemistry*, **183(1-2)**, 133 (1985).
7. B. Savova Stoynov, Z. Stoynov, 4-Dimentional Estimation of the Instantenious Impedance, *Electrochimica Acta*, **37(12)**, 2353 (1992).
8. Z. Stoynov, "Nonstationary Impedance Spectroscopy", *Electrochimica Acta*, **38(14)**, 1919 (1993).
9. Z. Stoynov, B. Savova Stoynov, Instrumental Error in Impedance Measurements of Non Steady-State Systems, *Journal of Electroanalytical Chemistry*, **112(1)**, 157 (1980).
10. Z. Stoynov, Advanced Impedance Techiques for Litium Batteries Study - Four Dimensional Analysis, Materials for Lithium-Ion Batteries, Ed. C. Julien and Z. Stoynov, NATO Science Series, 3. High Technology, 85, p. 359, Kluwer Academic Publishers (2000).

11. Z. Stoynov, B. Savova-Stoynov, T. Kossev, Nonstationary Impedance Analysis of Lead-Acid-Batteries, *Journal of Power Sources*, **30(1-4)**, 275 (1990).
12. Z. Stoynov, T. Nishev, V. Vacheva, et al., Nonstationary analysis and modelling of battery load performance, *Journal of Power Sources*, **64(1-2)**, 189 (1997).
13. Z. Stoynov, D. Vladikova, Non-stationary differential impedance spectroscopy in energy systems in: Z. Stoynov, D. Vladikova (Eds.), "Portable and Emergency Energy Sources", Marin Drinov Academic Publishing House, Sofia, p. 411, 2006.
14. M. Itagaki, A. Taya, K. Watanabe, *Electrochemistry*, **68**, 596 (2000).
15. M. Itagaki, S. Yotsuda, N. Kobari, K. Watanabe, S. Kinoshita, M. Ue, *Electrochim. Acta*, **51,** 1629 (2006).
16. M. Ujvári, D. Zalka, S. Vesztergom, S. Eliseeva, V. Kondratiev, G. Láng, Electrochemical impedance measurements in non-stationary systems- Application of the 4-dimensional analysis method for the impedance analysis of overoxidized poly(3,4-ethylenedioxythiophene)-modified electrodes, *Bulg. Chem. Communic*, **49 C**, 106 (2017).
17. V. Horvat-Radošević, K. Kvastek, K. Magdić Košiček, Application of Stoynov's 4-D analysis for nonstationary impedance spectra corrections of thin poly(o-ethoxyaniline) modified Pt electrode, *Bulg. Chem. Communic*, **49 C**, 119 (2017).
18. Z. Stoynov, Fourier Analysis in the Presence of Nonstationary Periodic Noise, Dissertation No 1839, Swiss Federal Institute of Technology, Zurich, 1985.
19. Z. Stoynov, Rotating fourier transform - new mathematical basis for non-stationary impedance analysis, *Electrochimica Acta*, **37(12)**, 2357 (1992).
20. Z. Stoynov, Rotating Fourier Transform – Engine for Non-stationary Impedance Spectroscopy, *Bulg. Chem. Communic* (this issue)
21. Z. Stoynov, D. Vladikova, Differential Coulometry spectroscopy in: Z. Stoynov, D. Vladikova (Eds.), Portable and Emergency Energy Sources, Marin Drinov Academic Publishing House, Sofia, 2006 p. 437.
22. http://www.bio-logic.net/wp-content/uploads/EC-BT-Lab-AN57.pdf
23. Z. Stoynov, B. Savova-Soynov, *Journal of Electroanalytical Chemistry*, **170(1-2)**, 63 (1984).
24. Z. Stoynov, Electrochimica Acta, **34**, 1187 (1989).
25. Z. Stoynov, *Polish J. Chem*., **71**, 1204 (1997).
26. Z. Stoynov, Advanced Impedance Techiques for Litium Batteries Study - Differential Impedance Analysis, Materials for Lithium-Ion Batteries, Ed. C. Julien and Z. Stoynov, NATO Science Series, 3. High Technology, 85, p. 371, Kluwer Academic Publishers (2000).
27. D. Vladikova, Z. Stoynov, *J. Electroanal. Chem.*, **572**, 377 (2004).
28. D. Vladikova, P. Zoltowski, E. Makowska, Z. Stoynov, *Electrochimica Acta*, **47**, 2943 (2002).
29. Z. Stoynov, D. Vladikova, "Differential Impedance Analysis", Marin Drinov Publ. House, Sofia, 2005.
30. Z. Stoynov, D. Vladikova, Impedance Spectroscopy of Electrochemical Power Sources in: U. Garche (Ed.) Encyclopedia of Electrochemical Power Sources, Elsevier, p. 632, 2009.
31. M. Viviani, M. Buscaglia, L. Mitoseru, A. Testino, P. Nani, D. Vladikova, *J. Europ. Ceram. Soc*., **24**, 1221 (2004).
32. D**.** Vladikova, A. Kilner, S. J. Skinner, G. Raikova, Z. Stoynov, *Electrochimica Acta*, **51**, 1611 (2006).
33. D. Vladikova, G. Raikova, Z. Stoynov, H. Takenouti, J. Kilner, St. Skinner, *Solid State Ionics*, **176**, 2005 (2005).
34. A. Barbucci, M. Viviani, P. Carpanese, D. Vladikova, Z. Stoynov, *Electrochimica Acta*, **51**, 1641 (2006).
35. D. Vladikova, Z. Stoynov, A. Barbucci, M. Viviani, P. Carpanese, G. Raikova, The Technique of the Differential Impedance Analysis - Applications for SOFC studies" in: L. Mitoseriu (Ed.), New Developments in Advanced Functional Ceramics, Transworld Research Network, Kerala, India, Ch. 16, p. 457, 2007.
36. A. Kirchev, A. Delaille, M. Perrin, E. Lemaire, F. Mattera , Studies of the pulse charge of lead-acid batteries for PV applications: Part II. Impedance of the positive plate revisited, *J. Power Sources*, **170(2)**, 495 (2007).
37. A. Kirchev, F. Mattera, E. Lemaire, K. Dong, Studies of the pulse charge of lead-acid batteries for photovoltaic applications: Part IV. Pulse charge of the negative plate, *J. of Power Sources*, **191(1)**, 82 (2009).
38. A.Kirchev, A.Delaille, F.Karoui, M.Perrin, E.Lemaire, F.Mattera, Studies of the pulse charge of lead-acid batteries for PV applications: Part III. Electrolyte concentration effects on the electrochemical performance of the positive plate, *J. of Power Sources*, **179(2)**, 808 (2008).
39. D. Vladikova, Z. Stoynov, G. Raikova, A. Thorel, A. Chesnaud, J. Abreu, M. Viviani, A. Barbucci, S. Presto, P. Carpanese, Impedance spectroscopy studies of dual membrane fuel cell, *Electrochimica Acta*, **56**, 7955 (2011).
40. D. Vladikova, Z. Stoynov, A. Chesnaud, A. Thorel, M. Vivianu, A. Barbucci, G. Raikova, P. Carpanese, M. Krapchanska, E. Mladenova, *International Journal of Hydrogen Energy*, **39(36)**, 21561 (2014)
41. Z. Stoynov, D. Vladikova, B. Burdin, J. Laurencin, D. Montinaro, A. Nakajo, P. Piccardo, A. Thorel, M. Hubert, R. Spotorno, A. Chesnaud, Differential Resistance Analysis - a New Tool for Evaluation of Solid Oxide Fuel Cells Degradation. MRS Advances, Cambridge University Press, (2017), DOI:10.1557/adv.2017.592.
42. Z. Stoynov, D. Vladikova, B. Burdin, Differential Resistance Analysis - Current Achievements and Applications, *Bulg. Chem. Communic*., (this issue)
43. Z. Stoynov, D. Vladikova, B. Burdin, J. Laurencin, D. Montinaro, G. Raikova, G. Schiller, P. Szabo, Differential Analysis of SOFC Current-Voltage Characteristcs, *Applied Energy*, **228,** 1584 (2018).

Здравко Стойнов - Ученият, който създаваше нови хоризонти

Д. Владикова

Институт по електрохимия и енергийни системи „Акад. Евгени Будевски“, Българска академия на науките, ул. Акад. Г. Бончев, бл.10, София 1113, България

Bulgarian Chemical Communications, Volume 50 Special Issue D (pp. 21 – 30) 2018

Differential Resistance Analysis – Current Achievements and Applications

Z. Stoynov[†], D. Vladikova[*], B. Burdin

Acad. E. Budevski Institute of Electrochemistry and Energy Systems- Bulgarian Academy of Sciences, 10 Acad. G. Bonchev Str., Sofia 1113, Bulgaria

Received August 12, 2018 Revised September 1, 2018

Some of the most severe hurdles towards deployment of fuel cells are lifetime and durability. For Solid Oxide Fuel Cells (SOFCs) the degradation rates (DR) currently reported are below 1% kh^{-1}, with a tendency for further decrease to 0.1% kh^{-1}. The SoA degradation already requires long term testing, which takes several years. In addition to the accelerated stress tests, the testing time can be shortened by increasing the sensitivity and accuracy of the monitoring and diagnostic tools. This work presents a new method for degradation evaluation with higher sensitivity due to its operation with derivatives, named Differential Resistance Analysis (DRA). It applies the Differential Resistance Rd extracted from the current-voltage (*i-V*) characteristics and its time-evolution. The introduction of a spectral transformation procedure additionally increases the noise immunity and sensitivity of the method. The DRA works with two new performance indicators: $R_{d,min}$ and ΔU^* which are more sensitive respectively to transport and to activation losses. A more detailed information illustrated with examples on SOFC about the methodology, the advantages in respect to sensibility and noise immunity, the possibilities to evaluate the state of health and to register early warning signals, is presented. The results show about 10 times higher sensitivity towards evaluation of the DR in comparison with the classical approach.

Key words: degradation rate, SOFC, current-voltage characteristics, differential resistance, spectral transform

INTRODUCTION

Some of the most severe hurdles towards deployment of fuel cells (FC) are lifetime and durability, which still determine large part of the total costs. For evaluation of their operational stability on cell, stack, or system level, the parameter "degradation rate" (DR) is introduced. For its definition more often the decrease of the voltage for 1000 hours operation ($mV.kh^{-1}$) at constant load is used after linearization of the voltage-time (*V-t*) dependence. It may be performed for the whole testing time, thus giving the average DR, or for segments defining degradation stages [1]. The voltage change may be replaced with that of the corresponding area specific resistance ($m\Omega.cm^2.kh^{-1}$) [2-4]. For convenience the DR is expressed also in %.

For Solid Oxide Fuel Cells (SOFCs), which have flexibility towards the type of fuel [5], ability to tolerate the presence of impurities, higher efficiency combined with application of non-noble metal catalysts, the degradation rates currently reported are below $1\%.kh^{-1}$, while the near future targets are for its further decrease to 0.1% kh^{-1} [6-8]. For Solid Oxide Electrolyzers (SOEL) it exceeds $2\ \%.kh^{-1}$ [1, 9].

For faster development and integration of new materials and architectures [10, 11, 12] and thus for increase of lifetime, it is important to understand and quantify the degradation and its mechanisms, to describe them with models validated and transformed into predictive performance tools for fast assessment of the different degradation sources, of their origin and interactions, of dominating aging factors. There are some successful results confirming the efficiency of this approach [1, 13-20]. However, the accumulation of reliable data requires long term testing, which takes several years. Obviously this is a serious barrier, because the needed testing time is not compatible with that requested for market deployment of the tested products.

The testing time may be decreased by introduction of accelerating tests and by increase of the testing sensitivity. The accelerating stress test (AST) procedures and protocols are well introduced in batteries testing. The application of this approach is more advanced in PEMFC, while in SOFC they are currently under development [21, 22]. ASTs have to shorten the testing time, however, activating the same ageing mechanisms as in non-accelerated testing. This is a critical moment in the procedure, since the measured degradation should be transferred to the real-world behavior of the

To whom all correspondence should be sent:
E-mail: d.vladikova@bas.bg

tested system. Thus the selection of the acceleration parameters and the level of acceleration are of critical importance and may differ a lot for different systems and applications. The risk of test „pre-acceleration“ can be decreased and the testing time shortened by increasing the sensitivity and accuracy of the monitoring and diagnostic tools and thus providing reliable quantitative information about the evolution of the system, which is the aim of the presented work. This approach should be compatible with both the existing test station hardware and the applied electrochemical testing procedures.

From system theory point of view, fuel cells, as electrochemical power sources, are nonlinear large statistical systems with multi-parametric conditioning. During long term testing in addition to the voltage-time dependences, periodically (on 500 - 1000 hours) current-voltage (*i*-*V*) characteristics are recorded for acquiring more informative outputs. They give integral picture of the system (cell, stack) for a given state, ensuring the simplest external general description of fuel cells ability to produce electrical energy. The *i*-*V* curves describe the interrelation between the power components – voltage and current, which cover the entire operating region and reflect the dominant phenomena governing the process of electrical energy generation.

There are several important parameters of the *i*-*V* curves which can be regarded as performance indicators of the generator: open circuit voltage (OCV) – the voltage at zero current; power characteristics - the derivative power-current (*P*-*i*) dependence which determines the maximum available power P_{max}; the corresponding internal resistance (R_i) which has a minimum value ($R_{i,min}$) at that point and can be also recalculated as surface resistance, named area specific resistance (ASR). The vector of the parameters extracted from the *i*-*V* curves which describes in the most general way the ability of a given power source to produce power is used for characterization of fuel cells during their design, optimization and operation analysis. It forms the kernel of the Performance Vector, which includes also the operation conditions.

The electrochemical processes generating the electrical energy take place at the triple phase boundaries in the porous electrodes structure. They are also tightly connected with the transport processes in the gas- and in the solid phases. As far as electrochemical reactions are in nature non-linear, in general the *i*-*V* characteristics have also non-linear behavior. The typical *i*-*V* shape has three regions (Fig. 1) – a non-linear quasi-exponential part at low currents (Region I), which reflects the non-linear electrochemical reactions, followed by the quasi-linear Region II, dominated by linear (electron and ion) transport processes. At high currents the curve becomes again non-linear and steep (Region III), due to the concentration (mass transport) voltage drop caused by the fast consumption of the reactive gases [23, 24].

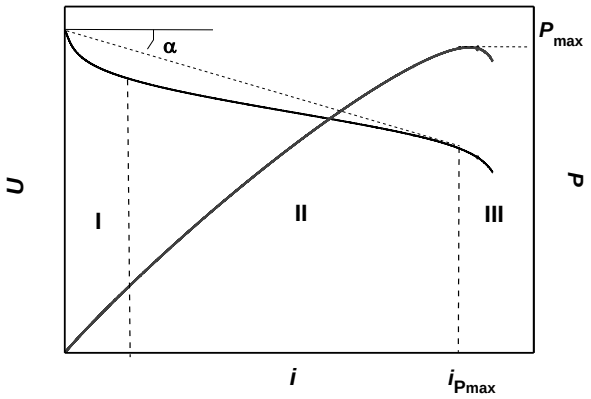

Fig.1. Current-voltage and current-power curves (schematic presentation).

Since the external behavior represented by the *i*-*V* curves is an integral product of a series of processes taking place in the constructive elements of the fuel cell and at their interfaces, it reflects all dominant phenomena governing the process of electrical energy generation and thus - the dominant barriers. However, the collection of more detailed information directly from the *i*-*V* measurements is still not possible, but challenging. To answer the demand for extraction of more information from the volt-ampere characteristics in respect to diagnostic and degradation, a new method with higher sensitivity, named Differential Resistance Analysis (DRA) was recently developed [25]. It is based on the differential analysis of the volt-ampere characteristics (DIVA). The information can be enriched with impedance measurements in selected working points of the *i*-*V* curves for deeper insight into the different degradation sources and improved understanding of ageing factors. The first publications on that topic aim to prove and evaluate the applicability of the method. This work is presenting more detailed information illustrated with examples on SOFC about the methodology, the advantages in respect to sensibility and noise immunity, the possibilities to evaluate the state of health (SoH) and to register early warning signals (EWOS), as well as requirements for collection of sufficient data with high quality. The experimental data are gathered from tests on button cells with dense YSZ electrolyte with thickness of about 5-10 μm supported by a thick porous Ni-YSZ hydrogen electrode of 260 μm. The oxygen electrode is a porous composite LSCF/CGO. A thin barrier layer

of CGO is deposited between the electrolyte and the LSCF electrode for limitation of the chemical reactivity. A pure LSC layer is used for current collector. The technology is a subject to proprietary information of SOLIDpower.

METHODOLOGY OF THE DIFFERENTIAL RESISTANCE ANALYSIS

To meet the challenge for sensitive degradation rate evaluation, a more detailed analysis of the current-voltage curves behavior and properties has been performed based on data from the literature, from producers catalogues, from own measurements and digital data from projects partners. The results confirm that *i-V* characteristics are sensitive to conditioning parameters such as temperature, quality and quantity of fuel and oxidizer, humidity etc. (Fig. 2a-c). At constant operating conditions they are dependent on the degradation (Fig. 2d). The parametric changes reflect in variations of the curves shape. Thus at constant operating conditions the deviations out of preliminary defined limits can serve as a measure for degradation. The quantitative estimation of the *i-V* shape can be accepted as performance indicator. For convenience the different profiles are classified in several general groups based on resemblance with letters from the alphabet. The most general is the "s" type shape in which the three regions presented in Fig. 1 are observed. It may be modified in "j" type curve with linear slope in Region I (Fig. 2c for wet hydrogen). Since the load current corresponding to Region III is not appropriate for operation, often the i-V curves include Regions I and II with the more typical "i" type curve (Fig. 2 a) and its "l" type modification with a quasi-constant slope. For more complicated structures, as double layered anodes or other types of structural or performance inhomogeneities more complicated shapes such as the "ss" one can be observed [26].

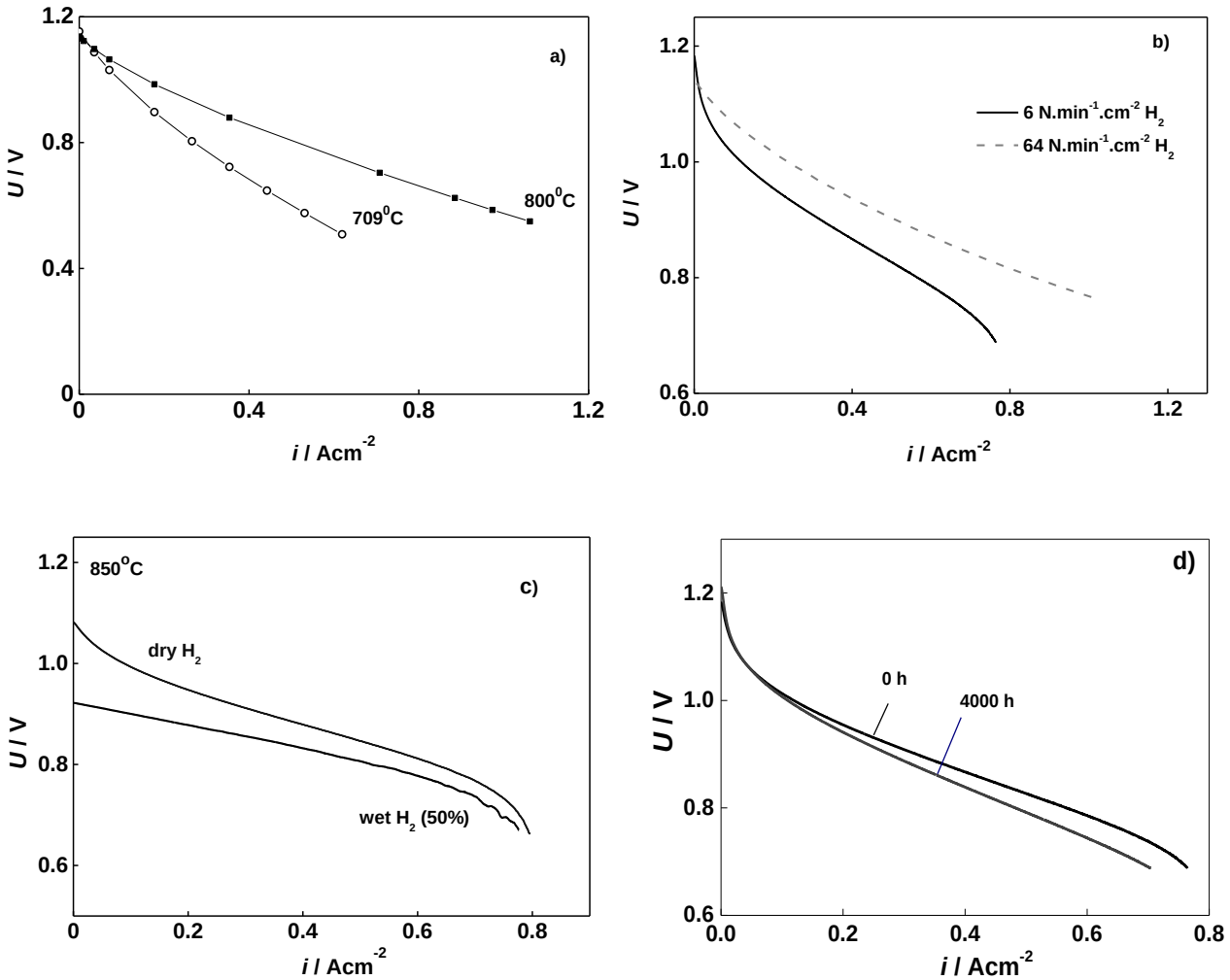

Fig. 2. Current-voltage curves at different operation conditions: a) different temperature; b) different quantity of fuel; c) wet and dry H2; d) at 0 h and 4000 h testing.

Shape Analysis

As it was already discussed the *i-V* curves are representing the integral external response of a series of internally linked processes that take place in the different components of the SOFC - in the volume, or at the different interfaces. The main purpose of the numerous studies is to go deeper into the elementary steps and mechanisms of the electrochemical reactions and to learn how to optimize and govern them. However, taking into account the different nature and the big variety of those internally linked processes, the total deterministic description of their integral external behavior becomes impossible. The problem solving approach is to represent the *i-V* characteristics as an external exhibition of the properties of a statistical and dynamically stochastic large system conditioned in definite operating environment. Those considerations suggest for application of statistical approaches for further analysis of the information coming from the *i-V* curves. One effective approach is the Shape analysis based on the derivative parameter differential resistance R_d. The application of R_d has been suggested by some authors [2,4,6,13], but there is no registered progress in the literature.

The differential resistance can be obtained by differentiation of Ohm's low – i.e. as the derivative of the voltage *V* with respect to the current *I*:

$$R_{d,k} = dU_k/dI_k. \quad (1)$$

Calculated for every *i-V* point, the values of R_d constitute a new function which describes the shape of the *i-V* curve:

$$R_d = f(I). \quad (2)$$

The new "Shape analysis", based on the analysis of R_d as a function of the current *I* (Eqn. 2), is named Differential Resistance Analysis (DRA).

In the general case the *i-V* dependence and its corresponding derivative function are non-linear. As presented in Fig. 3a for "s" type curve, the differential resistance sharply decreases in the beginning, reaching a minimum and then increases again. Three characteristic regions can be separated: Region I, which is connected with the activation losses, Region II, which concerns the transport losses and Region III, where the gas diffusion limitations are dominating. As far as the *i*-R_d dependence presents a derivative function, it offers additional new information which is coded in the *i-V* curves. It is important to find characteristic points of the *i*-R_d dependence which can quantitatively describe the new functional dependence and can serve as additional performance indicators.

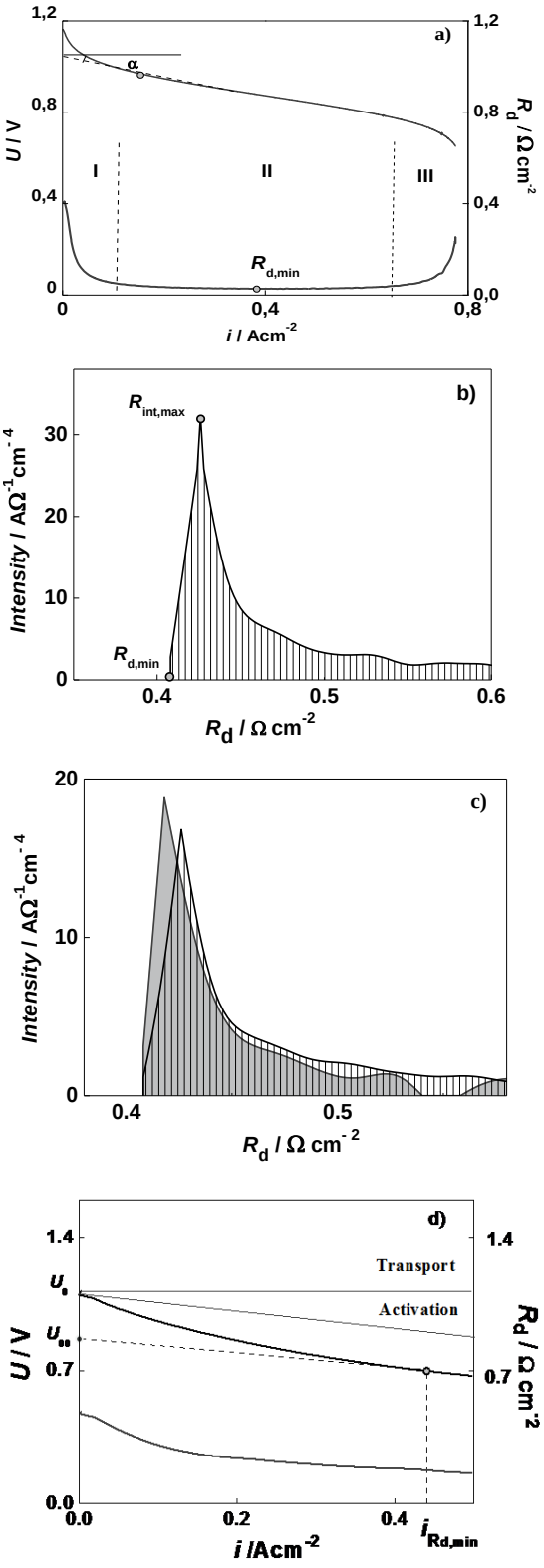

Fig 3. DRA procedure: a) *i-V* curve and R_d/I dependence; b) spectral transform of the R_d/I dependence; c) twin spectra; d) determination of the performance indicator ΔU^* (data from *i-V* curve of button cell sample tested 1200 h).

The minimum of the differential resistance $R_{d,min}$ can be regarded as an important characteristic point for the cell performance. It reflects the state of health at constant operating conditions, since it is determined by the intrinsic properties of the system and not by the external conditions as the load current. In addition, $R_{d,min}$ is more sensitive to changes since it corresponds to the point where the derivative becomes zero. It should be noted that Rd,min does not match R_{Pmax}. Impedance measurements could be important supporting information source.

Spectral Transform

The R_d-i curve can be presented in the more illustrative spectral form applying the Spectral Transform (ST) technique of aperiodic functions. It has been developed and applied for specialized analysis of impedance data, ensuring deeper observations based on enhanced sensibility, precision and noise immunity [27-29].

For DRA the ST converts the functional dependence (2) into the inverse one and produces the new functional dependence

$$dI/dR_d = F(R_d), \text{ i.e.} \quad (3)$$

$$S_{R_d} = \mathrm{ST}[F(R_d)]. \quad (4)$$

Thus the ST procedure converts the horizontal parts of the R_d/I plot into spectral picks with definite intensity (Fig. 3b). Since the parametric R_d spectrum is obtained by accumulating current regions with approximately equal values of this parameter, the intensity of the individual spectral peak is proportional to the length of the current range with similar values of the differential resistance.

In principle the spectral transform is not simply a presentation of the same data in different coordinates. By its nature it is a type of regression analysis which filters the statistical noises coming from the object itself and from the performed measurements, as well as non-statistical noises. Its high power of filtration is eliminating the possible wild points and the resulting "black" noise, since the presence of an outlier introduces a fuzzy low intensity line, located away from the spectral kernel of the assembly representing the basic phenomenon. The spectral peaks also provide objective information about the degree of dispersion, which is unavailable by other methods for analysis. The width of every spectral peak increases with the enhancement of the dispersion.

The produced Differential resistance spectrum of the "s" shaped *i-V* curve has two specific areas of interest – the spectral peak in the vicinity of $R_{d,min}$ which presents Segment II from Fig. 3a and the long tail corresponding to segments I and III. The spectral maximum has 2 characteristic points: $R_{d,min}$ - the minimum value of the differential resistance and $R_{int,max}$ – the value of the spectral maximum, which gives the most stable value of R_d observed in the widest current region. The spectral tail is produced by accumulation of similar R_d values, however coming from Segments I and II and thus with different origin in respect to the internal processes. To avoid the ambiguity, they can be separated as "twin spectra" describing the spectral behavior before and after $R_{d,min}$ (Fig. 3c).

Although reflecting the general internal behavior of the system, being situated in Segment II, $R_{d,min}$ is expected to be more sensitive to transport limitations. It is useful to find performance indicator with higher sensitivity towards activation losses. The DRA determines the value of $R_{d,min}$ and the corresponding current in the *i-V* curve (Fig. 2d). The tangential in this point ($I_{Rd,min}$) defines the voltage U_{00} which is the voltage at $I = 0$ in case the system would work with resistance equal to $R_{d,min}$. The difference $\Delta U^* = U_0 - U_{00}$ serves as a new indicator. Although connected with the position of $R_{d,min}$, it is more sensitive to activation losses.

The *i-V* shape analysis performed by the DRA introduces two additional performance indicators: $R_{d,min}$ and ΔU^*. Each of them has higher selectivity in respect to different degradation sources: ΔU^* is more sensitive to activation losses and $R_{d,min}$ - to transport hindrances which is a step forward towards identification of the degradation sources. A combined usage of the derived indicators is recommended since they may be sensitive to different degradation processes and sources. Additional impedance measurements can give more precise information about the origin of the degradation.

Applications and Specific Requirements

The DRA has very high sensibility towards degradation, since it works with the derivatives of the measured parameters, which are in principle more sensitive to small deviations. This is an opportunity for collection of reliable data from shorter tests avoiding severe accelerating conditions. Fig. 4 presents results from durability tests on button cell carried out for 1200 hours. For

the first 600 hours there is no significant difference in the *i-V* curves (Fig. 4a). The change of the voltage in the working point (U_{WP}) at current load 0.5 Acm^2 is less than 10 mV (Fig. 4b, Table 1), i.e. the accuracy of the measurements is low. The registered change corresponds to linearized DR about 1%.kh^{-1}. For reliable data longer testing is needed. The more detailed impedance characterization [30] shows temporal decrease of the ohmic resistance, very probably due to improved contacts (Fig. 4c). Obviously during the first 600 hours it compensates the progressive increase of the low frequency polarization resistance which is already dominating at 1200^{o}C.

Table 1. $R_{d,min}$ and calculated degradation rate from initial *i-V* curves measured on button cell tested for 1200 hours.

Time [h]	0	600	1200
U at I=0.5A/cm^2 [mV]	837	830	800
$R_{d,min}$ [mΩ.cm^{-2}]	334	365	408
R_d at I=0.5A/cm^2 [A.cm^{-2}]	435	420	360
DR_U [mV.kh^{-1}]	-	12	31
DR_U [%.kh^{-1}]	-	1.3	3.7
$DR_{Rd,min}$ [mΩ.kh^{-1}]	-	52	61.6
$DR_{Rd,min}$ [%.kh^{-1}]	-	15.4	18.5

The evaluation of the DRA degradation is based on the time-dependence of the new performance indicator $R_{d,min}$. Both $R_{d,min}$ and $R_{int,max}$ change noticeably – about 7% (Fig. 4d) which corresponds to DR about 15%.kh^{-1} (Table 1), i.e. the "zooming" effect of the DRA is about 10 times. For 1200 hours the degradation rate increases about 3 times, keeping the high "zooming" effect of the DRA (Table 1).

As it can be seen in Table 1, the testing current load (0,5 A/cm^2) is closer to that corresponding to $R_{d,min}$ of the pristine sample. However, with the increase of the degradation $R_{d,min}$ increases, while the corresponding current decreases, thus increasing the difference in respect to the testing load current. It is interesting to check if that increasing difference has accelerating effect in respect to degradation. Dedicated experiments for elucidating this hypothesis are under preparation.

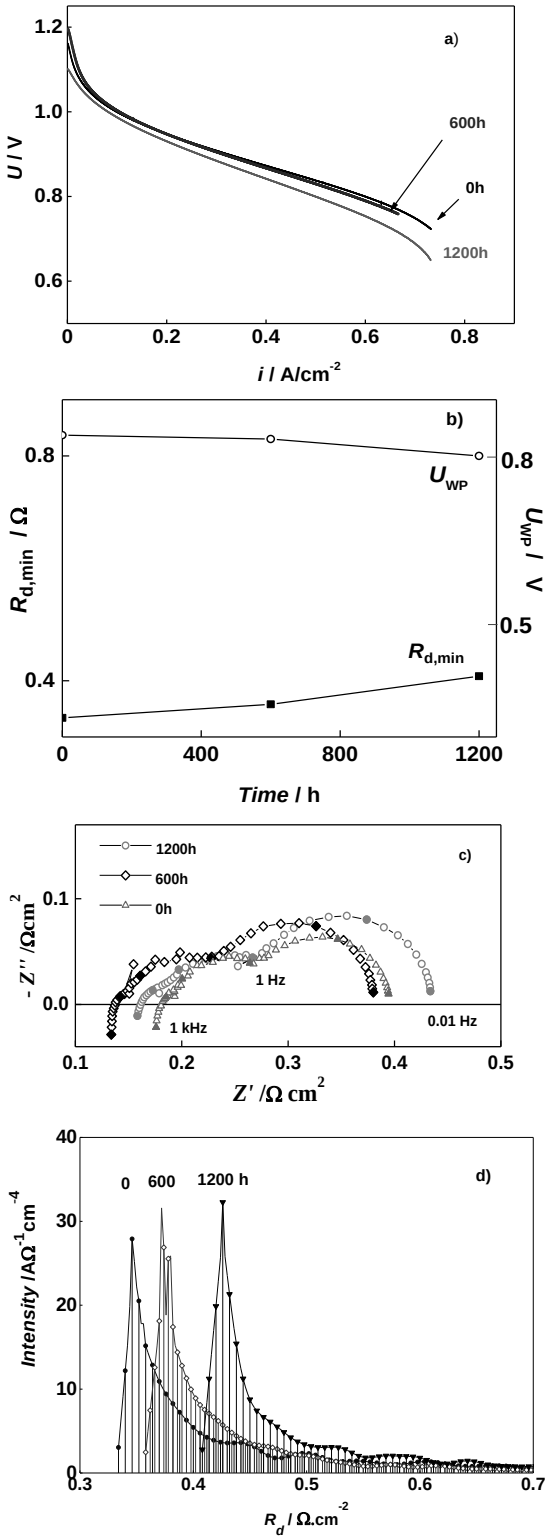

Fig. 4. DRA of button cell tested 1200 hours: a) *i-V* curves at 0; 600 and 1200 h; b) time dependence of $R_{d,min}$ and U_{WP}; c) impedance diagrams at I = 0.5 A/cm^2; d) corresponding DRA spectra. Operating conditions: 850° C; O_2 flow = 55 Nml.min^{-1}cm^{-2}; H_2 flow = 6 Nml.min^{-1}cm^{-2}.

The next example of DRA application is on button cell tested 2600 hours. The analysis is based on the time dependence of $R_{d,min}$ and ΔU^* as

performance indicators. The classical approach for calculation of DR, based on the operating voltage-time curve gives a very low value - below 0,4 %.kh^{-1} with low accuracy of the measurement (Fig. 5a). For higher data quality longer testing time is needed. As it can be seen in Fig. 5b, the *i-V* curves are also quite similar. The most pronounced changes during testing are registered for $R_{d,min}$ (Fig. 5c). The DR evaluated by the change of this parameter is 8%.kh^{-1} which is again an evidence for the high sensitivity of the DRA approach. The variation of ΔU^* is small. This result can be explained with low activation losses. For this testing interval they are not the rate limiting factor for degradation.

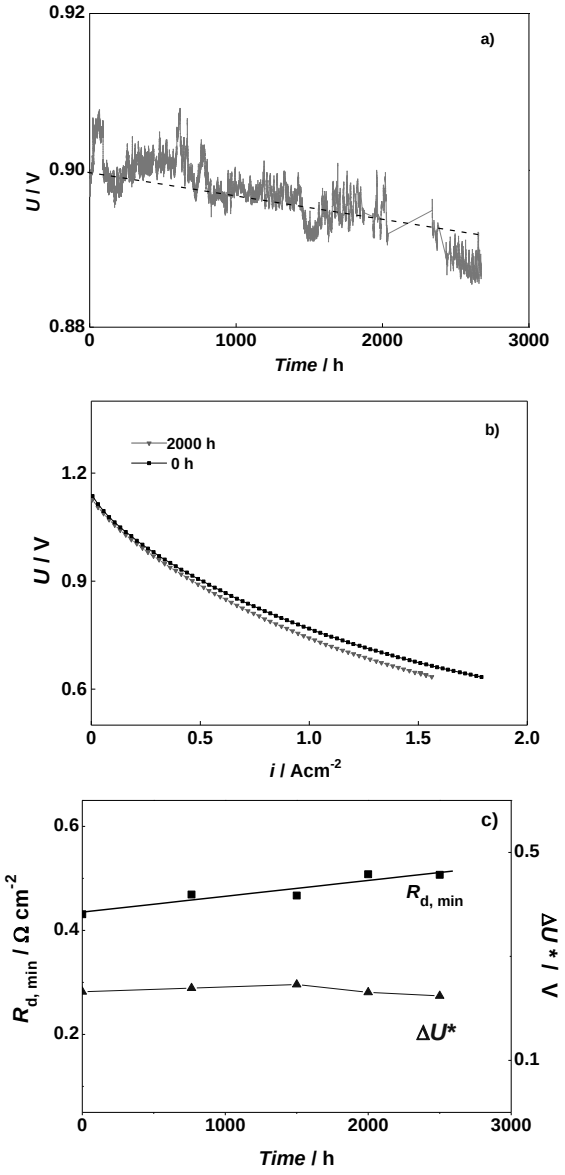

Fig.5. DRA of button cell tested 2600 hours: a) time dependence of U_{wp}; b) *i-V* curves at 0 and 2000 h; c) time dependence of $R_{d,min}$, ΔU^* ; Operating conditions: 750°C; air = 150 Nml.min^{-1}cm^{-2}; H_2= 64 Nml.min $^{-1}$cm^{-2}.

FURTHER APPLICATIONS OF THE DIFFERENTIAL RESISTANCE ANALYSIS

The presented examples for application of the DRA in degradation evaluation and monitoring confirm the high sensitivity of the new approach which comes from the operation with derivatives. As far as every differentiation increases data noise, the diagnostic success requires acquisition of more precise and confident initial data coming from the *i-V* measurements.

Data Quality Requirements

The current-voltage measurements in SOFC follow a step-wise increase of the current up to a given limit and a step-wise decrease back to zero current [31]. Thus the *i-V* measurements consist of a number of steps, i.e. of mini-cycles. Every mini-cycle should have a selected duration (hold time) with two periods - delay time and data acquisition time. The delay time is necessary (un-avoidable) for attaining a stable steady state of the object, since every change of the current to a new fixed value is followed by a relaxation period of the voltage, during which processes with different time-constants take place in the components of the cell. They are dependent on the cell/stack properties determined by various factors: selected materials, architecture, technology, external conditioning, state of the tested system etc. The relaxation ensures a stationary state needed for precise measurements, realized by the delay time before the measurement. After the end of the delay time starts the acquisition time, during which measurements of valid stationary data are carried out. The simplest way is to measure a single vector of data (time, voltage and current), however measurements of a set of data during the acquisition time provide for enhanced selectivity, precision and post-experimental assessment in respect to steady state and confidence. The full algorithm for a precise *i-V* measurement for application of the DRA can be found in [32]. One *i-V* curve measured for DRA performance should not exceed 40 measurement points.

Early warning Output Signals

The production of high quality data from the *i-V* measurements is a pre-requisite for the development of Early Warning Output Signals (EWOS) which is one of the most challenging targets in respect to SOFC monitoring and diagnostics since it paves the way towards development of urgent mitigation strategies during operation. The Warning Output Signals (WOS) practice is largely used in other technical zones

(machineries, buildings etc.). In the field of SOFCs, however, the accepted up to now approach of life testing applies simple measurements of the voltage at a constant current during operation at regular conditioning which cannot be effectively used for early diagnostic. An advanced approach is the periodic application of additional active input signals (*i-V* curves or impedance) for acquiring more informative outputs, necessary for diagnostic purposes.

The development of the Differential Resistance Analysis provides for the introduction of EWOS technique for SOFC. The differential resistance is a derivative function. The defined value of $R_{d,min}$ corresponds to the zero point of the R_d derivative – i.e. it is a second derivative. As a result, the changes of $R_{d,min}$ are observable much earlier than the changes of the other parameters. Thus the $R_{d,min}$ nature defines its properties to be used for early recognition of degradation, or other warning changes in the internal performance of the FC and thus for adequate diagnostic. The requirements for high quality initial data are mandatory.

The simplest EWOS procedure comprises:

- Precise measuremens of the *i-V* characteristics (up to a preliminary defined current lmit);
- Differential Resistance Analysis – calculation of R_d, Spectral Transform, determination of $R_{d,min}$ and ΔU^*;
- Consecutive performance of these two steps during life testing according to selected consequence of measurements;
- Calculation and monitoring of the DR, or the relative deviations of $R_{d,min}$ and ΔU^* in respect to its values in the pristine cell.

Since the DRA indicators are more sensitive, the early notification of sharper deviations from their smooth change can serve as EWOS for increased degradation, or another deterioration. Every indicator has higher selectivity in respect to different degradation source (ΔU^* is more sensitive to activation losses and $R_{d,min}$ - to transport hindrances). The application of additional indicators and impedance measurements can give more precise information about the origin of the degradation (ohmic losses, electrodes polarization etc.) [33].

DRA was performed on simulated *i-V* curves of a cell in a large stack operated for 36000 hours. The degradation affects the electrolyte, the anode (Ni-YSZ) and the cathode (LSM-YSZ). Cr contamination of LSM-YSZ causes the blocking of active sites. Thus the modeling conditions ensure high quality data (no external noise), constant operating conditions and constant degradation process reflecting both the activation and transport processes, with special accent on the blocking of the cathode active sites. The performed DRA operates with $R_{d,min}$ and ΔU^*. The ageing affects smoothly both $R_{d,min}$ and ΔU^*. It is more pronounced in ΔU^* (Fig. 6a,b). Thus the DRA confirms that the long term performance affects both the transport and the activation losses with stronger influence on the activation losses. The smooth linear increase of $R_{d,min}$ and ΔU^* indicates similar degradation which is introduced in the model and correctly captured by the DRA which guarantees an accurate description of the performance behavior reflecting the internal state of the system. It is expected that in case of degradation acceleration, this smooth dependence will be corrupted and the change will be observed earlier in respect to other indicators. For its experimental confirmation new modeling conditions will be introduced.

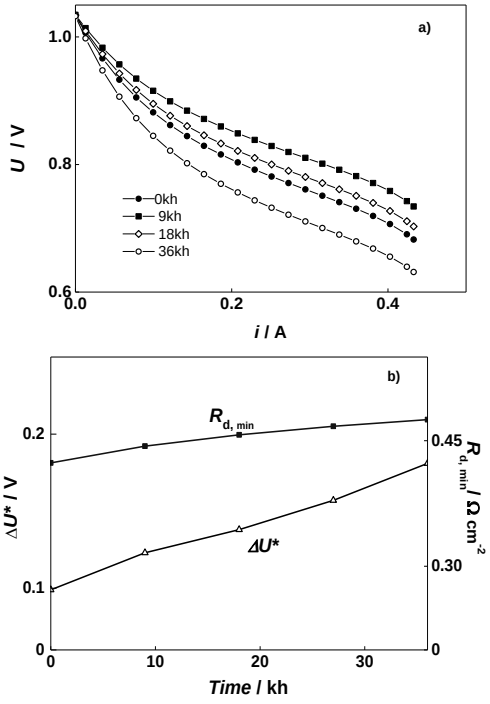

Fig.6. DRA of a cell in a large stack operated for 36000 hours: a) *i-V* curves at 0, 9, 18 and 36 kh; b) time dependence of $R_{d,min}$ and ΔU^*.

CONCLUSIONS

The development and approbation of the Differential Resistance Analysis technique based on the measured *i-V* curves (DiVA) shows that it can be applied as a useful tool with increased sensibility and accuracy for diagnostics and monitoring of SOFC (cells/stacks) and quantitative evaluation of the degradation rate. It operates with new and more selective performance indicators ($R_{d,min}$ and ΔU^*) which are extracted from the *i–V* curves and ensure

collection of reliable data from shorter tests avoiding severe accelerating test conditions.

However, since the high sensitivity of the new approach comes from the operation with derivatives which *apriori* increase the data noise, the diagnostics success requires acquisition of more precise measurements that ensure high quality initial data with limited number – up to 40 points on *i-V* curve.

Further development of the method is planned for its broader application, which can exceed the SOFC niche. Since the generally accepted parameter for evaluation of the degradation rate is based on the change of the potential at constant current load with the time, it will be useful if a correlation with the DRA performance indicators is found. An important direction for further development of the DRA is its application for detection of early warning output signals.

Acknowledgements. *The research leading to these results has received funding from the European Union's Seventh Framework Programme (FP7/2007-2013) Fuel Cells and Hydrogen Joint Undertaking (FCH-JU-2013-1) under grant agreement No 621207. The authors would like to thank Dr. Jerome Laurencin from CEA (Fr), Dr. Dario Montinaro form Solidpower (It) and Dr. Arata Nakajo from EPFL (CH) for samples preparation and support of the study with data from long term testing and from modeling.*

REFERENCES

1. J. Laurencin, M. Hubert, D.Sanchez , S. Pylypko, M. Morales, A. Morata, et al., *J.Electrochim. Acta*, **241**, 459 (2017).
2. N. Akkinapragada, B. Chowdhury, 38th North American Power Symposium, Sept. 17-19, 2006, Carbondale, IL, USA: Institute of Electrical and Electronics Engineers (IEEE), 553 (2007).
3. S. Jensen, C. Graves, M. Chen, J.B. Hansen, X. Sun, *J. Electrochem. Soc.*, **163**,(14), F1596 (2016).
4. R. Gemmen, M.C. Williams, K.Gerdes , *J. Power Sources*, **184**(1), 251 (2008).
5. S. Presto, A. Barbucci, M. P. Carpanese, M. Viviani, R. Marazza, *J. Appl. Electrochem.*, 39, 2257 (2009).
6. K. Park, S. Yu, J. Bae, H. Kim, Y.Ko, *J. Hydrogen Energy* , **35**, 8670 (2010).
7. L. Zhu, L. Zhang, A.V.Virkar, *J. Power Sources*, **29**, 138-55, (2015).
8. T-H. Lee, K-Y. Park, J-T. Kim, Y. Seo, K.B. Kim, S-J. Song, *J. Power Sources*, **276**, 120 (2015).
9. Fuel Cells and Hydrogen Joint Undertaking, 2018, ANNUAL WORK PLAN and BUDGET, p.68, (2018). http://www.fch.europa.eu/sites/default/files /FCH2JU2018AWPandBudget_final_11012018
10. D. Vladikova, Z. Stoynov, A. Chesnaud, A. Thorel, M. Viviani, A. Barbucci, G. Raikova, P. Carpanese, M. Krapchanska, E. Mladenova, *Int. J. Hydrogen En.*, **39**, 21561 (2014).
11. M. Viviani, G. Canu, M. P. Carpanese, A. Barbuccia, A. Sanson, E. Mercadelli, C. Nicolella, D. Vladikova, Z. Stoynov, A. Chesnaud, A. Thorel, Z. Ilhan, S.-Asif Ansar, *Energy Procedia*,, **28**, 182 (2012).
12. Carpanese, M.P., Barbucci, A., Canu, G., Viviani, M., *Solid State Ionics*, **269**, 80 (2015).
13. L. Zhu, L. Zhang, A.V. Virkar, *J. Power Sources*, **29**, 138 (2015).
14. M. Guida, F. Postiglione, G.Pulcini, *Reliability Engineering and System Safety*, **140**, 88-9, (2015).
15. A. Nakajo, A.P. Cocco, M.B. DeGostin, A.A. Peracchio, B.N. Cassenti, M. Cantoni, et al., *J. Power Sources*, **325**,786 (2016).
16. F. Usseglio-Viretta, J. Laurencin, G. Delette, J. Villanova, P.Cloetens, *J. Power Sources*, **256**, 394 (2014).
17. P. Polverino, C. Pianese, M. Sorrentino, D. Marra, *J. Power Sources*, **280**, 320 (2015).
18. W.G. Bessler, M. Vogler, H. Störmer, D. Gerthsen, A. Utz, et al., *Phys Chem Chem Phys* , **12**, 13888 (2010).
19. A. Hagen, R. Barfod, P.V. Hendriksen, Y-L. Liu, *J. Electrochem Soc*, **153(6)**, A1165 (2006).
20. S.J. Kim, M-B. Choi, M. Park, H. Kim, J-W. Son, J-H. Lee et al., *J. Power Sources*, **360**, 284 (2017).
21. A. Weber, J. Szász, S. Dierickx, C.Endler-Schuck, and E. Ivers-Tiffée, *ECS Trans.*, **68(1)**, 1953 (2015).
22. C. Duan, D. Hook, Y. Chen, J. Tongand, R. O'Hayre, *Energy Environ. Sci*., **10**, 176 (2017).
23. L. Jin, W. Guan, X. Ma, H. Zhai, W.G.Wang, *J. Power Sources*, **253**, 305 (2014).
24. Y. Zhu, K. Tomsovic, *Electric Power Systems Research* , **62**, 1 (2002).
25. Z.Stoynov, D.Vladikova, B. Burdin, J.Laurencin, D.Montinaro, Ar.Nakajo, P.Piccardo, Al.Thorel, M.Hubert, R.Spotorno, A.Chesnaud. Differential Resistance Analysis – a New Tool for Evaluation of Solid Oxide Fuel Cells Degradation. MRS Advances, Cambridge University Press, (2017).
26. N. Q. Minh, M. B. Mogensen, *Electrochem. Soc. Interface Winter*, **22**, 55 (2013).
27. D. Vladikova, P. Zoltowski, E. Makowska, Z. Stoynov, *Electrochim Acta* , **47**, 2943, (2002).
28. Z. Stoynov, D.Vladikova, Differential Impedance Analysis. Marin Drinov Academic Publishing House: Sofia, 2005.
29. Z.B. Stoynov, D.E.Vladikova, Electrochemical: Impedance Spectroscopy. In: Juergen Garche at all, editors. Encyclopedia of Electrochemical Power Sources, Amsterdam: Elsevier; **3**, 632, (2009).
30. G. Raikova, P. Carpanese, Z. Stoynov, D. Vladikova, M. Viviani, A. Barbucci, *Bulg. Cem. Comm.*, **41(2)**, 199 (2009).
31. Testing the voltage and power as function of current density Polarisation curve for a SOFC single cell, JRC Scientific and Technical Reports, https://ec.europa.eu/jrc/sites/jrcsh/files/sofc_sc_polarisation_curve.pdf
32. Z.Stoynov, D. Vladikova, B. Burdin, Recommendation for Measurements of Volt-Ampere

Characteristics of Fuel Cells for Diagnostic Purposes, Handbook of Test Procedures and Protocols, Chapter 3: ENDURANCE, Procedures and Protocols, http://www.durablepower.eu/index.php/handbook

33. A. Giuliano, M. P. Carpanese, M. Panizza, G. Cerisola, D. Clematis, A Barbucci, *El. Acta*, **240**, 258 (2017).

Диференциален анализ на съпротивлението - постижения и приложения

З. Стойнов†, Д. Владикова, Б.Бурдин*

Институт по електрохимия и енергийни системи „Акад. Евгени Будевски“, Българска академия на науките, ул. Акад. Г. Бончев, бл.10, София 1113, България

Постъпила на 12 август 2018г..; приета на 01 септември 2018г.

(Резюме)

Най-големите препятствия пред внедряването на горивните клетки са времето на експлоатация и издръжливостта им. При твърдооксидните горивни клетки (ТОКГ) цитираните в литературата стойности за скоростта на деградация (СД) са под 1% кчас$^{-1}$, с тенденция за по-нататъшно намаляване до 0,1% кчас$^{-1}$. При такива стойности, за изследване на деградационните процеси, са необходими дълготрайни тестове с продължителност няколко години. Освен чрез ускорените стрес-тестове, времето за изпитване би могло да бъде съкратено и чрез увеличаване на чувствителността и точността на инструменталните подходи за мониторинг и диагностика. Настоящата работа представя новия метод Диференциален анализ на съпротивлението (ДАС) за оценка на деградацията. Той осигурява повишена чувствителност, оперирайки с производната диференциално съпротивление R_d, което се изчислява от волт-амперните (*i*-*V*) характеристики и с неговата еволюция с времето. Въвеждането на процедурата на спектрална трансформация допълнително увеличава шумоустойчивостта и чувствителността на метода. ДАС работи с два нови характеристични за деградацията индикатора: R_d (минималното диференциално съпротивление) и ΔU^*, които са по-чувствителни съответно към активационните и към транспортните загуби. В работата е представена по-подробна информация, илюстрирана с примери върху ТОГК, които илюстрират методологията, предимствата по отношение на чувствителността и шумоустойчивостта, възможностите за оценка на състоянието н здраве и регистриране на ранни предупредителни сигнали за засилена деградация. Резултатите показват около 10 пъти по-висока чувствителност по-отношение на оценката на СД в сравнение с класическия подход.

Bulgarian Chemical Communications, Volume 50 Special Issue D (pp. 31 – 38) 2018

A Perspective on the Role of the Three-Phase Boundary in Solid Oxide Fuel Cell Electrodes

A. Bertei[1,2*], E. Ruiz-Trejo[2], D. Clematis[3], M. P. Carpanese[3], A. Barbucci[3], C. Nicolella[1], N. Brandon[2]

[1]*Department of Civil and Industrial Engineering, University of Pisa, Largo Lucio Lazzarino 2, 56122 Pisa, Italy*
[2]*Department of Earth Science and Engineering, Imperial College London, Prince Consort Road, SW7 2AZ London, UK*
[3]*Department of Civil, Chemical and Environmental Engineering, University of Genova, Via Montallegro 1, 16145 Genova, Italy*

Received May 14, 2018 Revised July 24, 2018

To the memory of Prof. Zdravko Stoynov

Within composite electrodes for solid oxide fuel cells (SOFCs), electrochemical reactions take place in the proximity of the so-called three-phase boundary (TPB), the contact perimeter where the electron-conducting, the ion-conducting and the porous phases meet. Strictly speaking, the TPB is a line and efforts have been made to increase its length per unit of electrode volume in order to reduce the activation losses. In this communication, by integrating physically-based modelling, 3D tomography and electrochemical impedance spectroscopy (EIS), a renovated perspective on electrocatalysis in SOFCs is offered, showing that the electrochemical reactions take place within an extended region around the geometrical TPB line. Such an extended region is in the order of 4 nm in Ni/$Sc_{0.2}Zr_{0.9}O_{2.1}$ (Ni/ScSZ) anodes while approaches hundreds of nanometres in $La_{0.8}Sr_{0.2}MnO_{3-x}$/$Y_{0.16}Zr_{0.92}O_{2.08}$ (LSM/YSZ) cathodes. These findings have significant implications for preventing the degradation of nanostructured anodes, which is due to the coarsening of the fractal roughness of Ni nanoparticles, as well as for the optimisation of composite cathodes, indicating that the adsorption and surface diffusion of oxygen limit the rate of the oxygen reduction reaction (ORR). In both anodes and cathodes, the results point out that the surface properties of the materials are key in determining the performance and lifetime of SOFC electrodes.

Key words: Solid oxide fuel cells, modelling, 3D tomography, degradation, electrochemical impedance spectroscopy, electrocatalysis

INTRODUCTION

Solid oxide fuel cells (SOFCs) are energy devices which produce electric power from the direct electrochemical conversion of a fuel, such as hydrogen. A SOFC consists of two porous electrodes, namely the cathode, which hosts the oxygen reduction reaction, and the anode, wherein fuel oxidation takes place [1]. The electrodes are separated by a dense ceramic electrolyte wherein oxygen ions, produced at the cathode, migrate towards the anode (Figure 1a).

SOFC can be used in reverse mode (Solid oxide electrolyzer cells, SOECs), to produce hydrogen. Then, innovative designs are also developed in the literature, based on properties of a mixed anionic and protonic conductor used as central membrane [2-6], or of electrolyte supported cells in symmetrical configuration [7] to improve operation as reversible solid oxide cells.

In composite electrodes, the cathodic and anodic electrochemical reactions involve gaseous species (i.e., H_2, O_2 and H_2O), electrons (e^-) and oxygen ions (O^{2-}) as follows:

$$\frac{1}{2}O_{2(g)} + 2e^-_{(el)} \leftrightarrow O^{2-}_{(io)} \quad (1)$$

$$H_{2(g)} + O^{2-}_{(io)} \leftrightarrow H_2O_{(g)} + 2e^-_{(el)} \quad (2)$$

These electrochemical reactions involve transport of neutral and charged species within different phases, namely the pores, the electron-conducting phase (*el*) and the ion-conducting phase (*io*). In both the cathode and the anode these electrochemical reactions are typically assumed to take place at the three-phase boundary (TPB), which is the contact perimeter among the electron-conducting, the ion-conducting and the pore phases, where both reactants and products can co-exist [8] (Figure 1b). This assumption effectively implies that the reactions take place along a mono-

To whom all correspondence should be sent:
E-mail: antonio.bertei@unipi.it

dimensional line, namely the TPB line. Following this assumption, efforts have been made in the past in order to maximise the TPB length per unit volume in both the electrodes to speed up the rate of electrochemical conversion and thus lower the electrode activation resistance [9-11].

However, generally catalysis and electrocatalysis indicate that heterogeneous reactions take place at the bi-dimensional interface between different phases, thus not along a mono-dimensional line. Therefore, also in SOFC electrodes the reaction zone must spread within an extended region around the geometrical TPB line.

This perspective article summarises the efforts of the authors in determining the lateral extension and the role of the TPB in both SOFC anodes [12] and cathodes [13-15] by combining experimental techniques, such as electrochemical impedance spectroscopy (EIS) and focused ion beam-SEM (FIB-SEM) tomography, as well as physics-based modelling. Rather than focusing on the details of the investigations, which can be found in a series of papers already published by the authors [12-15], this communication summarises the key findings and their practical implications in order to give a holistic overview of the role of the TPB in SOFC electrocatalysis.

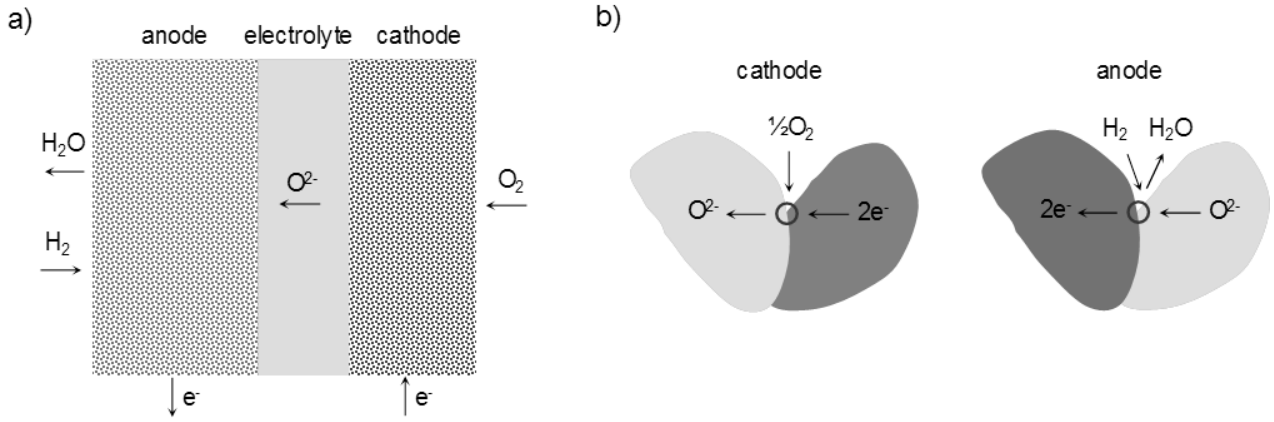

Fig. 1. a) Schematic representation of a solid oxide fuel cell. b) Cathodic and anodic reactions assumed to occur at the three-phase boundary, denoted with a circle.

THE ROLE OF THE TPB AT THE CATHODE

Experimental

The oxygen reduction reaction (ORR, Eq. (1)) was investigated in cathodes made of strontium-doped lanthanum manganite ($La_{0.8}Sr_{0.2}MnO_{3-\delta}$, LSM), which is the electron-conducting electrocatalyst, and yttria-stabilized zirconia ($(Y_2O_3)_{0.08}(ZrO_2)_{0.92}$, YSZ), which is the ion-conducting electrolyte. In fact LSM, with LSCF and BSCF and YSZ with doped ceria are the state of art materials respectively for cathode and electrolyte [16-17]. Thin layers (~3 μm in thickness) of porous LSM were sintered on both sides of a YSZ disk as described by Carpanese et al. [14]. Special attention was paid on the geometrical requirements of the working, counter and reference electrodes in order to ensure reliable EIS measurements in the three-electrode setup. EIS, in fact, is very powerful technique to study SOFC, if the appropriate corrections are performed [18].

Impedance spectroscopy measurements were carried out within the frequency range 10^6–10^{-1} Hz with different oxygen partial pressures (0.10–0.21 atm) in the temperature range 700–800 °C. The cathodic bias was varied between 0.0 V (i.e., open-circuit conditions) and 0.4 V (i.e., strong cathodic bias). The electrode thickness and porosity as well as the LSM particle size were evaluated through SEM analysis.

Modelling

The EIS data were interpreted by using a mechanistic model of the ORR mechanism [13,15]. It was assumed that molecular oxygen undergoes a dissociative adsorption on the LSM surface, then oxygen adatoms diffuse along the electrocatalyst surface to reach the TPB at the LSM/YSZ interface, where the proper charge transfer occurs (Figure 2). Thus, the global reaction in Eq. (1) was decoupled into two elementary steps:

$$\frac{1}{2}O_{2(g)} \leftrightarrow O_{(el,s)} \quad (3a)$$

$$O_{(el,s)} + 2e^-_{(el)} \leftrightarrow O^{2-}_{(io)} \quad (3b)$$

where the subscript *el,s* refers to the LSM surface.

This elementary mechanism was modelled by applying the conservation of oxygen adatoms on the LSM surface, taking into account the Langmuir dissociative adsorption and the Fick surface diffusion as in Eq. (4). The charge transfer in Eq. (3b) was modelled according to a linearized Butler-Volmer kinetics as in Eq. (5):

$$\frac{\partial\theta}{\partial t} = D_s^{eff}\frac{\partial^2\theta}{\partial x^2} + k_{des}\left(K\cdot p_{O_2}\cdot(1-\theta)^2 - \theta^2\right) \qquad (4)$$

$$i_{TPB} = i_{00}\cdot\left(\frac{\theta_0}{1-\theta_0}\right)^{1-\alpha}\cdot\frac{2F}{RT}\cdot\left(\eta_{cat} - \frac{RT}{2F}\ln\left(\frac{\theta_{eq}}{\theta_0}\frac{1-\theta_0}{1-\theta_{eq}}\right)\right) \qquad (5)$$

In Eqs. (4) and (5) θ represents the surface coverage fraction of oxygen adatoms $O_{(el,s)}$ (where θ_0 and θ_{eq} refer to the coverage fraction at the LSM/YSZ interface and in equilibrium condition, respectively), k_{des} and K the kinetic and equilibrium constants of oxygen adsorption, D_s^{eff} the effective surface diffusion coefficient of oxygen adatoms, p_{O2} the oxygen partial pressure, i_{00} the exchange current density pre-factor, η_{cat} the applied cathodic bias, T the absolute temperature, F and R the Faraday and gas constants, respectively. For more details on model equations the reader is referred to Bertei et al. [15].

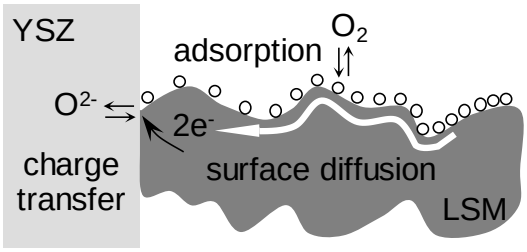

Fig.2. The proposed mechanism of the oxygen reduction reaction (ORR) in LSM/YSZ cathodes.

Results and interpretation

The mechanistic model in Eqs. (4) and (5) was used to fit experimental impedance spectra collected at different temperatures, oxygen partial pressures and cathodic bias [14]. The model was capable to reproduce the depressed shape of the cathode response as in Figure 3a, with minor deviations at low frequency likely due to possible heterogeneity of the electrode microstructure. The agreement between model and experimental results indicates that two contributions were present: a low-frequency feature, related to the coupled adsorption/surface diffusion process (i.e., Eq. (4)), and a medium-frequency feature, related to the charge transfer reaction at the TPB (i.e., Eq. (5)). In particular, simulations showed that the resistance of the charge transfer reaction was much smaller than the resistance associated to the adsorption/diffusion process, which represented the dominant resistance in the cathode (inset in Figure 3a).

In addition to reproducing the EIS behaviour, the model allowed for the prediction of the concentration profile of oxygen adsorbed on the surface of the electrocatalyst [15]. Figure 3b shows that the surface coverage of oxygen adatoms on the electrocatalyst surface differs from the equilibrium surface fraction in the proximity of the TPB, thus identifying the zone where adsorption and surface diffusion processes take place. The characteristic length of the adsorption/diffusion process was estimated as:

$$\delta = \sqrt{\frac{D_s}{2k_{des}\sqrt{Kp_{O_2}}}} \qquad (6)$$

which is equal to 0.2–0.3 μm within 700–800 °C. This value was found to hold also in composite LSM/YSZ cathodes, i.e., consisting of a mixture of LSM and YSZ particles, as reported by Fu et al. [13]. By varying the particle size, the authors showed that the cathode polarisation resistance scaled inversely with L_s/δ, where L_s is the semi-distance between two TPBs along the surface of an LSM particle (inset in Figure 3b).

Practical implications

The results summarised in the previous section imply that the characteristic length δ of the oxygen adsorption/diffusion process, equal to 0.2–0.3 μm, must be regarded as the effective width of the reaction zone around the geometrical TPB. Therefore, the oxygen reduction reaction does not take place along the mono-dimensional TPB line, rather, the rate-determining process (i.e., the adsorption and surface dissociation) extends for about 0.2–0.3 μm along the surface of the electrocatalyst. Such a lateral extension of the reaction zone can be neglected when LSM particles are bigger than 2–3 μm, that is, for $L_s/\delta >> 1$. However, when the particle size becomes comparable to the characteristic length δ, as in advanced electrodes produced via nanoparticle infiltration [19], the whole surface of the electrocatalyst nanoparticles may become active for the ORR, thus referring solely to the TPB as the reaction site would be meaningless.

Critically, this means that the surface properties of the electrocatalyst, such as the density of adsorption sites, the surface diffusion coefficient and the adsorption kinetic constant, are more

important than the increase in the TPB length because the charge transfer is not rate-limiting. In other words, the TPB length is not the only parameter to be maximised [15]. Rather, as also suggested by Banerjee and Deutschmann [20,21], research should focus on improving the adsorption and diffusion rates on the surface of the electrocatalyst.

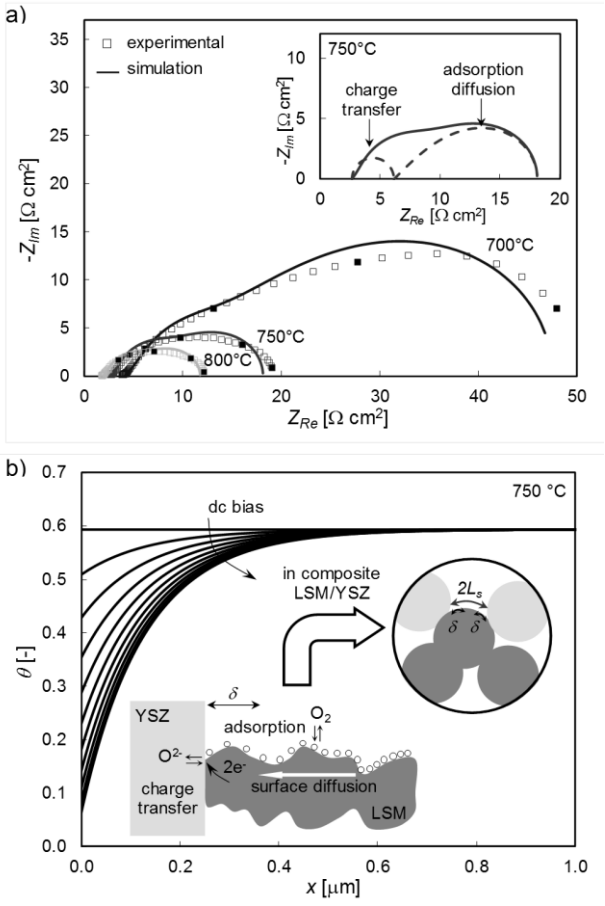

Fig 3. a) Fitting of the experimental EIS spectra of the porous LSM cathode at different temperatures (OCV, p_{O2} = 0.21 atm). The inset shows the deconvolution of the impedance in two contributions. b) Simulated profile of oxygen surface coverage along the LSM thickness. The insets show the extension δ of the adsorption/diffusion process in porous LSM and in composite LSM/YSZ cathodes compared to the semi-distance L_s between adjacent TPBs.

THE ROLE OF THE TPB AT THE ANODE

Experimental

The hydrogen oxidation reaction (Eq. (2)) was investigated in nanostructured anodes fabricated on the top of a YSZ disk. Scaffolds of scandia-stabilized zirconia ($(Sc_2O_3)_{0.10}(ZrO_2)_{0.90}$, ScSZ, i.e., the ion-conducting phase) were produced by tape casting and sintered at 1250 °C for 2 h as described elsewhere [12]. In fact, these are state-of-the art materials for SOFC, both in hydrogen and alternative fuels [16,22]. The electron-conducting phase was introduced within the scaffolds via multiple infiltrations of a 2 M $Ni(NO_3)_2$ ethanol solution followed by firing at 550 °C for 30 min to decompose the nitrate solution to NiO. The samples were finally fired in nitrogen at 750 °C for 30 min, then cooled at 550 °C where NiO was reduced to Ni in a 5% H_2/3% H_2O atmosphere.

The electrochemical degradation of the anodes was monitored continuously by using EIS within the frequency range 10^6–10^{-1} Hz at open circuit conditions, 550 °C in 5% H_2/3% H_2O atmosphere for up to 200 h. The anode microstructure was reconstructed ex-situ before and after degradation through FIB-SEM tomography [12]. A field emission gun-SEM (FEG-SEM) microscope was used to acquire images of the microstructure at higher magnification.

Modelling

The three-dimensional tomographic datasets were manually segmented in three phases (i.e., Ni, ScSZ and pore), allowing for the quantitative evaluation of the TPB length per unit volume L_{TPB} and the effective ionic conductivity σ_{io}^{eff} from the microstructural reconstructions [12,23].

A validated physically-based equivalent circuit [24] was adopted to deconvolve the impedance spectra and to relate the electrode charge transfer resistance R_{ct} to the microstructural properties:

$$R_{ct} = \sqrt{\frac{RT}{F}\frac{1}{i_0 L_{TPB}\sigma_{io}^{eff}}}\coth\left(\sqrt{h^2\frac{F}{RT}\frac{i_0 L_{TPB}}{\sigma_{io}^{eff}}}\right). \qquad (7)$$

where h is the electrode thickness and i_0 is the exchange current density of the hydrogen oxidation reaction. Notably, Eq. (7) assumes that the anodic charge transfer reaction takes place along the geometrical TPB line.

Hence, two independent estimations of the TPB density were obtained: one from the tomographic reconstruction of the anode microstructure, one through Eq. (7) from the charge transfer resistance evaluated from EIS data.

Results and interpretation

Figure 4a shows the evolution with time of the charge transfer resistance of the nanostructured Ni/ScSZ anode at 550 °C as obtained by the analysis of EIS data. Experimental results showed a rapid increase in charge transfer resistance within the first 100 h, followed by stabilisation [12,25]. Such a rapid increase in anode charge transfer resistance evidenced the presence of an electrochemical degradation mechanism affecting the hydrogen oxidation reaction (Eq. (2)).

Since the microstructure of the ScSZ scaffold can be considered stable at 550 °C, the increase in R_{ct} was attributed to a change in the active TPB length as a consequence of rearrangement of the Ni phase upon annealing [12]. Thus, Eq. (7) was used to estimate the temporal evolution of the TPB density from R_{ct}, as shown in Figure 4b. Figure 4b shows that the rapid increase in charge transfer resistance could be interpreted as a rapid decrease in TPB length per unit volume, followed by stabilisation (see line). However, Figure 4b shows that there was a mismatch between the TPB density estimated via EIS through Eq. (7) (line) and the TPB density measured by using FIB-SEM tomography (marks). In particular, while model predictions and tomography data matched after degradation (i.e., at 200 h), before degradation the L_{TPB} estimated electrochemically from EIS via Eq. (7) was excessively larger than the TPB length evaluated by FIB-SEM tomography. This means that while electrochemical impedance spectroscopy detected all electrochemical degradation, the microstructural evolution of the TPB evaluated with 3D tomography was not sufficient to explain on its own the rapid electrochemical degradation.

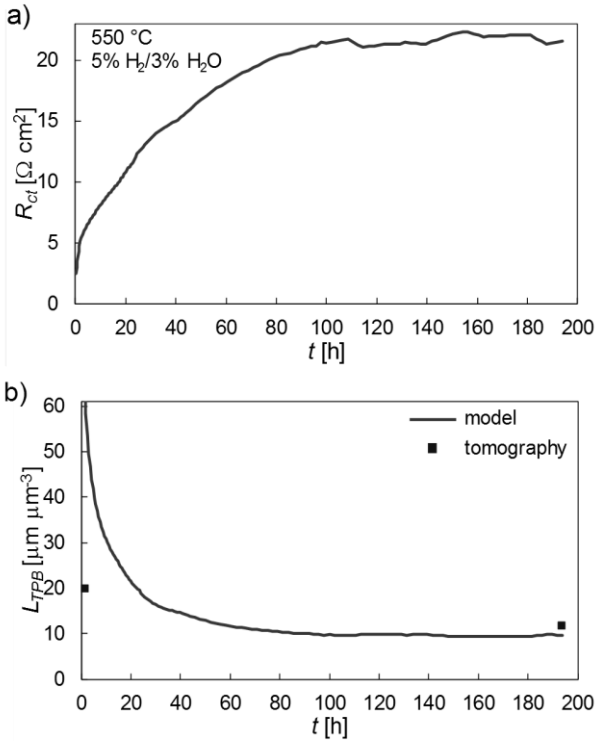

Fig. 4. a) Charge transfer resistance as a function of time of the infiltrated Ni/ScSZ anode as obtained from EIS analysis. b) TPB density as a function of time as estimated from the charge transfer resistance through Eq. (7) (line) and from FIB-SEM tomography (squares).

In order to explain such a mismatch between electrochemical response and microstructural analysis, the TPB line of the sample before degradation was observed at different magnifications, that is, at high resolution by using FEG-SEM (Figure 5a) and at lower resolution through FIB-SEM (Figure 5b). Figure 5a shows that, at high magnification, there are a lot of three-phase boundary points at the Ni/ScSZ interface which could not be resolved by FIB-SEM tomography with a resolution r = 27.2 nm, as shown in Figure 5b. So, the following hypothesis was made [12]: it was assumed that the TPB is rough at the nanoscale, that is, at a length scale which cannot be captured by the finite resolution of 3D tomography. In addition, it was assumed that the evolution of such a nanometric roughness was responsible of the rapid initial electrochemical degradation and of the mismatch of L_{TPB} shown in Figure 4.

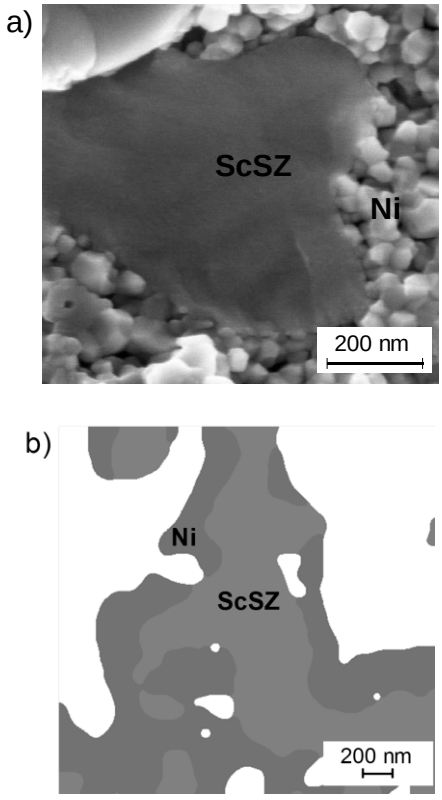

Fig. 5. TPB in a Ni/ScSZ nanostructured anode before degradation at different magnifications: a) FEG-SEM image; b) slice obtained from FIB-SEM tomography after phase segmentation.

In order to corroborate this hypothesis, the roughness of the TPB was quantified by calculating the fractal dimension D of the three-phase boundary according to the Mandelbrot formula [26]. The 3D microstructure was resampled with different voxel sizes r and the TPB density was evaluated at different resolutions as shown in Figure 6a.

Figure 6a shows that the smaller the voxel size r (i.e., better the resolution), the longer the TPB line,

in agreement with the empirical observation made above regarding Figure 5. This means that the TPB is rough at the nanoscale and that the TPB is a fractal in fresh nanostructured anodes [12].

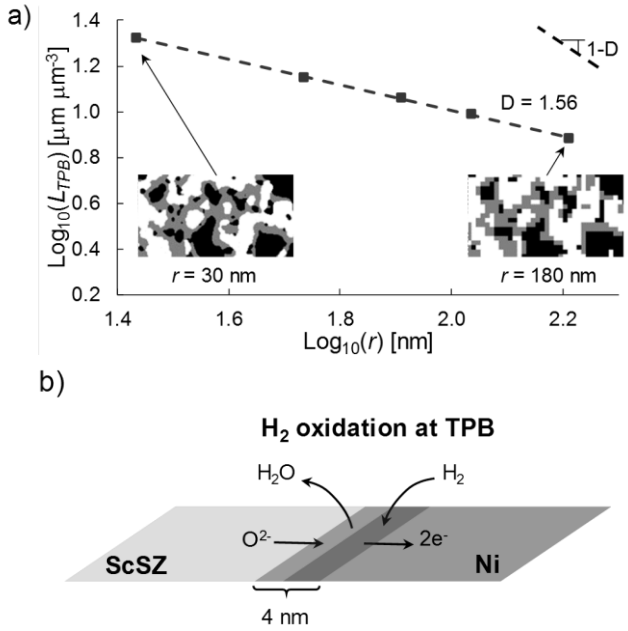

Fig. 6. a) Calculation of the fractal dimension of the TPB by resampling the 3D microstructure of the nanostructured Ni/ScSZ anode before degradation at different resolutions. b) Lateral extension of the reaction zone around the geometrical TPB line at the anode.

However, every fractal in nature is not infinitely rough, that is, there is always a cut-off resolution below which the roughness and nanometric features are not relevant anymore. In the case of the three-phase boundary, such a cut-off resolution must be related to the electrochemistry of the hydrogen oxidation reaction. Therefore, by comparing the TPB density estimated from impedance spectroscopy via Eq. (7) (L_{TPB}^{EIS} = 58.3 μm μm^{-3}, solid line in Figure 4b) and the TPB density measured with FIB-SEM tomography with a voxel size r = 27.2 nm (L_{TPB}^{tomo} = 19.8 μm μm^{-3}, mark in Figure 4b), the cut-off resolution $r_{cut\text{-}off}$ was estimated through the power-law dependence of the fractal TPB shown in Figure 6a, as follows [12]:

$$r_{cut-off} = r \cdot \left(\frac{L_{TPB}^{EIS}}{L_{TPB}^{tomo}} \right)^{1/(1-D)} = 27.2\ \text{nm} \cdot \left(\frac{58.3\ \mu\text{m}^{-2}}{19.8\ \mu\text{m}^{-2}} \right)^{1/(1-1.56)} = 4\ \text{nm} \quad (8)$$

Eq. (8) indicates that the nanometric roughness of the TPB does not affect the charge transfer reaction below 4 nm. This means that 4 nm represents the lateral extension of the hydrogen oxidation reaction zone across the geometrical TPB line, as depicted in Figure 6b. This is in good agreement with mechanistic predictions reported in the literature [27,28], which indicate that the reaction/surface diffusion width of the hydrogen oxidation reaction is in the order of 5 nm. Therefore, it is worth noting that the calculation of the TPB fractal dimension, which is a microstructural property, and its combination with the TPB density estimated by Eq. (7) from EIS data, which encode electrochemical information, provided an independent way to estimate the lateral extension of the anodic reaction around the geometrical TPB line.

Practical implications

The analysis reported in the previous section allowed for the identification of the width of the reaction zone in SOFC composite anodes, which is in the order of 4 nm. Such a lateral extension of the TPB can be neglected when dealing with micrometric particles, situation in which it can be safely assumed that the reaction occurs at the geometrical TPB line. However, this assumption is no longer valid when Ni nanoparticles are present, as in nanostructured electrodes [12,25] and in redox-cycled anodes [29]. Furthermore, the extension of 4 nm sets the minimum resolution requirements to resolve the TPB roughness and charge transfer phenomena in SOFC anodes.

The results shown above indicate that most of the rapid electrochemical degradation in infiltrated Ni-based anodes stems from the coarsening of the nanometric roughness of the three-phase boundary. This implies that the rapid electrochemical degradation can be limited or even prevented by controlling the interfacial properties between Ni and the ceramic scaffold to reduce the evolution of the nanometric roughness. Therefore, it is of fundamental importance to understand the nature of the interaction between Ni and ceramic particles. On the other hand, some strategies suggested in the literature, such as the co-infiltration of ceramic nanoparticles as big as 50 nm as sintering inhibitors [30], are expected to be ineffective because sintering inhibitors are too large when compared to the characteristic length of 4 nm of the TPB roughness.

CONCLUSIONS

This perspective paper summarised the efforts of the authors in investigating the nature of the three-phase boundary in SOFC electrodes and the limitations of assuming that charge transfer reactions take place at the geometrical TPB line. Through an advanced integration of mechanistic

modelling, electrochemical tests via impedance spectroscopy, microstructural analysis via SEM and 3D tomography, the lateral extension of the reaction zone around the geometrical TPB line was assessed in composite SOFC cathodes and anodes for the first time.

For the cathode side, results showed that the oxygen reduction reaction is limited by the adsorption and surface diffusion of oxygen on the electrocatalyst surface while the proper charge transfer process at the TPB is not rate-determining. The characteristic length of the oxygen adsorption/surface diffusion process was found to be in the order of 0.2–0.3 μm for LSM. For the anode, an innovative approach based on the calculation of the fractal dimension of the TPB revealed that the hydrogen oxidation reaction occurs within 4 nm around the geometrical TPB line. In addition, results showed that the evolution of the nanometric Ni roughness is responsible for the rapid electrochemical degradation of nanostructured Ni/ScSZ anodes.

These results highlighted that the common assumption of charge transfer reactions occurring at the mono-dimensional TPB line is fundamentally inappropriate, especially when the size of the particles becomes comparable to the characteristic width of the reaction zone. Considering the extension of the reaction zone around the TPB line reveals the importance of the surface properties of the electrocatalyst and of the wetting between metallic and ceramic phases, with practical implications for material selection, optimisation and control strategies to limit degradation phenomena.

REFERENCES

1. S.C. Singhal, *Solid State Ion.*, **135**, 305 (2000).
2. A.S. Thorel, J. Abreu; S.-A. Ansar, A. Barbucci, T. Brylewski, A. Chesnaud,. Z. Ilhan, P. Piccardo, J. Prazuch, S. Presto, K. Przybylski, D. Soysal, Z. Stoynov, M. Viviani, D. Vladikova *Journal of The Electrochemical Society*, **160(4)**, F360, (2013).
3. S. Presto, A. Barbucci, M. Viviani, Z. Ilhan, S.-A.Ansar, D. Soysal, A.S. Thorel, J. Abreu, A. Chesnaud, T. Politova, K. Przybylski, J. Prazuch, T. Brylewski, Z. Zhao, D. Vladikova, Z. Stoynov, *ECS Transactions*, **25(2)**, 773 (2009).
4. M. Viviani, G. Canu, M.P. Carpanese, A. Barbucci, A. Sanson, E. Mercadelli, C. Nicolella, D. Vladikova, Z. Stoynov, A. Chesnaud, A. Thorel, Z. Ilhan, S.-A. Ansar, *Energy Procedia*, **28**, 182 (2012).
5. D. Vladikova, Z. Stoynov, A. Chesnaud, A. Thorel, M. Viviani, A. Barbucci, G. Raikova, P. Carpanese, M. Krapchanska, E. Mladenova, *International Journal of Hydrogen Energy*, **39(36)**, 21561 (2014).
6. M.P. Carpanese, A. Barbucci, G. Canu, M. Viviani, *Solid State Ionics*, **269**, 80 (2015).
7. J. Xu, X. Zhou, J. Cheng, L. Pan, M. Wu, X.Dong, K. Sun, *Electrochimica Acta*, **257**, 64 (2017).
8. M. Mogensen, S. Skaarup, *Solid State Ion.*, **86-88**, 1151 (1996).
9. V.A.C. Haanappel, J. Mertens, D. Rutenbeck, C. Tropartz, W. Herzhof, D. Sebold, F. Tietz, *J. Power Sources*, **141**, 216 (2005).
10. B. Kenney, M. Valdmanis, C. Baker, J.G. Pharoah, K. Karan, *J. Power Sources*, **189**, 1051 (2009).
11. S. Amitai, A. Bertei, R. Blumenfeld, *Phys. Rev. E*, **96**, 052903 (2017).
12. A. Bertei, E. Ruiz-Trejo, K. Kareh, V. Yufit, X. Wang, F. Tariq, N.P. Brandon, *Nano Energy*, **38**, 526 (2017).
13. Y. Fu, S. Poizeau, A. Bertei, C. Qi, A. Mohanram, J.D. Pietras, M.Z. Bazant, *Electrochim. Acta*, **159**, 71 (2015).
14. M.P. Carpanese, D. Clematis, A. Bertei, A. Giuliano, A. Sanson, E. Mercadelli, C. Nicolella, A. Barbucci, *Solid State Ion.*, **301**, 106 (2017).
15. A. Bertei, M.P. Carpanese, D. Clematis, A. Barbucci, M.Z. Bazant, C. Nicolella, *Solid State Ion.*, **303**, 181 (2017).
16. F. S. Silva, T. M. Souza, *International Journal of Hydrogen Energy*, **42**, 26020 (2017).
17. A. Giuliano, M.P. Carpanese, M. Panizza, G. Cerisola, D. Clematis, A. Barbucci, *Electrochimica Acta*, **240**, 258 (2017).
18. G. Raikova, M. P. Carpanese, Z. Stoynov, D. Vladivkova, M. Viviani, A. Barbucci, *Bulg. Chem. Commun*., **41**, 199 (2009).
19. Z. Jiang, C. Xia, F. Chen, *Electrochim. Acta*, **55**, 3595 (2010).
20. A. Banerjee, O. Deutschmann, *J. Catalysis*, **346**, 30 (2017).
21. A. Banerjee, O. Deutschmann, *ECS Trans.*, **68**, 713 (2015).
22. S. Presto, A. Barbucci, M. P. Carpanese, M. Viviani, R. Marazza, *J. Appl. Electrochem*., **39**, 2257 (2009).
23. S.J. Cooper, A. Bertei, P.R. Shearing, J.A. Kilner, N.P. Brandon, *SoftwareX*, **5**, 203 (2016).
24. A. Bertei, E. Ruiz-Trejo, F. Tariq, V. Yufit, A. Atkinson, N.P. Brandon, *Int. J. Hydrog. Energy*, **41**, 22381 (2016).
25. J. Chen, A. Bertei, E. Ruiz-Trejo, A. Atkinson, N.P. Brandon, *J. Electrochem. Soc.*, **164**, F935 (2017).
26. B. Mandelbrot, *Science*, **156**, 636 (1967).
27. M. Vogler, A. Bieberle-hütter, L. Gauckler, J. Warnatz, W.G. Bessler, *J. Electrochem. Soc.*, **156**, B663 (2009).
28. D.G. Goodwin, H. Zhu, A.M. Colclasure, R.J. Kee, *J. Electrochem. Soc.*, **156**, B1004 (2009).
29. B. Song, E. Ruiz-Trejo, A. Bertei, N.P. Brandon, *J. Power Sources*, **374**, 61 (2018).
30. T. Klemensø, K. Thydén, M. Chen, H.-J. Wang, *J. Power Sources*, **195**, 7295 (2010)..

Нов аспект за ролята на трифазната граница при електроди в твърдо оксидни горивни клетки

А. Бертей[1,2 *], Е. Руиз-Трехо[2], Д. Клематис[3], М.П. Карпанезе[3], А. Барбучи[3], К. Николела[1], Н. Брендън[2]

[1]*Катедра по гражданско и промишлено инженерство, Университет в Пиза, Ларго Луцио Лазарино 2, 56122 Пиза, Италия*

[2]*Катедра по наука за Земята, Имериал колидж Лондон, ул. Принц Конкорд, СВ7 2АЗ Лондон, Великобритания*

[3]*Медицински факултет, Химическо и екологично инженерство, Университет в Генуа, Виа Монтегларо 1, 16145 Генуа, Италия*

Постъпила на 14 май 2018г.; приета на 24 юли 2018г.

(Резюме)

В памет на проф. Здравко Стойнов

В композитни електроди за твърдо оксидни горивни клетки (ТОГК), електрохимичните реакции се осъществяват в близост до така наречената трифазна граница (ТРВ), контактният периметър, където трите фази електрон-проводящи, йон-проводящи и пори се срещат. Строго погледнато, ТРВ е линия и за да се намалят активационните загуби, се налага да се увеличи дължината на тази линия на единица обем от електрода. В настоящата статия, чрез комбиниране на физическо моделиране, 3D томография и електрохимична импедансна спектроскопия (ЕИС) се предлага ново виждане на електродите за ТОГК, което показва, че електрохимичните реакции се осъществяват в разширена област около геометричната ТРВ линия. Тази разширена област е от порядъка на 4 нм в аноди от $Ni/Sc_{0.2}Zr_{0.9}O_{2.1}$ (Ni/ScSZ) и достига стотици нанометри в катоди от $La_{0.8}Sr_{0.2}MnO_{3-x}/Y_{0.16}Zr_{0.92}O_{2.08}$ (LSM/YSZ). Тези данни имат съществено значение за предотвратяване на деградацията на наноструктурирани аноди, дължаща се на загрубяване и фрактална грапавост на Ni-те наночастици, както и за оптимизиране на композитни катоди, което показва, че адсорбцията и повърхностната дифузия на кислорода ограничават скоростта на редукция на кислород (РК). Както в аноди, така и в катоди, резултатите показват, че повърхностните свойства на материалите са от ключово значение за определяне на експлоатационните качества и дълготрайност на електродите за ТОГК.

Bulgarian Chemical Communications, Volume 50 Special Issue D (pp. 39 – 47) 2018

A Comprehensive Approach to Improve Performance and Stability of State-of-the-Art Air Electrodes for Intermediate Temperature Reversible Cells: An Impedance Spectroscopy Analysis

M. P. Carpanese[1,2 *], D. Clematis[1], M. Viviani[2], S. Presto[2], G. Cerisola[1], M. Panizza[1], M. Delucchi[1], A. Barbucci[1,2]

[1]*Department of Civil, Chemical and Environmental Engineering (DICCA), University of Genova, Via all'Opera Pia 15, 16145 Genova, Italy*

[2]*Institute of Condensed Matter Chemistry and Energy Technologies (ICMATE), National Council of Research (CNR), c/o DICCA-UNIGE, Via all'Opera Pia 15, 16145 Genova, Italy*

Received May 15, 2018 Revised July 12, 2018

Solid oxide fuel cells (SOFC) are devices for the transformation of chemical energy in electrical energy. SOFC appear very promising for their very high efficiency, in addition to the capability to work in reverse mode, which makes them suitable for integration in production units powered with renewables.

Research efforts are currently addressed to find chemically and structurally stable materials, in order to improve performance stability during long-term operation.

In this work, we examine different approaches for improving stability of two state-of-the-art perovskite materials, $La_{0.6}Sr_{0.4}Co_{0.2}Fe_{0.8}O_{3-\delta}$ (LSCF) and $Ba_{0.5}Sr_{0.5}Co_{0.8}Fe_{0.2}O_{3-\delta}$ (BSCF), very promising as air electrodes. Two different systems are considered: (i) LSCF and BSCF porous electrodes impregnated by a nano-sized $La_{0.8}Sr_{0.2}MnO_{3-\delta}$ layer and (ii) LSCF-BSCF composites with the two phases in different volume proportions.

The study considers the results obtained by electrochemical impedance spectroscopy investigation, observing the polarisation resistance (R_p) of each system to evaluate performance in typical SOFC operating conditions. Furthermore, the behaviour of polarisation resistance under the effect of a net current load (cathodic) circulating for hundreds of hours is examined, as parameter to evaluate long-term performance stability.

Key words: LSCF, BSCF, LSM, stability, degradation, overpotential

INTRODUCTION

Among the existing devices devoted to energy production and storage, which could play an important role in the transition toward a sustainable energy scenario, high temperature solid oxide fuel and electrolysis cells (SOFC/SOEC) appear particularly promising.

Cheap catalysts can be used for electrode reactions and high temperature of operation allows obtaining high reaction rates and optimizing thermodynamic efficiencies; furthermore, flexibility of fuels [1-4] and reversible operation [5-11] are feasible, maintaining similar configuration and efficiency. New configurations, exploiting properties of a mixed anionic and protonic conductor used as central membrane [12,13], or taking advantages of a symmetrical configuration in an electrolyte supported cell [14] appear to be useful as reversible solid oxide cells.

Over the past few years, several materials have been investigated as anode materials for SOFC application [15]. Nowadays, Ni-YSZ based anode is widely used for SOFC, although facing long-term instability issues and suffering from carbon and sulfur poisoning and agglomeration of nickel particles at elevated temperature [16,17].

The Perovskite-based materials, such as $La_{0.8}Sr_{0.2}MnO_{3-\delta}$ (LSM), $La_{0.6}Sr_{0.4}Co_{0.2}Fe_{0.8}O_{3-\delta}$ (LSCF) and $Ba_{0.5}Sr_{0.5}Co_{0.8}Fe_{0.2}O_{3-\delta}$ (BSCF) perovskites have been extensively investigated as electrode materials in SOFC/SOEC devices over the last decade, since they can be used efficiently as air-side electrode [18-21]. Anyway, to make this technology affordable in order to gain market penetration, long-term operation without serious degradation must be achieved [22,23].

It has been widely proven that LSM is a stable material and, despite its intrinsically high ion migration energy [24], its oxygen ion diffusion can be strongly increased under reduction conditions, resulting in improvement of its activity [25]. On the other side, LSCF and BSCF, with their high oxygen ion surface exchange and transfer properties, show issues related to chemical and structural instability,

To whom all correspondence should be sent:
E-mail: carpanese@unige.it

which causes degradation during operation time [26-29]. Among the several causes of LSCF degradation, cations interdiffusion between interfaces have been reported as the most harmful, with consequent atoms depletion and phase separation [30].

Concerning BSCF, the same structural properties, which make it so active for oxygen reduction activity, also lead to lattice instability, which is a serious disadvantage for BSCF being considered as a reliable material at SOFC operating conditions.

Many different approaches have been applied in order to stabilise LSCF-based materials, and infiltration/impregnation is one of the most effective [31,32]. LSM has been frequently used as infiltrated continuous or discrete phase, improving in each case performances and stability [33,34].

Also the combination of different materials, based on producing a component that is superior to both of the components separately (generally a composite), has been widely used as an approach to improve properties. In SOFC case, whether it is an electrode [35-38] or an electrolyte [39,40], different conductive phases (ionic and/or electronic) are combined to produce a synergy result or to mitigate some original detrimental effect. Considering the "physiological" inclination of LSCF and BSCF to undergo a cation interdiffusion [22] under prolonged thermal effect or working time, the idea of the authors was to combine these materials to obtain a mutual chemical stabilisation, besides an optimisation of conduction transfer properties [41].

In any case, it is of primary importance to simulate real conditions of operation by the evaluation of the cathode redox behaviour under application of DC (direct current) overpotentials (η), which can drive oxygen incorporation (or release). To this purpose, electrochemical impedance spectroscopy (EIS) is a powerful fundamental technique adapted to the study of SOFC/SOEC systems, since it can be used as *in-situ* tool to characterise the performance of electrodes coupling the effect of a current load.

In this paper, a comprehensive experimental study was performed on the combination of LSM, LSCF and BSCF perovskites, with the purpose of investigating performance and long-term stability of these systems in SOFC working conditions. Two different types of air electrode were considered: *i)* LSCF- and BSCF-based, infiltrated by an LSM-discrete layer and *ii)* mixture of LSCF and BSCF, to obtain cathodes with different compositions of the two phases. The study was carried out mainly through impedance spectroscopy at open circuit (OCV) and under applied overpotential (η), to simulate real conditions of operations.

EXPERIMENTAL

Electrolyte substrates were fabricated from $Ce_{0.8}Sm_{0.2}O_{2-\delta}$ powders (SDC20-HP, Fuel Cell Materials) by cold pressing at 60 MPa, followed by one-step sintering at 1773 K for 5 hours in air. The resulting electrolyte disks had a diameter of 25 mm and a thickness of 1.2 mm. Infiltration procedure was applied on LSCF and BSCF electrodes, which were synthesized through a solution combustion synthesis method based on a mixed-fuel approach. The methodology for synthesis is reported elsewhere [42]. The LSM infiltrated layer was prepared as follows. A 2 M (mol l^{-1}) aqueous solution of $La_{0.8}Sr_{0.2}MnO_{3-\delta}$ precursors was prepared by dissolving proper amounts of $La(NO_3)_3 \cdot 6H_2O$ (99%), $Sr(NO_3)_2$ (>99%), and $Mn(NO_3)_2 \cdot 4H_2O$ (98%) (Sigma Aldrich) in distilled water, at room temperature. In order to better control phase formation and morphology, glycine (Sigma Aldrich) as chelating agent (volume ratio of glycine to LSM ~ 2.5:1) and polyvinyl pyrrolidone (PVP, Sigma Aldrich) as surfactant (0.05 wt% of LSM amount) were added to the metal nitrate solution. The solution was then heated to 473 K and stirred until a gel was obtained which was appropriate for cathode infiltration. A detailed description for infiltration is reported in a previous work [43]

Mixture of $Ba_{0.5}Sr_{0.5}Co_{0.8}Fe_{0.2}O_{3-\delta}$ (BSCF, Treibacher Industrie AG) and $La_{0.6}Sr_{0.4}Co_{0.2}Fe_{0.8}O_{3-\delta}$ (LSCF, FuelCellMaterials) commercial powders with three different volume ratios 50-50 v/v% (BL50), 70-30 v/v% (BL70) and 30-70 v/v% (BL30), were prepared using ball milling in distilled water for 20 h at room temperature. The procedure for the fabrication of the LSCF-BSCF composite electrodes is described in detail in a previous paper [39].

LSCF, BSCF and composite electrodes were deposited by slurry coating after mixing the powder in a mortar with alpha-therpineol (techn. 90%, Sigma Aldrich), to obtain suitable ink.

All the cells were prepared in three-electrode configuration and symmetry between working electrode (WE) and counter electrode (CE) was achieved by using a mask system. The reference electrode (RE) was placed on the WE side at a distance of 3 times the electrolyte thickness, as suggested in the literature to avoid polarization problems during impedance measurements [44,45]. All the cathodes were sintered at 1100 °C for 2 hours, obtaining after sintering a geometric area of 0.28 cm^2. The electrochemical impedance

spectroscopy (EIS) investigation was carried out with a potentiostat coupled to a frequency response analyzer (Autolab PGSTAT302N). Impedance measurements were performed both at open circuit voltage (OCV) and at applied cathodic overpotential (from −0.1 up to −0.3 V), applying a perturbation of 10 mV and between 0.1 Hz and 100 kHz of frequency range. Before performing the systematic electrochemical cell characterization, measurements of the cell rig inductance as well as a check on system linearity were carried out to obtain high quality EIS data [46]. Ageing tests were performed by applying a cathodic direct current (dc) of 200 mA cm^{-2} and checking the system evolution by impedance measurements at OCV, after interruption of the dc load at different times.

To observe cathode degradation, the polarization resistance (R_p) was evaluated as the difference between the low and high frequency intercepts with the real axis in the EIS Nyquist plots. Electrochemical impedance spectroscopy (EIS) measurements were carried out in a lab-constructed test station [47].

RESULTS AND DISCUSSION

Electrode performances – results of LSM infiltration and phase mixing

In Fig. 1 SEM images of LSM-LSCF and LSM-BSCF infiltrated electrodes are reported. The nanosized LSM layer is clearly visible on the electrode backbones. The electrochemical activity of LSCF and BSCF reference and infiltrated cathodes was evaluated with impedance measurements, whose results are reported in Fig. 1.

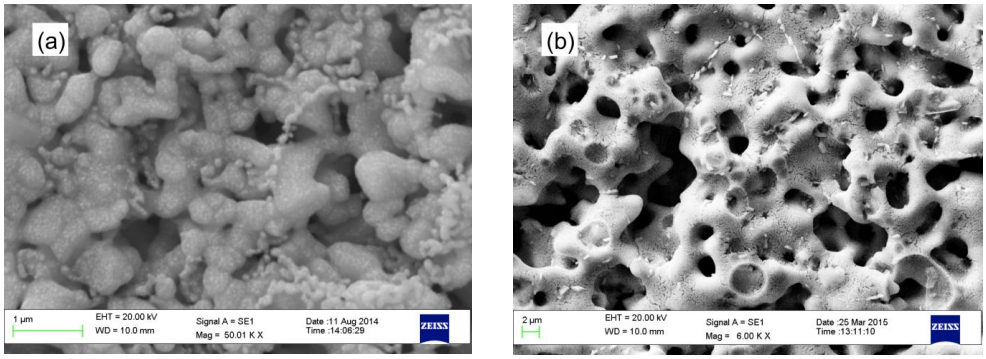

Fig. 1. SEM images of the top surfaces of the (a) LSM-LSCF and (b) LSM-BSCF infiltrated electrodes. The nano-sized LSM layer is apparent as the distributed phase on the porous backbones.

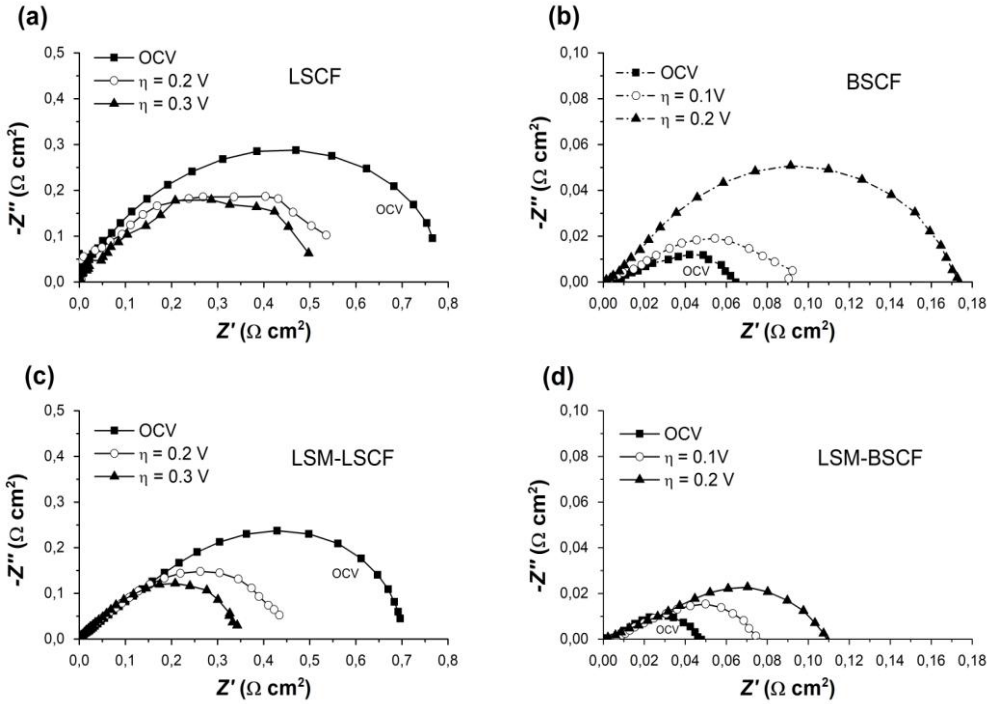

Fig. 2. Impedance spectra of the reference and LSM-impregnated LSCF cathodes ((a) and(c), respectively), and of the reference and LSM-impregnated BSCF cathodes ((b) and (d), respectively), at OCV and different overpotentials (η). Measurements conditions: 700 °C, 21% O_2 partial pressure; η: −0.1 V to −0.3 V (−0.2 V for BSCF).

The impregnation, applied with the purpose of stabilizing the initial cathode performances over time, produced, as expected, an improvement in the cathodic electrocatalytic activity, both in LSCF-based (Figs. 2a and 2c) and in BSCF-based (Figs. 2b and 2d) electrodes.It is worth highlighting that BSCF polarization resistance is one order of magnitude lower than in LSCF. Although LSCF and BSCF are mixed ionic-electronic conductors with substantial oxygen ions and electrons transport properties, the discrete and nano-sized LSM surface coverage introduced extra specific surface area, available for the oxygen exchange reaction at the cathode/gas interface.

This resulted in further improvement to the cathode electro-catalytic activity, both at OCV and when a net cathodic current flowed across the sample (applied η). At OCV, LSCF polarization resistance R_p decreased from about 0.78 Ω cm^2 at 700 °C, to 0.69 Ω cm^2 for the LSM-impregnated (see Figs. 2a and 2c). The improvement of BSCF in terms of R_p was from 0.066 Ω cm^2 to 0.046 Ω cm^2 (see Figs. 2b and 2d).

The results observed against the cathodic overpotential (η) appeared very interesting, since the behavior of BSCF and LSCF was contrasting. In Figs. 2a and 2c the Nyquist plots of LSCF and LSM-impregnated LSCF cathodes at OCV, η=−0.1V, η=−0.2Vand η =−0.3 V are reported. Cathodic polarization (η) has a beneficial effect, in terms of the reduction reaction kinetic, in both reference and impregnated LSCF performance, as pointed out by the decreasing trend of the polarization resistance. On the other hand, the trend of impedance spectra for the reference and impregnated BSCF electrodes, at OCV, η =−0.1 V and at η =−0.2 V conditions, shows that R_p increases with η (Figs. 2b and 2d).

It has been proposed for LSM and LSCF that, when electrons are injected by the applied overpotential, oxygen vacancies are formed to maintain charge neutrality [48,49]. This increase in vacancy concentration causes in LSM a change of kinetic regime, from a "surface" path to a "bulk" path, when a cathodic overpotential is applied higher than 0.2 V [19,20,50]. A similar improvement in the capability to incorporate and transfer oxygen ions takes place in LSCF. This clearly produces an improvement in oxygen surface activity and, in our study, this mechanism likely accounts for the impedance arch decrease displayed in Fig. 1 for LSCF-based cathodes: the synergic effect of LSM and LSCF results in the progressive decrease of the polarization resistance, as the potential applied increases. This improvement in activity is highlighted for LSM-LSCF (Fig. 2c), compared to pristine LSCF (Fig. 2a), both at OCV and under η.

Conversely, according to our results, in BSCF-based cathodes the situation appears quite different, since R_p increases as overpotential increases (Figs. 2b and d). Of course, there is a different way in which the injection of electrons influences the vacancies concentration, surmising that under the applied overpotential the formation of new vacancies is likely suppressed, resulting in the progressive decrease of oxygen activity [51,52]. It can be surmised that BSCF already has its largest concentration of oxygen vacancies before polarization, explaining the value observed of R_p lower for OCV conditions than for polarization, being this evident both for pristine and for LSM-BSCF electrodes (Fig. 2b and 2d, respectively). Similar phenomenon has been observed for other materials, which also have a large concentration of oxygen vacancies at room temperature [53,54]. If this is the case, the slower increase in R_p (Figs. 2b and d) observed for the infiltrated BSCF electrode (with respect to the pure one), has to be explained by the positive contribution of LSM, whose vacancy concentration increases and remains active, although not being able to compensate the opposite behavior of the scaffold material. Nevertheless, the results presented here show that BSCF-based electrodes decrease their activity under the reducing conditions caused by the increased cathodic overpotential.

Considering the electrodes made of LSCF and BSCF mixture, excellent results in terms of electrochemical performances were obtained, extracted in three-electrode configuration. In Fig. 3a impedance spectra of the three compositions (BL70, BL50 and BL 30) are reported at 650 °C, as compared to the those of the pristine LSCF and BSCF electrodes: considering the polarization resistance, all the composite cathodes displayed very promising performances, as compared to the literature, particularly to BSCF-based electrodes, which still remain the reference among state-of-the-art perovskite-based cathodes for SOFCs [55,56]. It is worth highlighting the excellent activity observed for BL70 sample and also for BL50 at this temperature: 0.021 and 0.027 Ω cm^2, respectively. Also BL30 sample showed improved performance of 0.045 Ω cm^2, if compared to the pure starting materials.

In Fig 3b the inverse of the global polarization resistance is reported ($1/R_p$), as function of temperature. In each case, an Arrhenius-type behavior was obtained and the corresponding activation energy was calculated. Despite its higher resistivity, BL30 shows the lower activation energy

value, 0.96 eV, indicating this composition as very suitable for low temperature of operation. BL70 shows an activation energy equal to 1.17 eV, very closed to that of pure BSCF (1.17 eV) and lower than pure LSCF (1.52 eV). The values obtained are in agreement with the literature (LSCF 1.45 eV [57] and BSCF 1.20 eV [58,59]).

Performance stability under current load

In order to evaluate the influence of the impregnation on cell performance stability, all the systems were tested over time at 700 °C under a DC current load of 200 mA cm^{-2} at 21% O_2 partial pressure. During the test, the current was periodically interrupted for the time necessary to perform OCV EIS measurements, in order to follow up the degradation of the electrode activity. The results obtained for the infiltrated system are reported in Figs. 4a and 4b. Degradation of electrode performance in the first operating hours is reported as key factor, because the analysis of performance losses in the first 100-300 working hours is often considered a good indication to evaluate electrode long-term stability [60-63].

Consequently, an ageing time of 200 hours was chosen to monitor the evolution of the LSCF system (Fig. 4a). For the BSCF-based system the ageing time was prolonged until 720 h of current load (Fig. 4b). In the case of the pristine LSCF cathode, a remarkable R_p increase (from 0.8 Ω cm^2 to 1.03 Ω cm^2) is visible already in the first 72 hours of working time, showing a 29% performance degradation, in accordance with that reported in literature [59,60,61].

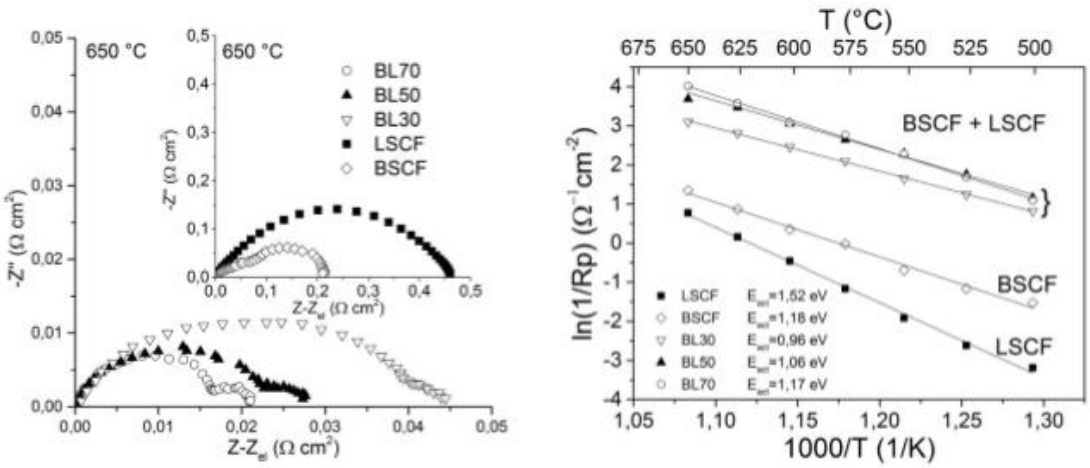

Fig. 3. (a) Impedance spectra at 650 °C and OCV for BL30, BL50, BL70. The inset shows impedance spectra for pure BSCF and LSCF. (b) Arrhenius plot for the five cathodes and calculated activation energy: BL30 (0.95 eV), BL50 (1.06 eV), BL70 (1.17 eV), BSCF (1.18 eV) and LSCF (1.52 eV).

Conversely, the polarization resistance related to the LSM-infiltrated LSCF electrode decreases over time from 0.7 Ω cm^2 to 0.515 Ω cm^2 (26% decrease) in 220 hours (see Fig. 4a), confirming a positive effect of the LSM infiltration on the long-term stability of the LSCF electrode. A meaningful effect due to the LSM impregnation is also observed on the BSCF electrodes (Fig. 4b).Although the LSM coating cannot prevent the increase in polarization resistance over time, it contributes to hindering BSCF degradation. According to other author [64] a possible beneficial effect on BSCF (which appears also in LSCF-based cathodes) could be related to a desirable cation inter-diffusion between the LSM and backbone, enable in inhibit structural modifications, albeit without blocking them altogether.

Considering an ageing time of 200 hours, for the LSM-impregnated BSCF electrodes R_p increases from 0.046 Ω cm^2 up to 0.08 Ω cm^2, with 74% of degradation, while R_p for the reference BSCF cathode increases from 0.081 Ω cm^2 to 0.16 Ω cm^2, with 98% of degradation. A comparable degradation is reached in the LSM-infiltrated BSCF electrode after 750 hours of working time (Fig. 4b).

Looking at the composite system, similar ageing tests were carried out, at the working temperature of 650 °C. All the electrodes showed a remarkable R_p increase in the first 24 h and each sample showed a different degradation rate. Anyway, after 75 hours of applied current load, in any case a slowdown on the R_p increase was observed (Fig. 5).

In particular, for BL70 sample, which is the most active electrode, three different intervals were identified, characterized by a different degradation rate: 0 - 24 h, 24-75 h and 75-200 h. Starting degradation was calculated as 6.67 x 10^{-4} Ω cm^2 h^{-1}, being this value in agreement with those extrapolated for BSCF and LSCF by the authors (~10^{-3} to 10^{-4} Ω cm^2 h^{-1}) and other authors [39,65].

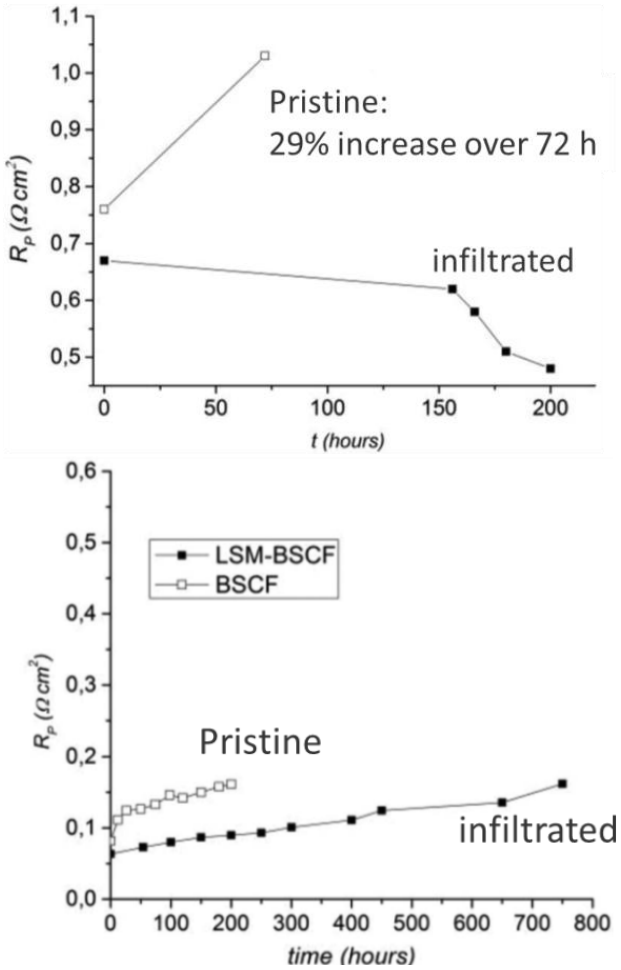

Fig. 4. Trend of the cathode polarization resistance (Rp) over time for (a) reference and LSM-infiltrated LSCF cathode and for (b) reference and LSM-infiltrated BSCF, during the ageing test under cathodic current load of 200 mAcm^{-2}. Conditions: 700 °C, OCV and 21% O_2 partial pressure. The testing duration time was 200 h for LSM-LSCF and 750 h for LSM-BSCF.

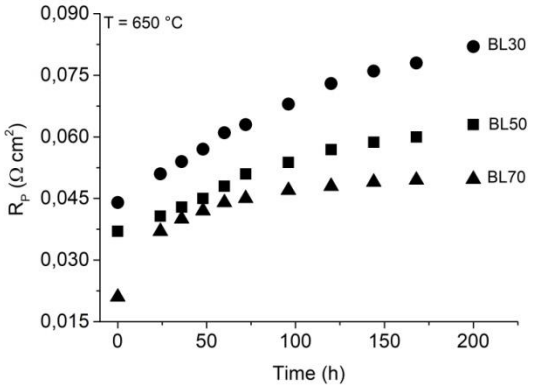

Fig. 5. Degradation rate for BL30, BL50, BL70 electrodes under an applied current load of 200 mA cm^{-2} at 650 °C.

In the final part of the ageing test (75 to 200 h) a trend toward 10^{-5} Ω cm^2 h^{-1} was evaluated, which represents an improvement in terms of stability. It is worth noticing that BL70 degradation rate slowdown had a positive effect on polarization resistance, which reached a noteworthy constant R_p value close to 0.048 Ω cm^2 (@650 °C), lower than those reported in literature by several authors for pure and fresh LSCF and BSCF electrodes [66,67] and comparable to data reported for BLSCF [64].

CONCLUSIONS

A diversified approach was carried out to increase long-term stability of perovskite-based materials, such as LSCF and BSCF. Two different systems were considered: (i) LSCF- and BSCF-porous electrodes, infiltrated by a nano-sized discrete layer of LSM and (ii) mixture of LSCF and BSCF materials to obtain composites with different amount of the two phases. The systems were characterized as cathodes on SDC electrolytes, in SOFC conditions of operation, by electrochemical impedance spectroscopy, in order to evaluate both cathode performance in terms of polarization resistance (R_p, at OCV and under applied cathodic overpotential, η) and long-term stability, by applying a current load of 200 mA cm^{-2} for 200 or 720 h, depending on LSCF or BSCF, respectively.

Very interesting results were found: LSM-impregnation had beneficial effects on the performance of LSCF and BSCF systems. The nano-sized layer on the cathode surface made available new surface area, resulting in improved oxygen surface exchange both at OCV and under applied η. Nevertheless, a contrasting behavior was highlighted for LSCF and BSCF when an increasing η was superimposed: it was apparent that, while LSCF-based electrodes improved their behaviour under reducing conditions, BSCF-based cathodes decreased their activity when a cathodic overpotential was applied.

Looking at the composite LSCF-BSCF electrodes, they revealed an excellent activity towards the oxygen reduction reaction. Particularly, BL70 sample showed an R_p value of 0.021 Ω cm^2 at 650 °C, confirming this composition as very promising to be used as cathode for low temperature SOFCs.

Although the results obtained from the long test under current load confirmed that LSCF and BSCF are intrinsically unstable materials, the two strategies pursued in this work to hinder degradation gave promising results. The polarization resistance of the LSM-LSCF electrodes decreased from 0.7 to 0.51 Ω cm^2 in 220 h at 700 °C, indicating even an improvement in electrocatalytic behavior over time. In the case of LSM-BSCF system, LSM layer could not totally compensate the BSCF degradation, although it

contributed to hinder it remarkably over almost 750 h of ageing test.

Considering the effect of LSCF and BSCF mixing on long-term stability, this appeared strongly correlated to the relative amount of the two phases. It has to be highlighted that the composition BL70, which showed an extremely low R_p value (0.021 Ω cm^2 at 650 °C), was also the one, which degraded more slowly. At the end of ageing time of 200 h, its R_p value was actually enough low to make BL70 composition as suitable for further promising investigation.

REFERENCES

1. A. Jun, Y.-W.Ju, G. Kim, *Faraday Discuss.*, **182**, 519 (2015).
2. A. Buttler, H. Spliethoff, *Renew. Sust. Energ. Rev.*, **82**, 2440 (2018).
3. N. Q. Minh, J. Mizusaki, S. C. Singhal, *ECS Transactions*, **78** (1) 63 (2017).
4. S. Presto, A. Barbucci, M. P. Carpanese, M. Viviani, R. Marazza, J. *Appl. Electrochem.*, **39**, 2257 (2009).
5. M. Viviani, G. Canu, M. P. Carpanese, A. Barbucci, A. Sanson, E. Mercadelli, C. Nicolella, D. Vladikova, Z. Stoynov, A. Chesnaud, A. Thorel, Z. Ilhan, S.-A. Ansar, *Energy Procedia*, **28**, 182 (2012).
6. S. Park, Y. Shao, J. Liu, Y. Wang, *Energy Environ. Sci.*, **5**, 9331 (2012).
7. D. Vladikova, Z. Stoynov, A. Chesnaud, A. Thorel, M. Viviani, A. Barbucci, G. Raikova, P. Carpanese, M. Krapchanska, E. Mladenova, *Int. J. Hydrogen Energy*, **39**, 21561 (2014).
8. C. H. Wendel, Z. Gao, S. A. Barnett, R. J. Braun, *J. Power Sourc*., **283,** 329 (2015).
9. P. Puengjinda, H. Nishino, K. Kakinuma, M. E. Brito, H. Uchida, *J. Electrochem. Soc.*, 164 (9), F889 (2017).
10. M. P. Carpanese, A. Barbucci, G. Canu, M. Viviani, *Solid State Ionics*, **269**, 80 (2015).
11. M. Hauck, S. Herrmann, H. Spliethoff, *Int. J. Hydrog. Energy*, **42** (15), 10329 (2017).
12. Thorel, A. S.; Abreu, J.; Ansar, S.-A.; Barbucci, A.; Brylewski, T.; Chesnaud, A.; Ilhan, Z.; Piccardo, P.; Prazuch, J.; Presto, S.; Przybylski, K.; Soysal, D.; Stoynov, Z.; Viviani, M.; Vladikova D. *Journal of The Electrochemical Society*, **160**(4), F360, (2013).
13. Presto, S.; Barbucci, A.; Viviani, M.; Ilhan, Z.; Ansar, S.-A.; Soysal, D.; Thorel, A. S.; Abreu, J.; Chesnaud, A.; Politova, T.; Przybylski, K.; Prazuch, J.; Brylewski, T.; Zhao, Z.; Vladikova, D.; Stoynov Z., *ECS Transactions*, **25** (2), 773 (2009).
14. Xu, J. ; Zhou, X.; Cheng, J.; Pan, L.; Wu; M.; Dong, X.; Sun, K., *Electrochimica Acta*, **257**, 64 (2017).
15. F. S. Silva, T. M. Souza, *Int. Journal of Hydrogen Energy*, **42** 26020 (2017).
16. Matsuzaki, Y.; Yasuda, I., *Solid State Ionics*, **132**, 261 (2000).
17. Khan, M. S.; Lee, S.-B.; Song, R.-H.; Lee, J.-W.; Lima, T.-H.; Park, S.-J., *Ceramics International*, **42**, 35 (2016).
18. J. Areum, K. Junyoung, S. Jeeyoung, K. Guntae, *ChemElectroChem.*, **3**, 511 (2016).
19. M. P. Carpanese, D. Clematis, A. Bertei, A. Giuliano, A. Sanson, E. Mercadelli, C. Nicolella, A. Barbucci, *Solid state Ionics*, **301**, 106 (2017).
20. A. Bertei, M. P. Carpanese, D. Clematis, A. Barbucci, M. Z. Bazant, C. Nicolella, *Solid State Ionics*, **303**, 181 (2017).
21. D. Heidari, S. Javadpour, S. H. Chan, *Energy Conversion and Management*, **136**, 78 (2017).
22. A. Gondolini, E. Mercadelli, A. Sangiorgi, A. Sanson, *J. Europ. Cer. Soc.*, **37** (3), 1023 (2017).
23. E. Mercadelli, A. Gondolini, P. pinasco, A. Sanson, *Metals Materials Int.*, **23** (1) 184 (2017).
24. M. M. Kuklja, E. A. Kotomin, R. Merkle, Y. A. Mastrikov, J. Maier, *Phys. Chem. Chem. Phys.*, **15**, 5443 (2013).
25. X. J. Chen, K. A. Khor, S. H. Chan, *Solid State Ionics*, **167**, 379 (2014).
26. R. Kiebach, W.-w. Zhang, W. Zhang, M. Chen, K. Norrman, H.-j. Wang, J.R. Bowen, R. Barfod, P. Vang, *J. Power Sources*, **283**, 151 (2015).
27. C. C. Wang, T. Becker, K. Chen, L. Zhao, B. Wei, S. P. Jiang, *Electrochim. Acta*, **139**, 173 (2014).
28. M. M. Kuklja, Y. A. Mastrikov, B. Jansang, E. A. Kotomin, *J. Phys. Chem. C*, **116**, 18605 (2012).
29. H. Gasparyan, J. B. Claridge, M. J. Rosseinsky, *J. Mater. Chem. A*, **3**, 18265 (2015).
30. J. S. Hardy, C. A. Coyle, J. F. Bonnett, J. W. Templeton, N. L. Canfield, D. J. Edwards, S. M. Mahserejian, L. Ge, B. J. Ingram, J. W. Stevenson, *J. Mater. Chem. A*, **6**, 1787 (2018).
31. T. E. Burye and J. D. Nicholas, *J. Power Sources*, **301**, 287 (2016).
32. A. J. Samson, M. Søgaard, P. V. Hendriksen, *Electrochim. Acta*, **229**, 73 (2017).
33. M. E. Lynch, L. Yang, W. Qin, J.-J. Choi, M. Liu, K. Blinn, and M. Liu, *En. Environm. Science*, **4**, 2249 (2011).
34. L. Almar, A. Morata, M. Torrell, M. Gong, T. Andreu, M. Liu, A. Tarancón, *Electrochim. Acta*, **235**, 646 (2017).
35. L. Navarrete, M. Balaguer, V. B. Vert, J. M. Serra, *Fuel Cells*, **17** (1), 100 (2017).
36. N. V. Lyskov, L. M. Kolchina, M. Z. Galin, G. N. Mazo, *Solid State Ionics*, **319**, 156 (2018).
37. A. Barbucci, M. P. Carpanese, M. Viviani, N. Vatistas, C. Nicolella, *J. Appl. Electrochem.*, **39**, 513 (2009).
38. A. Bertei, A. Barbucci, M. P. Carpanese, M. Viviani, C. Nicolella, *Chem. Eng. J.*, **2017-208**, 167 (2012).
39. Y. Yuan, T. Li, H. Nishijima, W. Pan, J. Gong, K. Wang, M. Wang, M. Zhang, X. Zhao, *J. Am. Ceram. Soc.*, **101**, 3130 (2018).
40. I. Khan, P. K. Tiwari, S. Basu, *Ionics*, **24** (1), 211 (2018).
41. A. Giuliano, M. P. Carpanese, M. Panizza, G. Cerisola, D. Clematis, A. Barbucci, *Electrochim. Acta*, **240**, 258 (2017).
42. F. Deganello, L. F. Liotta, G. Macrìı, E. Fabbri, and E. Traversa, *Materials for Renewable and Sustainable Energy*, **2,** 8 (2013).

43. A. Giuliano, M. P. Carpanese, D. Clematis, M. Boaro, A. Pappacena, F. Deganello, L. F. Liotta, A. Barbucci, *J. Electrochem. Soc.*, **164** (10), F3114 (2017).
44. M. Cimenti, V.I. Birss, J.M. Hill, *Fuel Cells*, **7**(5), 377, (2007).
45. J. Winkler, P. V. Hendriksen, N. Bonanos, M. Mogensen, *J. Electrochem. Soc.*,**145** (4), 1184 (1998).
46. G. Raikova, M. P. Carpanese, Z. Stoynov, D. Vladivkova, M. Viviani, A. Barbucci, *Bulg. Chem. Commun.*, **41**, 199 (2009).
47. M. P. Carpanese, M. Panizza, M. Viviani, E. Mercadelli, A. Sanson, A. Barbucci, *J. Appl. Electrochem.*, **45**, 657 (2015).
48. D.N.Müller, M. L.Machala, H.Bluhm, W. C.Chueh, *Nature Commun.*, **6**, 6097 (2015).
49. M. H. R. Lankhorst and J. E. ten Elshof, *J. Solid State Chem.*, **130**, 302 (1997).
50. F. H. van Heuveln, H. J. M. Biuwmeester, F. P. F. van Berkel, *J. Electrochem. Soc.*, **144** (1), 126 (1997).
51. A. S. Harvey, F. J. Litterst, Z. Yang, J. L. M. Rupp, A. Infortuna, and L. J. Gauckler, *Phys. Chem. Chem. Phys.*, **11**, 3090 (2009).
52. V. Bisogni, S. Catalano, R. J. Green, M. Gibert, R. Scherwitzl, Y. Huang, V. N. Strocov, P. Zubko, S. Balandeh, J. M. Triscone, G. Sawatzky, and T. Schmitt, *Nat Commun.*, **7**, 13017 (2016).
53. A. E. Bocquet, A. Fujimori, T. Mizokawa, T. Saitoh, H. Namatame, S. Suga, N. Kimizuka, Y. Takeda, and M. Takano, *Phys. Rev. B*, **45**, 1561 (1992).
54. M. Abbate, G. Zampieri, J. Okamoto, A. Fujimori, S. Kawasaki, and M. Takano, *Phys. Rev. B*, **65**, 165120 (2002).
55. L. Almar, H. Störmer, M. Meffert, J. Szász, F. Wankmüller, D. Gerthsen, E. Ivers-Tiffée, *Appl. En. Mater.*, **1**, 1316 (2018).
56. J. Areum, K. Junyoung, S. Jeeyoung, K. Guntae, *ChemElectroChem.*, **3**, 511 (2016).
57. J. M. Serra, J. Garcia-Fayos, S. Baumann, F. Schulze-Küppers, W. A. Meulenberg, *J. Memb. Sc.*, **447**, 297 (2013).
58. C. Duan, D. Hock, Y. Chen, J. Tong, R. O'Hayre, *Energy Environ. Sci*, **10**, 176 (2017).
59. Z. Shao and S. M. Haile, *Nature*, 431, 170 (2004).
60. J. Kim, S. Choi, A. Jun, H. Y. Jeong, J. Shin, G. Kim, *ChemSusChem*, **7,** 1669 (2014).
61. L.Zhi-Peng, T. Mori, J. A. Graeme, Z. Jin, J. Drennan, *Appl. Mater. Interfaces*, **3**, 2772 (2011).
62. S. P. Simner, M. D. Anderson, M. H. Engelhard, and J. W. Stevenson, *Electroch. Solid-State Lett.*, **9**, A478 (2006).
63. L. dos Santos-Gómez, J. M. Porras-Vázquez, E. R. Losilla, F. Martín, J. R. Ramos-Barrado, and D. Marrero-López, *J. Power Sources*, **347**, 178 (2017).
64. D. Ding, M. Liu, Z. Liu, X. Li, K. Blinn, X. Zhu, and M. Liu, *Adv. En. Mat.*, **3**, 1149 (2013).
65. B. Hirschorn, M. E. Orazem, B. Tribollet, V. Vivier, I. Frateur, M. Musiani, *Electrochim. Acta*, **55**, 6218 (2010).
66. X. Zhang, W. Zhang, L. Zhang, J. Meng, F. Meng, X. Liu, J. Meng, *Electrochim. Acta*, **258**, 1096 (2017).
67. L. Almar, J. Szász, A. Weber, E. Ivers-Tiffée, *J. Electrochem. Soc.*, **164**, F289 (2017)

Комплексен подход за подобряване производителността и стабилността на съвременни въздушни електроди за обратими горивни клетки при междинни температурни: анализ чрез импедансна спектроскопия

М.П. Карпанезе[1,2 *], Д. Клематис[1], М. Вивиани[2], С. Престо[2], Г. Герисола[1], М. Паница[1], М. Делучи[1], А. Барбучи[1,2]

[1]*Катедра по гражданско, химическо и екологично инженерство, Университет в Генуа, Виа але Опера Пиа 15, 16145 Генуа, Италия*

[2] *Институт за конвенционална материя по химия и енергийни технологии, Национален за съвет по научни изследвания (CNR) Виа але Опера Пиа 15, 16145 Генуа, Италия*

Постъпила на 15 юни 2018г..; приета на 26 юли 2018г.

(Резюме)

Твърдо оксидните горивни клетки (ТОГК) са устройства за преобразуване на химическа енергия в електрическа енергия. ТОКГ изглеждат много обещаващи предвид тяхната висока ефективност, в допълнение към способността им да работят в обратим режим, което ги прави подходящи за интегриране в системи, захранвани с възобновяеми енергийни източници.

Понастоящем, с помощта на научни изследвания, се полагат големи усилия да се намерят химически и структурно устойчиви материали, с цел за да се подобрят експлоатационните качества и стабилността на работа при дългосрочна експлоатация.

В този труд ние изследваме различни подходи за подобряване на стабилността на два от най-добрите перовскитни материали понастоящем: $La_{0.6}Sr_{0.4}Co_{0.2}Fe_{0.8}O_{3-\delta}$ (LSCF) и $Ba_{0.5}Sr_{0.5}Co_{0.8}Fe_{0.2}O_{3-\delta}$

(BSCF), много обещаващи като въздушни електроди. Разглеждат се две различни системи: i) LSCF и BSCF пористи електроди, импрегнирани с наноразмерен $La_{0.8}Sr_{0.2}MnO_{3-\delta}$ слой и ii) LSCF-BSCF композити с две фази в различни по обем пропорции. Статията разглежда резултатите, получени с помоща на електрохимична импедансна спектроскопия, като чрез измерване на поляризационното съпротивление (R_p) на всяка система, се определят експлоатационните качества при типични за ТОГК операционни условия. Освен това се изследва поведението на поляризационното съпротивление под действието на общо натоварване на тока (катодно) и циклично в продължение на стотици часове, като параметър за оценка на дългосрочната експлоатационна стабилност.

Bulgarian Chemical Communications, Volume 50 Special Issue D (pp. 48– 54) 2018

IT-SOFC Based on a Disaggregated Electrospun LSCF Nanofiber Electrode Deposited onto a GDC Electrolyte Disc: Preparation Technique and Morphological Characterization

C. Sanna[1], A. Lagazzo[1], E. M. Sala[2], R. Botter[1], P. Costamagna[3, †]

[1] *Department of Civil, Chemical and Environmental Engineering (DICCA), University of Genoa, Italy*
[2] *Department of Energy Conversion and Storage, Technical University of Denmark, Frederiksborgvej 399, DK-4000 Roskilde, Denmark*
[3] *Department of Chemistry and Industrial Chemistry (DCCI), University of Genoa, Italy*

Received May 15, 2018 Revised July 12, 2018

Laboratory-size intermediate temperature solid oxide fuel cells (IT-SOFCs) are manufactured, based on $La_{0.6}Sr_{0.4}Co_{0.2}Fe_{0.8}O_{3-\delta}$ (LSCF) nanofiber electrodes applied onto $Ce_{0.9}Gd_{0.1}O_{1.95}$ (GDC) electrolyte discs. The LSCF nanofiber electrodes are produced through electrospinning. The electrospun tissue is gently disaggregated in α-terpinol before been applied onto the electrolyte, in order to break the fibers into segments, while preserving their morphology. GDC electrolytes are obtained by uniaxial pressing of the GDC powders, followed by sintering. The dispersed nanofibers are deposited onto the electrolyte to form symmetrical IT-SOFCs, which are then heat treated. SEM characterisation of the heat treated IT-SOFCs proves that the nanofibers morphology is preserved, forming a 3-D structure with many contact points among the fibers themselves, which is expected to feature simultaneously enhanced charge conduction and electrochemical reaction. The cells are ready for electrochemical impedance spectroscopy (EIS), which is the ideal tool to characterize the electrochemical performance of the disaggregated electrospun LSCF nanofiber electrodes.

Key words: nanofiber; electrospinning; intermediate temperature solid oxide fuel cell (IT-SOFC); $La_{0.6}Sr_{0.4}Co_{0.2}Fe_{0.8}O_{3-\delta}$ (LSCF); sol-gel synthesis; $Ce_{0.9}Gd_{0.1}O_{1.95}$ (GDC).

INTRODUCTION

The upward trend of global energy emissions, and their likely multiple adverse effects, compel the adoption of eco-innovative energy supply solutions, to foster world transition into a paradigm of sustainability [1]. Fuel cells, featuring high efficiency and environmental compatibility, are considered the preferable candidate to substitute the conventional energy conversion technologies. Solid oxide fuel cells (SOFCs), based on ceramic materials, offer several advantages over other types of fuel cells, mainly due to the use of non-noble metals as catalyst, the possibility of being moulded in a variety of shapes, and the high fuel flexibility, which allows 100% tolerability towards CO and around 5% tolerability towards CH_4 (depending on the SOFC operating temperature) [2]. On the one hand, the traditionally high SOFC operating temperature (around 900°C) matches perfectly the feeding temperature of gas turbines (GTs), allowing an ideal coupling in hybrid cycles featuring up to 65% efficiency. Unluckily, on the other hand, this high operating temperature involves technological problems, primarily due to the different thermal expansion coefficient (TEC) of the SOFC components, causing delamination and eventually breaking. Another problem is that the high operating temperature favours an almost instantaneousdevelopment of the steam reforming of CH_4, whose endothermal behaviour can cause a steep temperature drop dangerous for the mechanical stability of the ceramic materials, limiting to about 5% the amount of CH_4 which can be fed directly into the SOFC and making internal CH_4 steam reforming practically unfeasible. These problems are heavily mitigated by lowering the operating temperature down to 550-850°C [3,4], which is the so-called intermediate temperature range. Furthermore, lower temperatures are expected to mitigate degradation, reduce sealing problems, enable the use of less expensive materials in the balance of plant and finally improve the response to rapid start-up. However, lowering the operating temperature also lowers the SOFC performance, since electrodes and electrolyte materials become less conductive. Furthermore, the kinetics of the electrochemical reactions decreases exponentially as temperature decreases; indeed, the

To whom all correspondence should be sent:
E-mail: paola.costamagna@unige.it

poor activity of the cathode is one of the key obstacles for the development of IT-SOFCs [5]. For these reasons, innovative materials are under investigation. For the electrolyte, $Ce_{0.9}Gd_{0.1}O_{1.95}$ (GDC) is used [6], while $La_{0.6}Sr_{0.4}Co_{0.2}Fe_{0.8}O_{3-\delta}$ (LSCF), which is a well - known MIEC (mixed ionic electronic con-ductor), is considered as of the most promising cathodes [3]. The number of active sites for the oxygen reduction reaction (ORR) is expected to increase dramatically with the increase of the specific surface area [7,8], and thus new electrode morphologies and architectures are under development. In this framework, nano-structured electrode scaffolds, often obtained through the electrospinning technique, are intensively investigated [9]. This preparation method offers advantages in terms of simplicity, efficiency, low cost and high degree of reproducibility of the obtained materials [10]. In addition, it allows to manufacture complex nanostructures, usually fiber-made, with specific properties, such as high surface area, high porosity and excellent mechanical strength, which make them very suitable for IT-SOFC electrode applications [11,2].

In the present paper, we present an innovative preparation technique for symmetrical cells employing LSCF electrospun electrodes, applied symmetrically onto GDC electrolyte discs. The LSCF tissue manufactured through the electrospinning technique is gently disaggregated before being applied onto the GDC electrolyte, in order to obtain short fiber segments which form a 3-D structure with a high number of contact points between the fibers, to be tested through the electrochemical impedance spectroscopy (EIS) technique in order to assess the electrochemical performance.

EXPERIMENTAL

Materials

LSCF fibers are synthesized using nitrates as precursors: lanthanum (III) nitrate hexahydrate $LaN_3O_9{\cdot}6H_2O$, strontium nitrate $Sr(NO_3)_2$, cobalt nitrate hexahydrate $Co(NO_3)_2{\cdot}6H_2O$ and iron (III) nitrate $Fe(NO_3)_3{\cdot}9H_2O$. Ethanol, N,N-Dimethylformamide (DMF) and distilled water are used as solvents. Polyvinylpyrrolidone (PVP) is used as carrier polymer. All these materials are provided by Sigma-Aldrich.

LSCF granular electrodes are manufactured using $La_{0.6}Sr_{0.4}Co_{0.2}Fe_{0.8}O_{3-\delta}$ powders provided by Sigma-Aldrich (product code 704288, particle size 0.7 - 1.1 μm, surface area 5-8 m^2/g).

GDC powders used for the electrolyte preparation are supplied by Fuelcellmaterials (GDC10-TC powder, particle size 0.1-0.4 μm, surface area 5.9 m^2/g). In the cases where the GDC powders are mixed with additives, 10 wt% ammonium polyacrylate/water and 5% polyvinyl alcohol (PVA)/water solutions are used, both supplied by Sigma-Aldrich.

Preparation Procedures

LSCF nanofiber electrodes

LSCF fibrous electrodes are manufactured through electrospinning. The starting solution is prepared by dissolution of 0.178 g of $Sr(NO_3)_2$ in 0.4 ml of distilled water. Subsequently, 4 ml of DMF and 6 ml of ethanol are added, followed by mixing for 2 minutes with magnetic stirrer. Then, 0.545 g of $LaN_3O_9{\cdot}6H_2O$, 0.122 g of $Co(NO_3)_2.6H_2O$ and 0.679 g of $Fe(NO_3)_3{\cdot}9H_2O$ are added to the solution, followed by mixing for 10 minutes. Lastly, 1.24 g of PVP are added, followed by 24 h mixing (always with magnetic stirrer). With this procedure, the molar ratio of the elements La, Sr, Co, Fe in solution is 6:4:2:8 respectively. After preparation, the solution is fed into a single-needle electrospinning device (Spinbow), consisting of four main parts: high-voltage generator, volumetric pump (KD Scientific), syringe and cylindrical collector (diameter 4 mm), which turns and shifts in order to ensure homogenous thickness to the electrospun tissue. The operating parameters for the electrospinning device have been discussed in a previous paper [3], and are reported in Table 1.

The LSCF nanofibers are heat treated following the procedure reported below [3]:

- 1°C/min from 20°C to 350°C;
- 0.2°C/min from 350°C to 500°C;
- 1°C/min from 500°C to 800°C;
- 1°C/min from 800°C to 20°C.

Table 1. Operating parameters of the electrospinning device [3].

Flow rate [ml/h]	Voltage [kV]	Needle-Collector Distance [cm]	Collector Translation Speed [mm/s]	Collector Rotation Speed [rpm]
0.5	17	12	1000	750

GDC electrolyte

For the preparation of the GDC electrolyte discs, two different ways of treating the raw GDC powders are employed. The first method consists in mixing a mass of 2 g of GDC powders with 50 mL of distilled water. Then 0.269 g of 10 wt% ammonium polyacrylate/water solution (dispersant) and 0.538 g of 10 wt% PVA/water solution (binder), and finally 50 mL distilled water are added, followed by 12 h treatment in an ultrasonic device (sonicator UR1 Retsch ultrasonic bath). Once the solution is dried, it is sieved and then it is ready for pressing. In the second procedure, the raw GDC powders are pressed with no preliminary treatment. Uniaxial pressing is performed, which is selected since it allows minimisation of the void degree of the electrolyte pellet. The press die body (13 mm diameter), is filled from the bottom: in this way the GDC powder distribution has a high degree of uniformity, resulting in a low void degree of the final electrolyte pellet. Applied pressure ranges from 50 MPa to 100 MPa. The GDC discs are then sintered in a furnace, following the procedure reported below:

- 1°C/min from 20°C to 200°C;
- 0.1°C/min from 200°C to 300°C;
- 10°C/min from 300°C to T_{max};
- T_{max} for 4h;
- 1°C/min from T_{max} to 20°C.

Three different values of T_{max} are tested: 1350°C, 1420°C and 1580°C. In all cases, after sintering, the GDC electrolyte diameter is 1.1 cm.

Symmetrical cell assembly

The LSCF nanofiber tissue is gently disaggregated in α-terpinol in the sonicator for 8 seconds. The resulting mixture is deposited symmetrically onto both faces of the GDC electrolyte discs.

Furthermore, symmetrical cells with LSCF granular electrodes are manufactured as well. In this case, the LSCF powder is dispersed in α-terpinol and deposited symmetrically onto the GDC electrolyte. All the symmetrical cells are heat treated following the procedure reported below:

- 1°C/min from 20°C to 350°C;
- 0.2°C/min from 350°C to 500°C;
- 1°C/min from 500°C to 1000°C;
- 1°C/min from 1000°C to 20°C.

In all cases, after heat treatment the electrodes have diameter 0.9 cm and thickness about 40 μm.

Characterisation methodology

With all the samples presented in this work, micrograph characterizations are carried out through a scanning electron microscope (SEM) Hitachi S-2500. SEM images of the GDC electrolyte surface are used to evaluate the average superficial porosity through the intercept method, using a 0.32 μm grid.

In addition, electrolytes are characterized in terms of geometrical density, Archimedes' principle density, mechanical bending, and thermal etching. Geometrical density is evaluated by measuring the pellet through a micrometer. The mechanical bending test is used to determine the Young's modulus and the ultimate strength point. The test is carried out through a Zwick-Roell Z0.5 instrumentation. The electrolyte disc is placed on an o-ring and a force is impressed through a sphere positioned in the centre (Fig.1). The ultimate strength (P) is measured at the breaking point of the sample, while the Young's modulus (E) and the maximum stress (σ_{max}) are calculated as follows [12]:

$$\sigma_{max} = \frac{6P}{4\pi t^2}\left((1+\nu)\ln\left(\frac{r}{e'}\right)+1\right) \quad (1)$$

$$e' = \left(\sqrt{1.6e^2 + t^2}\right) - 0.675t \quad (2)$$

$$E = \frac{0.552Pr^2}{t^3 y_m} \quad (3)$$

where σ_{max} [Pa]; ν = Poisson ratio – (assumed as 0.3); e = support footprint – (assumed as 0) [m]; P = ultimate strength [N]; r = o-ring radius [m]; t = sample thickness [m]; y_m = deformation [m]; E = Young's modulus [Pa].

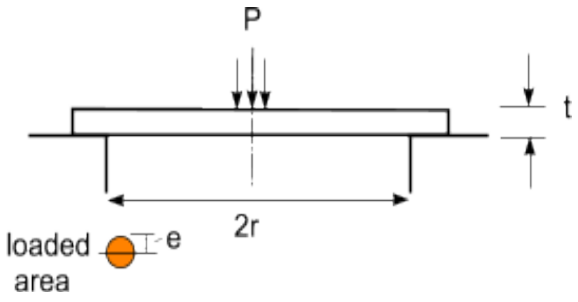

Fig.1. Schematic representation of the mechanical bending test.

GDC pellets are thermally etched, and then the linear intercept method is applied to the SEM pictures to evaluate the grain size [13]. The linear intercept method consists in drawing a set of randomly positioned line segments on the micrograph, counting the number of times each line segment intersects a grain boundary, and finding the ratio of intercepts to line length.

RESULTS AND DISCUSSION

LSCF nanofibers

SEM pictures of the heat treated LSFC nanofibers are reported in Fig. 2 In agreement with the results previously reported in [3], the nanofibers are continuous and randomly arranged. The average diameter is around 250 nm.

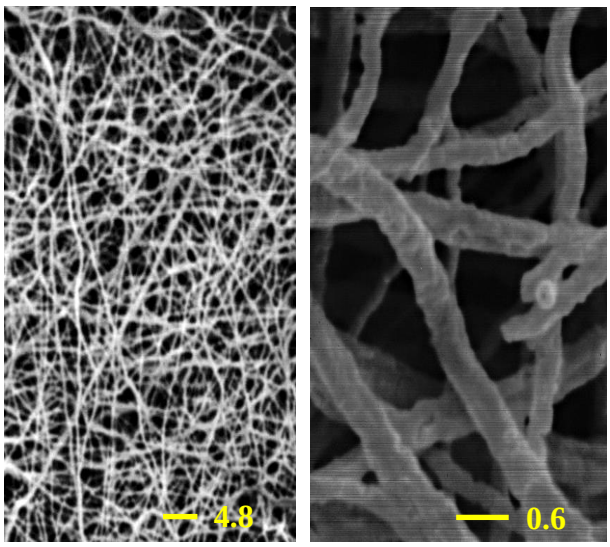

Fig. 2. SEM pictures of heat treated LSCF nanofibers.

GDC electrolyte

Fig. 3 reports SEM pictures of the surface of three different GDC discs. All the discs are obtained by mixing the GDC powders with a dispersant and a binder (first preparation method), followed by pressing at 80 MPa. Then, the GDC discs are sintered using three different T_{max} (1350°C, 1420 °C or 1580 °C). Fig.3(a) shows that with T_{max} = 1350°C, a high residual porosity (void degree) is clearly visible. Fig.3(b) displays that increasing the sintering temperature up to T_{max} = 1420°C, the residual porosity is significantly decreased. Finally, a further increase of sintering temperature up to T_{max} = 1580°C, leads to a further reduction of the residual porosity, as shown in Fig.3(c).

Fig. 3 shows that the reduction of residual porosity observed with increasing the sintering temperature. In particular, Fig. 3 (a) displays an intermediate stage of sintering, with interconnected porosity, while Fig. 3 (b) and (c) display a final stage of sintering with isolated pores. The increased stage of sintering is accompanied by an enlargement of grain size. This is an important parameter since it affects significantly the oxygen ion conductivity of the GDC electrolyte, as demonstrated by [14,15].

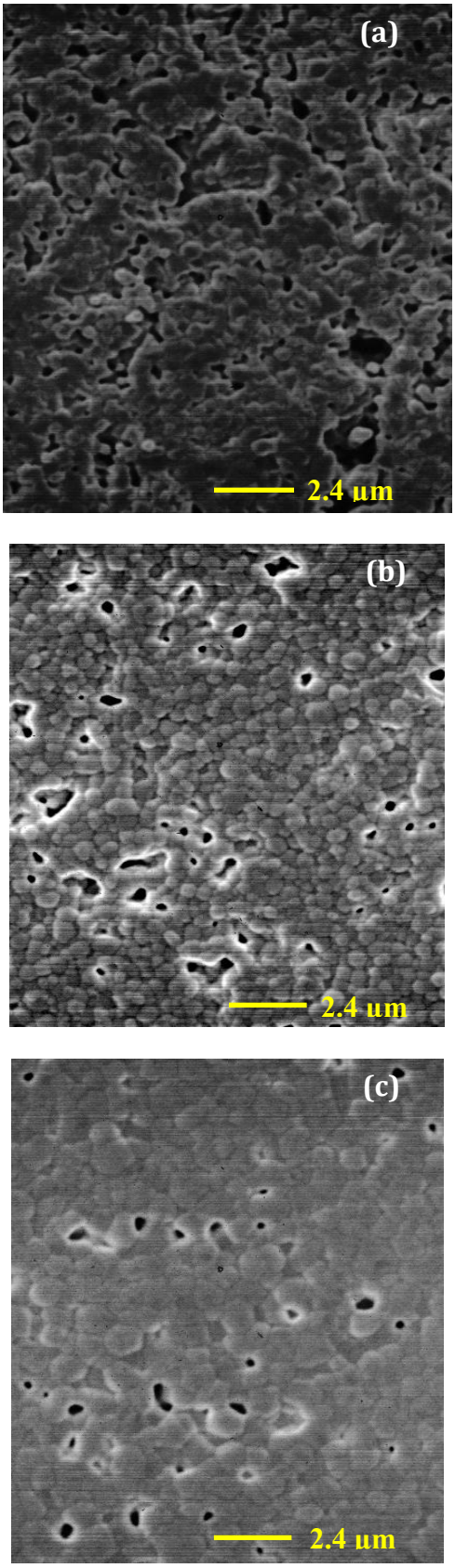

Fig. 3. SEM image of the surface of GDC electrolyte discs obtained by uniaxial pressing at 80 MPa, after sintering at T_{max} (a) 1350 °C, (b) 1420 °C, and (c) 1580 °C.

Nevertheless, Fig. 3 (c) shows that some residual porosity is clearly visible even with the

highest sintering temperature of 1580°C. This suggests that the dispersant and the binder added to the raw GDC powders may interfere with the process of grain agglomeration and growth during sintering. Thus, a different procedure is experimented, where the raw GDC powders are not pre-treated, but instead they are pressed straight as-received (second preparation method). Keeping the maximum sintering temperature fixed at 1580°C, the uniaxial pressing process is investigated by applying a pressure of 50 MPa or 100 MPa. Fig.4 shows SEM images of the surface of the GDC discs, displaying a reduced porosity and an increased grain size, especially with the highest applied pressure of 100 MPa. Tab. 2, for completeness, reports geometrical and Archimedes' density measurements. Considering that the bulk GDC density is 7.2 g/cm^3, for the sample pressed at 100 MPa the relative density is 0.924 according to the geometrical density measurement, and 0.937 according to the Archimedes' density measurement

The average superficial porosity, calculated with the intercept method applied to Fig. , is 0.1% for the electrolyte pressed at 50 MPa, whereas it is 0.04% for the electrolyte pressed at 100 MPa, which is in agreement with the results obtained from the density characterisation.

Table 2. Features of GDC electrolyte discs obtained with different applied pressures.

GDC disc						
Applied pressure [MPa]	Weight [g]	Diameter [cm]	Thickness [cm]	Volume [cm^3]	Geometrical Density [g/cm^3]	Archimedes' Density [g/cm^3]
50	0.224	1.108	0.037	0.036	6.299	6.503
100	0.202	1.110	0.032	0.031	6.651	6.743

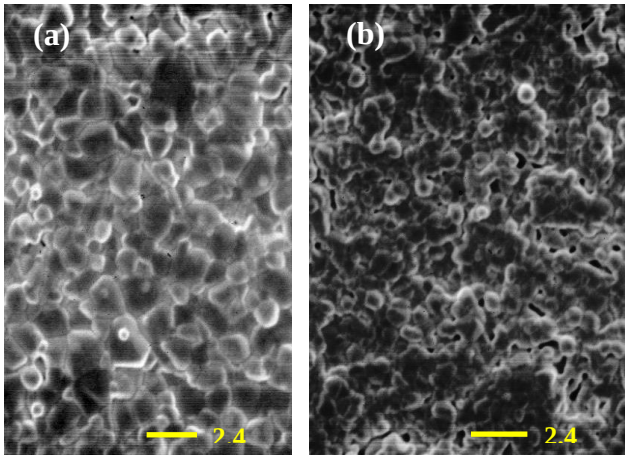

Fig. 4. SEM images of the surface of GDC electrolyte discs obtained by uniaxial pressing at (a) 50 MPa, and (b) 100 MPa.

An SEM picture of the surface of the GDC disc pressed at 100 MPa, after thermal etching, is reported in Fig. 5. The grain size evaluated through the linear intercept method is 0.5 µm.

The GDC disc obtained through uniaxial pressing at 100 MPa is further characterized through mechanical tests. The stress and strain diagram is reported, the corresponding ultimate strength is P = 11.7 N, the Young's modulus is E = 0.12 GPa, and the maximum stress is σ_{max} = 30.5 MPa. All these features comply with the requirements for a GDC disc to be used as the electrolyte of an IT-SOFC. Thus, the samples obtained by pressing the as-received GDC powders at 100 MPa, followed by sintering at T_{max} = 1580°C, are selected for manufacturing the symmetrical cells.

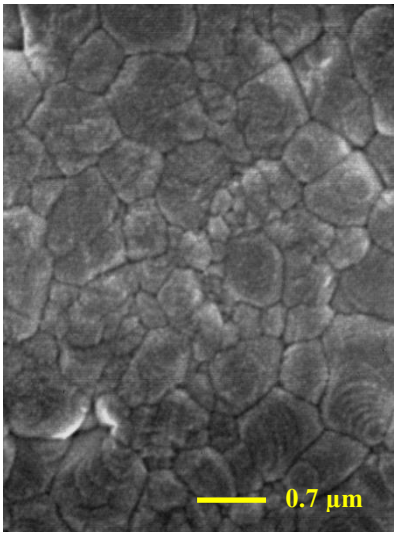

Fig. 5. SEM image of the surface of a GDC electrolyte disc obtained by uniaxial pressing at 100 MPa, after thermal etching.

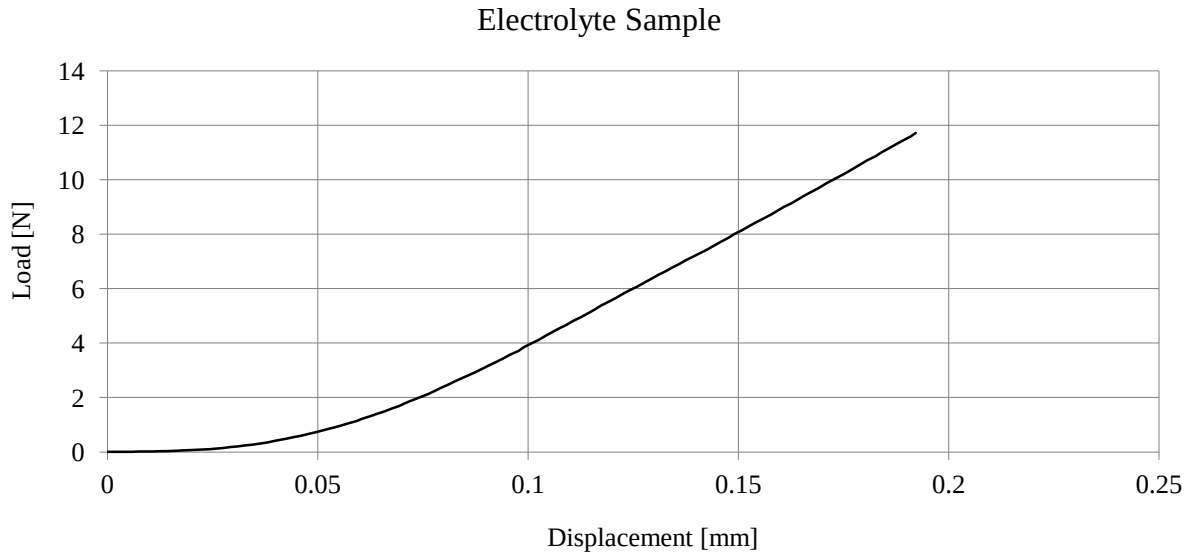

Fig.6. Experimental load and displacement diagram of the GDC electrolyte disc obtained by uniaxial pressing at 100 MPa, followed by sintering at T_{max} = 1580°C.

Symmetrical cells

Symmetrical cells are prepared employing LSCF nanofibers or LSCF granular powders, which are coupled to the GDC electrolyte. SEM pictures of the symmetrical cells (top-view) are reported in Fig.7, clearly displaying the electrodes. Fig. 7(a) and (b) show that the morphology of the fibers is preserved after disaggregation, even if the fibers are clearly broken into segments. This 3-D structure with many contact points between the fibers, is expected to feature simultaneously enhanced charge conduction and electrochemical reaction [3]. The high void degree is ideal to accommodate, in future developments, a high degree of infiltrations, which are expected to improve the electrochemical performance [3]. Fig.7(c) shows the morphology of the LSCF granular electrode, clearly displaying that the LSCF particles have irregular shape. In this case the void degree is much lower than with the fibrous electrode.

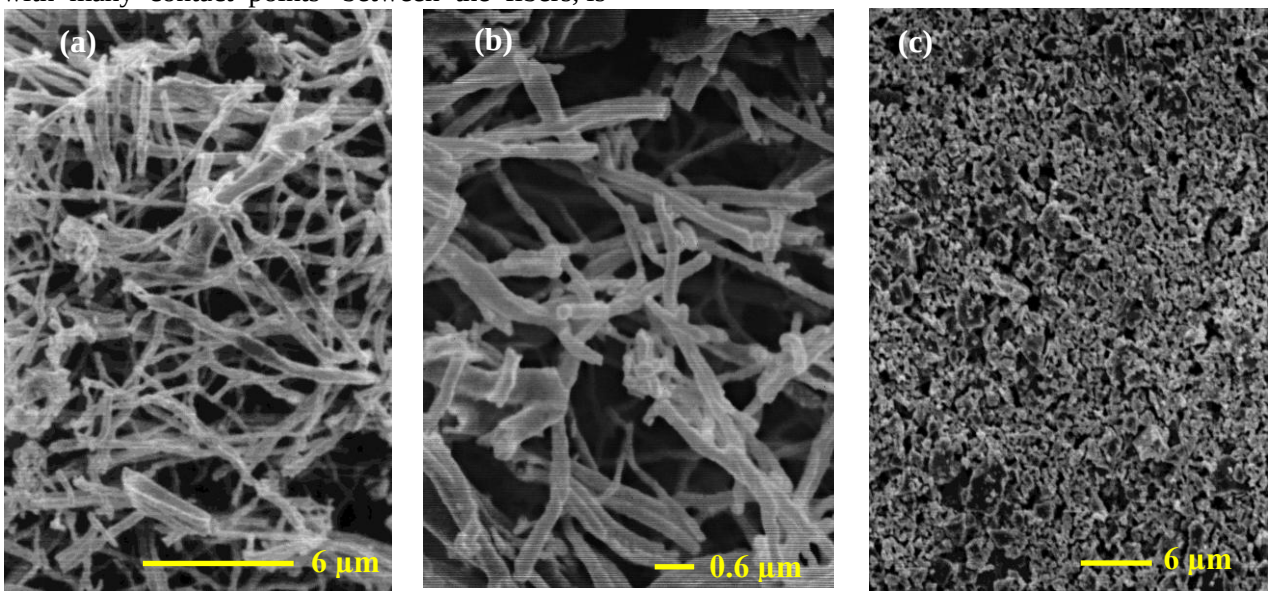

Fig.7. SEM pictures of LSCF electrodes (top view) after application onto GDC discs: (a) and (b) nanofiber electrode, and (b) granular electrode.

CONCLUSIONS

Laboratory symmetrical IT-SOFCs of 1.1 cm of diameter (electrode diameter 0.9 cm) are developed, employing in-house manufactured electrospun LSCF fibrous electrodes deposited onto in-house developed GDC electrolyte discs. In the electrodes, the fibers do not form a unique continuous wire along the whole electrode, but rather they are gently disaggregated to form a network of randomly distributed segments. As a comparison, symmetrical laboratory cells employing granular LSCF electrodes deposited on the same type of GDC electrolytes are manufactured as well.

Future plans include (i) testing through EIS, in order to assess the electrochemical performance; and (ii) comparison with laboratory IT-SOFCs employing LSCF electrospun electrodes applied onto the GDC electrolyte with a different procedure [16], where the fibers form a unique continuous wire along the whole electrode.

REFERENCES

1. A. Mehmeti, S.J. McPhail, D. Pumiglia, M. Carlini, *J. Power Sources*, **325**, 772, (2016).
2. S.T. Aruna, L.S. Balaji, S. S. Kumar, B. Shri Prakash, *Renew. Sust. Energ. Rev.*, **67**, 673, (2017).
3. A. Enrico, B. Aliakbarian, A. Lagazzo, A. Donazzi, R. Botter, P. Perego, P. Costamagna, *Fuel Cells*, **17**, 415 (2016).
4. Ding D., Li X., Lai S. Y., Gerdes K. and Liu M., *Energy Environ. Sci.*, , 552 (2014).
5. J. Cheng, Y. Jun, J. Qin, S.H. Lee, *Biomaterials*, 114, 121 (2017).
6. J.M. Ralph, A.C. Schoeler, M. Krumpelt, *J. Mater. Sci.*, **36**, 1161 (2001).
7. E. Zhao, Z. Jia, X. Liu, K. Gao, H. Huo, Y. Xiong, *Ceram. Int*., **40**, 14891 (2014).
8. L.M. Acuña, J. Peña-Martínez, D. Marrero-López, R.O. Fuentes, P. Nuñez, D.G. Lama, *J. Power Sources*, **196**, 9276 (2011).
9. A. Enrico, P. Costamagna, *J. Power Sources*, **272**, 1106 (2014).
10. J.T. Sill, H.A. von Recum, *Biomaterials*, **29**, 1989 (2008).
11. S. Thenmozhi, N. Dharmaraj, K. Kadirvelu, H.Y. Kim, Mater. Sci. Eng. B-Adv. Funct. S*olid-State Mater.*, **217**, 36 (2017).
12. W.C. Young, R.G Budynas, Roark's Formulas for Stress and Strain, McGraw-Hill Professional 8th Ed. (2011).
13. J.C. Russ, R.T. Dehoff, Practical Stereology, Springer 2nd Ed. (2000).
14. Y. Lin, S. Fang, D. Su, K.S. Brinkman, F. Chen, *Nat. Commun.*, **6**, 6824 (2015).
15. H. Bi, X. Liu, L. Zhu, J. Sun, S. Yu, H. Yu, L. Pei, *Int. J. Hydrog. Energy*, **42**, 11735 (2017).
16. A. Enrico, W. Zhang, M. Lund Traulsen, E.M. Sala, P. Costamagna, P. Holtappels, *J. Eur. Ceram. Soc.*, **38**, 2677 (2018).

СТ-ТОКГ на базата на дисегрегиран електроизплетен от нановлакна LSCF електрод, нанесен върху GDC електролит: начин на изработка и морфологична характеризация

К. Санна[1], А. Лагацо[1], Е.М. Сала[2], Р. Ботер[2], П. Костаманя[3, †]

[1] *Катедра по гражданско, химическо и екологично инженерство (DICCA), Университет в Генуа, Италия*
[2] *Министерство на енергийната конверсия и съхранение, Технически университет на Дания, Фредериксборгей 399, DK-4000 Рокшилд, Дания*
[3] *Катедра по химия и индустриална химия, Университет в Генуа, Италия*

Постъпила на 15 май 2018г.; приета на12 юли 2018г.

(Резюме)

Разработени са средно температурни твърдо оксидни горивни клетки (СТ-ТОКГ), на базата на електроди от $La_{0.6}Sr_{0.4}Co_{0.2}Fe_{0.8}O_{3-\delta}$ (LSCF) нановлакна, нанесени върху $Ce_{0.9}Gd_{0.1}O_{1.95}$ (GDC) електролит. Електродите от LSCF нановлакна се получават чрез електроизплитане. Електроизплетената тъкан се дисегрегира в α-терпинол, преди да се нанесе върху електролита, с цел да се накъсат влакната на отделни сегменти, като се запази тяхната морфология. Електролити GDC се получават чрез еднократно пресоване на GDC прахове, последвано от синтероване. Диспергираните нановлакна се отлагат върху електролита, за да образуват симетрични клетки, които след това се загряват. Характеризацията със СЕМ на топлинно обработените ИТ-ТОКГ образци доказва, че се запазва морфологията на нанофибровите влакна, образувайки 3-D структура с много контактни точки между самите влакна, което се очаква да се характеризира едновременно с подобрени проводимост и електрохимична реактивност. Клетките са изследвани с електрохимична импедансна спектроскопия (ЕИС), която е идеалният инструмент за характеризиране на електрохимичните експлоатационни качества на дисагрегираните електроизплетени от нановлакна LSCF електроди.

Bulgarian Chemical Communications, Volume 50 Special Issue D (pp. 55 – 61) 2018

Ionic Conductivity of Na-doped $SrSiO_3$

M. Viviani[1*], A. Barbucci[1,2], M. P. Carpanese[1,2], R. Botter[2], D. Clematis[2], S. Presto[1]

[1] *Institute of Condensed Matter Chemistry and Energy Technologies (ICMATE), National Council of Research (CNR), c/o DICCA-UNIGE, Via all'Opera Pia 15, 16145 Genova, Italy*

[2] *Department of Civil, Chemical and Environmental Engineering (DICCA), University of Genova, Via all'Opera Pia 15, 16145 Genova, Italy*

Received June 22, 2018 Revised September 1, 2018

The conductivity of a newly proposed ionic conductor Na-doped $SrSiO_3$ was studied. Powders were prepared by mixing of $SrCO_3$, Na_2CO_3 and SiO_2 in water or ethanol in order to explore the effect of solvents on the formation of secondary phases. X-ray diffraction was employed to study the phase composition of mixtures treated in air at different temperatures in the range 950-1050 C for 20 hours. Various heating schemes were applied to help the incorporation of Na in the monoclinic $SrSiO_3$ structure. Pressed pellets were sintered at 1000 °C for 20 hours and electroded with Ag paste for electrochemical characterization by impedance spectroscopy. For most compositions and thermal treatments, the formation of the insulating $Na_2Si_2O_5$ phase was observed as a matrix around grains of the monoclinic $SrSiO_3$ phase. Double calcination limited conductivity but increased its thermal stability. When ethanol was used for powder mixing, the material exhibited higher conductivity after long term ageing at 650 °C, also thanks to its low activation energy, without appreciable crystallization of other silicates

Key words: Ionic conductors, silicates, conductivity

INTRODUCTION

During last decades a lot of efforts have been spent to improve performances of Solid Oxide Fuel Cells (SOFC), and particularly to lower the operative temperature down to the 600 °C range. Some of them aimed to new designs [1-7]; other regarded the development of new materials [8, 8-11].

Recently, there has been some interest about alkali–doped $SrSiO_3$ and $SrGeO_3$ as oxide ion conductors with possible application as electrolyte materials in SOFC. In a series of papers [12,13] the formation of solid solutions, without any secondary phases, and with conductivity exceeding 0.05 S cm at 600 °C in air was reported.

Conductivity was ascribed to migration of oxygen vacancies, formed as an effect of replacement of Sr^{2+} with Na^+ ions [14].

Those findings were objected by several reports that pointed out the crucial role of glassy phases from the Na_2O–SiO_2 system [15- 17].

In particular, solid-state NMR spectroscopy studies allowed to associate conduction of SNS to migration of Na^+ ions in the amorphous phase [19, 20] and XRD analyses evidenced the very limited incorporation of Na into $SrSiO_3$ [21,22]. Conductivity also appeared to be strongly dependent on the crystallization of $Na_2Si_2O_5$ after some treatment at temperatures around 650 °C [21,23].

Some authors have reported the effect of synthesis method and processing conditions on the structure and conducting properties of alkali–doped $SrSiO_3$ and $SrGeO_3$. Alternatively to the conventional solid–state route, freeze drying of homogenous solutions of all cations was reported, resulting in more crystalline powders and in ceramics with lower conductivity [23].

Powders prepared by solid–state route were also sintered by spark plasma (SPS), which allowed obtaining single phase materials, with fine grains and with relatively high ionic conductivity [25].

From this brief summary, it appears that phase composition and consequently electrical properties must be highly sensitive to processing, particularly to reaction conditions of precursors and to the thermal history. In order to get insight on such aspects, the effects of some processing parameters, like the mixing medium and thermal treatments, have been studied for Na doped $SrSiO_3$ and results are reported in this paper.

EXPERIMENTAL

Powders with nominal composition $Sr_{1-x}Na_xSiO_3$ ($0.1 \leq x \leq 0.45$), denoted as SNSX, were prepared by the solid–state route, starting from $SrCO_3$, Na_2CO_3

To whom all correspondence should be sent:
E-mail: massimo.viviani@cnr.it

and SiO_2. Three dispersing liquids with different polarity (acetone, ethanol and distilled water) were employed in order to explore the effect of solvent on Na incorporation and glassy phase formation. After milling and freeze–drying calcination was carried out in air in order to get the final product following the reaction:

$$(1\text{-}x)SrCO_3+\frac{x}{2}Na_2CO_3+SiO_2 \rightarrow Sr_{(1-x)}Na_xSiO_{3-\frac{x}{2}}+\left(1-\frac{x}{2}\right)CO_2 \quad (1)$$

In case of acetone, four compositions with x = 0.1, 0.2, 0.3 and 0.4 were prepared, while in case of ethanol and water the composition reported with highest conductivity (x = 0.45) [0] was prepared only.

Powders were treated one or two times at temperatures ranging between 850 and 1050 °C and manually grinded after each thermal treatment. The details of all treatments are reported in Table 1.

Table 1. Thermal treatments applied to different compositions. Note that X = 100 x

SNSXa X = 10–40 acetone	SNS45e / SNS45w ethanol / water
A = 850 °C / 12 h	C = 1050 °C /20 h
B = A + 1000 °C /12 h	D = C + 950 °C /20 h
	E = C + D + 1000 °C /20 h

All compositions were also "aged" in air for 150 h at 650 °C in order to check their stability, and particularly to allow for crystallization or devitrification of any glassy phase.

Phase composition of powders was investigated by XRD (CubiX − Panalytical, Cu-K_α radiation, $\Delta 2\theta$ = 0.02 deg, integration = 7 sec/point) and morphology was observed by SEM (1450VP − LEO).

Ceramics were obtained by sintering at 1000 °C (see Table 1, treatments B and E) disk-shaped pellets which were prepared by uniaxial pressing. Microstructure was investigated by SEM (Phenom XL, Phenom World) on polished cross sections. Electrodes for electrical characterization were realized by brushing Ag paste (Euroinks) on both sides, followed by curing at 700°C for 30 min.

Electrochemical Impedance Spectroscopy (EIS) was carried out in laboratory air at different temperatures within a custom test rig and employing an automatic Frequency Response Analyzer (Iviumstat H, IVIUM). Spectra were collected each 25 °C during heating and cooling between room temperature and 650 °C. A 150h–long ageing at 650 °C enabled studying the dependence of conductivity on time for samples SNS40a and SNS45e.

RESULTS AND DISCUSSION

Na_2CO_3 is known to be highly soluble in water, weakly soluble in ethanol and insoluble in acetone. Therefore, the use of different dispersing media is expected to result in a different spatial distribution of Na within unreacted mixtures before calcination. In addition, some dissolution of Si into alkaline Na_2CO_3 solution at room temperature has to be taken into account [25], as well as the presence of strongly bonded hydroxyls due to the interaction between water, silica and Na_2CO_3.

XRD profiles of all SNSX powders are presented in Fig. 1 and observed phases are summarized in Table 2.

After the first treatment (calcination, A or C) all samples, reported in Fig. 1(i), contained only one crystalline phase, corresponding to the structure of $SrSiO_3$, with monoclinic symmetry (S.G. C2/c, JCPDS card 01-077-0233). Some flat−top parts can be detected in the diffraction profile of samples with lower Na amount (< 30 at. %) and of the powder prepared in ethanol (SNS45e). These features (marked with an asterisk) suggest the presence of amorphous or nanocrystalline regions. It is worth noting that for other samples minor peaks of the $SrSiO_3$ phase appear in the same parts of the profile.

Additional thermal treatments, as reported in Table 2, allowed for either the formation of new phases or crystallization of amorphous regions. In particular, for powders prepared in acetone the phase $Na_2Si_2O_5$ (JCPDS card 29-1261 and/or JCPDS card 22-1397) was found in compositions with higher Na content (≥30 at. %). In case of further aging at 650 °C, Na_2SiO_3 (JCPDS card 16-0818) was also detected in addition to two different forms of $Na_2Si_2O_5$, as can be seen in Fig.1(ii) for SNS40a. This is in agreement with several papers about SNS prepared with the same procedure, reporting the presence of glassy $Na_2Si_2O_5$, which could be devitrified after heating at T > 600 °C [20, 22]. For water- and ethanol-based preparations, aging of as-calcined powders resulted in crystallization of sodium silicate phase (JCPDS card 23-0529) as in case of acetone. On the contrary, a second thermal treatment at 950 °C deeply affected the resulting phase composition.

As can be seen in Figs. 1(iii-iv), aging at 650 °C caused the formation of $Na_2SrSi_2O_6$ (JCPDS card 32-1159) in both samples, showing that Na was partially incorporated in ternary oxide instead of the glassy $Na_2Si_2O_5$. Ageing of ceramics, i.e. after

sintering stage, introduced a difference between SNS45w and SN45e, and with the former being decomposed in several sodium silicates (see Fig. 1(iii) and the latter showing no evidence of any secondary phase (see Fig. 1(iv)

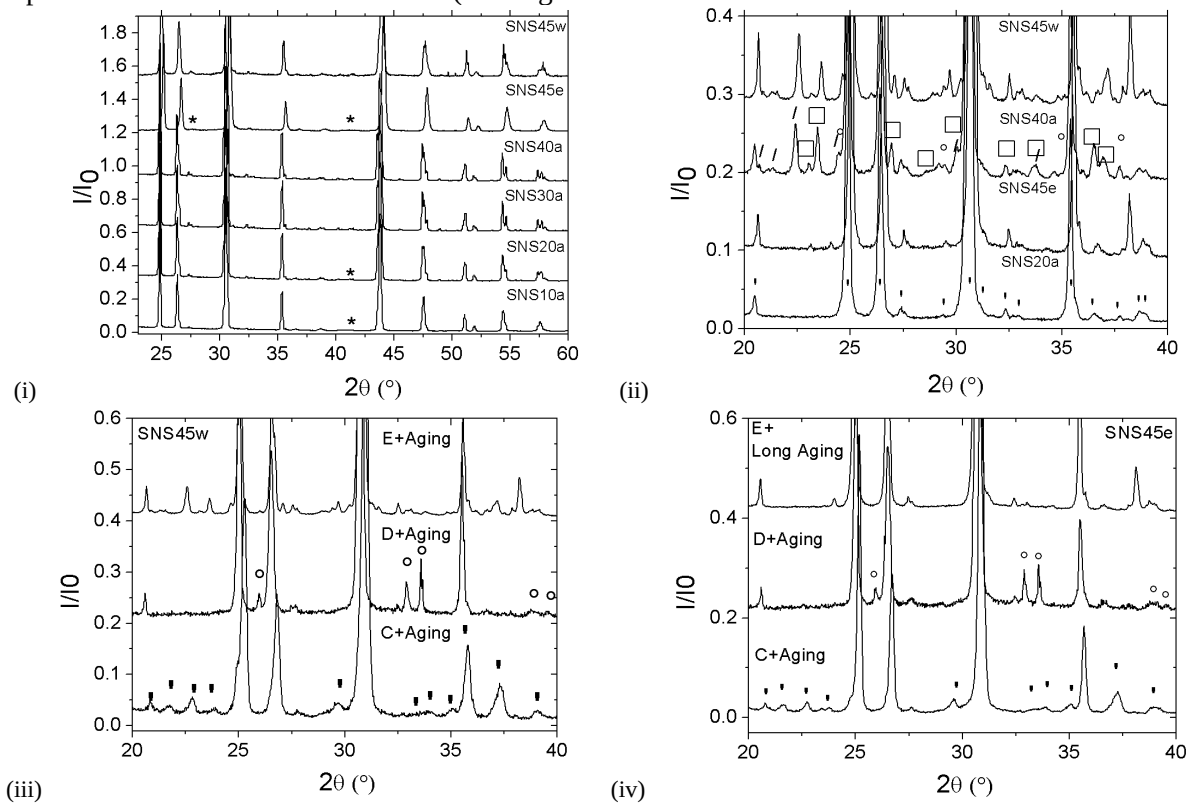

Fig. 1. XRD of SNSX. All compositions after thermal treatment at 850 °C or 1050 °C, * = amorphous or nanocrystalline regions (i); compositions as reported in label after EIS measurement, ' = $SrSiO_3$, ° = Na_2SiO_3, □ = α–$Na_2Si_2O_5$ (ii), SNS45w (iii) and SNS45e (iv), after ageing at 650 °C (°)=$Na_2SrSi_2O_6$, (')= $Na_2Si_2O_5$

Table 2. Activation Energy (E_a), conductivity value calculated @ 600°C and phase composition (JCPDS card numbers in brackets) of SNSX after different thermal treatments.

Sample	E_a **(eV)**	**Treatment**	**Phases**	**σ(S cm^{-1}) @600°C**
SNS10a		A	$SrSiO_3$ (01-077-0233)	
	1.89	B	$SrSiO_3$ (01-077-0233)	2.6 10^{-5}
SNS20a		A	$SrSiO_3$ (01-077-0233)	
	1.37	B	$SrSiO_3$ (01-077-0233)	2.2 10^{-4}
SNS30a		A	$SrSiO_3$ (01-077-0233)	
	1.33	B	$SrSiO_3$ (01-077-0233), $Na_2Si_2O_5$ (29-1261)	9.5 10^{-4}
SNS40a		A	$SrSiO_3$ (01-077-0233)	
	1.30	B		2.9 10^{-3}
		B+650 °C/150 h	$SrSiO_3$ (01-077-0233), $Na_2Si_2O_5$ (22-1397), $Na_2Si_2O_5$ (29-1261), Na_2SiO_3 (16-0818)	
SNS45w		C	$SrSiO_3$ (01-077-0233)	
		C+650 °C/150 h	$SrSiO_3$ (01-077-0233), $Na_2Si_2O_5$ (23-0529)	
		D+650 °C/150 h	$SrSiO_3$ (01-077-0233), $Na_2SrSi_2O_6$ (32-1159)	
	0.62	E		7.6 10^{-6}
		E+650 °C/150 h	$SrSiO_3$ (01-077-0233), $Na_2Si_2O_5$ (22-1397), $Na_2Si_2O_5$ (23-0529), Na_2SiO_3 (16-0818)	
SNS45e		C	$SrSiO_3$ (01-077-0233)	
		C+650 °C/150 h	$SrSiO_3$ (01-077-0233), $Na_2Si_2O_5$ (23-0529)	
		D+650 °C/150 h	$SrSiO_3$, $Na_2SrSi_2O_6$ (32-1159)	
	0.52	E		1.7 10^{-4}
		E+650 °C/150 h	$SrSiO_3$ (01-077-0233)	
		E+650 °C/300 h	$SrSiO_3$ (01-077-0233)	

SEM observation (backscatter mode) of cross sections of ceramics aged during electrical testing are reported in Fig. 2. Both SNS40a (i) and SNS45w (ii) show light grains with rounded shape immersed into a matrix with darker shades. EDAX analyses indicate that grains correspond to $SrSiO_3$ containing less than 5 at. % of Na, while matrix region composition is close to $Na_2Si_2O_5$ (light grey areas) and Na_2SiO_3 (dark grey areas).

The microstructure of SNS45e also is characterized by coexistence of light rounded grains, that were identified as corresponding to $SrSiO_3$ by EDAX analyses, and dark matrix. Differently from previous samples, in this case the matrix appears homogenous (white spots are Ag particles from electrodes) and therefore with one single composition (Fig. 2iv). Because XRD did not revealed other phases beyond $SrSiO_3$, this dark matrix is a glassy phase, still not crystallized after 300h (see fig. 2iv).

The electrical characterization was carried out in air by impedance spectroscopy, that is a very powerful technique when the appropriate corrections are applied [25].

An example of the results is presented in Fig. 3, where data collected at 500 °C for the SNS45e sample are represented as Nyquist plot.

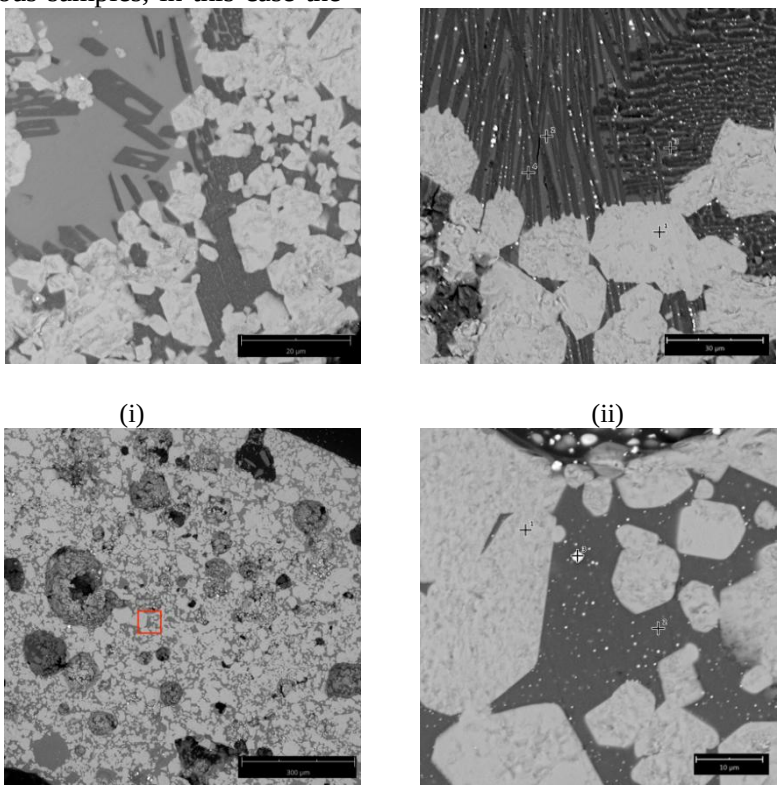

(i) (ii)

(iii) (iv)

Fig. 2. SEM backscatter on cross section of ceramics aged along electrical testing. SNS40a (i), SNS45w (ii), SNS45e (iii, iv). Red square in (iii) locates the area shown in (iv) at higher magnification.

The spectrum shows one semicircle, which is assigned to the electrolyte, and one feature at low frequency which can be considered contribution from electrodes. For the purpose of this work, low frequency intercept of the spectrum with real axis was considered as total resistance of samples. Those values were used to calculate the conductivity by using the Ohm's law.

From data reported in Table 2, it can be noted that for samples prepared in acetone, increasing the amount of Na leads to materials with increased conductivity and decreased E_a. On the contrary, materials prepared in ethanol or water shows much lower conductivity and lower E_a.

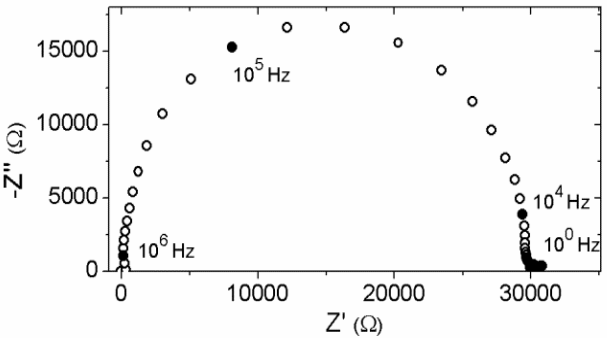

Fig. 3. Nyquist plot of SNS45e at 500 °C. Frequency decades are marked on the plot.

The activation energy of SNS is reported to be between 0.3 and 0.5 eV [0,12], while for both glassy and crystalline $Na_2Si_2O_5$ much larger values were measured (≥ 1.1 eV) [20,20].

By comparing literature data with present results, it is therefore possible to assimilate SNSXa to $Na_2Si_2O_5$. On the contrary, activation energy for conduction in SNS45e and SNS45w is closer to that of Na-doped $SrSiO_3$, although the conductivity is limited by considerable amount of glassy regions.

This is further confirmed by ageing behaviour of conductivity, presented in Fig. 4. The conductivity of SNS40a is strongly lowered by dwelling, which can be ascribed to the crystallization of $Na_2Si_2O_5$.

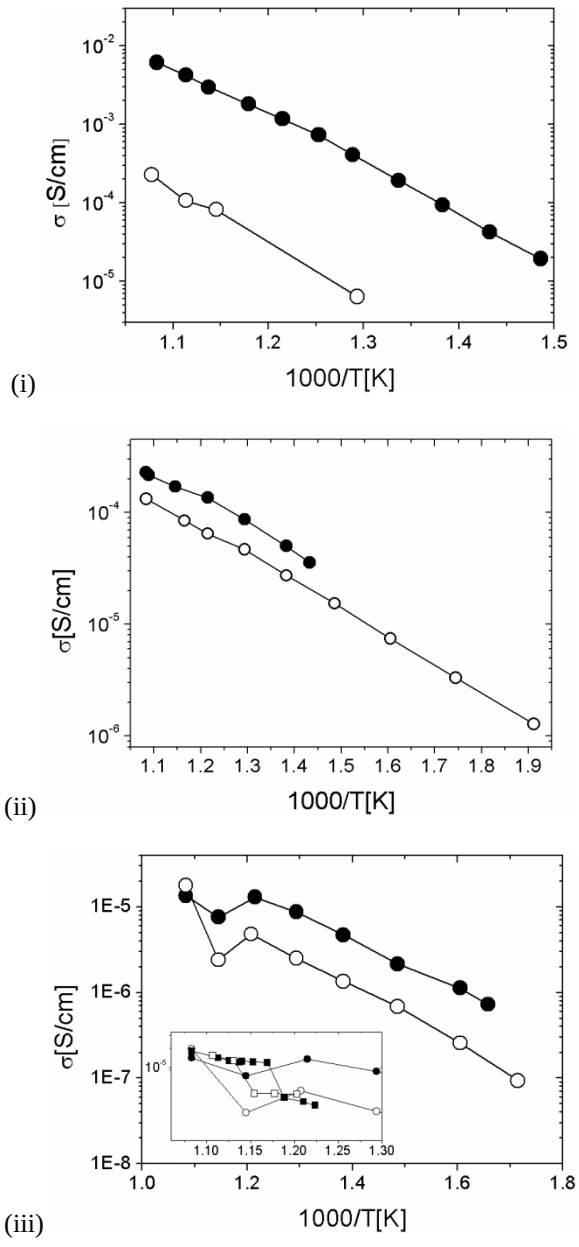

Fig. 4. Arrhenius plots of total conductivity during heating (red) and cooling after ageing (650 °C / 150 h) (blue) for SNS40a (i) SNS45e (ii) and SNS45w (iii).

This is not the case of SNS45e, were only a slight reduction of conductivity is observed after 150 h ageing. Accordingly, the crystallization of new phases was not observed for this sample. The conductivity of sample SNS45w shows some anomalies at temperatures between 550 and 650 °C, which are shown in Fig. 4iii. Inset also shows a second thermal cycle, which suggests the presence of a transition in that temperature range. The transition might be associated to glass crystallization, which is also supported by the acicular shape of Na-rich phases in this sample (Fig. 2ii).

From results reported above, it appears that processing can significantly modify the phase composition and the electrical properties of Na-doped $SrSiO_3$. XRD and SEM showed that Na incorporation in the monoclinic $SrSiO_3$ structure by the mechanism of eq. 1 is unfavourable, at least under the conditions explored in this work. Secondary phases from the Na_2O-SiO_2 system were detected in all materials with Na content higher than 20 at. %, and always present as amorphous regions. Ageing at 650 °C was effective in promoting crystallization of glassy phase in near all samples. An exception is represented by the samples processed with double calcination before sintering. Ageing at 650 °C for 150 h carried out after the second calcination revealed the formation of the 1:1 phase from the $SrSiO_3$–Na_2SiO_3 system ($Na_2SrSi_2O_6$), suggesting a beneficial effect from the double thermal treatment towards simultaneous incorporation of Na and Sr. In case of ethanol processing (SNS45e), further heat treatment at high temperature (sintering) was effective in stabilizing the amorphous regions which did not crystallize even after prolonged ageing (300 h) at 650 °C. This might be due to the composition of the glass as it is known that crystallization of alkali-silicates with high Si concentration is kinetically limited due to the high viscosity around the melting point [27]. Further investigation would be needed to clarify this aspect.

For the SNS45e sample, it is not possible to conclude whether the SNS or the glass are contributing to conduction. Given that only one semicircle is present in impedance diagrams, separation of two contributions is not possible. The very low total conductivity associated to low activation energy make this composite quite different from all previously reported about SNS.

For water processing (SNS45w), much lower conductivity was obtained and stabilization could not be achieved (see Table 2). Therefore, in this case a lower Si/Na molar ratio is expected in the

matrix or, in other terms, a lower incorporation of Na in the $SrSiO_3$ phase.

CONCLUSIONS

The effects of preparation and thermal treatment conditions on properties of $Sr_{1-x}Na_xSiO_3$, with $0.1 \leq x \leq 0.45$, were studied. The preparation was carried out by solid−state route with three different mixing media. Acetone, ethanol and water were selected for their large difference in polarity and therefore for the different solubility of Na_2CO_3. Calcination was carried out under different conditions, by changing temperature and number of treatments. Results from X-ray diffraction, SEM-EDAX and impedance spectroscopy confirmed that the Na-$SrSiO_3$ system is always a multi-phase structure, with some amount of sodium silicates (amorphous or crystalline) increasing with Na concentration. Quantity and crystallinity of sodium silicates determines both the level of conductivity and its thermal stability. Highest conductivity and degradation rate was obtained when synthesis was carried out in acetone with single calcination step at 850 °C. Double calcination limited conductivity but increased its thermal stability. When ethanol was used for powder mixing and double calcination was applied, the material exhibited higher conductivity after long term ageing at 650 °C also thanks to its low activation energy, without appreciable crystallization of other silicates. Such results make the ethanol-based preparation promising for the realization of a stable material suitable as electrolyte material in SOFC.

REFERENCES

1. Su, S.; Gao, X.; Zhang, Q.; Kong, W.; Chen, D., Anode- Versus Cathode-Supported Solid Oxide Fuel Cell: Effect of Cell Design on the Stack Performance. *Int. J. Electrochem. Sci*., **10**, 2487 (2015).
2. Thorel, A. S.; Abreu, J.; Ansar, S.-A.; Barbucci, A.; Brylewski, T.; Chesnaud, A.; Ilhan, Z.; Piccardo, P.; Prazuch, J.; Presto, S.; Przybylski, K.; Soysal, D.; Stoynov, Z.; Viviani, M.; Vladikova D. Proof of concept for the dual membrane cell I. Fabrication and electrochemical testing of first prototypes. Journal of *The Electrochemical Society*, **160(4)**, F360 (2013).
3. Presto, S.; Barbucci, A.; Viviani, M.; Ilhan, Z.; Ansar, S.-A.; Soysal, D.; Thorel, A. S.; Abreu, J.; Chesnaud, A.; Politova, T.; Przybylski, K.; Prazuch, J.; Brylewski, T.; Zhao, Z.; Vladikova, D.; Stoynov Z. IDEAL-Cell, innovative dual membrane fuel-cell: fabrication and electrochemical testing of first prototypes. *ECS Transactions*, , **25(2)**, 773 (2009).
4. Xu, J. ; Zhou, X.; Cheng, J.; Pan, L.; Wu; M.; Dong, X.; Sun, K. Electrochemical performance of highly active ceramic symmetrical electrode La0.3Sr0.7Ti0.3Fe0.7O3-δ-CeO2 for reversible solid oxide cells. *Electrochimica Acta*, **257**, 64 (2017).
5. Krishnan, V. V. Recent developments in metal-supported solid oxide fuel cells. *WIREs Energy Environ*, **6**:e246, 1 (2017).
6. Viviani, M., Canu, G., Carpanese, M.P., Barbucci, A., Sanson, A., Mercadelli, E., Nicolella, C., Vladikova, D., Stoynov, Z., Chesnaud, A., Thorel, A., Ilhan, Z., Ansar, S.-A., *Energy Procedia*, **28**, 182 (2012).
7. Vladikova, D., Stoynov, Z., Chesnaud, A., Thorel, A., Viviani, M., Barbucci, A., Raikova, G., Carpanese, P., Krapchanska, M., Mladenova, E., *International Journal of Hydrogen Energy*, **39(36)**, 21561 (2014).
8. N. Mahato, A. Banerjee, A. Gupta, S. Omar, K. Balani, Progress in Materials Science Progress in material selection for solid oxide fuel cell technology : A review, *Prog. Mater. Sci*. **72**, 141 (2015).
9. Carpanese, M.P., Barbucci, A., Canu, G., Viviani, M., *Solid State Ionics*, **269**, 80 (2015).
10. Giuliano, A., Carpanese, M.P., Panizza, M., Cerisola, G., Clematis, D., Barbucci, A., *Electrochimica Acta*, **240**, 258 (2017).
11. S. Presto, A. Barbucci, M. P. Carpanese, M. Viviani, R. Marazza, *J. Appl. Electrochem.*, **39**, 2257 (2009).
    P. Singh, J.B. Goodenough, $Sr_{1-x}K_xSi_{1-y}Ge_yO_{3-0.5x}$: a new family of superior oxide-ion conductors, *Energy Environ. Sci*. **5**, 9626 (2012).
12. P. Singh, J.B. Goodenough, Monoclinic Sr 1– x Na x SiO 3–0.5 x : New Superior Oxide Ion Electrolytes, *J. Am. Chem. Soc.* **135,** 10149 (2013).
13. T. Wei, P. Singh, Y. Gong, J.B. Goodenough, Y. Huang, K. Huang, $Sr_{3-3x}Na_{3x}Si_3O_{9-1.5x}$ (x = 0.45) as a superior solid oxide-ion electrolyte for intermediate temperature-solid oxide fuel cells, *Energy Environ. Sci.* **7,** 1680 (2014).
14. R. Martinez-Coronado, P. Singh, J. Alonso-Alonso, J.B. Goodenough, R. Martinez, J.A. Alonso, Structural investigation of the oxide-ion electrolyte with SrMO3 (M = Si/Ge) structure, *J. Mater. Chem.* A. **2,** 4355 (2014).
15. R.D. Bayliss, S.N. Cook, S. Fearn, J.A. Kilner, C. Greaves, S.J. Skinner, On the oxide ion conductivity of potassium doped strontium silicates, *Energy Environ. Sci*. **7**, 2999 (2014).
16. K. Sood, S. Basu, Co-existence of amorphous and crystalline phases in Na-doped SrSiO 3 system, *RSC Adv*. **6,** 20211 (2016).
17. I.R. Evans, J.S.O. Evans, H.G. Davies, A.R. Haworth, M.L. Tate, On Sr1–x Na x SiO3–0.5 x New Superior Fast Ion Conductors, *Chem. Mater.* **26**, 5187 (2014).
18. K.K. Inglis, J.P. Corley, P. Florian, J. Cabana, R.D. Bayliss, F. Blanc, Structure and Sodium Ion Dynamics in Sodium Strontium Silicate Investigated by Multinuclear Solid-State NMR, *Chem. Mater.* **28**, 3850 (2016)
19. P.-H. Chien, Y. Jee, C. Huang, R. Dervişoğlu, I. Hung, Z. Gan, K. Huang, Y.-Y. Hu, On the origin of high ionic conductivity in Na-doped SrSiO 3, *Chem. Sci*. **7**, 3667 (2016).

20. C. Tealdi, L. Malavasi, I. Uda, C. Ferrara, V. Berbenni, P. Mustarelli, Nature of conductivity in SrSiO3-based fast ion conductors., *Chem. Commun.* **50**, 14732 (2014).
21. Y. Jee, X. Zhao, K. Huang, On the cause of conductivity degradation in sodium strontium silicate ionic conductor., *Chem. Commun.* **51**, 9640 (2015).
22. Y. Jee, X. Zhao, X. Lei, K. Huang, Phase Relationship and Ionic Conductivity in Na-SrSiO 3 Ionic Conductor, *J. Am. Ceram. Soc*. **99**, 324 (2016).
23. S. Fernández-Palacios, L. do. Santos-Gómez, J.M. Compana, J.M. Porras-Vázquez, A. Cabeza, D. Marrero-López, E.R. Losilla, Influence of the synthesis method on the structure and electrical properties of Sr1−xKxGeO3−x/2, *Ceram. Int.* **41**, 6542 (2015).
24. F. Yang, Z. Yu, B. Meng, Y.J. Zhu, Q.Q. Yang, Z.L. Lin, H.M. Zhou, X.L. Liang, Microstructure and electrical properties of $Sr_{1-x}Na_xSiO_{3-x/2}$ ceramics prepared by SPS process, *Ionics (Kiel)*. **22**, 2087 (2016).
25. S.S. Jørgensen, The application of alkali dissolution techniques in the study of cretaceous flints, *Chem. Geol.* **6**, 153 (1970).
26. G. Raikova, M. P. Carpanese, Z. Stoynov, D. Vladikova, M. Viviani, A. Barbucci, *Bulg. Chem. Commun*., **41**, 199 (2009).
27. M.W. Barsoum, Fundamentals of ceramics, second, IOP Publishing Ltd, 2003, pp. 280-281.

Йонна проводимост на $SrSiO_3$ дотиран с натрий

М. Вивиани[1 *], А. Барбучи[1,2], М.П. Карпанезе[1,2], Р. Ботер[2], Д. Клематис[2], С. Престо[1]

[1] Институт по химия на кондензираната материя и енергийни технологии, Национален съвет по научни изследвания, Виа але Опера Пиа 15, 16145 Генуа, Италия
[2] Катедра по гражданско, химическо и екологично инженерство, Университет на Генуа, Виа але Опера Пиа 15, 16145 Генуа, Италия

Постъпила на.22 юни 2018г.; приета на 1 септгември 2018г.

(Резюме)

Изследвана е проводимостта на ново-открития йонен проводник $SrSiO_3$ дотиран с натрий. Чрез смесване на $SrCO_3$, Na_2CO_3 и SiO_2 бяха приготвени прахове във водна или етанолна среда, за да се проучи ефекта на разтворителите върху образуването на вторични фази. Използвана беше рентгенова дифракция за да се установи фазовия състав на смесите, третирани на въздух при различни температури в диапазона 950-1050 °C в продължение на 20 часа. Различни схеми на нагряване бяха приложени с цел да се подпомогне вграждането на Na в моноклинната $SrSiO_3$ структура. Пресованите таблетки се синтероват при 1000 °C в продължение на 20 часа и се покриват със сребърна паста за електрохимично характеризиране чрез импедансна спектроскопия. При повечето състави и термични обработки, образуването на изолираща фаза от $Na_2Si_2O_5$ се наблюдава като матрица от $SrSiO_3$ зърна в моноклинна фаза. Проводимостта е ограничена от двойно калциране, но се увеличава термичната стабилност. Когато се използва етанол за смесване на праховете, след дългосрочно стареене при 650 °C материалът има по-висока проводимост, също и по-ниска активационна енергия, без забележима кристализация на други силикати.

Bulgarian Chemical Communications, Volume 50 Special Issue D (pp. 62 – 67) 2018

Chronoamperometrically poised electrodes mimic the performance of yeast-based bioanode in MFC

Y. Hubenova [1,2,*], E. Hubenova [3], M. Mitov [4]

[1] *Acad. Evgeni Budevski Institute of Electrochemistry and Energy Systems, Bulgarian Academy of Sciences, Acad. G. Bonchev" Str., bl.10, 1113 Sofia, Bulgaria*
[2] *Paisii Hilendarski Plovdiv University, 24 "Tsar Asen" Str., 4000 Plovdiv Bulgaria*
[3] *Center for Pediatrics, University Clinics, University of Bonn, Adenauerallee 119 53113 Bonn, Germany*
[4] *Innovative Center for Eco Energy Technologies, South-West University Neofit Rilski, 66 Ivan Mihaylov Str., 2700 Blagoevgrad, Bulgaria*

Received June 08, 2018 Revised August 16, 2018

Poised electrodes in a three-electrode mode is recently used as an alternative tool for establishment of favorable redox conditions for extracellular electron transfer (EET) from biocatalysts to the anode in bioelectrochemical systems. It has been demonstrated that the optimal imposed potentials differ for a particular microorganism species, depending on its specific metabolic pathways. In this study, carbon felt electrodes were potentiostatically poised at +0.005, +0.405, +0.505 and + 0.605 V (vs. SHE) in the presence of exoelectrogenic yeast strain *Candida melibiosica* 2491. The results from chronoamperometric experiments show that the yeast is capable of performing EET at potentials higher than +0.5 V. The current generated at + 0.605 V (vs. SHE) follows the yeast growth phases, reaching stable maximal outputs of ca. 40 mA/m^2. The cyclic voltammetry analysis carried out reveals that the observed electrochemical activity is due to production and secretion of endogenous mediator of EET, mimicking the already established yeast performance in real biofuel cells. The differences in the electrochemical impedance spectra obtained with exploited yeast suspension and cellular-free fraction describe the contribution of the cellular processes to the anodic current generation.

Key words: microbial fuel cell mimicking, poised anode, endogenous mediator, chronoamperometry, cyclic voltammetry, electrochemical impedance spectroscopy.

INTRODUCTION

The oxidation–reduction processes are the basis of the cellular energetic mechanism. The most energy-efficient oxidation of a substrate by living microorganisms occurs at terminal electron acceptor possessing high positive potential like the oxygen. Under anaerobic or semi-aerobic conditions, the aerobic respiration processes are partially replaced by alternative pathways such as different kind of fermentations. Although less energetic favorable these pathways contribute to the equilibration of the intracellular redox cell balance providing oxidized NAD necessary as a cofactor of glycerinaldehyd-3-phosphat-dehydrogenase and thus for further conduction of glycolysis. The capability of using alternative electron acceptors is at the heart of Microbial fuel cell (MFC) technology development, where the intracellular produced electrons are transferred extracellularly to the anode serving as a final electron acceptor [1]. The bacteria utilizing the anode as electron acceptor are referred to as exoelectrogens or anode-respiring bacteria [2].

To gain these electrons (in form of electrical energy), the MFC-devices usually operate under polarization conditions, where the anode and the cathode are connected in an electrical circuit [3]. At a relatively constant cathodic potential during the operation, the lower the anodic potential, the higher the electrical outputs. Reaching anodic potential of ca. -0.3 V (vs. SHE) is reported as most thermodynamic profitable. This potential can be reached, however, for longer time at flow-batch operating bioelectrochemical systems (BES). The formation of microbial biofilm on the anodic surface leads to lowering the potential [4]. Having in mind the direct proportional relation between microbial metabolic activity and the generated electrical current, an alternative method for feeding potential (poised electrode) has been proposed [5-7]. From theoretical point of view, a more positive anode potential wil allow the cell capture more energy, but only if the cell is capable of capturing this energy by pumping additional

To whom all correspondence should be sent:
E-mail: y.hubenova@iees.bas.bg

protons across its cellular membrane.

Thus, the microbes must possess terminal proteins of respiratory chains that can use this additional potential provided by the anode [8]. Marsili et al. support this opinion by giving the following example [9]: If the anode of an acetate-fed (Eo′= -0.3 V vs. SHE) MFC is set to a highly positive value of +0.4 V and a microbe can only adjust its respiratory enzymes to a lower potential, e.g., Eo′enzyme = -0.05 V, then the microbe will only be able to capture a part of the total available free energy.

Set anode potentials in MFC differ widely from -0.2 V to +0.8 V (vs. SHE). It is accepted that the anode potential has to be more positive than that of the potential of the substrate and thus to simulate natural terminal electron acceptors. The use of different electrode materials such as stainless steel or graphite does not allow the comparison of the current generated at poised anodes. In their review article Wagner et al. [8] summarize the received data and show that current densities generated at different applied potentials have very different values. Some investigators suggest potential input at negative potentials, which would create conditions similar to those in a MFC. Others suggest that more positive potentials would provide more free energy to the microorganisms. Depending on the microorganisms used as biocatalysts, the optimal anode potentials, leading to high current densities and more rapid start-up times, needs further investigation.

In this study, the influence of the imposed potential on the extracellular electron transfer (EET) from *Candida melibiosica* 2491 yeast to carbon-felt electrode was examined. For this purpose, chronoamperometry (CA) with different imposed potentials between -0.2 and +0.4 V vs. Ag/AgCl was applied to the electrode, immersed in an acetate buffer, where yeast cells had been suspended for cultivation. The behavior of the culture and the cell response to the applied electrical voltage was explored by means of cyclic voltammetry (CV) and electrochemical impedance spectroscopy (EIS).

EXPERIMENTAL

Yeast cultivation

The yeast inoculum was fresh prepared after *C. melibiosica* 2491 was cultivated at enriched medium (YP_{fru}) as previously described [10]. 500 ml suspension was centrifuged at 5000xg and washed twice with acetate buffer. 6% inoculum with *Candida melibiosica* was determined by spectrophotometric measurement at A_{600}=0.630 at 100x dilution. The biocatalyst had been sterile inoculated in 40 ml 0.2 M acetate buffer, pH 4.6, allowing 3 h adaptation before the respective potential was applied.

Electrochemical analyses

Potentiostatically-controlled anodes at four different potentials (-0.2, +0.2, +0.3, +0.4 V vs. Ag/AgCl) have been examined for current generation for 50 h in a batch operation mode. At each particular potential, the experiment was carried out separately, however, the conditions have been unified (electrode surface, quantity of inoculum, temperature, electrolyte). The analyses have been performed in a three-electrode mode, where a carbon felt (SPC-7011, 30 g/m^2, Weissgerber GmbH & Co. KG) with geometric area of 16 cm^2 was connected as a working, Pt-wire as a counter and Ag/AgCl (3.5 M KCl) as a reference electrode. The experiments were carried out at 26 °C. The generated current was monitored during the whole experimental window and recorded every five minutes by PalmSens 3 potentiostat. For better comparison, the received data are presented as unified current density (mA/m^2) and the applied potentials referred to SHE (Table 1).

Table 1. Applied potentials to the working electrode in the presence of yeast suspension.

Half-cell samples	Poising potentials, V vs. SHE
$Anode_1$	+0.005
$Anode_2$	+0.405
$Anode_3$	+0.505
$Anode_4$	+0.605

The performance of yeast biocatalyst has been also examined by means of cyclic voltammetry (CV) for determination of the redox activity of the yeast suspension and electrochemical impedance spectroscopy (EIS) for clarification of the charge transfer hindrances after the anode poisoning. EIS was carried out in the frequency range from 50 kHz to 5 mHz with an applied ac signal with an amplitude 10 mV and Edc equal to characteristic peak potentials in CVs.

At the end of the chronoamperometric experiments the yeast suspension was collected and yeast cells were pelleted by centrifugation at 5000xg for 10 minutes. The obtained cellular-free anolyte was filtrated by sterile filter with 0.2 μm ϕ

pores` size. The electrochemical activity of the filtrate was analyzed by CV and EIS.

RESULTS AND DISCUSSION

Anodic set potentials have been chosen to be sufficiently positive so that to allow the use of the anodes for extracellular transfer of electrons by the yeast cells (Fig. 1). At +0.005 V (vs. SHE) the current began from too negative values, rising fast in the first hour, but remaining negative till the end of experiment (Fig.1a). At +0.405 V (vs. SHE) the response of the yeast in the beginning differed but still manifested in negative currents. These results show definitely that both potentials are insufficient to force the yeast cells to transfer electrons/protons to the anode. Increasing the set potentials up to +0.605 V (vs. SHE) (Fig.1b) leads to positive current densities, which slightly decreased at +0.505 V, but increased at +0.605 V. The best performance was obtained by poising at +0.605 V (vs. SHE). The resulting curve resembles the growth curve of the culture, previously established [10]. Relative stable current density of ca. 40 mA/m2 has been achieved.

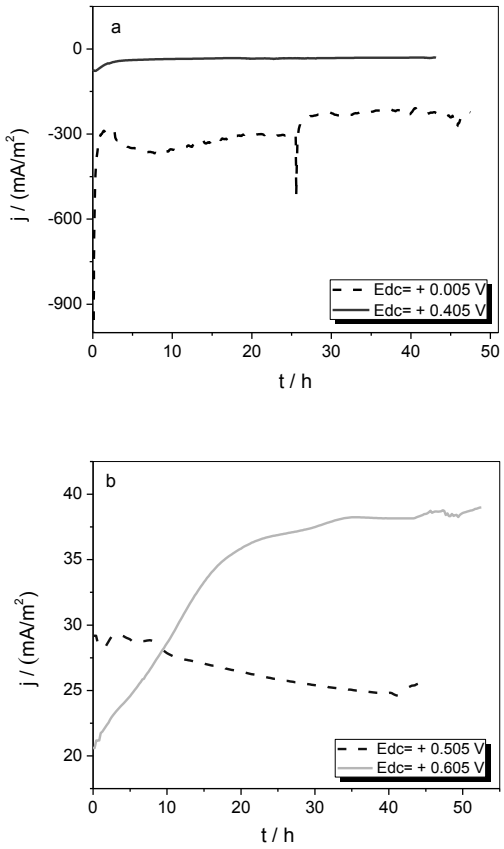

Fig. 1. Current densities over time with anodes set at: a) +0.005 V (dashed line) and +0.405 V (solid line) potentials; b) +0.505 V (dashed line) and +0.605 V (solid line) vs. SHE.

Having in mind that at the end of exponential phase of growth the electrogenic properties of *C. melibiosica* are characterized with the production of exogenous mediator (EnM), we carried out CV for tracing the redox activity of the yeast culture at the different set of potentials applied. The results are presented in Fig. 2.

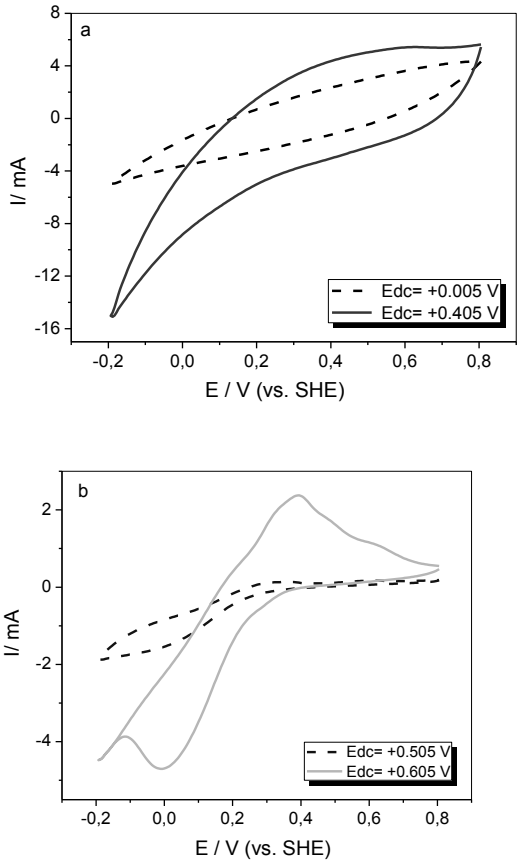

Fig. 2. CV of yeast suspension cultivated at applied potentials: a) +0.005 V (dashed line) and +0.405 V (solid line) potentials; b) +0.505 V (dashed line) and +0.605 V (solid line) vs. SHE. Scan rate 10 mV/s.

As expected, none visible redox peaks have been observed with the electrodes poised at +0.005 and +0.405 V (vs. SHE) (Fig. 2a). Unlike them, the cyclic voltammogram of the electrode poised at +0.505 V (vs. SHE) reveals slightly hinted peaks at +0.335 and +0.595 V (vs. SHE), respectively (Fig. 2b). The registered oxidation peaks directs that the yeast are electrochemically active around this potential range. A significant augmentation of yeast redox activity is observed after poising the anode at +0.605 V (vs. SHE). Both anodic and cathodic currents have been enlarged with a clearly distinguishable oxidation peak at +0.395 V and a reduction peak at -0.010 V (vs. SHE).

The yeast capability of secreting an EnM participating in electricity generation processes

with $Anode_4$ was additionally analyzed by both CV and EIS. The recorded CVs are characterized by appearance of broad anodic and cathodic peaks, which potential difference rises with the increase of scan rate, indicating a quasi-reversible electrochemical behavior (Fig. 3a). The estimated formal redox potential ($E^{o`}$) from the CV obtained at 10 mV/s is +0.195 V (vs. SHE), which is close to data from our previous studies carried out in real MFCs [2], in which the formal redox potential of non-fractionated yeast suspensions ranges between +0.200 and +0.285 V (vs. SHE) depending on the substrate used [12].

The linear dependence of the peaks` currents on the square root of scan rates reveals a presence of electroactive soluble compound, capable of transferring electrons from the yeast cells to the anode (Fig. 3a, inset). The impedance data (Fig. 3b) fit well to R_1-CR_2-QR_3 equivalent electrical circuit model. Because the second arc is not an ideal semi-circle but rather a depressed one, a constant phase element (CPE) was introduced instead of a second capacitor.

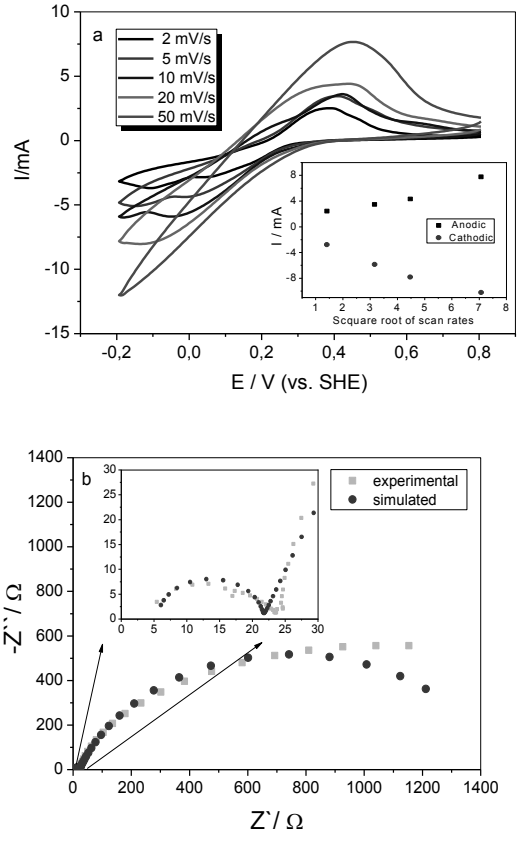

Fig. 3. Electrochemical analyses of yeast suspension after chronoamperometric experiments at +0.605 V (vs. SHE): a) CV with different scan rates. Inset: Dependence of anodic and cathodic peak currents on the square root of scan rate.; b) EIS-Nyquist plot – E_{ac}=10mV, E_{dc}= $E_{ox\ peak}$.

The results show that the ohmic resistance (R_1 = R_Ω = 5.5 Ω) and the charge transfer resistance (R_2 = R_{CT} = 16 Ω) are insignificant compared to R_3= 1455 Ω. Considering the presence of living cells, their redox activity and therefore the complexity of the system, the second arc might be attributed to internal cellular metabolic processes, as proposed by Sekar and Ramasamy [11], and the resistance R_3, denoted as R_{in}, is determined by the yeast ability to grow under these conditions and to produce electrochemically active compounds to communicate with the anode. It is considered that the in parallel connected capacitance and the resistance of the first arc describe the external processes, occurring on the electrode surface (that is why R_2 is referred to as R_{ex}) with the contribution of the biological elements (whole cells and secondary metabolites).

To distinguish the contribution of the yeast cells themselves from that of the secreted active metabolites to the current generation processes, the exploited anolyte was fractionated and the redox activity of the cellular-free supernatant was investigated by CV (Fig. 4a). The results show the presence of a soluble redox active substance with a formal potential $E^{o`}$= +0.192 V (vs. SHE). Assuming that all molecules secreted by the yeast cells are in a reduced form to complete their biological role for extracellular electron transfer to the anode, at a positive potential of +0.217 V (vs. SHE) the molecules contacting the electrode surface have been electrochemically oxidized, resulting in a sharp oxidation peak. Sweeping the potential in negative direction leads to their reduction and a formation of a cathodic peak with a maximum at +0.166 V (vs. SHE). Comparing the peak potentials obtained with cellular-free fraction and yeast suspension at the same scan rate (Fig 3a), it is seen that in the presence of yeast cells, the anodic peak is shifted in positive direction, while the cathodic peak is shifted to more negative values. The peak currents show with an order of magnitude higher values, which in turn directs to an enhanced oxidation ability in the presence of the yeast biocatalysts. Within the cells, EnM is reduced by NADH or $FADH_2$ (cofactors of important enzymes) in the cytoplasm or by cytochromes of the mitochondrial electron transport chains [14].

The impedance spectra also showed significant difference in comparison with the yeast suspension behavior (Fig. 4b). The lack of a second arc at the absence of yeast cells supports the hypothesis that this arc describes the hindrances connected with the

complex cellular processes contributing to the extracellular electron transfer (EET). Having in mind that in the yeast suspension, the oxidized EnM enters the cells to be reduced again and secreted in the medium to be re-oxidized on the anode repeatedly, the lack of yeast cells is responsible to the huge charge transfer resistance in the cellular-free fraction. The Bode plot data, however, show a maximum negative phase angle at mid frequencies (Fig. 4b - inset), which is attributed to the presence of EnM, as previously suggested [11].

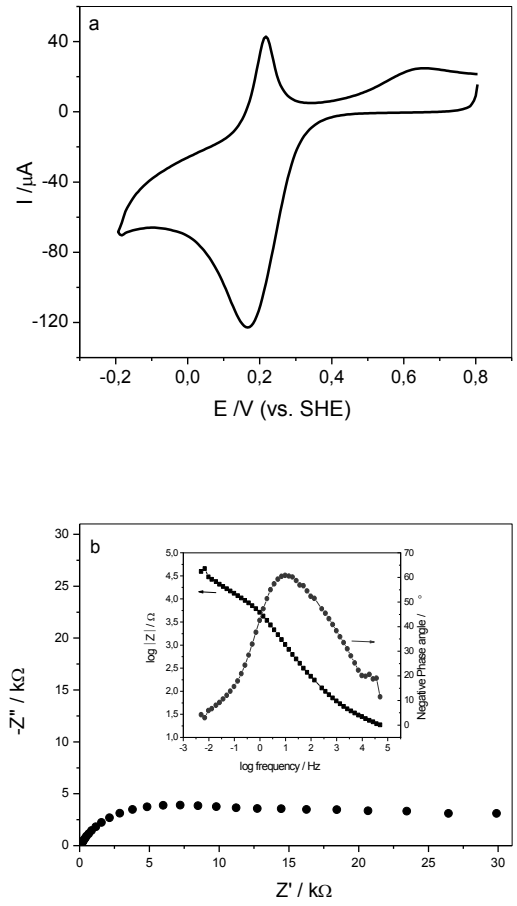

Fig. 4. Electrochemical analyses of filtrated cellular-free fraction, containing EnM: a) CV, scan rate 10 mV/s, second scan; b) EIS-Nyquist plot (Eac=10mV, Edc= Eox peak). Inset: EIS-Bode plot.

As stated by Wagner et al. [8], more positive anode potentials should allow microorganism to gain more energy per electron transferred than a lower potential, but this can only occur if the microbe has metabolic pathways capable of capturing the available energy. In our recent study [15], we proved that in the presence of acetate *C. melibiosica* yeast up-regulates the Glyoxylate cycle for acetate assimilation and biosynthesis of carbohydrate precursors such as malate, succinate and oxaloacetate.

The investigation was carried out in real two-chamber MFCs with continuously connected external load. The obtained results in this study reveal that +0.605 V (vs. SHE) is an appropriate potential to mimic MFC-conditions mentioned above, while the yeast use acetate as a substrate. This potential is sufficient also to up-regulate a secondary metabolic pathway for synthesis of active metabolite (EnM), contributing to the current generation under these conditions.

CONCLUSIONS

The half-cell studies with potentiostatically poised carbon felt electrodes and *C. melibiosica* 2491 yeast as a biocatalyst show that anodic reaction connected with the yeast electrochemical activity occurs at potentials higher than +0.5 V (vs. SHE). The current density at +0.605 V (vs. SHE) reached stable values of ca. 40 mA/m^2 in a batch operation mode. After reaching a steady-state, well-defined anodic and cathodic peaks appear in the cyclic voltammograms of the anolyte, indicating a production of endogenous mediator for accomplishment of extracellular electron transfer. The differences in the impedance spectra obtained in the presence and absence of yeast cells reveal the contribution of the cellular processes to the EET and the anodic current generation.

***Acknowledgments**: This study was supported by contract DFNI-TO2/2-12.12.2014 with the Bulgarian National Science Fund.*

REFERENCES

1. C. Santoro, C. Arbizzani, B. Erable, I. Ieropoulos, *J. Power Sources*, **356**, 225 (2017).
2. Y. Hubenova, M. Mitov, *Bioelectrochemistry*, **106A**, 177 (2015).
3. C. Santoro, C. Flores-Cadengo, F. Soavi, M. Kodali, I. Merino-Jimenez, I. Gajda, J. Greenman, I. Ieropoulos, P. Atanassov, *Sci. Rep*., **8**, 3281 (2018).
4. B.G. Lusk, I. Peraza, G. Albal, A.K. Marcus, S.C. Popat, C.I. Torres, *J. Am. Chem. Soc*., **140**, 5527 (2018).
5. C. Torres, A.K. Marcus, P. Parameswaran, B. Rittmann, *Environ. Sci. Technol*., **42**, 6593 (2008).
6. P. Aelterman, S. Freguia, J. Keller, W. Verstraete, K. Rabaey, *Appl. Microbiol. Biotechnol*., **78**, 409 (2008).
7. C.I. Torres, A.K. Marcus, B.E. Rittmann, *Appl. Microbiol. Biotechnol*., **77**, 689 (2007).
8. R. Wagner, D. Call, B. Logan, *Environ. Sci. Technol*., **44**, 6036 (2010).
9. E. Marsili, J. Sun, D.R. Bond, *Electroanalysis*, **22**, 865 (2010).

10. Y. Hubenova, M. Mitov, *Bioelectrochemistry*, **78**, 57 (2010).
11. N. Sekar, R.P. Ramasamy, *J. Microb. Biochem. Technol*., **S6**, 004 (2013).
12. Y. Hubenova, in: Encyclopedia of Interfacial Chemistry: Surface Science and Electrochemistry, K. Wandelt, (ed), vol. 7, Elsevier Inc., 2018, p. 537.
13. S. Babanova, Y. Hubenova, M. Mitov, *J. Biosci. Bioeng*., **112**, 379 (2011).
14. Y. Hubenova, M. Mitov, *Bioelectrochemistry*, **106A**, 232 (2015).
15. Y. Hubenova, E. Hubenova, E. Slavcheva, M. Mitov, *Bioelectrochemistry*, **116**, 10 (2017).

Хроноамперометрично приложено напрежение върху електрод имитира поведението на дрожден биоанод в биогоривна клетка

Й. Хубенова [1,2], *, Е. Хубенова [3], М. Митов [4]

[1] *Институт по електрохимия и енергийни системи „Акад. Евгени Будевски” - БАН, Акад. Г. Бончев ", бл.10, 1113 София, България*
[2] *Пловдивски университет „Паисий Хилендарски”, ул. "Цар Асен" 24, 4000 Пловдив България*
[3]*Център за педиатрия, Университетски клиники, университет в Бон, Аденауреале 119, 53113 Бон, Германия*
[4]*Инновационен център за екоенергийни технологии, Югозападен университет "Неофит Рилски", ул. "Иван Михайлов" 66, 2700 Благоевград, България*

Постъпила на26 май 2018г. ; приета на16 август 2018г.

(Резюме)

Подаването на напрежение на електроди в три електродна електрохимична клетка се използва като подход за установяване на благоприятни редокс-условия за извънклетъчен електронен трансфер (EET) от биокатализатора до анода. Демонстрирано е, че оптималните приложени потенциали се различават за отделните видове микроорганизми и зависят от специфичните им метаболитни пътища. В това изследване, потенциали от +0.005, +0.405, +0.505 и + 0.605 V (срещу SHE) са прилагани върху въглеродни електроди в присъствието на екзоелектрогенен щам на дрожди *Candida melibiosica* 2491. Резултатите от хроноамперометричните експерименти показват, че дрождите са способни да осъществяват EET при положителни потенциали, по-високи от +0.5 V. Токът, генериран при + 0.605 В (срещу SHE), следва фазите на растеж на дрождите, достигайки стабилни максимални нива от 40 mA /m^2. Извършената циклична волтамперометрия показва, че наблюдаваната електрохимична активност се дължи на произведен и секретиран ендогенен медиатор на EET, имитирайки вече установеното поведение на дрождения щам в реални биогоривни клетки. Разликите в електрохимичните импедансни спектри, получени със дрождена суспензия и безклетъчни фракции, описват приноса на клетъчните процеси към генерирането на аноден ток.

Bulgarian Chemical Communications, Volume 50 Special Issue D (pp. 68 – 74) 2018

Redox interactions between dye 4-(E)-1-ethyl-4-(2-(4-hydroxynaphthalen-1-yl)vinyl)quinolinium bromide and NAD^+/NADH

Y. Hubenova [1,2,*], R. Bakalska[2], E. Hubenova [3], M. Mitov [4]

[1] *Acad. Evgeni Budevski Institute of Electrochemistry and Energy Systems, Bulgarian Academy of Sciences, Acad. G. Bonchev" Str., bl.10, 1113 Sofia, Bulgaria*
[2] *Paisii Hilendarski Plovdiv University, 24 "Tsar Asen" Str., 4000 Plovdiv Bulgaria*
[3] *Center for Pediatrics, University Clinics, University of Bonn, Adenauerallee 119 53113 Bonn, Germany*
[4] *Innovative Center for Eco Energy Technologies, South-West University Neofit Rilski, 66 Ivan Mihaylov Str., 2700 Blagoevgrad, Bulgaria*

Received June 08, 2018 Revised August 16, 2018

An intrinsic property of the merocyanine dyes is the intramolecular charge transfer, which determines a variety of their applications in different fields like optical communication technology, molecular electronics, as optical chemosensors for analytical purposes and voltage-sensitive dyes for mapping membrane potential changes in excitable cells, etc. In this study, the electrochemical behavior of recently synthesized styrylquinolinium dye 4-(*E*)-1-ethyl-4-(2-(4-hydroxynaphthalen-1-yl)vinyl)quinolinium bromide and its possible interaction with NAD^+/NADH redox couple have been investigated. It has been established that in neutral and alkaline buffer solutions the dye co-exists in benzenoid (reduced) and quinoid (oxidized) forms and the equilibrium between both forms can be shifted by change of pH. A quasi-reversible electrochemical behavior, assigned to consecutive electroreduction and electrooxidation of dye, has been observed by means of cyclic voltammetry. The redox coupled interaction between the dye and NAD in solution is evaluated by juxtaposing the results obtained by UV-Vis spectroscopy, cyclic voltammetry and electrochemical impedance spectroscopy.

Key words: styrylquinolinium dye, electrochemical activity, NAD+/NADH, UV-Vis spectroscopy, cyclic voltammetry, electrochemical impedance spectroscopy.

INTRODUCTION

Microbial fuel cells (MFCs) are devices capable of converting the chemical energy of available organic substrates directly into electricity by using different microorganisms as bio-micro reactors. The main drawback of MFC technology, which limits the broader application as power sources, is the low achieved power and generated current. One of the factors influencing the microbial fuel cells' performance is the electron transfer from the living cells to the anode surface, which might be overcome by the addition of the so called exogenous mediators (ExMs) of extracellular electron transfer (EET). Among the most explored artificial mediators are methylene blue [1, 2], thionine [3], neutral red [1, 4, 5], 2,6-dichloro phenolindophenol, safranine-O, phenothiazine, resurofin [6], etc. It is proven that the formal potential of every exogenous mediator determines the possibility for exchanging electrons with cellular redox molecules possessing close potential [7]. The highest increase of the current (1 $A.m^{-2}$) and power (640 $mW.m^{-2}$) generated by yeast-based biofuel cell has been achieved with the methylene blue [1], possessing formal potential Eo`= +0.055 V (vs. SHE). Exogenous mediators with positive formal potentials like thionine (Eo`=+0.064), methyl red (Eo`= +0.385), etc., act as electron acceptors beeing reduced by electrons originating from various metabolic pathways, while mediators with too negative formal potentials like bromocresol green (Eo`= -0.380 V) and neutral red (Eo`= -0.290 V) are capable of exchanging electrons only with redox molecules with more negative potentials (like NADH) in a way important for balancing levels for gain of biological and electrical energy [8]. Diverting electrons from different energetic levels, the exogenous mediators actually affect the metabolic pathways. It is demonstrated that bromocresol green and neutral red are capable of up-regulating alcoholic fermentation, while those with more positive potentials like methylene blue redirects the yeast catabolism to predominant aerobic respiration [2].

To whom all correspondence should be sent:
E-mail: y.hubenova@iees.bas.bg

Thus, the use of ExMs becomes a new appropriate approach for studying energy levels of metabolic pathways and their contribution to the EET. The mechanisms of acting of ExMs are still unclear and need more in vivo as well as in vitro investigations for explanation of the processes occurring within biocatalysts and the biofuel cell. Finding new redox active molecules as putative exogenous mediators will contribute to better understanding and elucidation of the reaction mechanisms between ExMs and cellular redox couples.

Recently, the influence of dye 4-{(*E*)-2-[4-(dimethylamino)naphthalen-1-yl]ethenyl}-1-methylquinolinium iodide (DANSQI) on the electrical outputs of *Candida melibiosica* 2491 yeast-based biofuel cell was investigated [9]. Exploring the possible mechanisms for the observed improved performance, it was suggested that the dye acts as subcellular shuttle on account of its specific intramolecular charge transfer properties and the transition between its basic forms - benzenoid and quinoid. The exchange of electrons/protons between DANSQI and subcellular electronophores was proved. It was also established that the presence of the dye affects the yeast metabolism. Subcellular studies showed that 1 μM dye increased 30-times the peroxisomal catalase activity (1.15 ± 0.06 Unit/mg protein) and twice the mitochondrial cytochrome *c* oxidase activity (92 ± 5 Unit/mg protein).

In this study, another, recently synthesized and characterized styrylquinolinium dye 4-(E)-1-ethyl-4-(2-(4-hydroxynaphthalen-1-yl)vinyl)quinolinium bromide (shortly D3) [10, 11] was investigated in respect to establishment of its redox properties and possible interaction with NADH/NAD+ redox couple in solution. Like other styrylquinolinium dye [9], D3 contains 4-hydroxynaphthyl group and quinolinium moiety with quaternary nitrogen linked by conjugated bridge (−CH=CH–) [11]. Due to the conjugated structure, an intrinsic property of this class of dyes is the intramolecular charge transfer (ICT) from the phenol hydroxyl group (acting as an electron donor) through the π-conjugated bridge to the quinolinium moiety (acting as an electron acceptor). The results, obtained by means of electrochemical (EIS, CV) and spectrophotometric methods, are compared and discussed.

MATERIALS AND METHODS

Preparation of solutions

The styrylquinolinium dye 4-(E)-1-ethyl-4-(2-(4-hydroxynaphthalen-1-yl)vinyl)quinolinium bromide (D3) was synthesized as previously described [10]. Freshly prepared 2.5 mM dye in DMSO was used as a stock solution for further dilution to 50 μM in the respective 0.1M buffer (phosphate buffered saline (PBS), pH 7; Tris-HCl, pH 8; acetate buffer, pH 4.6 and potassium phosphate, pH 10) or 10 mM NaOH.

1 mM nicotinamide adenine dinucleotide (NADH or NAD+) solutions were freshly prepared just before the experiments and mixed with the dye in proportion 10:1. 10 mM sodium hydroxide, pH 12, was used for stabilization of NADH in solution and preventing its non-controlled oxidation. Water alone should not be used to prepare NADH solutions since it is a proton-donor solvent and would decompose NADH.

Electrochemical studies

The electrochemical behavior of D3 alone and in mixtures with NAD+ or NADH was investigated by means of electrochemical impedance spectroscopy (EIS) and cyclic voltammetry (CV). Both studies were performed in three-electrode mode by using platinum wires as working and counter electrodes and Ag/AgCl (3M KCl) as a reference electrode. The CV studies were carried out with different scan rates (from 10 mV/s to 1 V/s) by using PalmSens 2 potentiostat/galvanostat. The EIS measurements were conducted at frequency range varying from 50 kHz to 2 mHz, an ac signal of amplitude 10 mV and dc at a fixed potential module (vs. OCP). A PalmSence 3 potentiostat with EIS function was used for these analyses.

The capacitance of the double layer (C_{dl}) was estimated by formula (1):

$$C_{dl} = \frac{1}{\omega . R_{CT}} \quad (1)$$

where ω is the radial frequency (ω=2πf) and RCT is the charge transfer resistance determined from the impedance spectra.

The exchange current density (j0) was calculated using equation (2):

$$j_o = \frac{RT}{2FS} . \frac{1}{R_{CT}} \quad (2)$$

where R is the gas constant, T is the absolute temperature, F is the Faradaic constant, 2 is the number of exchanged electrons and S is electrode area in cm^2.

Spectrophotometric measurements

The spectrophotometric analyses for determination of the benzenoid (D3BF) and quinoid (D3QF) forms of the dye were performed in a wavelength scan mode between 200 nm and 800 nm, while the presence of the reduced or

oxidized form of NAD was traced up to 450 nm by using Hach-Lange UV-Vis spectrophotometer.

RESULTS AND DISCUSSION

In our previous study [9], it was demonstrated that the hemicyanine dye DANSQI can undergo transformations from quinoid to benzenoid form and vice versa depending on the solvent. Taking into consideration that these reversible transformations are connected not only with ICT of electrons but also with processes of protonation/deprotonation [11], it can be expected that they are pH-dependent, i.e. the equilibrium between both forms can be shifted by changes of pH. To check this hypothesis, D3 was dissolved in buffers with different pH and the obtained solutions were analyzed spectrophotometrically. Two characteristic absorption bands can be distinguished on the recorded spectra (Fig. 1). The shorter-wave absorption band at 460 nm, corresponding to the SO–CT (where SO is the singlet state and CT is the charge transfer state) transition, is referred to the benzenoid structure of the dye (D3BF) and the longer wavelength band - to the quinoid form (D3QF) [12]. Normally, the absorption bands of the dye D3 are broad, having half-widths of about 5000 cm^{-1}. The broadness of the absorption bands may arise due to a contribution of more than one electronic state to the absorption spectrum or a broad distribution of conformers (solvent-solute or intramolecular) in the ground state. Analyzing the individual spectra, it can be concluded that in acidic medium only the benzenoid form exists, while in neutral and alkaline buffer solutions a co-existence of both forms of the dye is observed. It should also be noted that in alkaline media the characteristic absorption band for benzenoid form is sharpen, which is probably connected with deprotonation of the phenol hydroxyl group at high pH and formation of an anion [11, 13]. Such narrowing of the band was also observed with the addition of an organic base piperidine to the D3 solution [12, 14]. In anhydrous DMSO solution, D3 exists only in a quinoid form (Fig. 1, inner graph). The splitting of the absorption maximum into two bands with λmax at 680 nm and 650 nm is associated with aggregation phenomenon [11]. The maximum at 680 nm is assigned to a monomer, while the lower one at 650 nm - to the quinoid dimer. Though not so clearly expressed, a shoulder from shorter-wave side at 650 nm can be also distinguished in the spectra of the dye in alkaline buffer solutions.

The existence of D3 in reduced (benzenoid) and oxidized (quinoid) forms suggests that the dye could play the role of an electron-acceptor (oxidizer) as well as an electron-donor (reductant). Thus, it can be supposed that D3 may undergo a reversible electrochemical conversion and participate in a variety of processes with an exchange of electrons and/or protons.

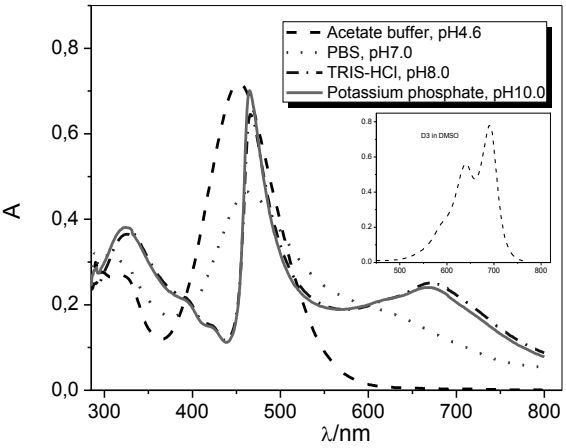

Fig. 1. UV-Vis spectra of dye D3 dissolved in buffers with different pH; inner graph – D3 in DMSO.

The electrochemical activity of D3 in alkaline buffer solution, where it exists in both reduced (D3BF) and oxidized (D3QF) forms, was examined by means of CV. When the potential was swept in negative direction, a well-defined cathodic peak appeared on the CVs, which shifted to more negative potentials with the increase of the scan rates (Fig. 2). At the lowest scan rate applied (50 mV/s), the cathodic peak potential in the presence of D3 (-54 mV vs. Ag/AgCl) significantly differs from that observed on the CV of the background NaOH electrolyte (-200 mV vs. Ag/AgCl), which supposes that the former one is attributed to the electroreduction of the dye on the electrode surface. After reversing the scan into positive direction, a big anodic peak is formed with a maximum at -540 mV vs. Ag/AgCl at 50 mV/s, shifting to more positive potentials with acceleration of the scan rate. It is worth noticing that at the same scan rate the position of this peak coincides with that of the anodic peak in the voltammogram of NaOH solution, which is firmly connected with the hydrogen desorption reaction. However, the much higher intensity of the corresponding anodic peak in the presence of D3 suggests a strong contribution of the dye to the formation of this peak. In a previous study [11], a two-step mechanism for oxidation of the reduced form of D3 was proposed, which first step includes a formation of negatively charged intermediate by deprotonation of the phenol hydroxyl group. Thus, it may be hypothesized that the enhanced anodic peak in the presence of D3 is due to the increased amount of protons as a product of dye deprotonation. Another evidence, supporting

such hypothesis, is the close intensity of the cathodic and anodic peaks at the same scan rates, supposing that the electroactive particles, participating in the oxidation reaction, originate from the reduced dye formed during the cathodic scan. At more positive potentials (above +400 mV vs. Ag/AgCl), an anodic hump (better distinguishable at higher scan rates) is observed, which could be assigned to the ICT and conversion of the intermediate dye anion into D3QF [11].

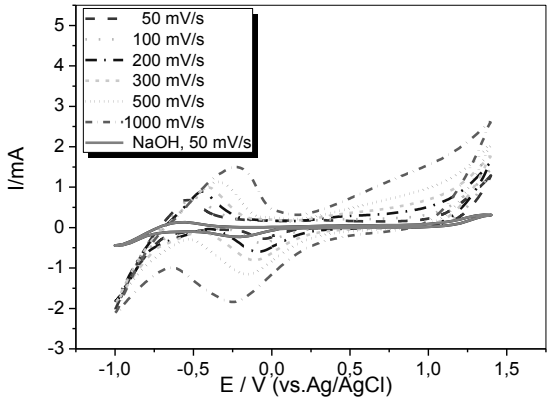

Fig. 2. Cyclic voltammograms of 50 μM 4-(E)-1-ethyl-4-(2-(4-hydroxynaphthalen-1-yl)vinyl)quinolinium bromide (D3 dye) obtained with increasing scan rates.

The established electrochemical activity of D3 motivated the investigation of the putative interactions between the dye and reduced or oxidized form of NAD^+/NADH couple, which is widely explored as a model redox system because of its important role in the energetics of the living cells [15].

Distinguished differences were observed in the CV patterns obtained with NAD^+ and its mixture with D3 (Fig. 3a). While well-defined broad cathodic and anodic peaks, assigned to multistep electroreduction and re-oxidation, appeared in the CV of NAD^+, the CV of the mixture of NAD^+ and D3 is similar to that of NADH (Fig. 3b), suggesting that the predominant form of the dye D3BF reduced NAD^+ to NADH. Though the CVs of NADH and its mixture with D3 look similar, some differences in the patterns exist. First, in the presence of the dye the observed cathodic peak is shifted to more positive potentials, and second, a new oxidation peak at ca. +250 mV (vs. Ag/AgCl) appears, which is missing in the CV of NADH. The lack of pronounced anodic peak, corresponding to the NADH electrooxidation, may be attributed to different reasons such as electrode fouling, formation of electrochemically inactive intermediates, etc. Elving et al. [16] emphasized the impact of the experimental protocol on the results obtained in the electrochemical studies of the NAD system in aqueous media, especially as related to the effects of adsorption of the various NAD species, the mediation role of adsorbed and other surface species on the electrode, and the time-scale of the particular experimental approach used.

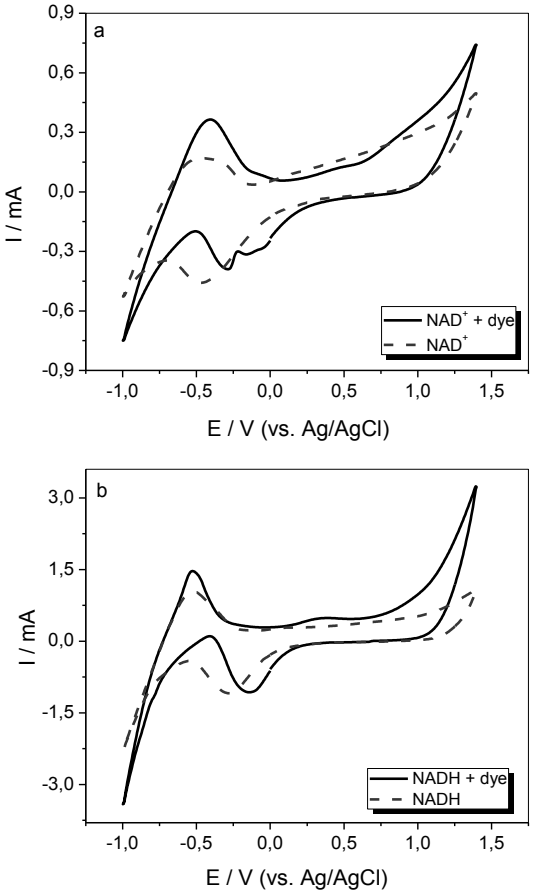

Fig. 3. Cyclic voltammograms of: a) 500 μM NAD+ (dashed line) and mixed solution of 500 μM NAD+ and 500 μM D3 (solid line); b) 500 μM NADH (dashed line) and mixed solution of 500 μM NADH and 500 μM D3 (solid line); Scan rate 200 mV/s.

It was supposed that in the case of Pt or Au electrodes, on which surface the adsorption of NAD^+ is negligible, the initial step in the NADH oxidation proceeds to at least some extent through mediator redox systems located close to the electrode surface such as OH^-_{ads}/H_2O, O_{ads}/OH^-_{ads} or other redox couples. It was also assumed that a key point in the NADH oxidation pattern is the deprotonation step and its relation to the initial electron-transfer step [16]. Thus, the appearance of the anodic peak at ca. +250 mV (vs. Ag/AgCl) in the CV of mixture of NADH and D3 could be related namely to the role of D3QF/D3BF redox couple as a mediator for initialization of NADH oxidation, probably associated with facilitated exchange of protons with the quinoid form of the dye.

Summarizing the results from the CV experiments, it can be concluded that due to the co-existence of both forms (D3QF and D3BF) in

alkaline buffer solutions the styrylquinolinium dye D3 may interact with NAD^+ as well as with NADH at appropriate conditions. Having in 3mind that the benzenoid form of the dye presents the reduced dye molecules, it is considered that the reduced dye donates electrons and a proton to the NAD^+, while the dye in its oxidized (quinoid) form may accept electrons/proton from NADH. In this way, the reduction of the dye occurs simultaneously with the oxidation of NADH and vice-versa in a non-enzymatic dynamic way (Fig. 4).

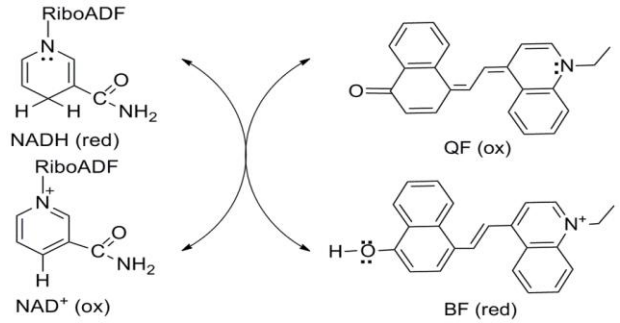

Fig. 4. Schematic presentation of the deductive reactions between D3 dye and NAD+/NADH.

The more evident differences in the CV patterns of NAD^+ and its mixture with D3 could be assigned to the predominance of the dye's reduced form (D3BF) in aqueous solutions, which interaction with the oxidized NAD is additionally forced by the applied electrochemical conditions. This hypothesis is supported by comparison of the UV-Vis spectra of mixture of NAD^+ and D3, recorded before and after the CV experiments (Fig. 5). The spectral data show that after electrochemical treatment of the mixture, the band of the benzenoid form decreases double, while the absorption band at higher wavelengths, representing the quinoid form, grows up, directing to a possible electrochemically forced coupled reaction between the dye and NAD.

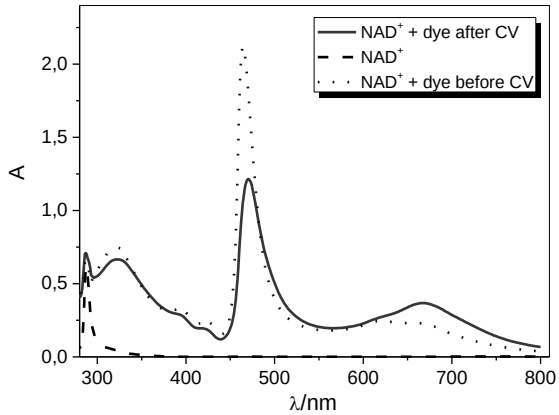

Fig. 5. UV-Vis spectra of 500 μM NAD+ and its mixture with 50 μM D3 before and after electrochemical experiments.

The interaction of the dye with NAD^+/NADH couple was additionally investigated by means of EIS. For the right interpretation of the obtained spectra, the data of the dye`s mixtures with NAD (Fig. 6a) have been compared with those of the substances alone (Fig. 6b). While all samples are diffusion limited at mid and low frequency range, the response to the applied sinusoidal signal in the high frequencies varied for the different substances (Fig. 6, insets; Table 1).

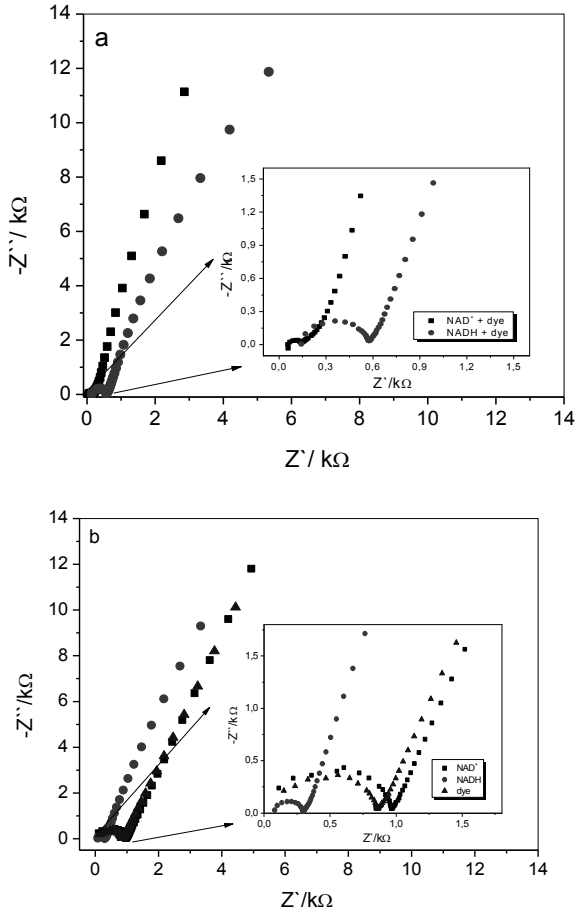

Fig. 6. Nyquist plots of: a) mixed solutions of 500 μM NAD+ + 50 μM D3 and 500 μM NADH + 50 μM D3; b) individual solutions of 50 μM D3; 500 μM NAD+ and 500 μM NADH, recorded at frequency range from 50 kHz to 2 mHz with sinus amplitude 10 mV. Insets - magnification of the impedance spectra at high frequencies.

It was assumed that the observed diverse parameters like ohmic (R_Ω) and charge transfer (R_{CT}) resistances as well as double layer capacitance (C_{dl}) are a consequence of occurred interaction in the case of mixed dye. For instance, the ohmic resistance of the dye itself remains identical in the presence of NADH (even when in excess), while the polarization resistance was twice lower and the capacitance – twice higher. Comparing the R_{CT} and C_{dl} of NADH alone to those of the mixture dye/NADH, it is seen that R_{CT} is

twice lower than that of the mixture but C_{dl} is twice higher. It was supposed that the capacitance of the mixed with NADH dye is lower because of their interaction in the solution and in the frame of the double layer exchanging electrons/protons, which would decrease their transfer to the electrode. In this way, although the smallest diameter was observed for NADH alone, showing the possible exchange of its 2 electrons and a proton with the electrode, the increasing arc diameter of the mixture indicates the exchange of NADH electrons and protons not with the electrode but with dye molecules instead. Having in mind, on the one hand, the intermediates formed and on the other one, the small surface of the Pt electrode, both could explain the increased resistances and bigger arc diameter. If we accept that a part of the NADH molecules are oxidized by the dye molecules (D3QF) we have to assume that NAD^+ is dynamically formed (thus D3BF, D3QF, NAD^+ and NADH are present in the sample). That is why the data obtained with NAD^+ alone and in mixture with the dye have been also compared. The presence of more reduced dye`s molecules in the sample, which might reduce NAD^+ molecules argues the lower ohmic resistance of the mixture dye/NAD^+ compared to NAD^+ alone. At the same time the R_{CT} of the mixture was 9-times lower than that of the NAD^+ and about 7-times lower than that of the dye alone. The highest capacitance of the dye/NAD^+ mixture could be due to the newly formed NADH, which itself shows the highest exchange current density among the pure explored substances. The similarity of the arc`s diameters of dye/NAD^+ and NADH itself supports this assumption.

Table 1. Extracted data from recorded electrochemical impedance spectra.

Sample	Ohmic resistance (R_Ω) Ω	Charge transfer resistance (R_{CT}) Ω	Double layer capacitance (C_{dl}) nF	Exchange current density (j_0) μA/cm^2
Dye D3 + NADH	145	431	25	37
Dye D3 + NAD^+	55	95	112	168
Dye D3	150	707	15	23
NADH	80	220	48	73
NAD^+	115	860	12	19

CONCLUSIONS

The dye 4-(*E*)-1-ethyl-4-(2-(4-hydro xynaphthalen-1-yl)vinyl)quinolinium bromide (D3), dissolved in neutral and alkaline buffer media, exists in benzenoid (reduced) and quinoid (oxidized) forms, which equilibrium is pH dependent. In alkaline buffers the dye can undergo reversible electrooxidation/electroreduction. It has been also established that dye D3 react with both oxidized and reduced forms of NAD, more pronounced with NAD^+, probably because of the predominance of benzenoid form (D3BF) at the explored experimental conditions. The coupled redox reactions can be detected by CV and EIS. The obtained results reveal a possibility for development of non-enzymatic method for detection of NAD *in vitro* as well as potential for utilization of the styrylquinolinium dye D3 as an exogenous mediator of electron transfer in bioelectrochemical systems as microbial fuel cells.

Acknowledgments*: This study was supported by the National Science Fund of Bulgaria through Contract DFNI-TO2/2-12.12.2014.*

REFERENCES

1. S. Babanova, Y. Hubenova, M. Mitov, *J. Biosci. Bioeng*., **112**, 379 (2011).
2. Y. Hubenova, M. Mitov, *Bioelectrochemistry*, **106**, 232 (2015).
3. M. Rahimnejad, G. D. Najafpour, A. A. Ghoreyshi, F. Talebnia, G. C. Premier, G. Bakeri, J. R. Kim, S.-E. Oh, *J. Microbiol*., **50**, 575 (2012).
4. S. Wilkinson, J. Klar, S. P. Applegarth, *Electroanalysis*, **18**, 2001 (2006).
5. M. Rahimnejad, G. D. Najafpour, A. A. Ghoreyshi, M. Shakeri, H. Zare, *Int. J. Hydrogen Energ.*, **36**, 13335 (2011).
6. H. P. Bennetto, J. L. Stirling, K. Tanaka, C. A. Vega, *Biotechnol. Bioeng*., **25**, 559 (1983).
7. Y. Hubenova, M. Mitov, *Bioelectrochemistry*, **106**, 177 (2015).

8. Y. Hubenova, in: Encyclopedia of Interfacial Chemistry: Surface Science and Electrochemistry, Klaus Wandelt (ed), Elsevier, 2018, p. 537.
9. Y. Hubenova, R. Bakalska, E. Hubenova, M. Mitov, *Bioelectrochemistry*, **112**, 158 (2016).
10. H. El Ouazzani, S. Dabos–Seignon, D. Gindre, K. Iliopoulos, M. Todorova, R. Bakalska, P. Penchev, S. Sotirov, Ts. Kolev, V. Serbezov, A. Arbaoui, M. Bakasse, B. Sahraoui, *J. Phys. Chem.* C, **116**, 7144 (2012).
11. Y. Hubenova, R. Bakalska, M. Mitov, *Bioelectrochemistry*, **123**, 173 (2018).
12. T. Kolev, R. Bakalska, M. Todorova, in: Proceedings of the Humboldt-Kolleg, Sofia, Faber Publishing House, 2016, Sofia, pp. 209-221.
13. S. Wahyuningsih, L. Wulandari, M. W. Wartono, H. Munawaroh, A. H. Ramelan, *IOP Conf. Ser.: Mater. Sci. Eng.*, **193**, 012047 (2017).
14. E. A. Ribeiro, T. Sidooski, L. G. Nandi, V. G. Machado, *Spectrochim. Acta A Mol. Biomol. Spectrosc.* **81**, 745 (2011).
15. D. S. Bilan, A. G. Shokhina, S. A. Lukyanov, V. V. Belousov, *Russ. J. Bioorg. Chem*., **41**, 341 (2015).
16. P. J. Elving, W. T. Bresnahan, J. Moiroux, Z. Samec, *Bioelectrochem. Bioenerg.*, **9**, 365 (1982).

Окислително- редукционни взаимодействия между багрилото 4- (E) -1-етил-4- (2- (4-хидроксинафтален-1-ил) винил) хинолиниев бромид и NAD+/NADH

Й. Хубенова [1,2,*], Р. Бакалска [2], Е. Хубенова [3], М. Митов [4]

[1] *Институт по електрохимия и енергийни системи „Акад. Евгени Будевски” - БАН, Акад. Г. Бончев ", бл.10, 1113 София, България*
[2] *Пловдивски университет „Паисий Хилендарски”, ул. "Цар Асен" 24, 4000 Пловдив България*
[3] *Център за педиатрия, Университетски клиники, университет в Бон, Аденауреале 119, 53113 Бон, Германия*
[4] *Инновационен център за екоенергийни технологии, Югозападен университет "Неофит Рилски", ул. "Иван Михайлов" 66, 2700 Благоевград, България*

Постъпила на26 май 2018г. ; приета на16 август 2018г.

(Резюме)

Присъщо свойство на мероцианиновите багрила е вътрешномолекулния пренос на заряд, който определя приложенията им в различни области като оптично- комуникационна технология, молекулярна електроника, използването им като оптични хемосензори за аналитични цели и картографиране на измененията на мембранния потенциал във възбудими клетки. В настоящото изследване е анализирано електрохимичното поведение на синтезираното наскоро багрило 4- (E) -1-етил-4- (2- (4-хидроксинафтален-1 -ил) винил) хинолиниев бромид и възможното му взаимодействие с редокс двойката NAD^+/NADH. Установено е, че в неутрални и алкални буферни разтвори багрилото съществува в своята бензоеноидна (редуцирана) и хиноидна (окислена) форма и равновесието между двете форми може да се измести чрез промяна на pH. Квази-обратимо електрохимично поведение, отнесено към последователни електроредукция и електроокисление на багрилото, е наблюдавано с помощта на циклична волтамперометрия. Сдвоеното окислително-редукционно взаимодействие между багрилото и NAD в разтвора е оценено чрез съпоставяне на резултатите от UV-Vis спектроскопия, циклична волтамперометрия и електрохимична импедансна спектроскопия.

Bulgarian Chemical Communications, Volume 50 Special Issue D (pp. 75 – 81) 2018

Hydrogen Evolution Reaction at Zirconium and Si-Modified Zirconium Electrodes. Electrochemistry at Fractal Interfaces.

M. Hromadová[1,*], J. Kocábová[1], L. Pospíšil[1], S. Cichoň[2], V. Cháb[2], M. Novák[3], J. Macák[3]

[1] *J. Heyrovský Institute of Physical Chemistry of the Czech Academy of Sciences, Dolejškova 3, 182 23 Prague, Czech Republic*

[2] *Institute of Physics of the Czech Academy of Sciences, 182 21 Prague, Czech Republic*

[3] *Department of Power Engineering, University of Chemistry and Technology, Technická 5, 166 28 Prague, Czech Republic*

Received May18, 2018 Revised J

In memory of Professor Zdravko Stoynov for his kind personality and innovative scientific contribution to electrochemistry

Hydrogen evolution reaction was studied by electrochemical impedance spectroscopy at a high purity grade zirconium and Si-modified zirconium electrode in borate buffer. Roughness factor and fractal dimension of the electrode surface were determined for both electrodes from topographic images obtained by atomic force microscopy. Electrochemical impedance spectra were fitted by a simple equivalent circuit containing constant phase element, which provided the exponent *n* that can be directly related to fractal dimension D_f of the electrode surface. For Zr electrodes a reasonable agreement between D_f values calculated from *n* exponent of the constant phase element and the experimentally-obtained fractal dimension was found, whereas this approach failed for Si-modified Zr electrodes. Further implication of this result for the determination of hydrogen evolution rate parameters is discussed.

Key words: zirconium, hydrogen evolution reaction, impedance, fractal dimension, atomic force microscopy

INTRODUCTION

This contribution is dedicated to the memory of Professor Zdravko Stoynov for his pioneering work in the field of electrochemical impedance analysis [1].

Presented work is focused on the interpretation of the constant phase element (CPE) by employing fractal analysis of the electrode | electrolyte interface. The nature of CPE has been discussed extensively in the past [2-15] and it is generally believed that the CPE behavior is a consequence of the current density distribution along the electrode | electrolyte interface due to the surface inhomogeneity. If the CPE is only the intrinsic property of the double layer, the fitting parameter *Q* is independent of the solution resistance R_s and there is no need to invoke the distribution function for the relaxation times [5]. In most of the experimental cases, however, this is not the case and several distribution models (ladder or other transmission line networks) have been assumed leading to the effective capacitance value C_{eff}, which can be obtained from *Q* parameter by several different expressions that include not only the solution resistance but the charge transfer resistance values as well [5,6].

Another concept that explains the CPE behavior uses the description of the surface inhomogeneity by a fractal geometry [8,9]. Based on this approach Nyikos and Pajkossy [8] suggested a simple relationship $n = 1/(D_f - 1)$ between the CPE parameter *n* and the effective dimension of the electrode surface D_f, which was experimentally verified for fractal blocking electrodes [10]. Subsequently, Mulder and Sluyters [9] used the surface fractal properties to explain depressed semicircular arcs in impedance plots for irreversible electrode reactions. Several subsequent experimental works took up on this concept [16-18].

Hydrogen evolution reaction (HER) on two different types of zirconium–based interfaces, namely on pure zirconium and Si–modified zirconium electrode materials, has been used for this evaluation. Electrochemical impedance spectroscopy (EIS) measurements were obtained under the experimental conditions that enabled

To whom all correspondence should be sent:
E-mail: magdalena.hromadovajh-inst.cas.cz

simplification of the impedance response and subsequent spectra analysis by utilization of a simple R_s(CPE-R_{ct}) electric circuit, where R_s is the solution resistance, R_{ct} is the charge transfer resistance and CPE represents the constant phase element referring to the electrode capacitive behavior. This simplification was achieved by using a sufficiently negative applied potential with respect to the equilibrium potential (open circuit potential) [19] thus eliminating salient contribution from the charge transfer kinetics related to the oxide film formation. Two experimental parameters Q and n were obtained from the impedance corresponding to the CPE using the expression $Z_{CPE} = Q^{-1}(j\omega)^{-n}$. Parameter *n* represents a frequency–independent phase angle different from 90°. If the phase angle is 90° degrees, parameter *n* equals to 1. For smaller phase angles, n values are smaller than 1. The atomic force microscopy (AFM) was used for ex–situ imaging of the electrode surface topography, which allowed determination of two characteristic surface parameters, namely, a roughness factor R_f and a fractal dimension D_f. These experimental values were then used to interpret the CPE parameters *Q* and *n* obtained from the analysis of EIS spectra. We are not aware of any previous work that utilizes the AFM method for the interpretation of the CPE values as is presented in this communication.

EXPERIMENTAL

Zirconium samples were prepared from two types of Zr, wire and rod. Zirconium wire (Alfa Aesar, 0.25 mm diameter, 99.95% purity, metallic impurity 29 ppm Hf, 190 ppm Fe, 1.8 Cu, 8.4 ppm Cr and 4.1 ppm Ni) was soldered to a support copper wire, inserted in a thick walled tight glass capillary and fixed with a TorrSeal™ resin (Varian Inc., USA). The exposed part of the wire was polished with silicon carbide paper (5000, WS Flex 16 Waterproof, Hermes, Germany). Exposed geometric electrode area of thus prepared Zr microelectrode (mZr-5000) was 4.91×10^{-4} cm^2. Zirconium rod (Alfa Aesar, 12.7 mm in diameter, annealed, 99.2+ % (metals basis excluding Hf), Hf 4.5% max.) was cut into small 4 mm thick pellets, which were consecutively polished on one side with the silicon carbide paper (WS Flex 16 Waterproof, Hermes, Germany) of increasingly smaller grit sizes (P1200, P2000, P2500 and 5000). Zr pellet electrode polished with 5000 grit paper is labelled as Zr-5000. Final step consisted of polishing with a diamond paste (particle size 3 μm, D3 Urdiamant polishing paste, Czech Republic). Thus prepared surface was rinsed copiously with water and acetone, cleaned with ultrasound and dried. This electrode is labelled as Zr-D3. Zirconium pellets were then used for further surface modification. Si-modified Zr electrode (SiZr-D3) with approximately 1 to 1 ratio of Si to Zr atoms in the surface layer was prepared employing DC magnetron sputtering from pure Si and Zr targets in Ar plasma at 2 Pa. All targets were at least 3N purity. Composition was probed by the scanning electron microscopy with energy dispersive X-ray analysis (SEM-EDX), X-ray photoelectron spectroscopy (XPS), glow-discharge optical emission spectroscopy (GD-OES) and Raman spectroscopy. Before the deposition, samples were annealed in-situ in an ultrahigh vacuum at 700°C for 30 min with the aim to prepare a clean surface for subsequent deposition. This step ensured the absence of detrimental oxide layer interface. Deposition was performed at 300°C. After the deposition, samples were annealed in-situ in Ar at 2 Pa at 700°C so as to promote alloying and silicide formation.

All ex-situ Atomic Force Microscopy (AFM) topography images were obtained in the contact mode regime using Agilent 5500 Scanning Probe Microscope (Agilent Technologies, USA). A large AFM scanner (100 μm × 100 μm) and PPP-CONT cantilevers (Agilent Technologies, USA) of nominal force constant of 0.2 N/m and resonant frequency 13 kHz were used. The recording speed was in the range of 0.2–0.7 lines/s. AFM images were analyzed using the visualization and analysis software Gwyddion 2.35 from the Czech Metrology Institute [20]. Both the roughness factor R_f and the fractal dimension D_f (using cube counting algorithm [21]) were determined by this software. Ideally flat electrode surface has the roughness factor $R_f = 1$ (real electrode area equals to the geometric one) and the fractal dimension $D_f = 2$. All AFM images shown in this publication are plane–corrected.

EIS spectra were measured in the special electrochemical cell [22] that permits measurement on a selected sample area of 4.02×10^{-2} cm^2 using a three–electrode setup and employing Autolab PGSTAT30 potentiostat/ galvanostat equipped with a frequency response module FRA (Metrohm, Switzerland). An aqueous borate buffer solution consisting of 0.2 M boric acid and 0.05 M sodium tetraborate decahydrate of pH 7.33 was used. Experimental procedure was similar to that reported for Zr microelectrode [19], when electrode was immersed in the solution under the potential control. In the case of pellet electrodes, the main compartment of the electrochemical cell was mounted on top of a dry–polished Zr pellet and the

electrode surface was always contacted with a deaerated electrolyte solution under the potential control reported. This step is extremely important for an achievement of sufficient experimental reproducibility of the EIS measurement. This procedure allowed local measurements on approximately 6 areas of the sample surface. EIS spectra were analyzed with Zview software, version 3.2b (Scribner Associate, Inc., North Carolina, USA).

RESULTS AND DISCUSSION

Figure 1 shows anodic polarization curves for Zr microelectrode (mZr-5000) and Zr pellet electrode (Zr-5000) that were dry–polished with the silicon carbide paper (5000 grit, WS Flex 16), and for Si-modified Zr pellet electrode (SiZr-D3) that was used as received.

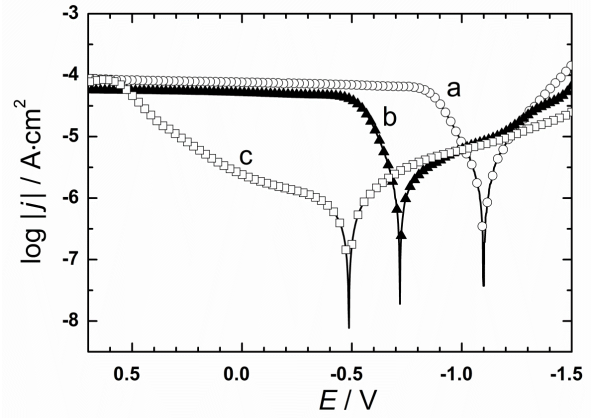

Fig. 1. Anodic polarization curves obtained in borate buffer solution (pH = 7.33) at potential scan rate 0.01 V/s and starting at –1.5 V for: a) mZr-5000, b) Zr-5000 and c) SiZr-D3 electrode.

Curves were obtained at pH = 7.33 after 120 seconds of waiting period at the open circuit potential (OCP). An equilibrium potential, at which the anodic and cathodic currents are equal (effectively the OCP value), amounts to –1.1V for mZr-5000, –0.72V for Zr-5000 and –0.48V for SiZr-D3 against the Ag|AgCl|1M LiCl reference electrode. Differences between the zirconium microelectrode and pellet electrode may be due to a higher content of metallic impurities in the latter case. Si-modified zirconium electrode (SiZr-D3) has the most positive OCP value of all three electrodes and gives the lowest value for the HER current at –1.5V.

Qualitatively the same result was obtained by a conventional voltammetric scan starting from potential –1.0V in the cathodic direction using the potential scan rate of 0.1 V/s (see Figure 2). In this case the cathodic current has lower value for SiZr-D3 electrode compared to Zr-5000 electrode.

Impedance spectra were obtained for all studied samples at –1.5V against the reference electrode using 5mV amplitude for AC component of the potential. The electrochemical cell was filled under the potential control at –1.1V with the electrolyte, which was previously bubbled with argon to minimize the amount of dissolved oxygen. Then the potential was stepped to –1.5V and the impedance spectra were measured. Representative EIS spectra for Zr-D3, Zr-5000 and SiZr-D3 pellet electrodes are shown in Figure 3. Fitting parameters for these individual curves are summarized in Table I, whereas Table II contains the average *Q* and *n* parameters from all measured curves under the same experimental conditions.

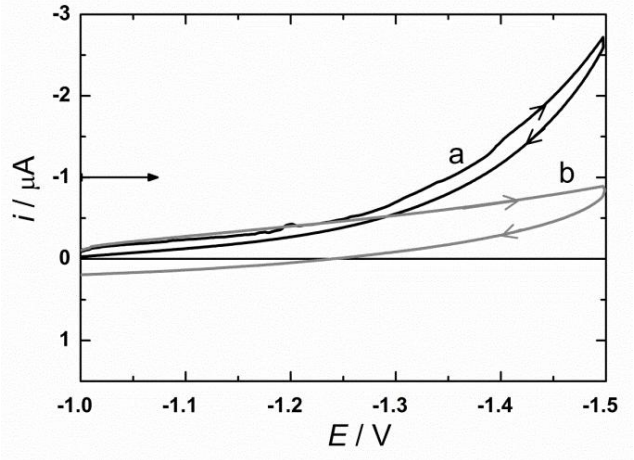

Fig. 2. Cyclic voltammogram for HER process in borate buffer solution (pH = 7.33) at potential scan rate 0.1 V/s on: a) Zr-5000 and b) SiZr-D3 electrode. Contact of the electrode with solution was done under potential control at –1.0 V.

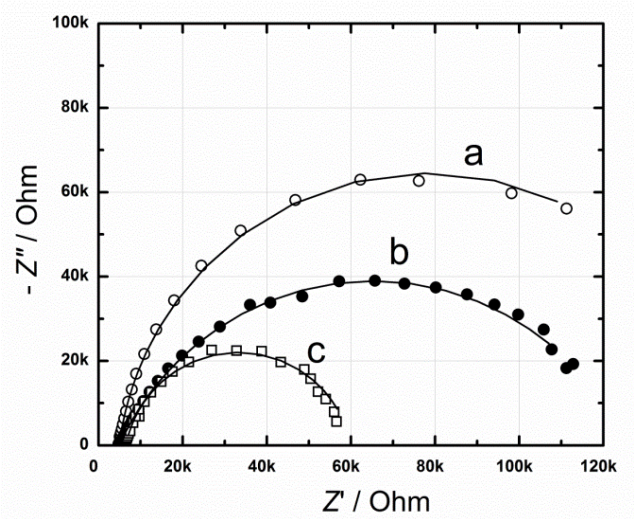

Fig. 3. The representative complex impedance plot for HER obtained at –1.5V on: a) Zr-D3, b) SiZr-D3 and c) Zr-5000 pellet electrode. Symbols indicate the experimental data and lines the best fit to the Rs(CPE-Rct) equivalent circuit.

Table 1. EIS fitting parameters for data in Figure 3

Electrode	R_s / Ω	R_{ct} / Ω	n	Q / Ω^{-1} s^n
Zr-5000	6 526	53 445	0.87	1.5×10^{-6}
Zr-D3	4 914	146 730	0.92	3.6×10^{-7}
SiZr-D3	4 961	120 680	0.73	1.8×10^{-6}

Surface structures of samples Zr-5000, Zr-D3 and SiZr-D3 were analyzed ex-situ employing the AFM technique. Topographic images from several areas of each sample were obtained. Only the largest one (50 × 50 μm^2 area) was used for determination of the roughness factor R_f and fractal dimension D_f parameters. The cube counting algorithm implemented within the Gwyddion software was used for fractal analysis. [21].

Figure 4 shows the ex-situ AFM topography images (50 μm × 50 μm) of the Zr pellet polished with a 3μm diamond paste (Zr-D3) and the Si-modified zirconium (SiZr-D3) pellet electrodes. Left image represents Zr-D3 and right image SiZr-D3, whereas scale z of the left image is 0.48 μm and of the right image 1.2 μm, respectively. Below the images are the height profiles obtained along the black line indicated in the image. Evidently, there is a large difference between the surface corrugations of these two samples. This observation is consistent with the differences of the roughness factor and fractal dimension values obtained from Gwyddion software and summarized in Table II. Similar analysis was done for Zr-5000 sample and the corresponding R_f and D_f values are also shown in Table II. Due to the construction of mZr-5000 electrode, it was not possible to obtain the relevant topography information for this surface. Since the same surface treatment was used for both mZr-5000 and Zr-5000 electrodes, we assumed that R_f and D_f parameters are the same as those obtained for Zr-5000 electrode.

Atomic force microscopy technique was used also for analysis of the surface morphology before and after the HER process. Figure 5 shows the AFM topography images taken on the same electrode SiZr-D3 in the area that was not subjected to the HER (left) and inside the region subjected to HER (right). AFM measurement was done in contact mode; z scale is 1.5 μm (left) and 1.1 μm (right), respectively. The relevant region subjected to HER was identified by the O-ring imprint.

Large scale images shown in Figure 5 confirm that the surface morphology does not change significantly before and after HER process, but it is evident (also from the height profiles) that the surface becomes somewhat smoother.

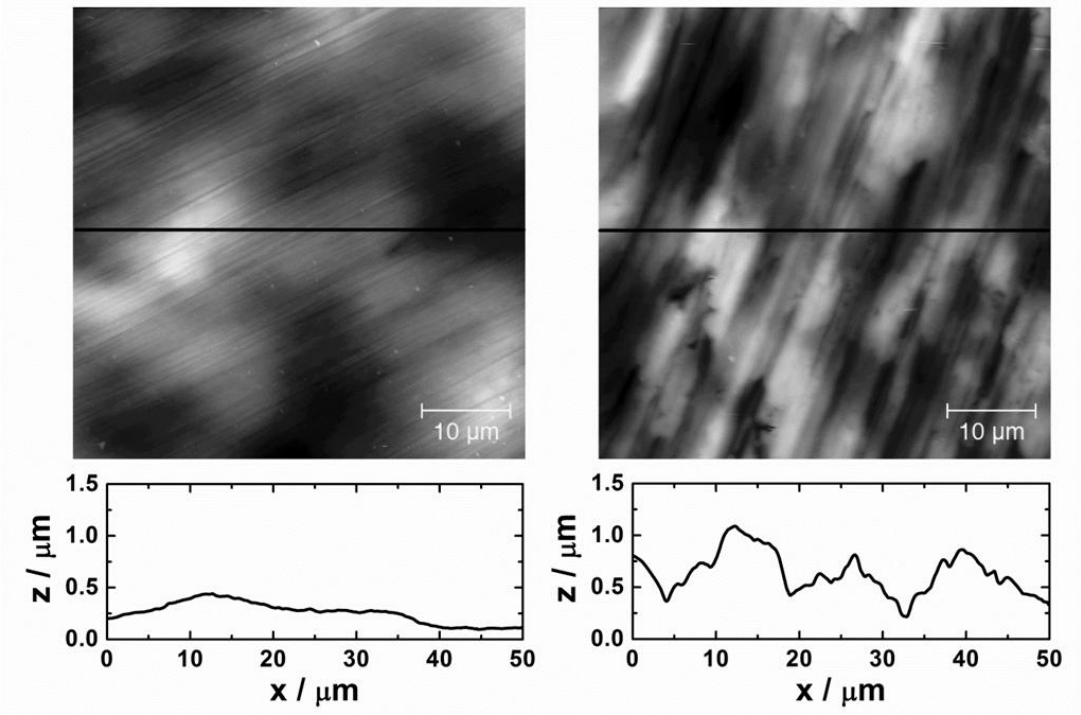

Fig. 4. Ex-situ AFM topography image of Zr-D3 (left) and SiZr-D3 (right) pellet electrode obtained before the HER. The height profile obtained along the black horizontal line is shown below.

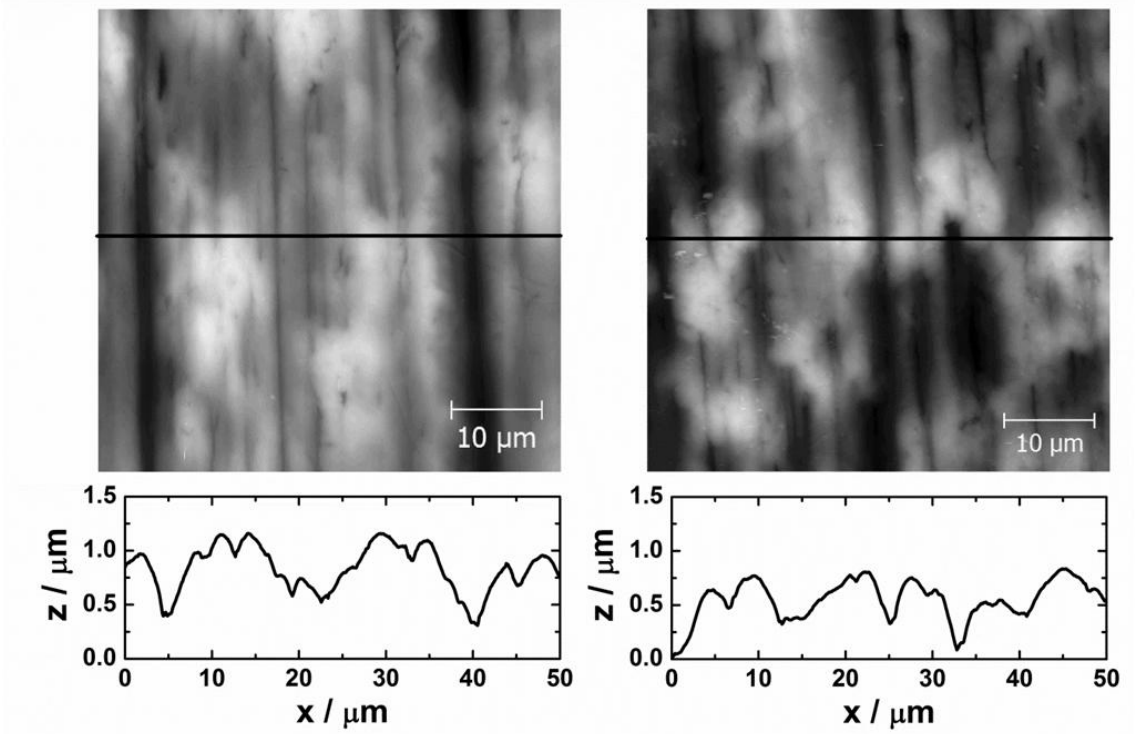

Fig. 5. Ex-situ AFM topography images of SiZr-D3 surface before (left) and after (right) HER studied by impedance spectroscopy at –1.5V. The height profile obtained along the black horizontal line is shown below.

Both, the roughness factor and fractal dimension decrease slightly. For this SiZr-D3 sample R_f changes from 1.015 to 1.011 and D_f changes from 2.19 to 2.17, respectively. These changes are small in view of the fact that from all of the imaged areas and SiZr-D3 samples the average R_f is 1.012 ± 0.001 (change from 1.015 ± 0.002) and the average D_f is 2.19 ± 0.02 (change from 2.18 ± 0.01), respectively.

Once all relevant information is summarized from the EIS and AFM experiments, we can put into the test a suggested interpretation of the CPE parameter n in terms of the fractal dimension D_f of the sample surface. As previously suggested and experimentally verified for fractal blocking electrodes [8,10], the relationship between these two parameters should follow a simple expression $n = 1/(D_f - 1)$. In this work we obtained experimentally fractal dimension D_f values from which one can compute parameter n, which we label for the purpose of comparison as $n(D_f)$. Its values are summarized in Table II. Comparison of $n(D_f)$ with the experimentally obtained exponent n from the EIS spectra gives an excellent agreement for Zr-5000 and Zr-D3 samples. Interestingly, it also explains the n parameter obtained from impedance spectra analysis for mZr-5000 under the assumption that experimental D_f would be the same for both electrodes. These electrodes have different geometric area, but were subjected to the same pretreatment procedure before the HER measurement. The only time that we did not get a quantitative agreement between $n(D_f)$ and n values is in the case of Si-modified Zr pellet electrode, when experimentally obtained parameter n from EIS measurements was much lower than the $n(D_f)$ calculated one.

Table 2. Roughness factor R_f, fractal dimension D_f, CPE parameters Q and n for different electrode surfaces.

Electrode	R_f [a]	D_f [a]	$n(D_f)$	n	Q / Ω^{-1} s^n
mZr-5000	–	–	–	0.82 ± 0.01	$(2.3 \pm 0.3)\times10^{-8}$
Zr-5000	1.053 ± 0.004	2.24 ± 0.03	0.81 ± 0.02	0.82 ± 0.04	$(1.6 \pm 0.2)\times10^{-6}$
Zr-D3	1.003 ± 0.001	2.08 ± 0.03	0.93 ± 0.03	0.91 ± 0.01	$(3.2 \pm 0.6)\times10^{-7}$
SiZr-D3	1.015 ± 0.002	2.18 ± 0.01	0.85 ± 0.01	0.74 ± 0.01	$(1.8 \pm 0.2)\times10^{-6}$

[a] calculated for area 50 × 50 μm^2 (see for example Fig. 4)

This experiment suggests that the current distribution on SiZr-D3 electrode is not related primarily to the surface geometry, but rather to the fact that the electrode surface is heterogeneous and composed of the Si and Zr atoms, which have very different behavior with respect to the HER kinetics. This in turn leads to the surface distribution of time-constants [6]. One may invoke the fact that the surface of the SiZr-D3 electrode has approximately the same amount of Si and Zr atoms. However, we do not know from the AFM experiments alone the actual distribution of these chemical elements at the electrode|electrolyte interface. The experiment that correlates n(D_f) and n values may give us a hint on the role of local surface inhomogeneities on the charge transfer kinetics. In the case of HER one should additionally consider the Volmer-Heyrovský-Tafel mechanism that includes hydrogen adsorption step [19].

CONCLUSIONS

The ex–situ AFM was used to characterize several zirconium–based electrode surfaces prior and after the HER at potentials negative of the open circuit potential value. Two main characteristic parameters were reported, namely, the roughness factor R_f and fractal dimension D_f of the studied surface. A reference zirconium system gave R_f and D_f values in accord with the expectation that the roughness factor and fractal dimension of the surface should decrease for the electrode consecutively polished with 5000 silicon carbide paper and subsequently with a 3μm diamond paste. Both parameters increase when zirconium surface is modified by Si adlayer in the ratio 1:1 with respect to zirconium. The effect of HER on the electrode surface morphology was found to be almost negligible leading to a small decrease in the roughness factor and surface fractal dimension. Experimental D_f values were obtained by the cube counting analysis of the ex-situ AFM topography images and were used successfully to explain the non–ideality of the interfacial capacitance (CPE) behavior for Zr-based electrodes.

***Acknowledgments**: This research has been supported by the Czech Science Foundation (16-03085S) and the Czech Academy of Sciences RVO: 61388955.*

REFERENCES

1. Z. Stoynov, D. Vladikova, Differential Impedance Analysis, Marin Drinov Publ. House, Sofia, 2005.
2. R. de Levie, *Electrochim. Acta*, **10**, 113 (1965).
3. W. Scheider, *J. Phys. Chem*., **79**,127 (1975).
4. A. Le Mehaute, G. Crepy, *Solid State Ionics*, **9/10**, 17 (1983).
5. G. J. Brug, A. L. G. van den Eeden, M. Sluyters-Rehbach, J. H. Sluyters, *J. Electroanal. Chem*., **176**, 275 (1984).
6. B. Hirschorn, M. E. Orazem, B. Tribollet, V. Vivier, I. Frateur, M. Musiani, Electrochim. Acta, **55**, 6218 (2010).
7. Ch. L. Alexander, B. Tribollet, M. E. Orazem, *Electrochim. Acta*, **188**, 566 (2016).
8. L. Nyikos, T. Pajkossy, *Electrochim. Acta*, **30**, 1533 (1985).
9. W. H. Mulder, J. H. Sluyters, *Electrochim. Acta*, **33**, 303 (1988).
10. T. Pajkossy, L. Nyikos, *J. Electrochem. Soc*., **133**, 2061 (1986).
11. R. de Levie, *J. Electroanal. Chem*., **261**, 1 (1989).
12. Z. Lukács, *J. Electroanal. Chem*., **432**, 79 (1997).
13. Z. Lukács, *J. Electroanal. Chem*., **464**, 68 (1999).
14. M. H. Martin, A. Lasia, *Electrochim. Acta*, **56**, 8058 (2011).
15. T. Pajkossy, *J. Electroanal. Chem*., **364**, 111 (1994).
16. U. Rammelt, G. Reinhard, *Electrochim. Acta*, **35**, 1045 (1990).
17. Z. Kerner, T. Pajkossy, *J. Electroanal. Chem*., **448**, 139 (1998).
18. Z. Kerner, T. Pajkossy, *Electrochim. Acta*, **46**, 207 (2000).
19. L. Pospíšil, N. Fanelli, M. Hromadová, *Bulg. Chem. Commun*. C, **49**, 128 (2017).
20. P. Klapetek, D. Nečas, A. Campbellová, A. Yacoot, L. Coenders, *Meas. Sci. Technol*., **22**, 025501 (2011).
21. http://gwyddion.net/documentation/user-guide-en/fractal-analysis.html
22. M. Mucha, E. Kaletová, A. Kohutová, F. Scholz, E. S. Stensrud, I. Stibor, L. Pospíšil, F. von Wrochem, J. Michl, *J. Am. Chem. Soc*., **135**, 5669 (2013).

Bulgarian Chemical Communications, Volume 50 Special Issue D (pp. 75 – 81) 2018

Реакция на отделяне на водород при циркониеви и Si-модифицирани циркониеви електроди. Електрохимия на фрактални повърхности

М. Хромадова[1, *], Я. Кочабова[1], Л. Пошпишил[1], К. Кихон, В. Чаб[2], М. Нивак[3], Я. Масак[3]

[1] *Институт по физикохимия „Я. Хейровски" на Чешката академия на науките, Долеяскова3, 182 23 Прага, Чешка република*

[2] *Институт по физика на Чешката академия на науките, 182 21 Прага, Чешка република*

[3] *Катедра "Енергетика", Химически и технологичен университет, Техническа 5, 166 28 Прага, Чешка република*

Постъпила на18 май 2018г.; приета на30 юли 2018г.

(Резюме)

В памет на проф. Здравко Стойнов, неговата любяща личност, иновативен и научен принос в електрохимията

Реакцията на отделяне на водород беше изследвана чрез електрохимична импедансна спектроскопия в цирконий с висока чистота и в циркониев електрод модифициран със силиции в боратен буфер. Коефициентът на грапавост и фракталният размер на повърхността на електрода са определени за двата електрода от топографски изображения, получени чрез атомно силова микроскопия. Електрохимичните импедансни спектри бяха анализирани с помоща на проста еквивалентна схема, съдържаща елемент с постоянна фаза, определящ коефициента *n*, който е непосредствено свързан с фракталния размер D_f на повърхността на електрода. За циркониеви електроди съотношението между стойностите на D_f, изчислени от експонентата *n* на елемента с постоянна фаза и експериментално получените фрактални измервания, е приемливо, от друга страна този подход не дава резултати при Zr електроди модифицирани със Si. Значението на този резултат за определяне на параметрите на скоростта на отделяне на водород се дискутира.

Bulgarian Chemical Communications, Volume 50 Special Issue D (pp. 82– 89) 2018

EIS as a Tool to Characterize Nanostructured Iron Fluoride Conversion Layers for Li-Ion Batteries

B. Guitián, X.R. Nóvoa, A. Pintos*

University of Vigo, ENCOMAT group, EEI, Campus Universitario, 36310 Vigo, Spain

Received May 21, 2018 Revised July 23, 2018

In memory of Professor Zdravko Stoynov for his kind personality and innovative scientific contribution to electrochemistry

The present study aims at developing FeF_3 conversion layer on cheap mild steel substrates for use as cathode materials in Li-ion batteries. The coatings, grown in an ethylene glycol based electrolyte are characterised by SEM, FIB and EDX techniques that show the formation of similar porous structures but thicker for the mild steel substrate than for the iron substrate. The porous structure is characterised by EIS using a transmission line model that allows obtaining relevant parameters of the layer as the conductivity or the reactivity at pore walls. The conductivity of the FeF_3 layer is higher for the mild steel substrate than for the iron substrate. The FeF_3 layers react to some extent in LiBOB electrolyte which is interpreted as iron corrosion and Fe^{3+} reduction with Li^+ insertion in the FeF_3 structure.

Key words: Iron fluoride, Li-ion batteries, electronic conductivity.

INTRODUCTION

The Li-ion batteries sector is a major actor in the field of energy conversion and storage, mainly dealing with portable devices. The reaction mechanism in these batteries involves insertion reactions at both electrodes, the anode and the cathode. The cathode material and the electrical contact between active material and current collector continue to be the main limitations to increasing the capacity of Li-ion cells. An alternative strategy aimed at overcoming (at least partially) these drawbacks involves increasing the available charge and decreasing the internal ohmic resistance through the use of electrode materials directly grown on the current collector. Directly grown layers guarantee good electrical contact between the current collector and the active material. Moreover, if the electrode material is able to undergo conversion reactions, the nominal capacitance increases with respect to that of insertion reactions. Thus, the electrode material will reach all its entire range of oxidation states. Due to their high nominal capacity, transition metal fluorides, such as FeF_3 are good candidates for the conversion reactions with lithium ions [1,2].

Direct formation of a fluoride-based layer has been achieved by anodizing of iron strips in ethylene glycol and NH_4F as the electrolyte. Highly nanoporous layers of iron hydroxifluorides were obtained [3]. Nevertheless, those fluoride layers were of poor electronic conductivity, which limits their performance as electroactive materials.

One possible strategy to improve fluorides' conductivity is the incorporation of foreign conducting materials, such as carbon or conducting polymers[4]. The present work focuses on a different approach, according to which electronic conductivity improvements can be reached through the incorporation of conducting elements from inner sources. The idea is to synthesize active material as in [3], but using carbon steel as the substrate instead of pure iron. It is expected that the carbon dissolved in the alloy will accompany dissolving iron and will remain trapped in the matrix of fluorides, thus increasing its electronic conductivity. Electrochemical impedance spectroscopy (EIS) has been chosen as the tool to quantify the electronic conductivity of the porous layers formed, by modelling the electrochemical response obtained as a transmission line type distribution of the electric field.

EXPERIMENTAL

Preparation of the conversion coatings

The development of the conversion coatings was carried out by anodizing the substrate material in a two-electrodes cell as in [3]. The substrate material ran as a working electrode and a platinum mesh as

To whom all correspondence should be sent:
E-mail: apintos@uvigo.es

the counter electrode. The potential applied was 50V for 15 min and the electrolyte solution used was 0.1 M NH_4F in ethylene glycol containing water (3%). An Ivium® potentiostat (IviumStat.XRe) was employed for the anodizing procedure.

Two different materials were used as the substrate, iron strips as those employed in [3], and low carbon steel strips. The mild, with low carbon content steel, is expected to produce a conversion layer structurally close to that found for iron, although of higher electronic conductivity due to trapped carbon. Table 1 summarises the chemical composition of the main alloying elements.

Table 1. Main elements in the composition of the samples tested

		C	Fe
Mild steel	Atomic%	4.87	94.06
	Weight%	1.09	97.53
Iron		0.0	99.99

Morphological characterization of the conversion coatings

The morphological characterization of the films was done using Focused Ion Beam Scanning Electron Microscopy (FIB-SEM). The microscope was a Dual-Beam FEI Helios NanoLab. The SEM technique allowed us to gather information on the nanoporous morphology of the thin film, and the FIB technique was used to measure its thickness and to investigate the cross-section morphology.

Electrochemical characterization

The electrochemical characterization of the coatings obtained was performed through electrochemical impedance spectroscopy (EIS) and charge and discharge cycles. EIS measurements were performed using a Methrom-Autolab® potentiostat (PGSTAT 30). The EIS characterization was performed in two experiments:

a) Just after anodizing, with fresh electrolyte. In this case a three-electrode cell arrangement was employed, using a Pt mesh as a counter electrode, and a Pt wire as a pseudo–reference electrode.
b) Ageing in the typical electrolyte for Li-ion batteries. Lithium bis-oxalate-borate (LiBOB, 1M) + 2% fluoroethylene carbonate (FEC) dissolved in ethylene carbonate (EC) and dimethyl carbonate (DMC) (1:1 [v/v]) was chosen as electrolyte. Symmetrical cells were assembled in a pouch cell case inside a glove box with a dry atmosphere. We employed two nominally identical electrodes, one acting as a working electrode and the other as a counter electrode. A film of glass fibre was used as a separator.

Cycling of the conversion coatings was also performed on pouch cell case arrangements, using the electrolyte described above. This electrolyte was chosen due to its good properties in the cycling of lithium ion batteries [5–7]. A lithium foil was employed as a counter electrode and a film of glass fibre as a separator. The cell was galvanostatically cycled applying 15 $\mu A \cdot cm^{-2}$ of current density in a potential window of 1 V - 4 V.

RESULTS AND DISCUSSION

Preparation of the conversion coatings

Figure 1 compares the chronoamperograms obtained for the Fe and steel anodizations. The general appearance is similar for both substrates. The three domains reported in [3] can be differentiated: germination, growth, and a pseudo steady can be differentiated. However, the higher current density values reached during the coating synthesis on the mild steel reveal some structural differences. The coating thickness can be higher for the carbon steel, or the porosity reached can be different. The structure and the geometry of both layers are analysed in next section.

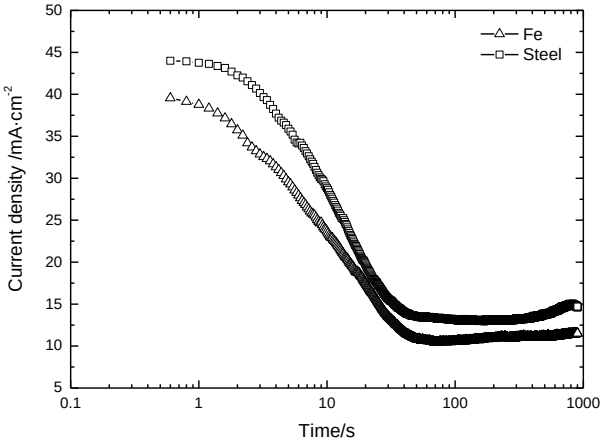

Fig. 1. Chronoamperograms obtained during the anodizing of carbon steel and Fe substrates in ethylene glycol containing water (3%) and 0.1M NH_4F.

Morphological characterization of the conversion coatings

The morphology of the formed FeF_3 layers was analysed by SEM. The general appearance clearly shows a difference between both coatings. The conversion coating generated on the iron is continuous (Fig. 2a) while the conversion coating synthesized on the mild steel strips reveals the grain boundaries (Fig. 2d), which is because of the reduced growth at grain boundaries.

The SEM images presented in Fig. 2 are arranged in increasing magnification (from left to right). The upper row (Fig. 2a-c) corresponds to the iron substrate and the lower row (Fig. 2d-f) to the steel substrate. A well-developed porous nano-structure can be observed for both substrates. The average pore diameter is similar in both samples; around 75 nm and the density of pores can be estimated at about 10^{10} pores cm^{-2}. Based on these parameters and assuming cylindrical geometry, the open porosity can be estimated at around 44% for both coatings.

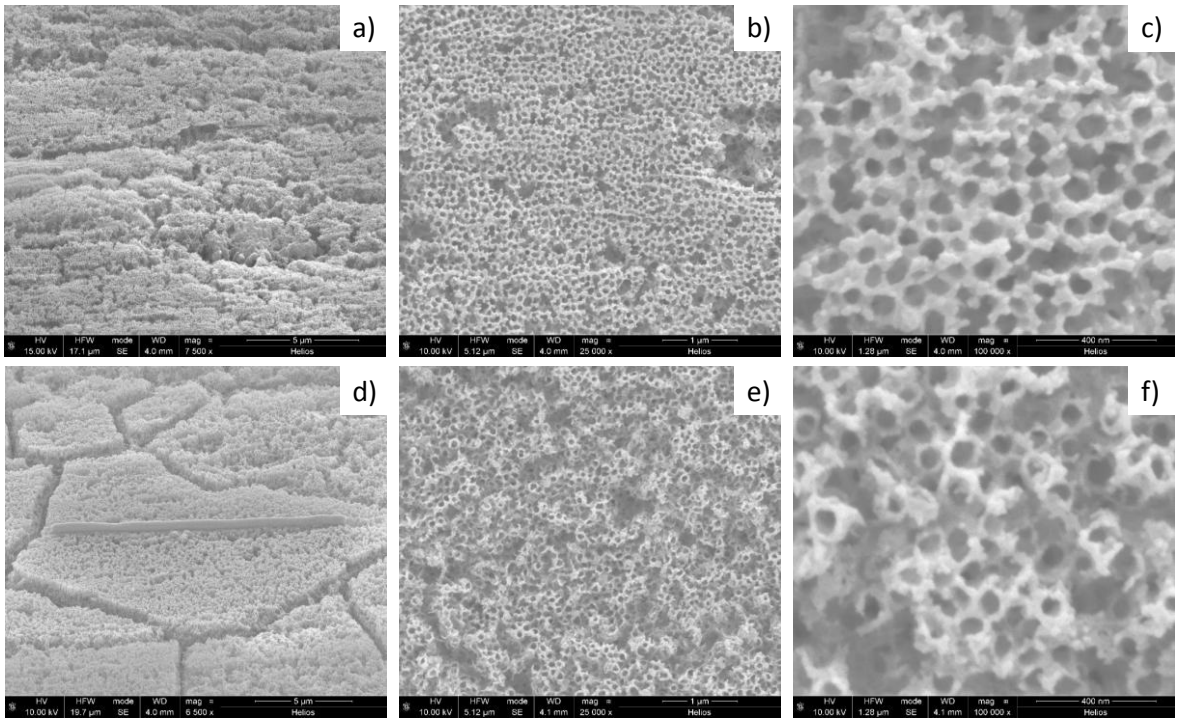

Fig. 2. SEM images of the FeF_3 conversion layers synthesized. The upper row corresponds to the iron substrate, and the lower row to the steel substrate. Magnification increases from left to right. a) 7500x; d) 6500x; b), e) 25000x; c), f) 100000x.

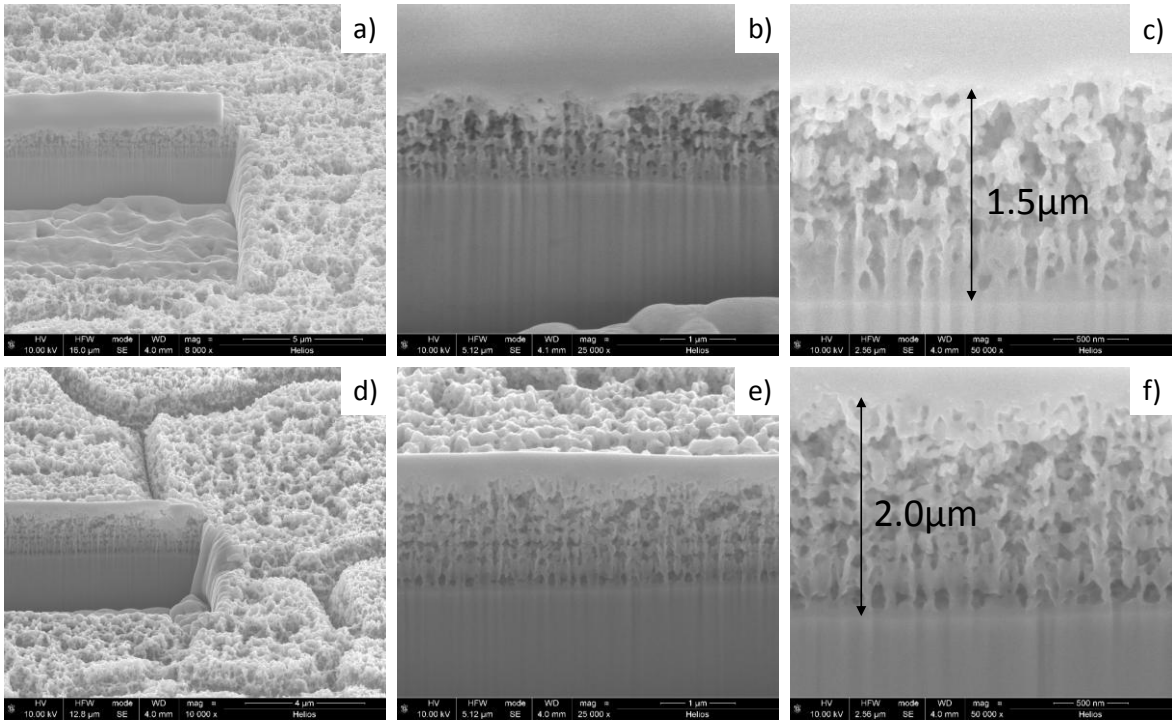

Fig. 3. FIB-SEM images of cross sections of the synthesized FeF_3 coatings. The upper row corresponds to the iron substrate, and the lower row to the steel substrate. (a and d) general view of the section created by Ga^+ bombardment. (b and e) detail of the layer cross sections with, on top, the Pt layer deposited for conductivity purposes. (c and f) detail of the layer's cross section showing the estimated thickness

Figure 3 summarizes the FIB-SEM observations aimed at obtaining information about the thickness and morphology of the coatings. Figures 3a and 3d clearly show the difference in grain boundaries specific to the steel substrate. The coating is thinner at those regions. The general view presented in Figures 3b and 3e shows that the coating is thinner for the iron substrate than for the steel substrate. The detailed view given in Figures 3c and 3f reveals that the FeF_3 layer generated on the iron strips is thinner than that generated on the mild steel. The layer for the iron substrate is about 1.5 μm thick, while on the mild steel this reaches 2.0 μm. This result is in concordance with the higher current density recorded during the anodizing process for the steel substrate.

The images of Figure 3 also show clearly a homogeneous high porosity from the top to the bottom of the layer that guarantees the access of the electrolyte to the substrate. Nevertheless, the geometry of the pores shown in Figures 3c and 3f deviate somehow from the cylindrical shape. The diameter of the pores bottom seems smaller than at the pores mouth. So, considering the pore geometry as conical instead of cylindrical, as considered according to Figure 2, the estimated porosity results three times lower, around 17% open porosity.

Using the thickness and porosity data, we were able to estimate the mass of active material per surface unit. The maximum active mass corresponds to the conical-shaped pores (i.e., 0.658 $mg \cdot cm^{-2}$) for the FeF_3 coating on steel and 0.494 $mg \cdot cm^{-2}$ for the coating on iron. The minimum active mass corresponds to the cylindrical-shaped pores (i.e. 0.433 $mg \cdot cm^{-2}$) for the FeF_3 coating on steel and 0.325 $mg \cdot cm^{-2}$ for the coating on iron.

The elemental composition of FeF_3 coatings synthesized on mild steel was analysed using the EDX capability of the SEM. The chemical composition is given in Table 2. The formation of FeF_3 is confirmed by the Fe/F ratio. Moreover, the enrichment in C with respect to the matrix is confirmed. Comparing Tables 1 and 2, the atomic ratio C/Fe increases by one order of magnitude. The presence of O corresponds to partial surface hydration of the fluoride layer, in the form of $FeF_x(OH)_y$.

Table 2. EDX analysis of the conversion coating synthesized on the mild steel substrate.

	C	Fe	F	O
Weight%	2.03	82.52	9.31	3.1
Atomic%	7.19	62.83	20.84	8.24

Electrochemical characterization

Model of behaviour

The Nyquist diagrams of both coatings obtained directly in fresh synthesis electrolyte are depicted in Fig. 4. Two main aspects are of interest in these plots. The high frequency shift observed in detail in the inset of Fig. 4, and the diffusion-like feature observed for frequencies lower than 1 Hz.

The presence of a high frequency shift with a nearly 45° slope, for nominally constant cell geometry and electrolyte properties, can only be understood assuming a potential distribution through the pores of the FeF_3 structure formed. The model proposed by Macdonald for porous magnetite-based layers on steel [8] can be applied here. The corresponding impedance function, Eq. 1, contains a purely resistive term, which is the parallel association of the solid and liquid phases resistivities (R_m and R_s, respectively) times the thickness of the coating, L. Thus, the high frequency limit of the impedance contains two terms, the (constant) electrolyte resistance plus the variable part corresponding to the layer conducting properties.

The low-frequency diffusional tail can be attributed to the relaxation of fluorides, in excess in the pore network upon anodizing, or to oxygen diffusion associated to the corresponding cathodic reaction at pore walls that continue to sustain the iron corrosion at pore bottom[9]. In fact, the diffusion layers of the individual pores will overlap to some extent leading to a nearly planar diffusion feature[10].

The impedance spectra in the frequency window from 100 kHz to 1 Hz provides information about the microstructure and reactivity of the conversion layer. The experimental data were modelled using Eq. 1, where R_0 corresponds to the electrolyte resistance between the reference electrode and the pores mouth. R_m represents the resistance per unit of length of the fluoride phase, and R_s corresponds to the resistance per unit of length of the electrolyte inside the pores. Z_2 represents the impedance at the bottom of the pores and Z_1 is the interfacial impedance at the wall of the pore. Both impedances contain a resistive term, R_i, corresponding to the charge transfer, in parallel to a capacitive term, C_i, that holds for the corresponding double layer capacitance. A Cole-Cole dispersion term, α_i, has also be considered for each R_iC_i time constant. Figure 5 corresponds to a representation of the equivalent circuit parameters associated with the morphology of the pore structure as seen in the SEM images discussed in the previous section.

$$Z(\omega) = R_0 + \frac{R_m \cdot R_s}{R_m + R_s} \cdot L + \frac{\sqrt{\gamma}\left(2R_m R_s + \left(R_m^2 + R_s^2\right) cosh(L\sqrt{\gamma})\right) + \delta R_s^2 \, sinh(L\sqrt{\gamma})}{\sqrt{\gamma}(R_m + R_s)(\sqrt{\gamma} sinh(L\sqrt{\gamma}) + \delta \, cosh(L\sqrt{\gamma}))} \quad (1)$$

with

$$\gamma = \frac{R_m + R_s}{Z_1(\omega)}, \quad \delta = \frac{R_m + R_s}{Z_2(\omega)},$$

$$Z_i(\omega) = \frac{R_i}{1 + (j\omega R_i C_i)^{\alpha_i}} \; (i = 1, 2)$$

The impedance data presented in Fig. 4 were modelled using the equivalent circuit given in Fig. 5. To match the experimental data with the physical model, only the frequency window relevant to the coating microstructure and reactivity was considered, (i.e. 100 kHz to 1 Hz).

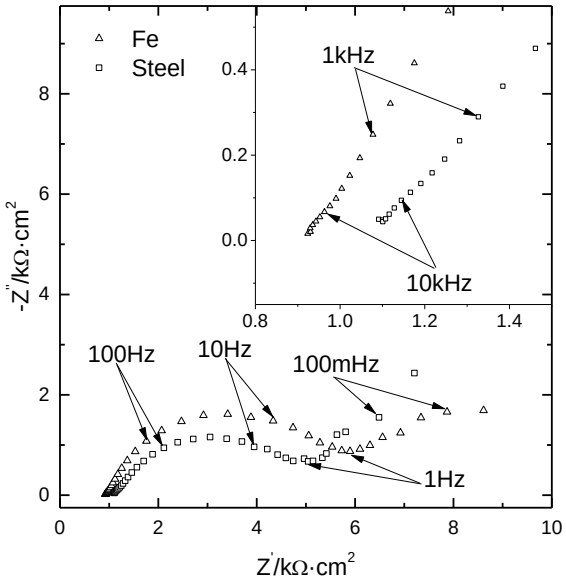

Fig. 4. Nyquist impedance diagrams obtained in fresh synthesis electrolyte after completing the anodizing process.

The fitted data reported in Table 3 clearly show the distinct electrical behaviour between the conversion layers formed on iron and mild steel. As it concerns the main objective of the study, the improvement of the fluoride solid phase conductivity, we can confirm that our hypothesis was good because the conductivity increases. The R_m parameter value decreases by one order of magnitude, from 3.0 to 0.3 MΩ cm, probably due to the incorporation of C to the FeF_3 structure. The kinetic parameters, R_1 and R_2 are also lower for the coating developed on the steel substrate, which indicates faster reaction rates at both of the interfaces, the pore walls and pore bottom.

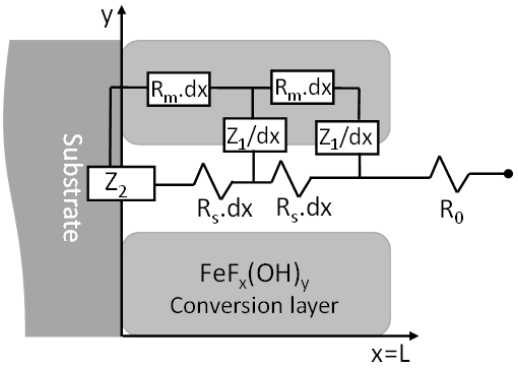

Fig. 5. Equivalent circuit corresponding to the synthesized iron fluorides porous structures. The impedance function is given in the Equation (1).

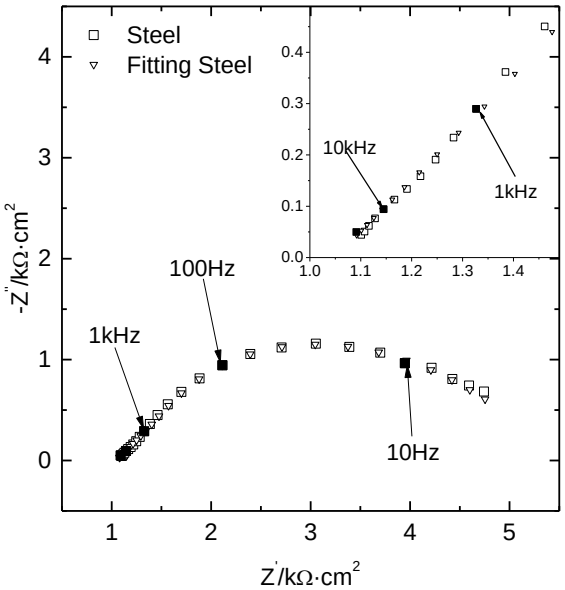

Fig. 6. Experimental and fitted impedance data corresponding to the steel sample in Fig. 6. The frequency window was limited to f> 1Hz. The impedance data were modelled using Eq. 1. The best fitting parameters are collected in Table 3.

Table 3. Best fitting parameters for the impedance data in Fig. 4 using Eq. 1 to model the impedance data. The frequency window was 100 kHz to 1 Hz. The coating thickness was fixed to 2 μm.

	R_0 Ω·cm²	R_m MΩ·cm	R_s MΩ·cm	R_1 MΩ·cm³	C_1 mF·cm⁻³	α_1	R_2 kΩ·cm²	C_2 μF·cm⁻²	α_2	L μm
Fe	494	3.08	5.66	2.32	3.2	1	4.4	1.3	0.64	2
Mild Steel	988	0.31	10.0	1.85	8.3	1	2.6	6.0	0.50	2

Ageing of the conversion coating

In a recent investigation, the feasibility of obtaining in-situ active material by direct corrosion of Fe in the presence of an oxidizing electrolyte ($LiPF_6$) was demonstrated[11]. The objective here was to study the stability of the FeF_3 conversion layers formed on the steel substrate in the presence of a non-oxidizing Li salt, such as LiBOB. The impedance results, obtained in a symmetrical pouch cell at the null potential difference between both electrodes, are presented in Fig. 7. A clear evolution is observed during the first 5 h of immersion, with the presence of a diffusional tail similar to that observed in Fig. 4. From 10 h onwards, the resistance associated to the time constant centred at about 1 Hz increases initially and remains unchanged after about 40 h, at which point the diffusion tail has completely moved outside of the considered frequency window. The high frequency part of the spectrum remains essentially unchanged after about 15 h.

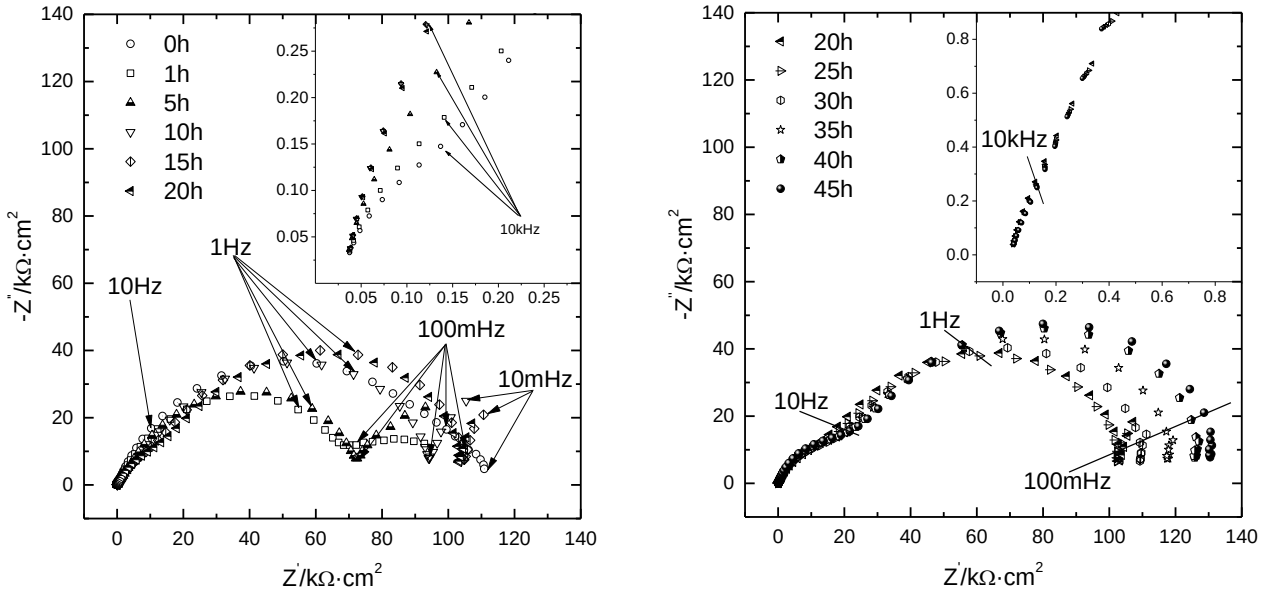

Fig. 7. EIS evolution of the conversion coating grown on mild steel and assembled in a symmetrical cell using 1 M LiBOB + 2% FEC in EC:DME (1:1 [v/v]).

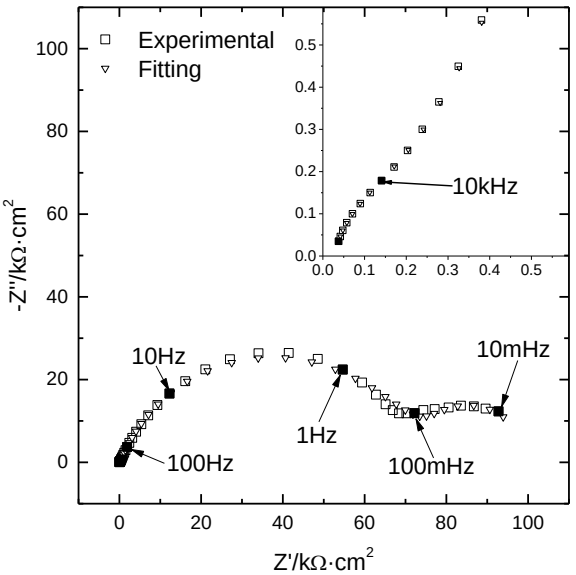

Fig. 8. Experimental impedance data obtained after 1h in the symmetrical cell and fitted data using Equations 1 and 2 as model impedance.

The interpretation of the impedance spectra presented in Fig. 7 is similar to that given in section 3.3.1, with the only difference being the cathodic reaction involved. As no oxidants are present in the electrolyte, one can imagine self-corrosion of Fe as Fe^{2+} at the pore bottom sustained by the reduction process Fe^{3+}/Fe^{2+} at the pore walls. The cathodic reaction will involve Li^+ insertion in the fluoride-based structure for electro-neutrality reasons. In parallel, BOB^- will migrate to the pores bottom to compensate the Fe^{2+} charge being generated. Overall, a linear diffusion from the electrolyte can be considered, involving Li^+ and BOB species for the cathodic and anodic process, respectively.

Figure 8 corresponds to an example of the performance of the model described here. The pore structure of the layer is described by Eq. 1 and the linear diffusion, Z_d, (in series) by Eq. 2, where R_d corresponds to the diffusion resistance and τ_d to the diffusion time constant (δ^2/D). To describe the small high frequency arc observed in the inset of Fig. 8, it was necessary to include a 99 nF capacitance in parallel to the impedance of the coating, which accounts for the geometrical capacitance of the coating.

$$Z_d(\omega) = R_d \frac{tanh(\sqrt{j\omega\tau_d})}{(\sqrt{j\omega\tau_d})} \quad (2)$$

The best fitting parameters for the selected times of evolution are summarised in Table 4. The evolution of R_1 shows an initially fast cathodic process, associated with Li^+ insertion, which slows down with immersion time. The Li^+ insertion (and Fe^{3+} reduction) leads to an increase of the coatings conductivity (R_m decreases with time, as the ratio Fe^{2+}/Fe^{3+} increases). The associated structural change leads to some pore blocking (R_m increases from 1 to 76 MΩ cm). Comparing the nearly constant R_2 values and the R_1 evolution, it is clear that the cathodic reaction represents the final energy barrier for stopping the self-transformation of the coating.

Cycling in a pouch cell

Charge and discharge curves of the conversion coating of FeF_3 developed on mild steel are shown in Fig. 9. A voltage plateau is observed around 1.8 V which is in agreement with a conversion reaction, according to the literature [12]. The specific capacity recorded during the first cycle corresponds to the theoretical value for FeF_3 (712 mA h g^{-1}) if a cylindrical porosity is considered (see section 3.2). If a conical geometry is considered, the specific capacity drops by 32%, to 483 mA h g^{-1}. The real value will lie between both limits.

During the second discharge the coating capacity values experience a noticeable decrease (43%), indicating that the process is not as reversible as expected. However, comparing this loss of capacity of the conversion coating on mild steel to that obtained on iron [3], the difference is only 7%, which can be considered a good result owing the difference in potential windows. The layer on iron was cycled between 4.0 V and 1.5 V while the coating on mild steel was cycled in the potential window 4.0 V to 1.0V, a deeper discharge that induces more irreversible changes in the active material.

Table 4. Fitting parameters obtained for the fitting data in Fig. 7 to the impedance given in Equation (1) and Equation 2.

	R_0 Ω·cm^2	R_m kΩ·cm	R_s MΩ·cm	R_1 MΩ·cm^3	C_1 mF·cm^{-3}	α_1	R_2 kΩ·cm^2	C_2 µF·cm^{-2}	α_2	R_d kΩ·cm^2	T_d s	L µm
0h	14.6	371	1.05	0.04	183	0.74	51.5	0.120	0.91	5.1	9.98	2
1h	12.9	61.0	1.87	0.18	195	0.76	34.8	0.019	0.66	14.3	19.90	2
5h	16.3	278	5.50	2360	1.43	1	42.6	1.60	0.65	---	---	2
45h	23.0	3.6	75.8	36000	5.70	1	53.9	4.50	0.83	---	---	2

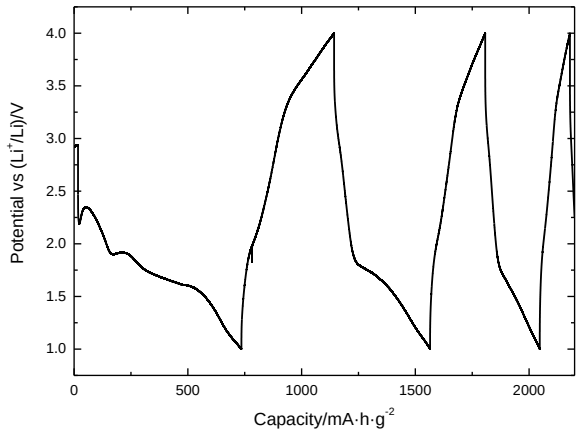

Fig. 9. Discharge and charge curves of a FeF_3 conversion layer grown on mild steel substrate. The electrolyte was 1 M LiBOB salt + 2% FEC in 1:1 EC: DMC. The charge density was calculated assuming cylindrical geometry for the pores (see text).

CONCLUSIONS

Based on our data, the following conclusions can be drawn:

a) FeF_3 conversion layers were developed on iron and mild steel substrates. The layers on steel substrates are thicker than on iron substrate.
b) EIS was successfully employed to study the microstructure and properties of the layers formed. The layers formed on mild steel are of higher conductivity than those formed on iron.
c) FeF_3 conversion layers immersed in LiBOB electrolyte tend to transform partially incorporating Li^+, as evidenced by the EIS results.
d) The FeF_3 conversion layers developed on mild steel substrate are able to cycle in Li-ion battery configuration with performance similar to that found for layers developed on pure iron.

REFERENCES

1. F. Badway, N. Pereira, F. Cosandey, G.G. Amatucci, Carbon-Metal Fluoride Nanocomposites, *J. Electrochem. Soc*. **150**, A1209 (2003).
2. F. Badway, F. Cosandey, N. Pereira, G.G. Amatucci, Carbon Metal Fluoride Nanocomposites, *J. Electrochem. Soc*. **150**, A1318 2003).
3. B. Guitián, S. Lascaud, X.R. Nóvoa, L. Ribeaucourt, E. Vidal, On the growth of nanostructured iron hydroxy-fluorides for Li-ion batteries, *J. Power Sources*. **241**, 567 (2013).
4. E. Vidal, L. Ribeaucourt, X.R. Nóvoa, B. Guitián, Metal halide electrode with improved conductivity, and associated production method, EU patent WO 2017102424, 2017.
5. C.C. Nguyen, B.L. Lucht, Comparative Study of Fluoroethylene Carbonate and Vinylene Carbonate for Silicon Anodes in Lithium Ion Batteries, J. *Electrochem. Soc*. **161**, A1933 (2014).
6. V. Aravindan, J. Gnanaraj, S. Madhavi, H.-K. Liu, Lithium-Ion Conducting Electrolyte Salts for Lithium Batteries, *Chem. - A Eur. J*. **17**, 14326 (2011).
7. S.S. Zhang, A review on electrolyte additives for lithium-ion batteries, *J. Power Sources.* **162**, 1379 (2006).
8. J.R. Park, D.D. Macdonald, Impedance studies of the growth of porous magnetite films on carbon steel in high temperature aqueous systems, *Corros. Sci*. **23**, 295 (1983).
9. B. Díaz, B. Guitián, X.R. Nóvoa, M.C. Pérez, The effect of long-term atmospheric aging and temperature in the electrochemical behaviour of steel rebars in mortar, *Corros. Sci.* **140**, 143 (2018).
10. N. Godino, X. Borrise, F.X. Muñoz, F.J. Del Campo, R.G. Compton, Mass transport to nanoelectrode arrays and limitations of the diffusion domain approach: theory and experiment, *J. Phys. Chem. C*. **113**, 11119 (2009).
11. E. Vidal, L. Ribeaucourt, X.R. Nóvoa, B. Guitián, Self-forming metal halide electrode, and associated production method, EU patent WO2017102427, 2017.
12. N. Pereira, F. Badway, M. Wartelsky, S. Gunn, G.G. Amatucci, Iron Oxyfluorides as High Capacity Cathode Materials for Lithium Batteries, *J. Electrochem. Soc.* **156**, A407 (2009).

ЕИС като инструмент за охарактеризиране на наноструктурирани слоеве железен флуорид за катодни материали в литиево-йонни батерии

Б. Гуитиан, Х.Р. Новоа, А. Пинтос*

Университет Виго, група ЕНКОМАТ, кампус Университетски, 36310 Виго, Испания

Постъпила на .21 май 2018г. ; приета на 23 юли 2018г.

(Резюме)

В памет на проф. Здравко Стойнов за неговата невероятна личност и иновативен научен принос към електрохимията

Настоящото изследване има за цел да разработи FeF_3 слоеве нанесени върху евтини подложки от мека стомана за използване като катодни материали в литиево-йонни батерии. Покритията, отложени в електролит на базата на етилен гликол, се характеризират с помоща на SEM, FIB и EDX и показват образуването на аналогични порести структури, но с по- голяма дебелина на подложките от мека стомана, от колкото за железните подложки. Порестата структура се характеризира с ЕИС, използвайки линеен предавателен модел, който позволява да се определят значими параметри на слоя като проводимостта или реактивността на порите. Проводимостта на слоя от FeF_3 е по-висока за подложката от мека стомана, отколкото за подложката от желязо. Слоевете от FeF_3 до известна степен реагират в електролит от LiBOB, което се обяснява като корозия на желязото и редукция на Fe_3^+ с внедряване на Li^+ в структурата на FeF_3.

Bulgarian Chemical Communications, Volume 50 Special Issue D (pp. 90 – 98) 2018

Slow Charging/Discharging Processes of the Electrochemical Double Layer

T. Pajkossy

Institute of Materials and Environmental Chemistry, Research Centre for Natural Sciences, Hungarian Academy of Sciences, Magyar tudósok körútja 2, Budapest H-1117, Hungary

Received May 2, 2018 Revised June 29, 2018

Dedicated to the memory of Zdravko Stoynov

It is demonstrated for two cases of apparently ideal, ideally polarizable electrochemical interfaces that charging-discharging following potential changes is not instantaneous hence the double layer is not (solely) of electrostatic nature – as assumed in „classical" double layer theories. That is, physico-chemical interactions must also be considered to account for the slow double layer rearrangement processes.

Key words: double layer, impedance, capacitance, kinetics, ionic liquids, single crystal

INTRODUCTION

In general, the electrochemical double layer, in the absence of Faradaic reactions, is capacitive – at least, according to the textbooks and common electrochemical knowledge. The term "capacitive" implies two properties: ability of charge storage and inverse proportionality of the impedance, *Z*, on angular frequency, ω. In what follows, the latter property will be in the focus.

Disregarding the rare, exceptional cases, even in the complete absence of Faradaic reactions the interfacial impedance deviates from the inverse proportionality on frequency. Such an electric element is often approximated by a constant-phase element (CPE), which is defined through its admittance $Y(\omega) = \sigma(\mathrm{i}\omega)^{\alpha}$ where i is the imaginary unit, $\sigma>0$ and $0\leq\alpha\leq1$ are the CPE coefficient and exponent, respectively. Accordingly, the capacitance defined as $C(\omega) \equiv Y(\omega)/(\mathrm{i}\omega)$, is also a power-law function of frequency. However, we do not use this approximation for the frequency dependence of the interfacial capacitance, or in other words, for the "capacitance dispersion". The subject of this paper are the reasons why we get $C(\omega)$ rather than a frequency independent *C*.

In general, the frequency dependence can be attributed (a) either solely to the double layer or (b) to a coupling of the solution resistance and the ideal, frequency-independent interfacial capacitance. Obviously, both effects can appear simultaneously, yielding very complicated $C(\omega)$ dependence. Case (b) is a result of a purely physical effect associated with the geometry of the cell or of the working electrode: current density is not uniform along the electrode surface and the "effective electrolyte resistance" varies along the surface. There are two important archetypes of the "case (b)" models.

First, those of porous electrodes are usually based on de Levie's finite transmission line model [1]; for a modern, comprehensive version see [2]. Second, the embedded disk electrode (often used as a rotating disk) exhibit edge effects, i.e. the local current density at the rim of the disk is higher than at the center. The related theories predict capacitance dispersion at high frequencies [3,4]. The present author has also developed "case (b)" theories on capacitive electrodes of fractal geometry [5-7]; however, he finished that theoretical work with a final conclusion: for microscopically rough electrodes the observed $C(\omega)$ capacitance dispersion is not due to the coupling of solution resistance with the interfacial capacitance. Instead, it is an inherent property of the double layer [8]. That is, for rough electrodes case (a) prevails.

For case (a) two sub-cases can be distinguished: First, when the surface is energetically homogeneous (like for single crystal surfaces) and second, when energetic inhomogeneities of the surface exist, e.g. due to atomic scale roughness. If there are other-than-electrostatic processes (like adsorption) involved in double layer charging, then energetic inhomogeneities lead to a certain

To whom all correspondence should be sent:
E-mail: pajkossy.tamas@ttk.mta.hu

activation energy distribution which in turn causes a time constant distribution of that charging process. This is why by decreasing atomic scale roughness the extent of capacitance dispersion can be decreased [9]. However, capacitance dispersion may appear also when the surface is energetically homogeneous. This is the subject of the present paper: we demonstrate this effect with capacitance spectra measured on single crystal electrodes in aqueous and also in ionic liquid electrolytes.

METHODS: IMPEDANCE SPECTROSCOPY AND CALCULATIONS OF CAPACITANCES

Electrochemical impedance spectroscopy (EIS) has an abundant literature, hence the basics of this technique is skipped; a couple of less-emphasized features is mentioned as follows:

1. Impedance and derived quantities consist of a magnitude and a phase angle; this is why they can be handled in terms of complex calculus, as it was recognized by Kennelly [10], and can be plotted on the complex plane to yield Argand-diagrams. These are named as Nyquist-diagrams in the context of impedances. The frequency dependence of the impedance spectra is better seen if the Bode representation is used. Note that this representation is also a plot of a complex quantity because $\log(Z) \equiv \log(Z_{\text{abs}} \cdot \exp(i\varphi)) = \log(Z_{\text{abs}}) + i\varphi$, i.e. the logarithm of the magnitude and the phase angle are the real and imaginary components of $\log(Z)$, respectively.

The Nyquist and Bode plots are the „natural" representations of the impedance spectra and its derivatives. This is why the use of other than these plots (like $\log(\text{Re}(Z))$ *vs.* $\log(\omega)$, $\log(\text{Im}(Z))$ *vs.* $\log(\text{Re}(Z))$ etc) are to be avoided. In the similar vein, it is a bad practice to use real and imaginary axes with non-equal units, yielding anisotropy of the complex plane.

2. The „as measured", or the pre-processed data often comprise contributions bearing no relevance to the phenomenon studied. After their removal it is worth to use a representation which shows the essence and contains little if any of the incidental factors. This is why in double layer studies the use of the interfacial capacitance, $C(\omega)$ is preferred to the measured impedance spectrum, $Z(\omega)$. The latter is transformed to $C(\omega)$ spectrum using the $C(\omega) = Y_{\text{int}}/(i\omega) = 1/[i\omega \cdot (Z(\omega) - R_{\text{s}})]$ equation, where the subscript int refers to the interface, i is the imaginary unit and $R_{\text{s}} = Z(\omega \to \infty)$.

Such a representation has two advantages: First, it refers solely to the interface rather than both the interface and the electrolyte bulk. Second, the impedance (and also admittance) of an almost purely capacitive interface considerably depends on frequency; it is difficult to visualize a spectrum taken in a broad range of frequency as a complex plane plot. Points of a capacitance spectrum appear on a complex plane plot much more evenly, than those of impedance spectra.

3. The information obtained from EIS is always a potential derivative of a structural or a kinetic parameter (we get differential capacitances and resistances which are d/dE potential derivatives of surface charge and of charge transfer rates, respectively). For the determination of these latter quantities other considerations or quantities are needed. For example, for the determination of surface charge an integration constant is required.

4. Analysis of a measured $Z(\omega)$ spectra is usually carried out with a comparison with the network function of an appropriate equivalent circuit. This is a straightforward method if the topology of the circuit corresponds to connection scheme of the processes. There are, however, cases when one cannot find an equivalent circuit comprising of a few lumped elements only, whose topology of could be related to the system studied. In this case the ingenious method of Stoynov and coworkers [11,12] may help: their "structural" or "differential" analysis of impedances may reveal characteristic time constants or time constant distributions.

5. The definition of impedance implies that the system is in equilibrium or at least in a steady state. Slowly changing systems can also be characterized by impedance spectroscopy; in these cases the low frequency limit of the spectra should be determined by the Kramers-Kronig transform [13,14] or similar tests [15,16]; all points below this limit frequency should be discarded. There exists a simple method, elaborated by Stoynov [17] to correct for the system's drift: Consider a number of subsequent spectra measured with the same set of frequencies, on a slowly changing system. The moment of the measurement is recorded together with the spectrum data points (frequency, Re(Z), Im(Z)) for each points. Afterwards, for the impedance points of identical frequencies, ω_{k} frequency one fits an appropriate smooth curve (typically a spline) to yield the $Z(\omega_{\text{k}}, t)$ function. Having $Z(\omega_{\text{k}}, t)$, one can calculate the $Z(\omega_{\text{k}})$ data points for any moment. This way the spectra can be corrected as if all points of one spectrum would have been measured in the same moment. Using such a procedure of interpolation (or extrapolation), the rates of slow processes could be evaluated [18,19].

6. It is very important to ensure homogeneous current density distribution along the electrode surface. Nowadays EIS setups are commercially available with fairly high upper frequency limit. With these, it is tempting to measure, analyze and present impedance spectra also in the frequency range even higher than 10-100 kHz. Unfortunately in this frequency range various artefacts appear due to inhomogeneous current density distributions; these are more pronounced when the electrolyte conductivity is low. As a thumb's rule we suggest the use of cells where all the current streamlines are uniform everywhere (this condition is fulfilled with thin layer cells where the counter and working electrodes are parallel to each other). In general, the reference electrode junction point – e.g. the "Luggin capillary tip"– should be located at a position where the current streamlines are not bending (an example for inappropriate location is when the reference electrode sensing point is just at the edge of an embedded disk electrode). Because of cleanliness point of view it is often advisable to keep the reference electrode in a separate compartment – then the use of a capacitively coupled auxiliary reference electrode placed close to the reference compartment's junction point is suggested [20].

DOUBLE LAYER CAPACITANCE IN AQUEOUS SOLUTIONS

Many of the double layer studies have been carried out in aqueous electrolytes with Hg; on its smooth, energetically homogeneous surface the double layer is indeed capacitive. In contrast, on solid electrodes, even on noble metals, the appearance of a capacitive interface is an exception rather than a rule. For example, on Au(111), in perchloric acid solution, at potentials at which neither hydrogen evolution nor hydroxide adsorption proceeds, the interface is almost ideally capacitive. As it is demonstrated with Fig. 2 of Ref. 21, were the interfacial impedance approximated by a *single* CPE in four orders of magnitude of frequency, then its exponent would be very close to the unity (>0.99). If this interface is regarded to be ideally capacitive, then its specific capacitance is around 20 $\mu F/cm^2$. This value is generally accepted as that of an electrostatic double layer, i.e. of the Stern-layer.

Whenever adsorption of anions is possible, then the frequency dependence is much more pronounced. Two cases are to be clearly distinguished:

(a) Double layer charging and adsorption are independent of each other. This is the case when we have some adsorbing species of minority concentration in a base electrolyte. Then, the double layer capacitance and the impedance of adsorption are parallel to each other and can be clearly separated – the latter term is a usual adsorption impedance comprising of resistive, diffusional and capacitive elements. This case can be adequately analyzed by the theory of adsorption impedance whose two roots are the papers of Dolin and Ershler [22] and of Frumkin and Melik-Gaykazyan [23]. These two theories were compiled to one in Ref. 24, for an interpretation of the present author, see the Appendix of Ref. 21. This case is irrelevant from the point of view of the present paper.

(b) Double layer charging and of adsorption are coupled processes (hence are not independent of each other). The simplest case is when the adsorbate species is the same as the one forming the double layer – as it is the case with binary electrolytes. The same ion takes part in the charging of the electrostatic double layer and in the adsorption process. In what follows, the examples refer to such a situation.

It is worth to start with the well-known system of polycrystalline platinum in aqueous sulphuric acid solution. It is known from radiotracer studies [25,26] that in the double layer region (between approximately 0.4 and 0.8 V vs RHE) the surface is covered with adsorbed sulfate ions (to be precise, by bisulphate ions). The impedance in this region is not ideally capacitive, some frequency dispersion can be observed [3]. The frequency dispersion practically diappears for well-defined single crystalline surfaces, like for Pt(111), see Fig.2. of Ref. 27 and for Pt(100), Fig.3 of Ref. 28. The high value of the interfacial capacitance – 60-80 $\mu F/cm^2$ rather than the 15-25 $\mu F/cm^2$ prevailing for the electrostatic double layer – points to a thin double layer, i.e. sulphate on platinum is in an adsorbed state. The little if any frequency dispersion implies that movement of adsorbate across the double layer is fast.

In contrast, in hydrochloric acid the interfacial capacitance exhibits a remarkable frequency dispersion in the double layer region of various single crystalline platinum group metal electrodes [29]. Two of these systems, Ir(100) and Pt(100) in HCl deserve a closer look [28,30].

The cyclic voltammogram (CV) of Ir(100) in 0.1M HCl is shown in Fig. 1a. There is an approximately 0.4V broad featureless potential region, which might be called as double layer region. Since the potential of zero total charge, *pztc*, is just in the peak at -0.1 V; in the double layer region the electrode surface is covered by the

anions, i.e. by chloride ions. The impedance spectra there can be well fitted with the impedance spectra of an *empirical* equivalent circuit of Fig.1b; the capacitance spectra (both the measured and fitted) are shown in Fig.1c.

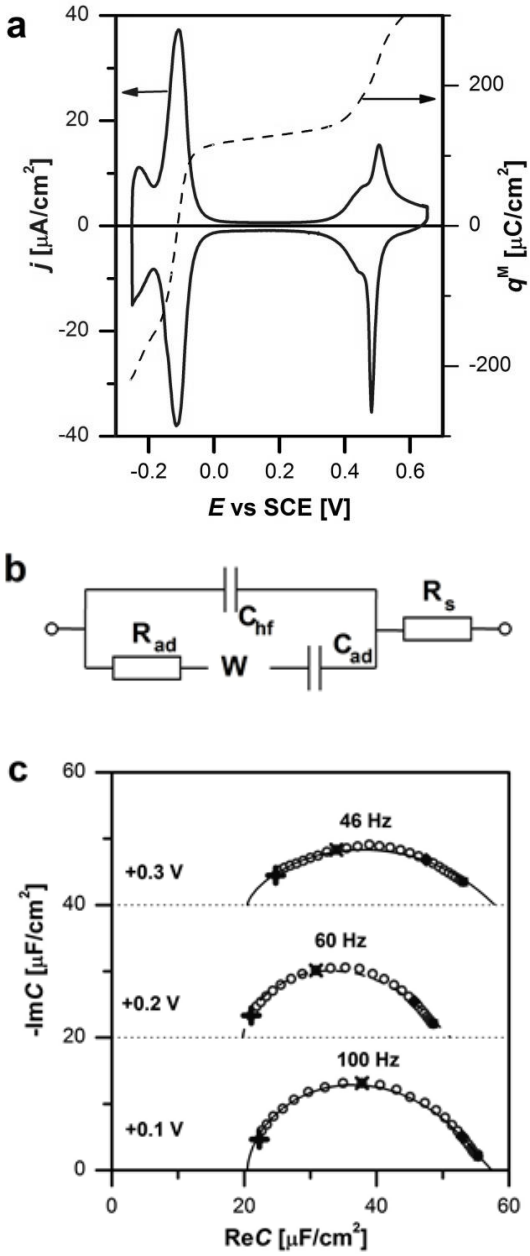

Fig.1. (a) CV of 50 mV/s of Ir(100) in 0.1M HCl (solid line) and the metal's charge as function of the potential (dashed line). (b) The equivalent circuit of the electrode. R_s is due to the electrolyte bulk, whereas the other elements represent properties of the interface. The W element is an empirical "pseudo-Warburg" element. (c) Capacitance spectra at potentials as indicated. Points at frequencies 1kHz, 100Hz, 10Hz and 1 Hz are marked by solid symbols; the frequency of the topmost spectrum points are labelled. Solid lines: fitted spectra; the equivalent circuit is shown in (b). The spectra are shifted along the abscissa due to visibility reasons.

The fits are quite good; the high frequency limit of the capacitance is about 20 μF/cm^2, ie. the same as that of the electrostatic double layers. In contrast, the low frequency limit is about 50-60 μF/cm^2 implying a two-three times thinner double layer. This is in accord with a view that following a very fast positive potential change, the chloride ions can enter the outer Helmholtz plane (OHP) from the bulk of the solution; whereas in a much longer time they can approach also the surface taking an adsorbed position in the inner Helmholtz plane (IHP). Note that the ion which gets adsorbed, first has to cross the OHP, so adsorption and double layer charging are sequential rather than parallel processes. The kinetics of the anion moving between the OHP and the IHP is expressed by the R and W (Warburg) terms of the equivalent circuit. We have no theory for the appearance of W – we regard it as an empirical element of the model. Nevertheless, even if a model is lacking, we still may claim that the ω_{max} frequency (or its reciprocal, a time constant) of the topmost point of the arc characterizes the rate of the process; and the shape of the arc gives a clue whether the time constant distribution of the adsorption is narrow or broad. As it is seen on the arcs of Fig. 1c, the arcs are semicircle-like at +0.1V and depressed semicircle at +0.3V, respectively – according to that the W term of the RW branch plays a more important role at more positive potential. The topmost frequency is also smaller for more positive potentials, i.e. more time is needed then for the adsorption-desorption processes. These properties of the RW branch can be tentatively connected to the "crowded" nature of the chloride adlayer. In general, adsorption onto a zero-coverage, homogeneous surface is a single-time-constant process. In contrast, when coverage is close to unity, adsorption requires a concerted movement of many adsorbate species: The sequence of the steps are first the formation of an empty place, then the adsorption step, finally the rearrangement of the adlayer. Such a collective movement requires more time; the many individual processes imply a certain time constant distribution.

The CV of the other system to be discussed: Pt(100) in 1M HCl solution is shown in Fig.2a, the capacitance spectrum at the positive potential end of the CV is displayed in Fig.2b. The capacitance spectra for HCl solutions on Ir(100) and Pt(100) are rather similar to each other. We note that similar spectra of arc shapes have been found by us using other Pt-group metal single crystals, also with Br^- and I^- containing electrolytes [29].

For comparison, Fig.2 consists also the CV and a capacitance spectrum of Pt(100) in 0.5M H_2SO_4,

measured the just the same way as in the 1 M HCl solution. The voltammograms and the *pztc* values (as displayed in Fig.2a) just as the capacitance spectra are rather different. Since the H^+ concentration of the two solutions is approximately the same, the difference – at least positive to the *pztc* – is evidently due to the different properties of the anion adlayer. The spectrum in H_2SO_4 solution is practically a single point, at about 80 μF/cm^2. We note that similar single-point like spectra have been found by us using other Pt-group metal single crystals, also with phosphate (at the given pH, $H_2PO_4^-$) ion containing electrolytes [29].

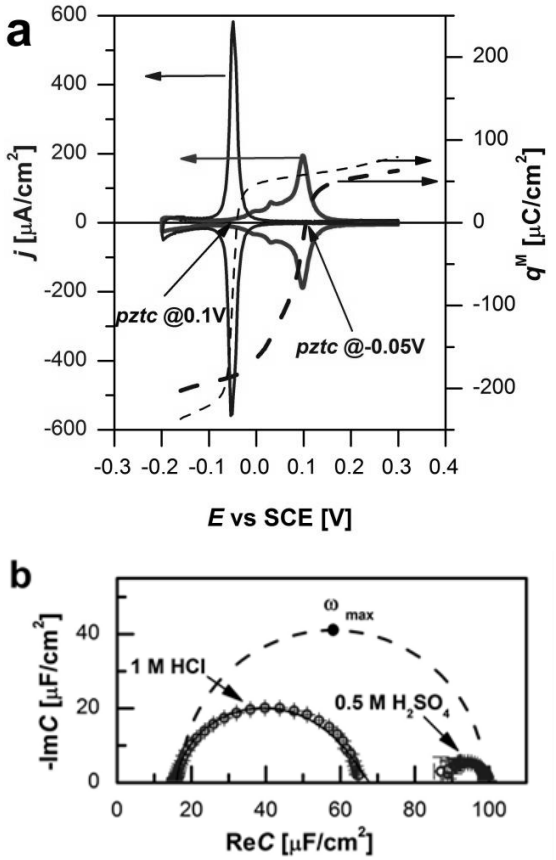

Fig.2. (a). CVs of 50 mV/s (solid lines) along with the metal's charge vs potential curves (dashed lines) of Pt(100) in 0.5M H_2SO_4 (thick lines) and in 1M HCl (thin lines); (b) Capacitance spectra at +0.3V (points: measured spectra), solid line: fitted spectrum (in HCl solution); dashed line: hypothetical high frequency spectrum in H_2SO_4 solution.

This single-point behaviour can be interpreted in the following way: also for this system, the high frequency end of the capacitance arc is assumed to be at about 20 μF/cm^2; this hypothetical arc is indicated by a dashed line in Fig.2b. The topmost frequency of this arc, ω_{max} is at very high frequencies, orders of magnitudes higher than the audio-frequency range of the capacitance (probably in the MHz range). In other words, adsorption-desorption of sulphate appears to be much (orders of magnitudes) faster than of chloride. This difference can be easily explained as follows: With impedance measurements we get information on the displacement of charges – without learning anything on their chemical nature. That is, in the case of (bi)sulphate adsorption-desorption we cannot distinguish between bisulphate adsorption and H^+ release from an adsorbed bisulphate ion. Both processes lead to one electron removal from the metal surface. However, adding one bisulphate ion to an already crowded adlayer requires much more time than removing one H^+ ion from a bisuphate anion – this dissociation process does not require the rearrangement of the neighbourhood within the adlayer. Hence we conclude that the "single-point" capacitance spectrum is due to the dissociation of the adsorbed bisulphate ions which process appears as H^+ desorption/adsorption. We note that the H^+-releasing nature of the bisulhate/sulphate adlayer has already been demonstrated by combined voltammetric and radiotracer measurements [31].

DOUBLE LAYER CAPACITANCE IN IONIC LIQUIDS

Ionic liquids (ILs) are salts whose melting point is below 100 ^{o}C; many of them are (more-or-less viscous) fluids at room temperature. Due to their properties like non-volatility, non-flammability and electric conductance these salts attracted much interest in various areas of chemistry [32]. For practical purposes they are regarded as promising electrolytes [33]. An important group of ILs comprises imidazolium cations [34].

As ILs are concentrated electrolytes, the $C(E)$ function of the metal | IL interfaces is relevant from theoretical point of view. In the related models the charge density is limited everywhere (in contrast to theories with of dilute electrolytes, "lattice saturation" prevents accumulation of much charge anywhere). Since the start of the ionic liquid electrochemistry studies one of the important issues was whether or not the measured $C(E)$ curves can be interpreted in terms of Kornyshev's IL double layer model [35,36], predicting "bell-shaped" or "camel-shaped" $C(E)$ curves. Up till now this question is open; the measurements are still not good enough to support or disprove related statements. There are two reasons for this. One is a cleanliness problem: the ionic liquids are usually much less pure than the aqueous electrolytes; the second is related to modelling problem as will be explained in the following paragraphs.

Various groups reported *C*(*E*) measurements (either performed at one frequency with scanned potential, or calculated from impedance spectra) made on poly- or single-crystalline gold [37-41] or other electrodes like polycrystalline Pt [42], on carbon [43,44], on Bi(111) [45-50]; in most studies the electrolytes were the commercially available imidazolium-based ILs. We have focused our attention to the behaviour of two single crystal faces of gold, Au(111) and Au(100), because we regarded gold to be just as inert as in aqueous solutions. In most cases we used 1-butyl-3-methyl-imidazolium (BMI) salts, with PF_6 or bis(trifluoromethylsulfonyl) imide, Tf_2N, anions. After a few years of laboratory work with these systems [51-55], we recognized that gold is far from being inert in $BMIPF_6$ and other N-heterocycles-consisting ILs. Up till this recognition the low frequency impedance behaviour was attributed to the double layer charging rather than to a dissolution + eventual re-deposition process. But in-situ scanning tunneling microscopy (STM) images, demonstrating the presence of etch-pits and corrugating step-edges provided direct evidence for the latter case [56]. Thus, even on the noble metal of gold, we face the problem of separation of charging and charge transfer processes.

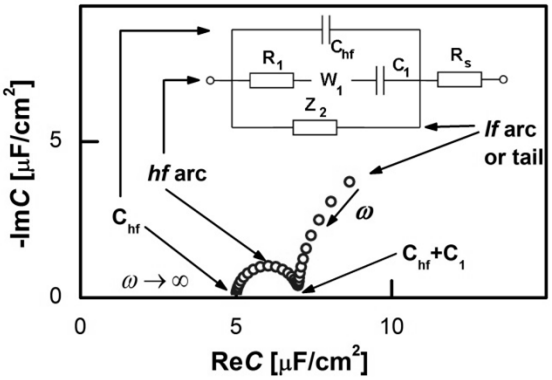

Fig. 3. Schematic capacitance spectrum of the metal-ionic liquid interface and its general equivalent circuit. R_s is due to the electrolyte bulk, whereas the other elements represent properties of the interface. The W_1 element is an empirical "pseudo-Warburg" element. In some cases this W element was replaced by a CPE. The Z_2 impedance (if any) is a serial R–CPE–C circuit, or a subset of it (CPE, R–W–C etc.).

A couple of typical measured capacitance spectra are shown in Fig.4; they can be well interpreted in terms of the equivalent circuit of Fig.3. The corresponding theoretical spectra, as shown on the complex plane plot of Fig. 3 comprise a high frequency (*hf*) arc between C_{hf} and C_{hf}+C_1 and a low frequency (*lf*) arc or tail. Accordingly, we have to analyze the measured spectra using the equivalent circuit of the inset, then draw conclusions regarding double layer charging from C_{hf}, C_1, R_1 and W_1 elements only – all elements related to the *lf* tail can be disregarded.

The *hf* arc was apparent in all but one systems studied by us. (The exception is our first IL measurement series [51], where cleanliness, reproducibility and measurement precision was not sufficient to resolve the *hf* arc.) First, C_{hf} appeared to be independent of the metal (cf. Fig.4); its potential dependence is little if any (the potential dependences of the spectra are well documented in Refs. 53-56). C_{hf} was found to depend on the cation rather than the anion: the larger the cation the smaller C_{hf} values were found. Second, for C_1, the span of the *lf* arcs is in the range of 1–3 μF/cm^2, we found neither trends of the values nor can we offer any explanation for the order of magnitude of these values. Third, the order of magnitude of the characteristic frequency of the *hf* arcs, ω_{max}, is in the range between 100 Hz and 1 kHz. This frequency increases with higher temperatures (see Fig.6a of Ref. 56). Whereas C_{hf} and C_1 do not depend on temperature, the temperature dependence of ω_{max} (the "Arrhenius plot" and the associated activation energy) is rather similar to that of the bulk conductivity of the ionic liquid (Ref. 56, Fig. 6b). This is why we suspect that the rearrangements of the double layer and the ionic movements require similar activation processes.

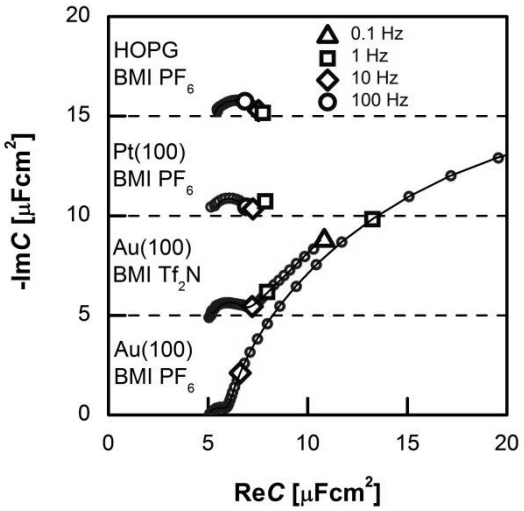

Fig. 4. Capacitance spectra of various electrodes – unless otherwise noted – in $BMIPF_6$. All spectra have been measured at, or the close vicinity of, –0.1 V. The characteristic frequency of the high frequency arcs is in the range of 100 Hz – 1 kHz. The spectra are shifted along the ordinate for visibility reasons.

There exist reports on similar studies – for an overview on these see, e.g. Ref. 57. One group's work deserves mentioning here: Roling and

coworkers studied a number of similar electrochemical systems with Au(111) [38-41]. Though the representation of their impedance/capacitance spectra markedly differs from that of ours; – after all – their conclusions are similar to the above ones.

The main, phenomenological outcome of these studies is that the double layer capacitance, C_{dl} of a metal |ionic liquid interface at a given potential is not a single, frequency independent value, but is a function of frequency, involving (at least) three parameters. The high and low frequency limiting values of $C_{dl}(\omega)$ (C_{hf} and $C_{hf} + C_1$ in this model) can be interpreted as they refer to the "frozen" and "relaxed" states, respectively. The characteristic time (reciprocal of the angular frequency of the topmost point along the capacitance arc) represents the kinetics of the rearrangement of the double layer.

SUMMARY AND CONCLUSIONS

It is demonstrated for two cases of apparently ideal, ideally polarizable electrochemical interfaces that the interfacial capacitance does depend on frequency. In other words, charging-discharging following potential changes is not instantaneous. A double layer with non-zero characteristic time cannot be interpreted in terms of electrostatics – as the name of electrostatics implies, in that discipline there is no time involved as a variable. Electrostatic charging/discharging is infinitely fast; hence, for the rationalization of the – not infinitely fast – charging/discharging we have to assume processes of physico-chemical origin.

The existing double layer theories (Helmholtz, Gouy-Chapman-Stern, Bockris-Devanathan-Müller, etc) are all based on electrostatic interactions and hence time/frequency is not a variable therein (this applies also to newer MC, MD, DFT calculations). Double layer theories are wanted which include kinetic processes based on physico-chemical interactions.

The frequency dependence of the double layer has a consequence on how we evaluate electrode kinetics data: These are calculated from transient or EIS measurements, the procedures require the proper separation of the Faradaic and charging currents (provided that it is possible). Corrections of kinetics data by taking into account the double layer charging are typically approximations using C_{dl} or CPE, which in turn affect the accuracy of data on electrode kinetics.

***Acknowledgments**: The research within project No. VEKOP-2.3.2-16-2017-00013 was supported by the European Union and the State of Hungary, co-financed by the European Regional Development Fund.*

Additional support of the Hungarian Science Research Fund OTKA (No. K112034) is acknowledged.

REFERENCES

1. R. de Levie, On porous electrodes in electrolyte solutions—IV, *Electrochim. Acta* **9**, 1231 (1964).
2. J. Huang, J. Zhang, Theory of impedance response of porous electrodes: simplifications, inhomogeneities, non-stationarities and applications, *J. Electrochem. Soc*. **163**, A1983 (2016).
3. S.H. Glarum, J.H. Marshall, An A- C Admittance Study of the Platinum/Sulfuric Acid Interface, *J. Electrochem. Soc.*, **126**, 424 (1979).
4. S-L Wu, M.E. Orazem, B. Tribollet, V. Vivier, The impedance response of rotating disk electrodes, *J. Electroanal. Chem.* **737**, 11 (2015).
5. L. Nyikos, T. Pajkossy, Fractal dimension and fractional power frequency dependent impedance of blocking electrodes, *Electrochim. Acta* **30**, 1533 (1985).
6. T. Pajkossy, L. Nyikos, Scaling-law analysis to describe the impedance behaviour of fractal electrodes, *Phys. Rev. B* **42**, 709 (1990).
7. T. Pajkossy, Generalization of Basic Laws of Electrochemistry for Fractal Surfaces, *Heterogeneous Chemistry Reviews* **2**, 143 (1995).
8. T. Pajkossy, Impedance of rough capacitive electrodes, *J. Electroanal. Chem.* **364**, 111 (1994).
9. Z. Kerner, T. Pajkossy, On the origin of capacitance dispersion of solid electrodes, *Electrochim. Acta* **46**, 207 (2000).
10. A.E. Kennelly, Impedance, *Transactions of the American Institute of Electrical Engineers* **X**, 172 (1893).
11. Z Stoynov, Structural spectral analysis of electrochemical impedance, *Electrochim. Acta* **34**, 1187 (1989).
12. Z. Stoynov, D. Vladikova, Differential Impedance Analysis, Marin Drinov Publ. House, Sofia, 2005
13. D. D. Macdonald, M. Urquidi, Application of Kramers- Kronig Transforms in the Analysis of Electrochemical Systems I. Polarization Resistance, *J. Electrochem. Soc*. **132**, 2316 (1985).
14. B.A.Boukamp, J.R. Macdonald, Alternatives to Kronig-Kramers transformation and testing, and estimation of distributions, *Solid State Ionics* **74**, 85 (1994).
15. W. Ehm, H. Göhr, R. Kaus, B. Röseler, C.-A. Schiller, The evaluation of electrochemical impedance spectra using a modified logarithmic Hilbert transform, *ACH-Models Chem.*, **137**, 145 (2000).
16. C.-A. Schiller, F. Richter, E. Gülzow, N. Wagner: Validation and evaluation of electrochemical impedance spectra of systems with states that change with time, *Phys.Chem. Chem. Phys.* **3**, 374 (2001).

17. Z.Stoynov, Nonstationary impedance spectroscopy, *Electrochim. Acta* **38**, 1919 (1993).
18. M. Ujvari, D. Zalka, S. Vesztergom, S. Eliseeva, V. Kondratiev, G.G. Láng, Electrochemical impedance measurements in non-stationary systems - application of the 4-dimensional analysis method for the impedance analysis of overoxidized poly(3,4-ethylenedioxythiophene)-modified electrodes, *Bulg. Chem. Comm.* **49**, 106 (2017).
19. V. Horvat-Radosevic, K. Kvastek, K.M. Kosicek, Application of Stoynov's 4-D analysis for nonstationary impedance spectra corrections of thin poly(o-ethoxyaniline) modified Pt electrode, *Bulg. Chem. Comm.* **49**, 119 (2017).
20. C.C. Herrmann, G.P. Perrault, A.A. Pilla, *Anal. Chem*. **40**, 1173 (1968).
21. Z.Kerner, T.Pajkossy, Measurement of adsorption rates of anions on Au(111) electrodes by impedance spectroscopy, *Electrochim. Acta* **47**, 2055 (2002).
22. P. Dolin, B. Ershler, Kinetics of processes on the platinum electrode, *Acta Physicochim. URSS* **XIII**, 747 (1940).
23. A.N. Frumkin, V.I. Melik-Gaykazyan, Determination of the kinetics of organic substances by measuring the capacitance and conductivity at the electrode-solution boundary (in Russian), *Dokl. Akad. Nauk*. **5** 855 (1951).
24. W. Lorenz, F. Möckel, Adsorptionsisotherme und Adsorptionskinetik kapillaraktiver organischer Molekeln an der Quecksilberelektrode, *Z. Elektrochem*. **60**, 507 (1956).
25. G. Horányi, J. Solt, F. Nagy, Investigation of adsorption phenomena on platinized platinum electrodes by tracer methods, II. The potential dependence of anion adsorption, *J. Electroanal. Chem.*, **31**, 95 (1971).
26. Maria E. Gamboa-Aldeco, Enrique Herrero, Piotr S. Zelenay and Andrzej Wieckowski, Adsorption of bisulfate anion on a Pt(100) electrode: a comparison with Pt(111) and Pt(poly), *J. Electroanal. Chem*., **348**, 451 (1993).
27. E. Siebert, R. Faure, R. Durand, Electrosorption impedance on Pt(111) in sulphuric media and nature of the "unusual" state, *Electrochem. Comm*. **3**, 181 (2001).
28. T. Pajkossy, Impedance Spectra of Pt(100) in Aqueous H2SO4 and HCl Solutions Around the Hydrogen Adsorption-Desorption Peak. *Z. Phys. Chem.* **226**, 935 (2012).
29. T. Pajkossy, D.M. Kolb, Anion-adsorption related frequency-dependent double layer capacitance of the platinum group metals in the double layer region, *Electrochim. Acta* **53**, 7403 (2008).
30. T. Pajkossy, and D.M. Kolb, Double layer capacitance of the platinum group metals in the double layer region, *Electrochem.Comm*. **9**, 1171 (2007).
31. 1 A. Kolics, A. Wieckowski, Adsorption of Bisulfate and Sulfate Anions on a Pt(111) Electrode, *J. Phys. Chem. B* **105**, 2588 (2001).
32. A. Kokorin (Ed.), Ionic Liquids: Applications and Perspectives, InTech, Rijeka, Croatia, 2011.
33. M. Galiński, A. Lewandowski and I. Stępniak, Ionic liquids as electrolytes, *Electrochim. Acta* **51**, 5567 (2006).
34. J. S. Wilkes and M. J. Zaworotko, Air and water stable 1-ethyl-3-methylimidazolium based ionic liquids, *J. Chem. Soc. Chem. Comm.* **13**, 965 (1992).
35. A.A. Kornyshev, Double-layer in ionic liquids: paradigm change?, *J.Phys.Chem.B* **111**, 5545 (2007).
36. M. V. Fedorov, A. A. Kornyshev, Towards understanding the structure and capacitance of electrical double layer in ionic liquids, *Electrochim.Acta* **53**, 6835 (2008).
37. T. R. Gore, T. Bond, W. Zhang, R.W.J. Scott, I.J. Burgess, Hysteresis in the measurement of double-layer capacitance at the gold–ionic liquid interface, *Electrochem. Comm.* **12**, 1340 (2010).
38. M. Drueschler, B. Huber, B. Roling, On Capacitive Processes at the Interface between 1-Ethyl-3-methylimidazolium tris (pentafluoroethyl) trifluorophosphate and Au (111), *J. Phys. Chem.C* **115**, 6802 (2011).
39. B. Roling, M. Drüschler, B. Huber, Slow and fast capacitive process taking place at the ionic liquid/electrode interface, *Faraday Discuss.* **154**, 303 (2012).
40. M. Drüschler, N. Borisenko, J. Wallauer, C. Winter, B. Huber, F. Endres, B. Roling, New insights into the interface between a single-crystalline metal electrode and an extremely pure ionic liquid: slow interfacial processes and the influence of temperature on interfacial dynamics, *Phys. Chem. Chem. Phys.* **14**, 5090 (2012).
41. R.Atkin, N. Borisenko, M. Drüschler, F. Endres, R. Hayes, B. Huber, B. Roling, Structure and dynamics of the interfacial layer between ionic liquids and electrode materials, *J. Mol. Liquids* **192**, 44 (2014).
42. M. Drueschler, B. Huber, S. Passerini, B. Roling, On Capacitive Processes at the Interface between 1-Ethyl-3-methylimidazolium tris (pentafluoroethyl) trifluorophosphate and Au (111), *J. Phys. Chem.C* **114**, 3614 (2011).
43. V. Lockett, M. Horne, R. Sedev, T. Rodopoulos, J. Ralston, Differential capacitance of the double layer at the electrode/ionic liquids interface, *Phys.Chem.Chem.Phys.* **12**, 12499 (2010).
44. F. Silva, C. Gomes, M. Figueiredo, R. Costa, A. Martins, C. M. Pereira, The electrical double layer at the [BMIM][PF6] ionic liquid/electrode interface– Effect of temperature on the differential capacitance, *J. Electroanal. Chem.* **622**, 153 (2008).
45. L.Siinor, K.Lust, E.Lust, Electrical Double Layer Structure at Bi (111) | 1-ethyl-3-methyl-imidazolium Tetrafluoroborate Interface, *ECS Transactions*, **16**, 559 (2009).
46. L. Siinor, K. Lust, E. Lust, Electrical Double Layer Capacitance at Bi (111) | 1-Ethyl-3-methylimidazolium Tetrafluoroborate Interface as a Function of the Electrode Potential, *J. Electrochem.Soc.* **157**, F83 (2010).
47. L.Siinor, K.Lust, E.Lust, Influence of anion composition and size on the double layer capacitance

for Bi (111)| room temperature ionic liquid interface, *Electrochem. Comm.* **12**, 1058 (2010).
48. L. Siinor, C. Siimenson, V. Ivaništšev, K. Lust and E. Lust, Influence of cation chemical composition and structure on the double layer capacitance for Bi (1 1 1)| room temperature ionic liquid interface, *J. Electroanal. Chem.* **668**, 30 (2012).
49. E. Anderson, V. Grozovski, L. Siinor, C. Siimenson, V. Ivaništšev, K. Lust, S. Kallip, E. Lust, Comparative in situ STM, cyclic voltammetry and impedance spectroscopy study of Bi (111)| 1-ethyl-3-methylimidazolium tetrafluoroborate interface, *J. Electroanal. Chem.* **709**, 46 (2013).
50. E. Anderson, V. Grozovski, L. Siinor, C. Siimenson, E. Lust, *J. Electroanal. Chem.* **758**, 201 (2015).
51. M. Gnahm, T. Pajkossy, D.M. Kolb, The interface between Au(111) and an ionic liquid, *Electrochim. Acta* **55**, 6212 (2010).
52. T. Pajkossy, D.M. Kolb, The interfacial capacitance of Au(100) in an ionic liquid, 1-butyl-3methyl-imidazolium hexafluorophosphate, *Electrochem. Comm.* **13**, 284 (2011).
53. M. Gnahm, C. Müller, R. Répánszki , T. Pajkossy, D.M. Kolb, The interface between Au(100) and 1-butyl-3-methyl-imidazolium-hexafluorophosphate, *Phys.Chem. Chem. Phys.* **13**, 11627 (2011).
54. C. Müller, S. Vesztergom, T. Pajkossy, T. Jacob, The interface between Au(100) and 1-butyl-3methyl-imidazolium-bis(trifluoromethylsulfonyl)imide, *J. Electroanal. Chem.* **737**, 218 (2015).
55. C. Müller, S. Vesztergom, T. Pajkossy, T. Jacob, Immersion measurements of potential of zero total charge (pztc) of Au(100) in an ionic liquid, *Electrochim. Acta* **188**, 512 (2016).
56. C. Müller, K. Németh, S. Vesztergom, T. Pajkossy, T. Jacob, The interface between HOPG and 1-butyl-3-methyl-imidazolium hexafluorophosphate, *Phys.Chem.Chem.Phys.* **18**, 916 (2016).
57. T. Pajkossy, C. Müller and T. Jacob, The metal–ionic liquid interface as characterized by impedance spectroscopy and in situ scanning tunneling, *Phys.Chem.Chem.Phys*., **20**, 21241 (2018).

Процеси на бавен заряд / разряд в електрохимичния двоен слой

Т. Пайкоши

Институт по материали и химия на околната среда, Изследователски център за природни науки, Унгарска академия на науките, Магияр тудошок корутия, 2, Будапеща H-1117, Унгария

Постъпила на 2 май 2018г.; приета на29 юни 2018г.

(Резюме)

В памет на Здравко Стойнов

За два случая на очевидно идеални, идеално поляризуеми електрохимични повърхности е демонстратирано, че заряда / разряда след изменение на потенциала не се осъществява мигновенно, поради което двойният слой не е (единствено) електростатичен по природа - както се предполага в "класическите" двойни слоеве. Това означава, че физико-химичните взаимодействия също трябва да се взимат в предвид при процеси на бавно преобразуване описващи се с двоен електричен слой.

Bulgarian Chemical Communications, Volume 50 Special Issue D (pp. 99 – 107) 2018

Molten Carbonate Fuel Cells in Integrated Systems for the Exploitation of Poor Fuels and the Segregation of CO_2

E. Audasso[1], P. Campbell[2], M. Della Pietra[3], M.C. Ferrari[2], B. Bosio[1,*], E. Arato[1]

[1] *Process Engineering Research Team, Dipartimento Ingegneria Civile Chimica e Ambientale, University of Genova, Via Opera Pia 15, 16145, Genova, Italy*

[2] *School of Engineering, University of Edinburgh, The King's Buildings, Robert Stevenson Road, EH9 3FB, Edinburgh, UK*

[3] *ENEA Research Center Casaccia, Via Anguillarese 301, 00123, Rome, Italy*

Received May 16, 2018 Revised August 2, 2018

A multi-scale approach for the analysis of reactant systems is a very important mean for the improvement of the understanding of the phenomena occurring at different scales of space and time, and for the support it brings to the experimental and design activities in particular for scale-up purposes. In previous works, the authors developed kinetics, cell and stack models for molten carbonate fuel cells, integrating all these scales of simulation in a code called SIMFC, which has been successfully validated on experimental data. The aim of the present work is to show the benefits that the coupling of plant simulation and small scale models can bring to the study of innovative applications and the design of particular configurations. In the frame of this paper, the authors analysed the integration of the calcium-looping technology coupled with molten carbonate fuel cells for the capture and sequestration of carbon dioxide using a series of different sources of fuel gas to evaluate the best options. In particular, this work analyses the exploitation of poor fuels in fuel cell that would not be possible without enrichment. The availability of a small scale model allowed to identify critical operating conditions (of both local temperature and composition) that decrease the performance and that cannot be easily identified with the use of only large scale model commonly employed for plant design and simulations.

Key words: Molten carbonate fuel cell, calcium-looping, plant simulation, CO_2 sequestration

INTRODUCTION

The emissions of CO_2 in the atmosphere, especially due to energy production, are a major concern due to the effects that this greenhouse gas has on the climate. Carbon Capture, Utilization and Storage (CCU and CCS) are regarded as the main solution to mitigate these effects [1]. CCU and CCS consist of a number of technologies that can be used to separate and collect the CO_2 generated in industrial processes for its reuse in other chemical plants or for its storage in underground facilities to prevent emissions into the atmosphere.

Molten carbonate fuel cells (MCFCs) are a valid example of a technology that can be used for carbon capture thanks to its operating principles [2]. MCFCs are deeply studied by Electrochemical Impedance Spectroscopy [3,4], that is a valuable tool for the investigation of reactions and phenomena taking place in different materials [5-10]. In literature, different studies already exist concerning its application as mean for carbon capture [11–13]. Investigations on MCFCs vary from studies to improve the used materials [14–21], to reduce the pollutant effects and to increase their resistance [22–26] and to realize robust computer simulations [27–29] in particular for integrated systems [12, 30, 31].

Computer simulation can be a useful instrument to support experimental and design activities. In particular, a multi-scale approach that integrates the modelling from the small to the large scale can highly improve the scale-up process.

In previous works, the authors developed a kinetics formulation to simulate the performance of MCFC [24, 32, 33]. This formulation has been integrated into a Fortran code coupled with a cell level simulation to accurately consider mass, energy and momentum balances. Through a series of experimental campaigns, the model has been tested and proved reliable for the simulation of the MCFC behaviour. In this work, the aim is to show the benefit of the integration of a local model into the overall plant simulation.

For this activity, an MCFC stack was integrated after a calcium-looping process for carbon capture and sequestration.

This integration is interesting because it allows the use of poor fuels in MCFC. In fact, for particular fuels such as the exhaust of a gas furnace

To whom all correspondence should be sent:
E-mail: barbara.bosio@unige.it

or the product of the gasification of waste, the amount of fuel and the high content of CO_2 induce instability in the cell. If the calcium looping process is integrated upstream the cell, it removes CO_2, enriching the fuel. Moreover, performing the regeneration of the sorbent in the calcium looping with air and not pure O_2, allows significant cost reduction and removal of CO_2 in the cell. In this way the two technologies brings mutual benefit [34]. A simple scheme that shows the integration of these two technologies is represented in figure 1.

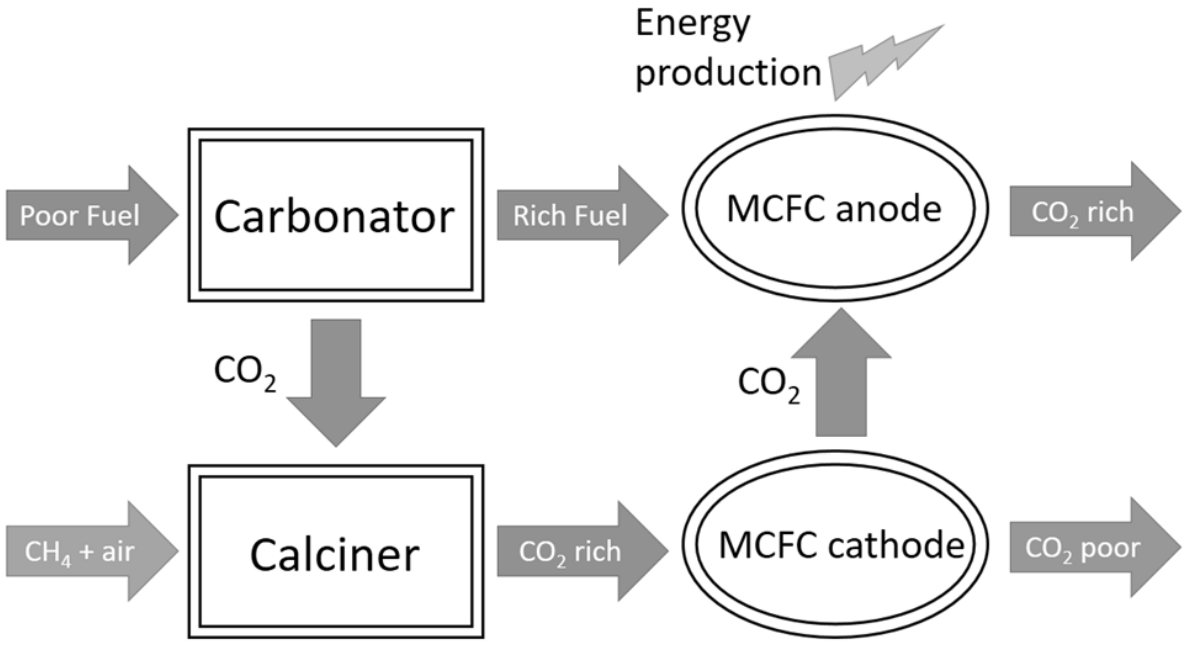

Fig. 1. Schematic representation of the integration between calcium looping process and MCFC.

MOLTEN CARBONATE FUEL CELL & SIMFC CODE

A molten carbonate fuel cell is an electrochemical device that directly converts the chemical energy presents in fuel to electrical energy. The electrochemical reactions that allow this conversion are the following:

$$\frac{1}{2}O + CO_2 + 2e^- \rightarrow CO_3^= \text{ (at the cathode)} \quad (1)$$

$$H_2 + CO_3^= \rightarrow H_2O + CO_2 + 2e^- \text{ (at the anode)} \quad (2)$$

$$\frac{1}{2}O + H_2 + 2e^-(+CO_{2,Cathode}) \rightarrow H_2O(+CO_{2,Anode}) \text{ (overall reaction)} \quad (3)$$

An important characteristic of MCFC that can be seen from the overall equation (eq. 3) is that the CO_2 at the cathode moves to the anode side where is released. This process allows the depletion of CO_2 from the cathode feed and the subsequent enrichment of the anode stream. At the end of the process, ideally, the cathode outlet will have a low content or none CO_2, while the anode one will consist of a mixture of CO_2 and water that can be separated with less energy consumption compared to the CO_2 and N_2 mixture of the cathode feed. For this reason and for the surplus energy that they produce, MCFCs are deemed as a valid instrument for carbon capture and segregation.

The performance of an MCFC can be expressed through the following equation:

$$\Delta V = \Delta E - J\,R_{Tot} \quad (4)$$

where ΔV is the measurable voltage (V), ΔE the voltage at the thermodynamic equilibrium given by the Nernst equation (V), J the total current density (A m^{-2}) and R_{TOT} the overall cell resistance (Ω m^2) which includes all the voltage losses of the cell which are Ohmic, concentration and activation losses.

In the model developed by the authors [24, 32, 33, 35] and named SIMFC, the resistance term has been expressed as:

$$R_{Tot} = P_1 e^{\frac{P_2}{T}} + \frac{P_3 T e^{\frac{P_4}{T}}}{p\,ln\left[1-\frac{1.5}{1+\vartheta}(y_{CO_2}+y_{H_2O})\right]^{-1}} + P_5 T e^{\frac{P_6}{T}} {p_{CO_2}}^{0.5} {p_{O_2}}^{-0.75} + \frac{P_7 T e^{\frac{P_8}{T}}}{p\,ln(1+y_{H_2})} \quad (5)$$

where T is the operating temperature (K), p is the operating pressure (atm), $P_i s$ and ϑ are empirical parameters, $p_i s$ are the partial pressure of the i-th gas (atm) and y_{H_2} is the molar fraction of H_2. In the formulation, each addend represents a particular aspect of the resistance: the first is the ohmic term, while the others are the polarization resistances due to respectively CO_2, O_2 and H_2.

The model has been tested with different operating conditions (temperature and composition) and electrode materials (with opportune parameters re-evaluation), and showed always a satisfying fit [24,32,33].

The SIMFC code uses equations 4 and 5 to describe the performance of an MCFC and is completed with the addiction of energy, mass and momentum balances. Through the code it is possible to obtain good fitting results of a single cell or a stack performance, composition and temperature maps and other kind of electrochemical information.

This model can be helpful if integrated in a plant simulation because it can provide information about parameters that usually plant scale design models ignore, such as local compositions, current and temperatures.

CALCIUM-LOOPING

The calcium looping is a carbon capture technology that is based on the reversibility of the lime carbonation [36]. The process can be divided into two main phases: carbonation and calcination.

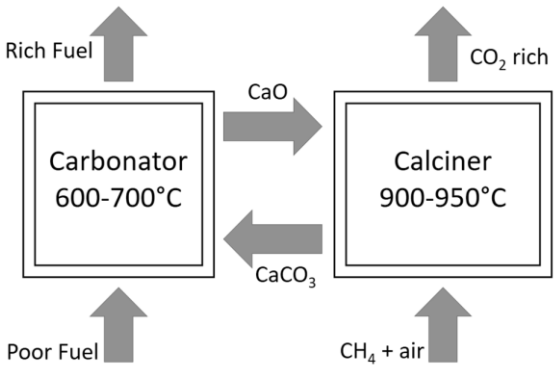

Fig. 2. Calcium looping process scheme.

The carbonation consist in an exothermic step where a flue gas containing CO_2 enters a carbonator reactor where the CO_2 reacts with CaO to form $CaCO_3$ (usually at an operating temperature between 870 and 970 K), according to the following reaction [37].

$$CO_2 + CaO \rightarrow CaCO_3$$
$$\Delta H_{r,298K} = -178\ KJ\ mol^{-1} \quad (6)$$

Through this first phase the feeding is depleted of CO_2 and can be used for different scopes as gas with a higher heating value.

Subsequently, the formed carbonate is sent to a calciner where, at temperature higher than 1170 K, it dissociate to CO_2 and CaO. The gaseous CO_2 can be collected, while the solid can be recycled to the carbonator reactor. This step is endothermic and heat is usually provided with combustion with pure O_2 in order to obtain a highly concentrated stream of CO_2 [37]. This represents one of the main disadvantages of this process [38] due to the high cost of pure oxygen. A possible solution considers the use of air, but it would require a subsequent separation of N_2 and CO_2 for carbon sequestration. This separation can be carried out exploiting an MCFC where the CO_2 rich stream can be used as cathode feed while the previously enriched fuel can be used as the anode one.

DESCRIPTION OF THE SYSTEM

The studied system consists in the integration of the technologies of calcium looping and MCFC for the segregation of carbon dioxide and the exploitation of poor fuels. The development of the calcium looping process was based on the ZECOMIX high efficiency hydrogen power plant currently operating at the ENEA research centre Cassaccia (Italy) [39], where the process is positioned downstream of a gasifier for the decarbonisation of raw syngas.

A fuel gas reach in CO_2 and that cannot be directly used in MCFC is sent to the calcium looping system, after a treatment to remove possible poisonous gases as sulphur compounds (This aspect has not been treated in this work). In the carbonator the fuel is depleted of CO_2 thanks to reaction 6 and can be used as anode inlet for an MCFC. The $CaCO_3$ moves to the calciner where the thermal regeneration of the solid sorbent occurs. Combustion of methane in air is utilized to ensure an adequate temperature rise to facilitate the regeneration. The integration of the MCFC downstream allows for methane combustion in the presence of air instead of pure O_2, reducing the energy and cost penalty associated with producing pure oxygen in an air separation unit. The regenerated CaO is recycled back to the carbonator while the CO_2 rich gas is used as the cathode inlet to the MCFC, allowing for further CO_2 concentration and the generation of useable electrical power. The utilization of the decarbonized syngas for electricity generation in an MCFC is preferable due to the higher electrical efficiencies observed in MCFCs

compared to the commonly utilized gas turbines. At the end of the process the enriched CO_2 should undergo a further separation to remove steam or other impurities. In this work three different possibilities have been investigated: simple condensation, burner and condensation to remove possible unreacted O_2, and membranes [40, 41]. A scheme of the proposed solution with the integration of the burner and condensation separation process as used in the simulation in Aspen is presented in figure 3.

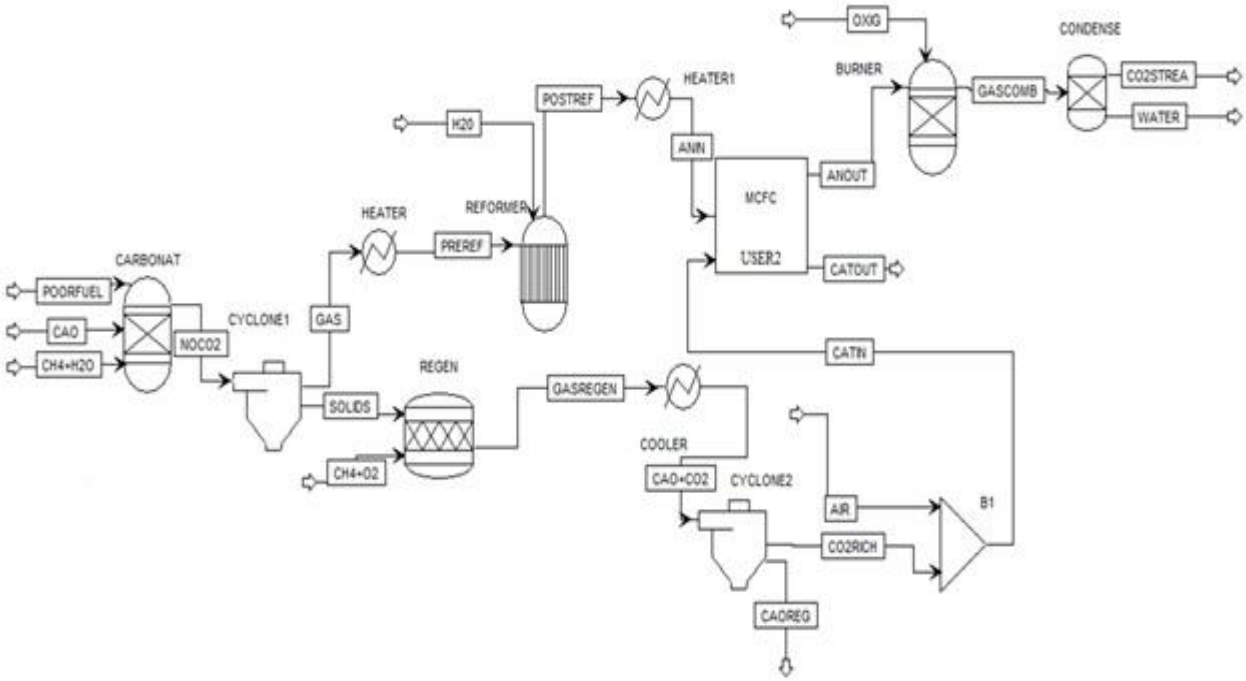

Fig. 3. Aspen representation of the calcium looping and MCFC integration.

The following assumptions have been made for the simulation of the process:

1. The removal of pollutants happens before the beginning of the studied process.
2. The carbonator works at 973 K. The carbonation reaction is at the thermodynamic equilibrium, while the conversion of CH_4 is fixed at 80% as literature suggests [42]. CH_4 and CaO feed flow rates are optimized as function of the operating conditions.
3. The regeneration works at 1173 K at the calciner. The regeneration reaction is at the thermodynamic equilibrium, while the conversion of CH_4 is total. The amount of the "CH_4+O_2" stream has been calculated in order to ensure an adiabatic reaction.
4. The solid phases after the carbonator and the regenerator are completely separated from the gas phases in downstream cyclones.
5. A reformer is placed before the anode inlet enters the cell to convert all the CH_4 in H_2. Prior to this reaction the stream is preheated up to 1123 K. Also, steam is added to increase the content up to 10 mol% since it is necessary to avoid carbon deposition.
6. The cathode inlet stream is mixed with air to ensure an amount of O_2 equal to 20% and the thermal management of the cell.
7. In the cell the fuel utilization factor (at the anode) is assumed to be 70%, while the CO_2 utilization factor (at the cathode) is assumed to be 90%.
8. The cells of the stack are considered to have an area of 1 m^2 each working with a current density of 1000 A cm^{-2}.
9. The performance of the cell is calculated on the basis of the local SIMFC model.
10. At the anode outlet a burner is used for the combustion of excess H_2 to obtain only CO_2 as gas outlet and water which is separated thanks to a condensation. The O_2 flow rate is optimized as a function of the operating conditions.
11. In case a membrane is considered downstream, it is assumed that the CO_2 removal efficiency is of 90% and that it produces a 95% pure CO_2 stream [43].

For this analysis, three different feeds have been studied to describe three different possible applications: blast furnace exhaust [44], gasified waste [45] and syngas

Table 1. Compositions (in molar fractions) of the three kinds of fuel gas used for the simulation.

Type of fuel	H_2	CO	CO_2	H_2O	N_2	H_2S	HCN	NH_3
Blast furnace exhaust	0.048	0.228	0.190	0.062	0.472	$1.97\ 10^{-5}$	$1.66\ 10^{-4}$	$1.32\ 10^{-5}$
Gasified waste	0.292	0.425	0.161	0.068	0.054	0.0036	$9.95\ 10^{-5}$	0.0025
Syngas	0.282	0.350	0.139	0.198	0.031	0.0068	-	0.0015

SIMULATION RESULTS

The capture of CO_2

The main interest of this integrated application is its applicability to the capture of CO_2 to reduce emissions in the atmosphere and the simultaneous exploitation of poor fuels. For this reason the main results presented will be focused on the flow rate and the molar fraction of CO_2 released and captured during the process as well as the energy efficiency.

Before showing the results of the integrated process, the results of the single units (fuel cell and calcium looping separately) should be presented for comparison. However, since poor gases are considered, they cannot be used directly in a fuel cell stack efficiently, and therefore only the calcium looping results are shown in table 2. The use of the calcium looping allows to ideally obtain a pure stream of CO_2, but the emissions in atmosphere still contain CO_2 in the order of 5 mol%.

In table 3 and 4, the main results concerning the CO_2 captured and released in atmosphere of the simulation for the integrated process are presented for the three different types of fuel gas with three different methods for the final downstream separation.

In table 3, the column "CO_2 molar fraction" represents the values in the final enriched stream of CO_2 after the calcium looping process, the fuel cell operation (anode outlet) and one of the three processes of separation considered. In all the analysed cases, it appears clear that the use of the condensation only is not sufficient to obtain a stream of CO_2 suitable for sequestration or other possible uses since it is still rich in other compound

s (mainly N_2 and unreacted H_2). The addiction of a burner will favour the process, but the best solutions is to add a further separation by means of membranes. This kind of separation does not only allow to obtain a stream very reach in CO_2, but also to reduce the final flow rate.

Table 4 refers to the sum of all CO_2 presents in all the streams that are released into the atmosphere during the overall process. In particular the column "CO_2 molar fraction" indicates the molar fraction of CO_2 if all the emissions were grouped in one stream. As expected, for all the three fuel gas cases, the lowest value of CO_2 emission is obtained when membrane separation is used. In particular it appears that there is no actual difference between the use of only condensation and burner coupled with condensation.

Table 2. Main results concerning the CO_2 captured and released in atmosphere for the simulation of the calcium looping process only.

Type of fuel	CO_2 stream	Molar fraction	CO_2 Flowrate/ CO_2 Flowrate in the fuel	CO_2 Flowrate/ MCFC Power Output ($kmol\_CO_2\ MW^{-1}$)
Blast furnace	CO_2 released	0.060	0.288	6.635
	CO_2 captured	1.000	1.208	27.830
Gasified waste	CO_2 released	0.034	0.183	1.680
	CO_2 captured	1.000	0.979	8.980
Syngas	CO_2 released	0.050	0.344	2.628
	CO_2 captured	1.000	1.785	13.618

Table 3. Simulation results for the three studied types of fuel gas.

Type of Fuel	Downstream separation	CO_2 Molar fraction	Flowrate/ CO_2 Flowrate in the fuel	Flowrate/ MCFC Power Output (kmol MW^{-1})
Blast furnace exhaust	With Condensation Only	0.351	1.767	421
	Burner + Condensation	0.444	1.985	27.446
	CO_2 Selective Membrane	0.950	1.590	21.979
Gasified waste	With Condensation Only	0.647	3.166	24.872
	Burner + Condensation	0.909	3.554	27.916
	CO_2 Selective Membrane	0.950	2.850	22.385
Syngas	With Condensation Only	0.687	3.510	28.048
	Burner + Condensation	0.941	3.886	31.052
	CO_2 Selective Membrane	0.950	3.159	25.243

Table 4. Simulation results for the three studied types of gas concerning the captured CO_2.

Type of Fuel	Downstream Separation	CO_2 Molar Fraction	Flowrate/ CO_2 Flowrate in Fuel	Flowrate / MCFC Power Output (Kmol MWh^{-1})
Blast furnace exhaust	With Condensation Only	0.005	0.202	2.791
	Burner + Condensation	0.005	0.202	2.791
	CO_2 Selective Membrane	0.0009	0.379	5.233
Gasified waste	With Condensation Only	0.005	0.360	2.826
	Burner + Condensation	0.005	0.360	2.826
	CO_2 Selective Membrane	0.0011	0.676	5.313
Syngas	With Condensation Only	0.005	0.355	2.834
	Burner + Condensation	0.005	0.355	2.834
	CO_2 Selective Membrane	0.0010	0.706	5.639

Finally in table 5 the global efficiency of the integrated solutions in terms of electrical energy and CO_2 capture are reported for the three type of analysed fuels. For all the gases the efficiencies are similar and in particular the segregation values reached are significantly high.

Compared to the calcium looping only solution, it is clear that the molar fraction of CO_2 emitted into the atmosphere is much lower, allowing larger savings on CO_2 emissions tax.

On the basis of this analysis it is possible to say that the burner coupled with a condensation step and the membrane separation are the best scenario; the difference between the two would require a further economic analysis which is beyond the scope of this work.

Table 5. Electrical energy and CO_2 segregation global efficiency of the integrated solution.

Type of Fuel	Electrical energy efficiency	CO_2 segregation efficiency
Blast furnace exhaust	0.287	0.933
Gasified waste	0.286	0.922
Syngas	0.285	0.922

The benefits of a small scale model

An important aspect of a multi-scale approach is the possibility to rely on low level analysis to verify the reliability of larger scale processes. In particular the use of both a detailed kinetics model and a cell level model allows to verify the stability of each element of the MCFC stack in each point in the possible operating conditions.

In figure 4 the maps that describe the molar fraction of CO_2 on the cell plane at the anode and cathode side are presented. Relying on these type of maps can be useful to determine the best operating conditions. For example, they can help determine whether it is necessary to increase the surface and therefore increase the capture rate or decrease the surface because the cell is working in very unstable conditions (in this case the analysis of the H_2 or O_2 maps is also necessary).

In figure 5 the maps that represent the temperature of the solid structure (a), the cathode gas (b) and the anode gas (c) are presented. The use of these maps is important to verify that there are no hotspots that can compromise the cell performance and stability in any point of the cell.

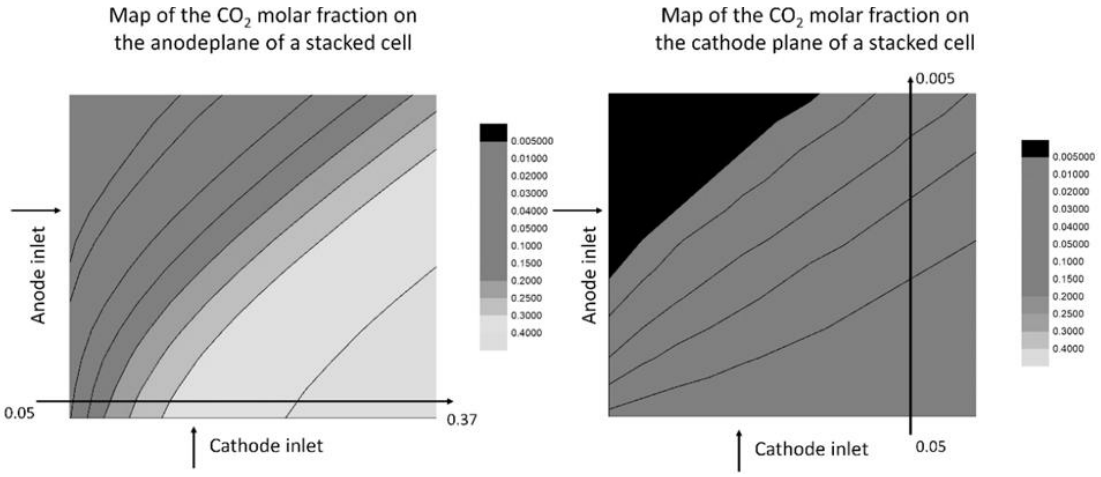

Fig. 4. Example of maps of the CO_2 molar fraction on a cell plane at the anode and cathode side of the gas deriving from the treatment of the blast furnace exhaust with the cell operating at operating at 1000 A m^{-2}

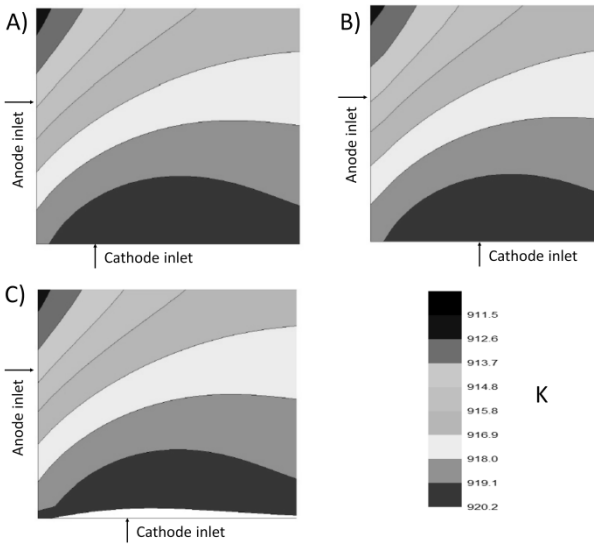

Fig. 5. Map of the temperature on a cell plane of the solid structure (A), the anode (B) and the cathode (C) gas of a cell operating at 1000 A m^{-2}.

CONCLUSION

The aim of this work is to show the benefits that the coupling of plant simulation and small scale models can bring to the design of plants and the study of particular configurations. In the frame of this work, the authors analysed the integration of the calcium-looping technology coupled with MCFCs for the capture and sequestration of CO_2 and the exploitation of a series of different sources of poor fuel gases.

The availability of a small scale model allows the identification of critical operating conditions (of both local temperature and composition) that can decrease the performance and that cannot be easily identified with the use of only large scale model that are mainly used for plant design and simulations.

A further feasibility analysis will be carried out taking into account the detailed plant battery limits and economical considerations in order to evaluate the benefit of the proposed system integration as a function of specific applications.

Symbols

ΔE	cell reversible potential, V
ΔH_{reaz}	enthalpy of reaction, kJ mol^{-1}
J	cell current density, A m^{-2}
p	pressure, atm
p_i	partial pressure of the i-th gas, atm
P_y	empirical parameters, variable
R_{TOT}	total cell resistance, Ω m^{-2}
T	temperature, K
ΔV	cell measurable voltage, V
y_i	molar fraction of the i-th gas
ϑ	empirical parameter

REFERENCES

1. J.F.D. Tapia, J.-Y. Lee, R.E.H. Ooi, D.C.Y. Foo, R.R. Tan, *Sustain. Prod. Consum.*, **13**, 1 (2018).
2. E. Audasso, L. Barelli, G. Bidini, B. Bosio, G. Discepoli, *J. Power Sources.*, **348**, 188 (2017).
3. Impedance Spectroscopy Theory, Experiment, and Applications, ed. E. Barsoukov, J. Ross Macdonald, John Wiley & Sons, New Jersey, Second Edition, 2005
4. G. Raikova, M. P. Carpanese, Z. Stoynov, D. Vladivkova, M. Viviani, A. Barbucci, Bulg. Chem. Commun., 41, 199 (2009).
5. Ivers-Tiffée, E., Weber, A. Journal of the Ceramic Society of Japan, 125 (4), 193 (2017).
6. Viviani, M., Canu, G., Carpanese, M.P., Barbucci, A., Sanson, A., Mercadelli, E., Nicolella, C., Vladikova, D., Stoynov, Z., Chesnaud, A., Thorel, A., Ilhan, Z., Ansar, S.-A., Energy Procedia, 28, 182 (2012).
7. Vladikova, D., Stoynov, Z., Chesnaud, A., Thorel, A., Viviani, M., Barbucci, A., Raikova, G., Carpanese, P., Krapchanska, M., Mladenova, E., International Journal of Hydrogen Energy, 39 (36), 21561 (2014).
8. Carpanese, M.P., Barbucci, A., Canu, G., Viviani, M., Solid State Ionics, 269, 80 (2015).
9. Giuliano, A., Carpanese, M.P., Panizza, M., Cerisola, G., Clematis, D., Barbucci, A., Electrochimica Acta, 240, 258 (2017).
10. S. Presto, A. Barbucci, M. P. Carpanese, M. Viviani, R. Marazza, J. Appl. Electrochem., 39 2257 (2009).
11. L. Mastropasqua, M. Spinelli, A. Paganoni, S. Campanari, *Energy Procedia*, **126**, 453 (2017).
12. L. Duan, S. Sun, L. Yue, W. Qu, Y. Yang, *Energy*, **87**, 490 (2015).
13. L. Duan, L. Yue, T. Feng, H. Lu, J. Bian, Energy, **109**, 737 (2016).
14. D. Frattini, G. Accardo, A. Moreno, S.P. Yoon, J.H. Han, S.W. Nam, *J. Power Sources*, **352**, 90 (2017).
15. G. Accardo, D. Frattini, A. Moreno, S.P. Yoon, J.H. Han, S.W. Nam, *J. Power Sources*, **338**, 74(2017) 74–81. doi:10.1016/J.JPOWSOUR.2016.11.029.
16. G. Accardo, D. Frattini, S.P. Yoon, H.C. Ham, S.W. Nam, *J. Power Sources*, **370**, 52 (2017).
17. D. Frattini, G. Accardo, A. Moreno, S.P. Yoon, J.H. Han, S.W. Nam, *J. Ind. Eng. Chem.*, **56**, 285 (2017).
18. J.M. Hernandez, D.-H. Lim, H.V.P. Nguyen, S.-P. Yoon, J. Han, S.W. Nam, C.W. Yoon, S.-K. Kim, H.C. Ham, *Int. J. Hydrogen Energy*, **39**, 12251 (2014).
19. H.V.P. Nguyen, M.R. Othman, D. Seo, S.P. Yoon, H.C. Ham, S.W. Nam, J. Han, J. Kim, *Int. J. Hydrogen Energy*, **39**, 12285 (2014).
20. H.V.P. Nguyen, S.A. Song, D. Seo, D.-N. Park, H.C. Ham, I.-H. Oh, S.P. Yoon, J. Han, S.W. Nam, J. Kim, *Mater. Chem. Phys.*, **136**, 910 (2012).
21. A. Sabattini, E. Bergaglio, *J. Power Sources*, **131**, 237 (2004).
22. H.V.P. Nguyen, S.A. Song, D. Seo, J. Han, S.P. Yoon, H.C. Ham, S.W. Nam, *J. Power Sources*, **230**, 282 (2013).
23. N. Di Giulio, E. Audasso, B. Bosio, J. Han, S.W. Nam, S. McPhail, A. Moreno, in: EFC 2013 (Proc. 5th Eur. Fuel Cell Piero Lunghi Conf.), Napoli, 2013.

24. E. Audasso, S. Nam, E. Arato, B. Bosio, *J. Power Sources*, **352**, 216 (2017).
25. I. Rexed, C. Lagergren, G. Lindbergh, *Int. J. Hydrogen Energy*, **39**, 12242 (2014).
26. N. Di Giulio, E. Audasso, B. Bosio, J. Han, S.J. McPhail, *Int. J. Hydrogen Energy*, **40**, 6430 (2015).
27. C.-W. Lee, M. Lee, S.-P. Yoon, H.-C. Ham, S.H. Choi, J. Han, S.W. Nam, D.-Y. Yang, *J. Ind. Eng. Chem.*, **51**, 153 (2017).
28. J. Milewski, G. Discepoli, U. Desideri, *Int. J. Hydrogen Energy*, **39**, 11713 (2014).
29. K. Czelej, K. Cwieka, J.C. Colmenares, K.J. Kurzydlowski, *Appl. Catal. B Environ.*, **222**, 73 (2018).
30. R. Carapellucci, R. Saia, L. Giordano, *Energy Procedia*, **45**, 1155 (2014).
31. G. Falcucci, E. Jannelli, M. Minutillo, S. Ubertini, J. Han, S.P. Yoon, S.W. Nam, *Appl. Energy*, **97**, 734 (2012).
32. E. Audasso, B. Bosio, S. Nam, *Int. J. Hydrogen Energy*, **41**, 5571 (2016).
33. E. Arato, E. Audasso, L. Barelli, B. Bosio, G. Discepoli, *J. Power Sources*, **336**, 18 (2016).
34. M. Della Pietra, M. Santarelli, S. Stendardo, S. McPhail, J.P. Perez-Trujillo, F. Elizalde-Blancas, *J. CO_2 Util*, **25**, 14 (2018).
35. B. Bosio, D. Marra, E. Arato, *J. Power Sources*, **195**, 4826 (2010).
36. M. Erans, V. Manovic, E.J. Anthony, *Appl. Energy*, **180**, 722 (2016).
37. C.C. Dean, J. Blamey, N.H. Florin, M.J. Al-Jeboori, P.S. Fennell, *Chem. Eng. Res. Des.*, **89**, 836 (2011).
38. A. Perejón, L.M. Romeo, Y. Lara, P. Lisbona, A. Martínez, J.M. Valverde , *Appl. Energy*, **162**, 787 (2016).
39. A. Calabrò, P. Deiana, P. Fiorini, G. Girardi, S. Stendardo, *Energy*, **33**, 952 (2008).
40. D.M. Turi, M. Ho, M.C. Ferrari, P. Chiesa, D.E. Wiley, M.C. Romano, *Int. J. Greenh. Gas Control*, **61**, 168 (2017).
41. E. Lasseuguette, M. Carta, S. Brandani, M.-C. Ferrari, *Int. J. Greenh. Gas Control*, **50**, 93 (2016).
42. D. Chiaramonti, F. Martelli, R. Galante, M. Celli, D. Colognesi, M. Zoppi, 2005.
43. T.C. Merkel, H. Lin, X. Wei, R. Baker, Power plant post-combustion carbon dioxide capture: An opportunity for membranes, *J. Memb. Sci.*, **359**, 126 (2010).
44. P. Campbell, Master Thessi, University of Edimburgh, 2018.
45. . Watanabe, Y. Izaki, Y. Mugikura, H. Morita, M. Yoshikawa, M. Kawase, F. Yoshiba, K. Asano, *J. Power Sources*, **160**, 868 (2006).
46. Z. Wang, J. Yang, Z. Li, Y. Xiang, *Front. Energy Power Eng. China*, **3**, 369 (2003).

Горивни клетки със стопен карбонат в интегрирани системи с използванае на бедни горива и сегрегация на CO_2

Е. Аудасио[1], П. Кампбел[2], М. Дела Пиетра[3], М.К. Ферари[2], Б. Босио[1,*], Е. Арато[1]

[1]*Изследователски екип за процесно инженерство, Катедра "Гражданско и химическо инженерство", Университет на Генуа, Виа але Опера Пиа 15, 16145, Генуа, Италия*
[2]*Инженерно училище, Университет в Единбург, Робърт Стивънсън Роуд, EH9 3FB, Единбург, Великобритания*
[3]*Изследователски център ENEA, Виа Ангуиларессе 301, 00123, Рим, Италия*

Постъпила на 16 май 2018г.; приета на 2 август 2018г.

(Резюме)

Многомащабния подход за анализ на реагиращите системи е много важно средство за подобряване на разбирането за явленията, настъпили в различни мащаби на пространството и времето, както и за подпомагане на експерименталното и дизайнерското решение, специално при увеличение на мащаба. В предишни трудове авторите разработват кинетичен модел на клетката и на стека при горивни клетка със стопен карбонат, интегриращи всички тези мащаби на симулация в код, наречен СИМФК, който е успешно валидиран на базата на експериментални данни. Целта на настоящата работа е да покаже ползите, които могат да донесат свързването на симулацията на централи и на по-малко мащабни модели при изучаването на иновативни приложения и проектиране на определени конфигурации. В рамките на тази статия авторите анализират интеграцията на технологията Регенериращ цикъл на калции успоредно с горивни клетки със стопен карбонат за улавяне и отвеждане на въглероден двуокис, използвайки серия от различни източници на горивен газ за определяне на най-добрите варианти. По-специално, този труд прави анализ на употребата на бедни горива в горивните клетки, което не би било възможно без тяхното обогатяване. Наличието на малко-мащабни модели позволява да се идентифицират критичните работни условия (както на локалната температура, така и на състава), които понижават експлоатационните качества и които не могат да бъдат лесно идентифицирани с използването само на широкомащабен модел, използван обикновено при симулации и проектиране и на централи.

Bulgarian Chemical Communications, Volume 50 Special Issue D (pp. 108 – 113) 2018

Strategies to Optimise Organic Coating Systems

M. Delucchi *, A. Barbucci, G. Cerisola

Department of Civil, Chemical and Environmental Engineering, University of Genova, Via all'Opera Pia 15, 16145 Genoa, Italy

Received July 30, 2018 Revised September 7, 2018

Organic coatings are generally used for metal protection. The coating process involves several steps, such as chemical pretreatment, priming and application of top coats. Electrochemical Impedance Spectroscopy (EIS) is a valuable tool to tailor each step and/or optimise the protective performances of the complete coating system.

EIS on deformed, T-bent and damaged samples of complete systems can be used as a tool to obtain a selective evaluation of the best chemical pretreatment/primer combinations.

Impedance data analysis and equivalent circuit modeling on undamaged and artificially damaged coatings exposed to aggressive environments can be used to evaluate the influence of formulation parameters, as Pigment Volume Concentration (PVC), on the protective performance and the retention of the coating adhesion, respectively.

EIS data obtained for intact coatings can be analysed to evaluate water permeability coefficients, often influenced by the molecular weight and the chemical nature of the resins constituting the coatings.

Several case histories will be presented to gain further insight on the power of EIS for the optimisation of organic coating systems.

Key words: Electrochemical Impedance Spectroscopy, Organic coatings, Industrial applications

INTRODUCTION

Organic coatings are generally used for metal protection. The coating process involves several steps, which can be summarised as follows:

- metal cleaning
- chemical pre-treatment
- priming
- top coat application

Electrochemical Impedance Spectroscopy (EIS) [1, 2] is a valuable tool for the investigation of reactions and phenomena taking place in different materials [3-8]. It can be also applied to study "at different level" the coating systems. For example, it can be used to study i) the protective performances of the complete coating system, ii) the formulation of a coating layer or iii) the properties of the resin constituting the coating.

In the following some case histories are presented, to gain further insight on the power of EIS for practical industrial applications in the optimisation of organic coating systems.

CASE HISTORY 1: OPTIMISATION OF THE PRETREATMENT-PRIMER COMBINATION

The first case history is about the study of the performance of a complete coating system. Coil coatings are mainly used to coat metal strips which are post-fabricated to desired products later. Coil-coating products are generally tested in quality control laboratories using T-bend deformations. If the metal is pressed together, it gives a 0T bend. 1T, 2T bends, etc., can be obtained with one, two or more thicknesses of the metal around which the bend is made. In this way the flexibility and adhesion performance of the coating as well as its barrier properties are analysed when the precoated metal is produced.

The critical area of the coil-coated products corresponds to the top of the bends, where the presence of induced defects is often unavoidable. Fig. 1 reports the appearance of one bent system, where cracks in the top coat are readily visible.

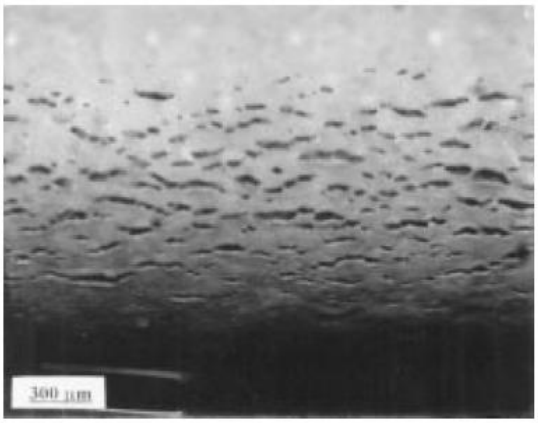

Fig. 1. Top of a bend of a coated sample

To whom all correspondence should be sent:
E-mail: marina.delucchi@unige.it

The aim of this study was to verify the reliability of innovative pretreatment/primer combinations for a coil coating product.

The materials under test were five experimental pretreatments, named from 1 to 5, in which the reference one, 1, was a nitro-cobalt chemical conversion, and three different primers, named A, B and C, among which the reference one, A, was a modified polyester-urethane resin containing non-toxic inhibitors, which were tested in all the possible combinations.

A three electrode electrochemical cell used for the analysis is given in Fig. 2, where the WE had the top of the bend in contact with the artificial sea water used as electrolyte.

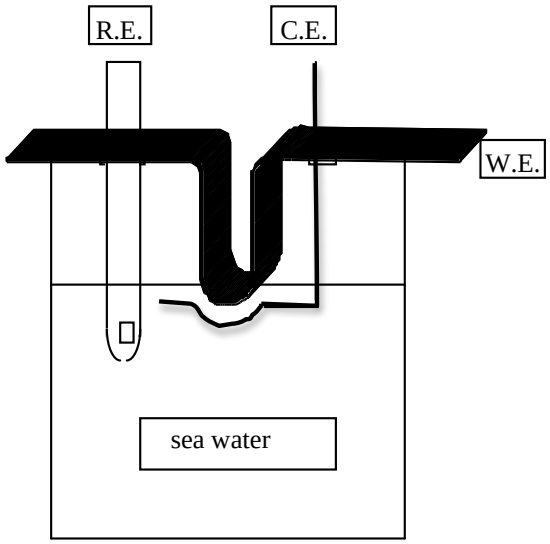

Fig. 2. Electrochemical cell for EIS measurements on bent samples

Generally, quantitative analysis of impedance data is carried out over a wide frequency range in order to determine the individual components of an equivalent electrical circuit model that represents the system under test. The high number of pretreatment/primer combinations and the preliminary nature of the analysis led us to consider an alternative way of data interpretation. Since the total impedance of the system at the low frequency can be considered as a rough estimation of the system condition, only the impedance modulus at 0.1 Hz was considered, and recorded as a function of time of exposure to the electrolyte for all the systems. But the different amounts of cracks in the top coat and/or in the primer, and hence the extension of the surface exposed to the aggressive solution at the initial time of the measurement, could greatly influence the initial impedance response, with impedance moduli ranging between 10^6 and 10^8 ohm cm^2 at 0,1 Hz.

Then, a relative variation of the impedance modulus was calculated and a degradation factor, η, was defined as:

$$h = 1 - \frac{Log|Z_0|_{0,1Hz} - Log|Z_t|_{0,1Hz}}{Log|Z_0|_{0,1Hz}} \quad (1)$$

where $|Z_0|_{0,1Hz}$ is the impedance at 0,1 Hz and time 0 and $|Z_t|_{0,1Hz}$ is the impedance at 0,1 Hz and time t. η ranges between 1, which is related to the starting condition or no degradation, and 0, which means total degradation of the coating.

Fig. 3 reports the general trend of η as a function of time for some of the specimens with a 4T bend, so low deformed samples, and a 2T bend, as an example.

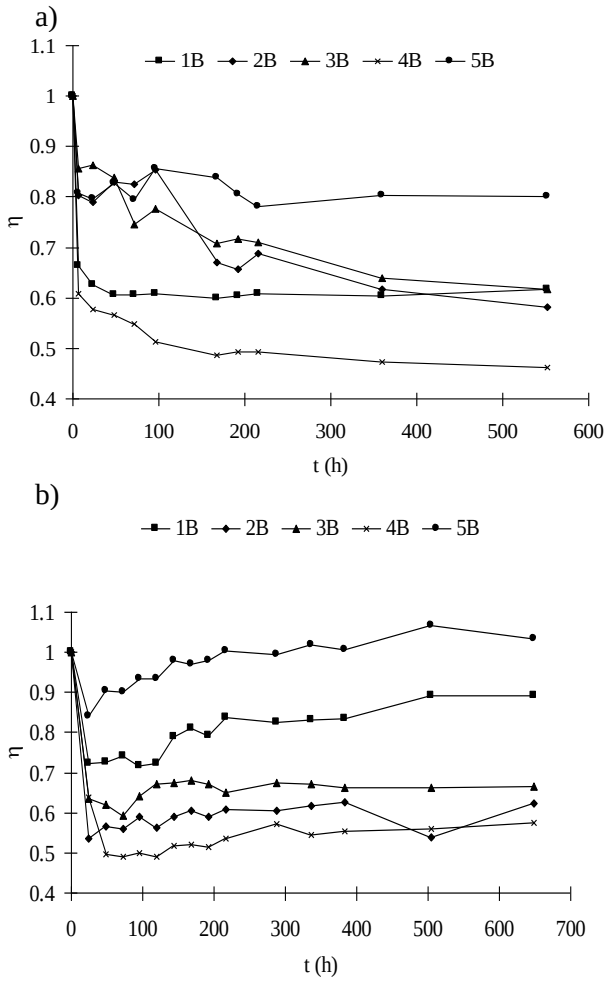

Fig. 3. Degradation factor, η, as a function of time for primer B coupled with all the preatreatments 1, 2, 3, 4 and 5 a) 4T bend; b) 2T bend

It is worth noticing that η constantly decreases for the low deformed samples, indicating a general progressive deterioration of the system; this result can be interpreted as a degradation of the top coat or top coat/primer layers and hence a development of more and larger pores which allow an increasing

water penetration through the first layers of the system. It means that the quite severe bend (4T) did not cause an immediate and complete top coat cracking and this prevents a clear discrimination between the different pretreatment/primer performances. On the contrary, the general defected surface of the 2T bend specimens caused a rapid water up-take through the top coat, allowing a reliable investigation on the inhibitive action of the primer or pretreatment.

The increasing values of η after an initial drop can be readily assumed as indexes of the primer/pretreatment inhibitive action.

Since a clear distinction between the system performance was not possible from these qualitative results, a quantitative attempt was made. Then, the variation of η ($\Delta\eta$) calculated as the difference between the value of η at the time of final measurement and the minimum value of η, generally obtained after an initial time of activation, was estimated. Table. 1 reports the values obtained for the fifteen 2T bend systems.

Table. 1. Δη values for the 2T bend samples

	Pretreatment				
Primer	1	2	3	4	5
A	0,16	0,07	0,11	0,07	0,11
B	0,17	0,09	0,03	0,08	0,19
C	0,13	0,04	0,07	0,03	0,20

The effectiveness of the system is related to the value of $\Delta\eta$: the higher the value, the better the performances. Considering that the combination 1A is the reference one, the performances of the different systems are evident: pretreatments 2, 3 and 4, regardless the primer, have lower inhibitive action than the reference system, while pretreatment 5, coupled with primer A and B, results very promising.

So, from this experience, a fast and reliable strategy to select an effective novel pretreatment/primer combination on a real complete coated system was found.

CASE HISTORY 2: OPTIMISATION OF THE PVC OF THE TOPCOAT

The second case history is about the study of the formulation of a coating layer.

Paint formulations are complex systems because they are a mixture of a binder, solvents, fillers, pigments and additives. An important parameter that takes into account the balance between most of these components is the Pigment Volume Concentration (PVC), defined as the volume percentage of solid particles in the system after film formation. Depending on this concentration, the properties of the coatings can vary considerably [9]. For example corrosion resistance and gloss decrease with PVC, on the other hand porosity and blistering increase with PVC.

In this work the need of obtaining the best compromise between protective and aesthetic properties of a fluorinated moisture curing coating has been the driving force behind the study of the loading of the system.

The materials were coatings from the same binder, with PVC equal to 0, 5, 7, 10 and 15%. The pigment was a powder of TiO_2, alumina and amorphous silica.

A series of Q-panels coated with 40 μm of the resins was subjected to impedance analysis to follow the water permeation process. The importance of assessing the water uptake into coatings has been acknowledged because water penetration is an initial step in the degradation process. The initial behaviour of the coatings can be simulated as that of an ideal capacitor, so the impedance results obtained in the frequency range between 1 kHz and 40 kHz were analysed using an R(RC) equivalent circuit and the capacitance was used to evaluate the increase of capacitance of the coating over time. In fact the large difference between the dielectric constant of water (about 80) and that of an organic coating (2-7) evidences if a coated substrate absorbs water. The whole procedure was automated to perform a large number of measurements in the first hours of the experiment.

The water permeabilities of top-coats with different pigment contents are reported in Fig. 4.

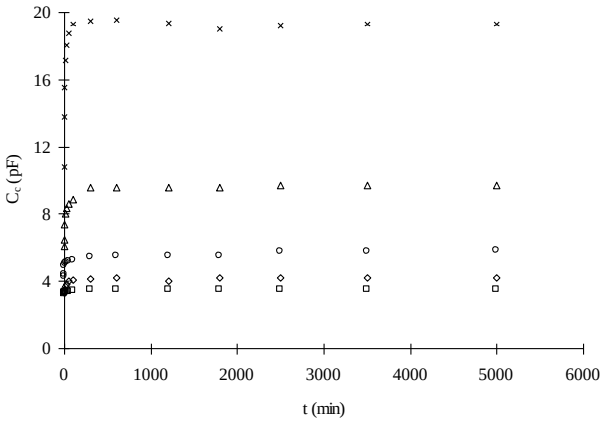

Fig. 4. Capacitance trends over time for the coatings with PVC: 0, □; 5, ◊; 7, ○; 10, Δ; 15, ×

The starting values of the curves, C_0, are determined by the composition of the coating and display an increase with the coating pigment

content. This is readily explained considering that the dielectric constant of the fluorinated binder is at least one order of magnitude lower than the dielectric constant of the pigment TiO_2.

A first stage of water up-take where the coating capacitance, C_c, increases is followed by a nearly asymptotic trend, which reaches the limiting value corresponding to the saturation of coating voids and porosity by water (C_s). Then dielectric constants were converted to water volume fractions through Brasher and Kingsbury equation [10-11], and the volume of water at saturation (V_s) vs the pigment content of these coatings was evaluated.

Table 2. Volume of water at saturation as a function of the PVC

	PVC				
	0	5	7	10	15
V_s	$3\ 10^{-4}$	$1{,}1\ 10^{-3}$	$1{,}3\ 10^{-3}$	$2\ 10^{-3}$	$2{,}5\ 10^{-3}$

The presence of higher pigment contents in the polymer matrix evidently emphasizes the formation of easy pathways for water uptake and/or the presence of voids in the coating structures where excess water can be retained if it is available.

Regarding the aesthetic properties, the gloss, an optical property which indicates how well a surface reflects light in a specular direction, was evaluated too. The maximum gloss is 100, and it decreased with increase of PVC.

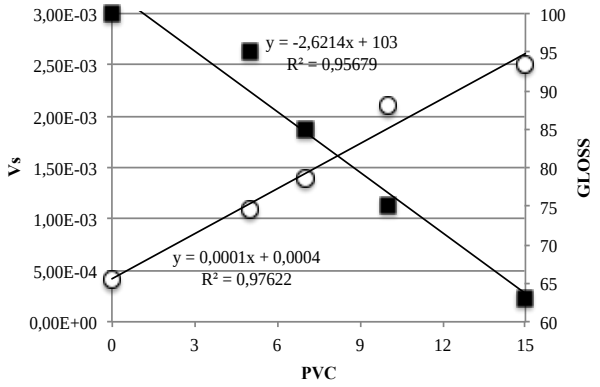

Fig. 5. Trend of volume of water at saturation and gloss as a funcion of PVC

Fig. 5 reports the properties of the coating depending on the coating loading. Linear relationships between the parameters and PVC is found.

Also from this experience, a reliable strategy to select the best formulation to obtain optimum compromise between aesthetic and barrier properties specific to our system was found.

CASE HISTORY 3: CHEMICAL STRUCTURE

The third experience refers to the study of the properties of the coating resulting from slightly different resins.

The polymer network of the binder greatly influence the properties of the coatings [12].

In this work the influence of the chemical nature of the coatings on their technological properties was investigated.

Different polyurethane (PU) coatings were prepared starting from –N=C=O terminated resins obtained by addition of perfluoropolyether (PFPE) macrodiols of molecular weight 500 or 1000 and cross-linked by exposure to environmental moisture, monocomponent, MC, formulations or by addition of stoichiometric amounts of PFPE macrodiols, bicomponent, BC, formulations. Two series of samples were prepared, characterised by the presence of hexamethylene diisocyanate (HDI) or isophorone diisocyanate (IPDI) polyisocyanurates in the formulation. The samples are generally named with four alphanumeric groups separated by a dash. The first two letters stand for the type of crosslinking: MC and BC. The first number stands for the molecular weight of the PFPE diol in the prepolymer: 5 = 500 or 10 = 1000. The second group of letters stands for the nature of the poly- isocyanurate constituting the coatings: IPDI or HDI. The last number defines the molecular weight of the PFPE used to crosslink the BC coatings.

DSC measurements and stress-strain measurements were carried out on self supported samples, while water permeability tests, through EIS measurements, were carried out on aluminium panels coated with 25–40 μm of the fluorinated polyurethane coatings.

Table 3 reports the technological parameters for the different coatings.

Calorimetric measurements showed that all the coatings are amorphous and most of them are biphasic due to the segregation of a soft PFPE rich phase and a hard, mainly urethane phase. When both well-resolved glass transition temperatures are present, the low Tg value, indicated as Tg F, and the high Tg value, indicated as Tg H, are attributed to the segregated PFPE moiety and to the urethane phase, respectively.

Regarding the mechanical properties of the coatings, they are rather diversified; in general, the use of IPDI leads to harder and brittle materials. In addition, the position of the thermal transition of the rigid phase of the polyurethane markedly affects the mechanical behaviour of the coatings.

The higher the Tg_H, higher than room T, the harder and more brittle the coatings. Also the electrochemical impedance measurements gave different spectra depending on the change of the structure of the resin (Fig. 6).

The analysis of the phase shift allows an effective differentiation of the behaviour of the different coatings. From an ideal capacitive behaviour, characteristic of only one coating, BC-5-IPDI-5, the phase shift θ decreases at low frequencies and a second time constant, attributed to the electrodic process, appears. On this basis the ranking of the tested materials was determined. Within each series, IPDI or HDI, monophasic structures are characterised by a fine fluorine dispersion, which guarantees better barrier properties; coatings having Tg higher than ambient temperature are characterised by glassy structures which inhibit water permeation. Comparing the IPDI and HDI series, coatings from IPDI behave better than the corresponding HDI compositions, probably due to the rubbery character of the HDI coatings, whose Tg_H values are lower than those of the IPDI coatings and lower than ambient temperature in many cases.

From this work, a reliable strategy to evaluate the wide diversification of structures, morphologies and resulting barrier properties of the final coatings was found.

Table 3. Glass transition temperatures and mechanical properties of the PFPE PU coatings

	TgF (°C)	TgH (°C)	Tensile Strength (MPa)	Rupture Strain (%)
BC-10-IPDI-10	-51	52	28,8	25-35
BC-10-IPDI-5	-30	80	31,2	3
BC-5-IPDI-5	10	88	21,3	2
MC-10-IPDI	-67	90	48,6	4
MC-5-IPDI	ND	ND	n.a.	n.a.
BC-10-HDI-10	-61	-22	n.a.	n.a.
BC-10-HDI-5	-60	-7	5,3	80-90
BC-5-HDI-5	-	-1	n.a.	n.a.
MC-10-HDI	-59	41	23,4	40-50
MC-5-HDI	-	50	35,6	4

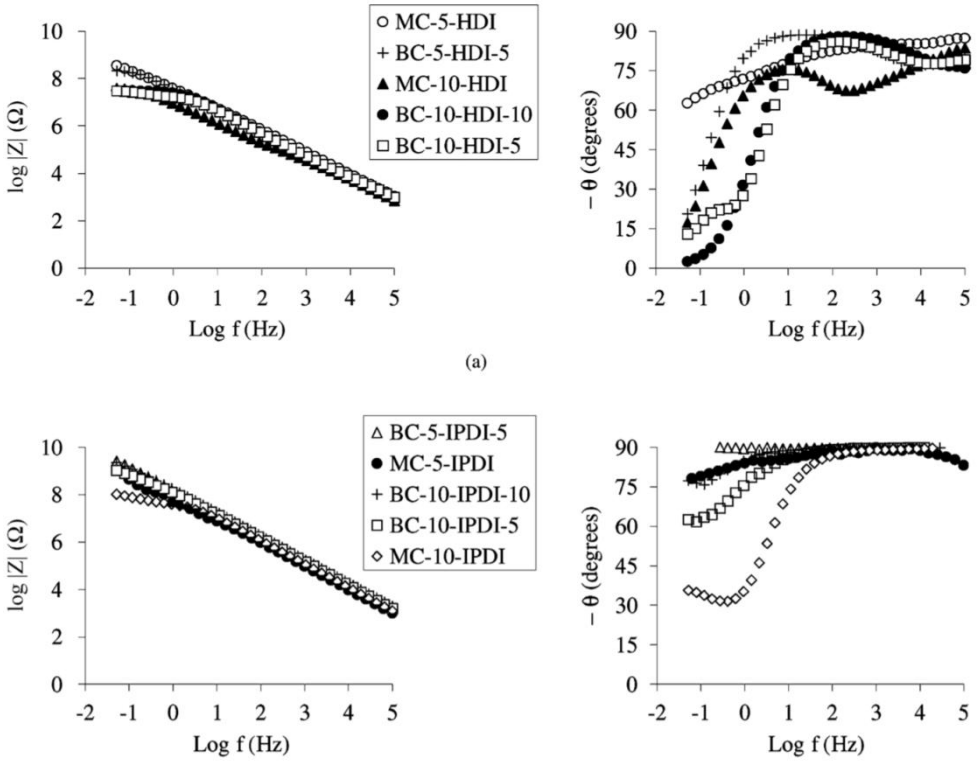

Fig. 6. EIS data for the IPDI and HDI coatings after 4 months of exposure to the electrolyte

CONCLUSIONS

Electrochemical impedance spectroscopy is a well-established technique for investigating the properties of painted metals. Some simple strategies to apply EIS in the industrial coating optimisation have been shown. Even if the industrial applications of EIS are not very common, in these cases the integration of chemico-physical and electrochemical investigations allowed the enhancement of specific properties of the coatings.

REFERENCES

1. Impedance Spectroscopy Theory, Experiment, and Applications, ed. E. Barsoukov, J. Ross Macdonald, John Wiley & Sons, New Jersey, Second Edition, 2005.
2. G. Raikova, M. P. Carpanese, Z. Stoynov, D. Vladivkova, M. Viviani, A. Barbucci, *Bulg. Chem. Commun*., **41**, 199 (2009).
3. Ivers-Tiffée, E., Weber, A. *Journal of the Ceramic Society of Japan*, **125 (4),** 193 (2017).
4. Viviani, M., Canu, G., Carpanese, M.P., Barbucci, A., Sanson, A., Mercadelli, E., Nicolella, C., Vladikova, D., Stoynov, Z., Chesnaud, A., Thorel, A., Ilhan, Z., Ansar, S.-A., *Energy Procedia*, **28**, 182 (2012).
5. Vladikova, D., Stoynov, Z., Chesnaud, A., Thorel, A., Viviani, M., Barbucci, A., Raikova, G., Carpanese, P., Krapchanska, M., Mladenova, E., *International Journal of Hydrogen Energy*, **39 (36),** 21561 (2014).
6. Carpanese, M.P., Barbucci, A., Canu, G., Viviani, M., *Solid State Ionics*, **269**, 80 (2015).
7. Giuliano, A., Carpanese, M.P., Panizza, M., Cerisola, G., Clematis, D., Barbucci, A., *Electrochimica Acta*, **240**, 258 (2017).
8. S. Presto, A. Barbucci, M. P. Carpanese, M. Viviani, R. Marazza, *J. Appl. Electrochem*., 39 2257 (2009).
9. C. Vosgien Lacombre, D. Trinh, G. Bouvet, X. Feaugas, S. Mallarino, S. Touzain, *Electrochim. Acta*, **234**, 7 (2017).
10. C. Vosgien Lacombre, G. Bouvet, D. Trinh, S. Mallarino, S. Touzain , *Electrochim. Acta*, **231**, 162 (2017).
11. A. S. Nguyen, N. Causse, M. Musiani, M. E. Orazem, N. Pébère, B. Tribollet, V. Vivier, *Prog. Org. Coat*. **112**, 93 (2017).
12. Sh. Montazeri, Z. Ranjbar, S. Rastegar, *Prog. Org. Coat*. **111**, 248 (2017).

Стратегии за оптимизиране на системи за органично покритие

М. Делучи*, А. Барбучи, Г. Герисола

Катедра "Гражданско, химическо и екологично инженерство", Университет на Генуа, Виа але Опера пиа15, 16145 Генуа, Италия

Постъпила на 30 юли 2018г.; приета на 7 септември 2018г.

(Резюме)

Органичните покрития обикновено се използват за защита на метал. Процесът на нанасяне на покритие включва няколко етапа, като предварителна химическа обработка, грундиране и нанасяне на горен слой. Електрохимичната импедансна спектроскопия (ЕИС) е ценен инструмент за проследяване на всяка стъпка и / или за оптимизиране на защитните качества на системата за нанасяне на покрития като цяло.

ЕИС върху деформирани, Т-огънати и повредени образци на завършени системи може да се използва като инструмент за придобиване на селективна оценка на най-добрите химически комбинации за предварително третиране / грундиране.

Анализът на импеданснитет данни чрез еквивалентни моделни схеми върху неповредени и изкуствено повредени покрития изложени на агресивни среди може да се използва за оценка на влиянието на параметрите на формулиране, като обемната концентрация на пигмент (ПВЦ), съответно, върху защитните качества и съхранение на адхезията на покритието.

Данните получени с помоща на ЕИС, за ненарушени покрития, могат да бъдат анализирани за определяне на коефициентите на водопропускливост, често повлияни от молекулното тегло и химическата природа на смолите, съставящи покритията.

Разгледани са последователно наколко случая, за да се получи по-задълбочен поглед върху ЕИС като мощен способ за оптимизиране на системите за нанасяне на органични покрития.

Bulgarian Chemical Communications, Volume 50 Special Issue D (pp. 114 – 122) 2018

Methanol Synthesis from Renewable Electrical Energy: A Feasibility Study

M. Rivarolo*, D. Bellotti, L. Magistri

Thermochemical Power Group, University of Genoa, 1 Via Montallegro Str., 16145 Genova Italy

Received June 07, 2018 Revised September 01, 2018

This paper aims to present a feasibility study of an innovative plant for methanol synthesis from carbon dioxide and hydrogen, produced by water electrolyser fed by renewable electrical energy. The analysis aims to examine a methanol production plant, based on 1MW of installed electrolyser, from both the management and economic standpoints: the 1MW plant size has been chosen to represent a modular plant for the power to fuel distributed generation, which may be powered by renewable energy.

The thermo-economic investigation is performed using two different approaches: a detailed design point analysis, carried out in order to identify the optimal component sizes and operating parameters followed by a time-dependent plant management optimization.

Both the studies are carried out with two simulation tools, named WTEMP (Web-based Thermo-Economic Modular Program) and W-ECoMP (Web-based Economic Poly-generative Modular Program), both developed by the Thermochemical Power Group at University of Genoa.

Key words: power to fuel, thermo-economic analysis, methanol production.

INTRODUCTION

According to recent evaluations, world energy demand is expected to increase significantly by 2050: despite fossil fuels will be still the predominant primary source, renewable energy sources (RES) contribution is expected to increase as well 1. At the same time, European Countries are investigating innovative systems in order to reduce CO_2 emissions developing new kind of fuels (i.e. biofuels), which have low carbon footprint for the energy production. On the other hand, the increasing RES penetration, in particular in case of not fully controllable sources as solar and wind, introduces new issues in terms of electrical system management and energy balance: in particular, the wide exploitation of not predictable and storable RES which have the priority in the energy market, has recently caused significant troubles to traditional power plants (i.e. combined cycles), forcing them to operate in strong off-design conditions at lower efficiencies, with numerous on/offs that affect negatively the plant lifetime and pollutant emissions.

The power-to-fuel (PtF) technologies seem to represent a good solution in this sense, allowing to absorb electrical energy (i.e. RES overproduction), converting and storing it into chemical form, for example for the production of biofuels.

According to recent evaluations, world energy demand is expected to increase significantly by 2050: despite fossil fuels will be still the predominant primary source, renewable energy sources (RES) contribution is expected to increase as well 1. At the same time, European Countries are investigating innovative systems in order to reduce CO_2 emissions developing new kind of fuels (i.e. biofuels), which have low carbon footprint for the energy production. On the other hand, the increasing RES penetration, in particular in case of not fully controllable sources as solar and wind, introduces new issues in terms of electrical system management and energy balance: in particular, the wide exploitation of not predictable and storable RES which have the priority in the energy market, has recently caused significant troubles to traditional power plants (i.e. combined cycles), forcing them to operate in strong off-design conditions at lower efficiencies, with numerous on/offs that affect negatively the plant lifetime and pollutant emissions. The power-to-fuel (PtF) technologies seem to represent a good solution in this sense, allowing to absorb electrical energy (i.e. RES overproduction), converting and storing it into chemical form, for example for the production of biofuels. Currently, on the industrial scale methanol is predominantly produced from natural gas by steam reforming or coal gasification:

To whom all correspondence should be sent:
E-mail: massimo.rivarolo@unige.it

however, with this method, about 0.6-1.5 tons of CO2 are emitted for each ton of produced methanol 45. This paper analyzes an alternative and sustainable method for methanol production: methanol is synthesized from a mixture of hydrogen and carbon dioxide. The hydrogen is produced by water electrolysis employing renewable electrical energy, while CO2 is sequestrated from the flue gas of a fossil power plant 67. The reaction is reported below:

$$CO_2 + 3H_2 \leftrightarrow CH_3OH + H_2O \quad (1)$$

The catalytic reaction takes place in ranges of temperature and pressure of 250 – 300 °C and 50 - 100 bar, respectively on CuO/ZnO/Al2O3 as catalyzer 89.

The study is performed using two different software, both developed by the authors' research group at University of Genoa, named respectively WTEMP (Web-based Thermo-Economic Modular Program) and W-ECoMP (Web-based Economic Cogeneration Modular Program).

WTEMP allows the thermos-economic analysis of a large number of energy systems (steam plants, gas turbines, combined cycles, power to fuel systems, biomass gasification, fuel cells, etc.). Some components of energy systems can be studied, previously, varying operative conditions by Impedance Spectrocopy [10,11], that is is a valuable tool for the investigation of reactions and phenomena taking place in different materials [12-177]. Operating characteristics and mass and energy balances of each component, in the on-design state, are calculated sequentially until the conditions (pressure, temperature, mass flow, etc.) at all interconnections converge on a stable value. After the thermodynamic calculation, the thermo-economic analysis is performed: at first each component purchase cost is defined through the use of cost or costing equations, therefore the internal thermo-economic and exergoeconomic analysis is carried out through the cost and exergy balances of each module 18.

W-ECoMP is a software which aims to the management strategy optimisation, minimizing a target function which is rapresentative of the annual costs of the plant; the optimization process is based on a genetic algorithm. Compared to WTEMP, W-ECoMP is a software that performs a time-dependent thermo-economic analysis, usually by dividing the operational time (usually a year) with sufficient number of representative periods (one hour or less depending on the particular application) 18.

The first step for the economic analysis is the calculation of the Purchased Equipment Cost (PEC), which is determined on the basis of the cost funtions of the different components of the plant under analysis. Starting from the PEC, it is possible to calculate the Total Capital Investment (TCI), taking into account different costs depending on the economic scenario where the plant is operating (i.e. construction and installation costs, the start-up cost, working capital, licensing, allowance etc). The final aim of the analysis is the calculation of the investment's profitability in order to choose the best solution, taking into account the initial investment and the associated risks related to the economic scenario and to the characteristic of the plant.

More details about W-ECoMP can be found in other authors' publications 192021.

THERMODYNAMIC ANALYSIS

Before performing the economic analysis, a thermodynamic analysis is necessary in order to define the operating parameters of the plant. The mass flows, the electrical consumption and the thermal energy input and output must be defined for each plant component in order to understand the mutual interaction between the different parts of the system. The PtF plant under investigation is composed by three main components:

- Carbon capture system (CCS): the CCS is connected to the coal-fired power plant and sequestrates, the CO_2 required by the methanol production process, from the flue gases;
- Water electrolyser: this device employs electrical energy to produce, by water electrolysis, the hydrogen for the methanol synthesis; furthermore a significant amount of oxygen (about 8 times the hydrogen, in mass terms) is co-produced by the process;
- Methanol reactor: the mixture of hydrogen and carbon dioxide is sent to the reactor for the methanol production, according to Equation (1).

The simplified scheme of the plant is reported in Figure.1.

In order to produce the so called "green methanol", only renewable generators are considered for the electrolyser energy supply. To this aim, different renewable energy sources, such as solar and wind, are taken into account. Moreover, different management options (only solar, only wind or a combination of both) are analyzed in order to define the best solution from both the economic (based on costs-revenues and on the total capital investment) and the operating point of view (based on the utilization factor and the exploitation rate of the RES).

The thermodynamic analysis is performed using the WTEMP software, described above. Several technical data are necessary for the characterization of each module of the plant to perform the thermodynamic analysis. All the data assumed for the simulations are reported below; in this analysis, most of the data are taken from literature or from real commercial data.

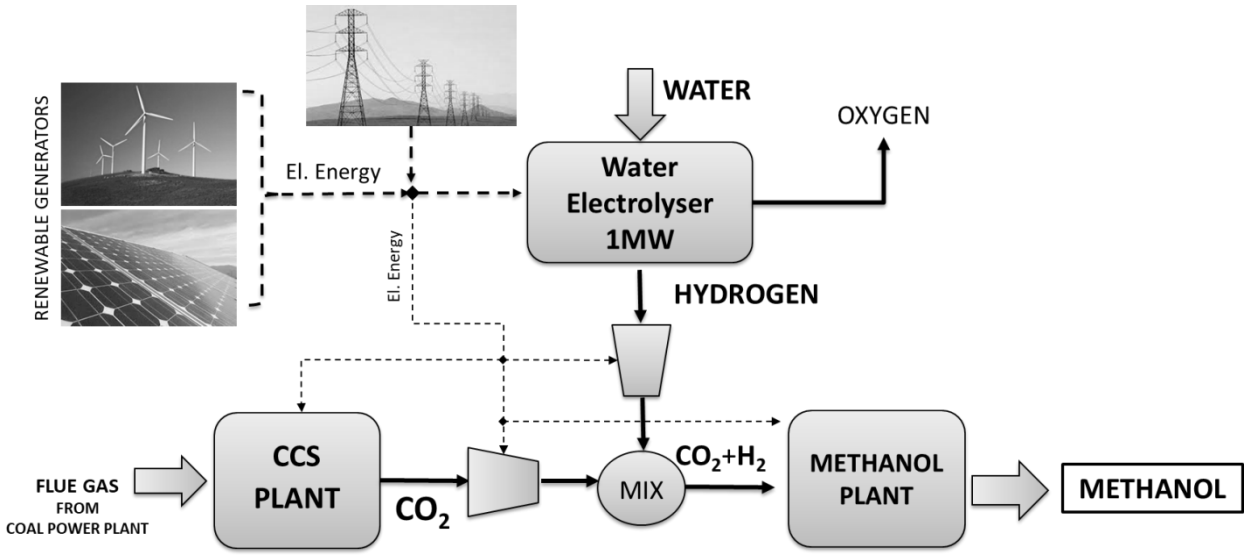

Fig. 1. Reference plant scheme

Table 1. Thermodynamic main assumption

AEC Electrolyser	
Electrical consumption	4.7 kWh/Nm^3 H_2
Pressure	30 bar
Temperature	80 °C
Efficiency	68%
Carbon Capture system	
Treatment kind	Amines MEA (30%)
Flue gases inlet T[°C] and p[bar]	40°C, 2bar
Thermal energy consumption per ton of CO_2	3 GJth/kgCO2
CO_2 outlet temperature[°C] pressure[bar]	40°C, 2 bar
CO_2 capture rate	90%
Methanol Reactor	
Working Pressure	80 bar
Temperature	240 °C
Recirculation factor of unreacted syngas	0.85
Conversion efficiency	96%
Molar H_2:CO_2 ratio	3:1

The reference plant size is based on 1MW of installed electrolyser: on the base of the parameters reported in Table 1, the electrolyser produces about 19kg/h of hydrogen and 151kg/h of oxygen (H_2:O_2 mass ratio is 8). Considering the stoichiometric methanol reaction, for 19kg/h of hydrogen, about 140kg/h of CO_2 are needed: the CCS system is sized in order to be able to produce that amount of CO_2, meaning that it is able to process about 824kg/h of flue gases, assuming a CO_2 average content equal to 17%.

The CO_2 exits the CCS section at 2bar; consequently it is pre-compressed up to 30bar before being mixed with the hydrogen. Then, hydrogen and carbon dioxide are mixed together and compressed to the reactor working pressure, equal to 80bar. In the table 2 below, the results of the thermodynamic analysis, in terms of mass flows, electrical energy consumption and thermal energy input and output, are summarized.

It is worth noting that the largest energy consuming component of the plant is the AEC (1MW installed), the energy demand of the other components (about 30 kWh in total) is just the 3% of the total demand and therefore it results considerably lower compared to the electrolyser demand.

Table 2. Thermodynamic simulation main results

AEC Electrolyser	
Power installed	1MW
Hydrogen outlet	19 kg/h
Oxygen outlet	152 kg/h
Water consumption	195 kg/h
CCS system	
Flue gas in	823 kg/h
wt% CO_2 in flue gas	17%
CO_2 out	140kg/h
Thermal energy consumption	117 kWh_{th}
Electrical energy consumption	7 kWhe
Methanol reactor	
Mixture inlet	159kg/h
Methanol outlet	97 kg/h
Thermal energy outlet	31kWh_{th} (based on the heat of reaction)
Compressors	
CO_2 compression (from 2 up to 30 bar)	9.8 kWh
H_2 + CO_2 compression (from30 up to 80 bar)	13 kWh

THERMO-ECONOMIC ANALYSIS

The thermo-economic analysis aims to study a reference methanol production plant, based on 1MW of installed electrolyser, from both the management and economic point of view. For simplicity, the 1MW plant size has been chosen to represent a modular plant for the PtF distributed generation, which may be powered by RES. In the following, the influence of the plant size on the economic feasibility will be presented. First, in order to analyze the production process of 100% green methanol, the direct coupling of different RES plants (wind, solar or a combination of the two), to the methanol plant is investigated.

Main assumptions

The RES under analysis are the solar energy (using PV panels), wind energy or a combination of both. In order to simulate the energy production from RES, it is necessary to extrapolate the solar insulation curve and the wind velocity curve from the database available for the area near to the installation site. In the Figure 2 average monthly solar irradiation is reported: each curve represents the trend in a typical day representative of the month. The magnitude of the curves changes during the year, following the seasons.

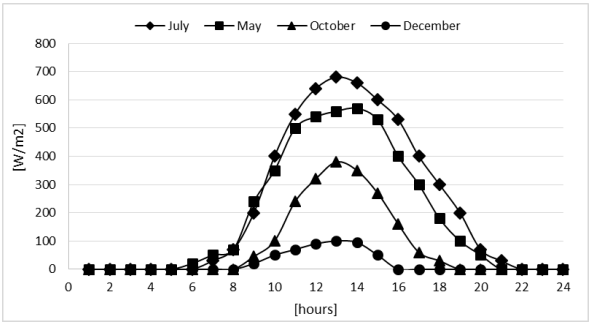

Fig. 2. Average monthly solar irradiation [22]

In Figure 3, the values of the wind velocity hour by hour are reported; in this case it is not possible to recognise a specific profile because the values are completly stochastich. It is just possible to identify an average trend season by season.

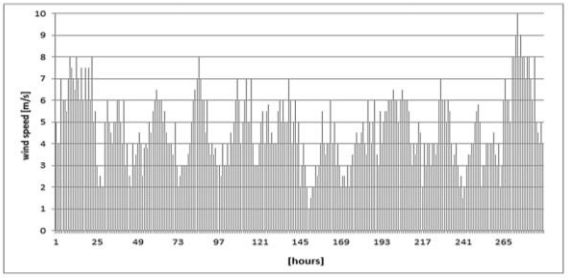

Fig. 3. Wind velocity profile [23]

To perform the analysis, the German economic scenario is chosen and the following economic assumptions are considered:

Methanol selling price is assumed to be 400 €/ton, that is the average market price between 2014 and 2015 in Europe, as reported in 24;

Oxygen selling price highly depends on its diffusion on the market, which is related to local conditions, applications, etc. In the case under analysis, oxygen price is assumed 100 €/ton, which represents the minimum selling price for industrial use of oxygen (rates are higher for medical use). It is worth noting that the purity of oxygen produced by electrolysers (>99.9%) is sufficient for industrial applications, therefore no further purification treatments are needed;

Electrical energy cost represents a term of primary importance to determine optimal system

configuration. The electrical energy to feed electrolysers is produced by renewable sources that are strongly variable hour by hour and it is not always available to feed the system at the nominal conditions. When the renewable energy is not available and it is assumed to operate at nominal conditions, the electrical energy is purchased from the grid. The average energy cost is assumed equal to 0.037€/kWh that is the market value for 5 MW maximum installed plant in Germany 25;

Electrical energy selling price: the possibility of selling the surplus (respect the methanol plants demand) energy produced by the renewable sources is also taken into account. The market price of renewable energy sold to the grid is assumed equal to 0.073 €/kWh, which is the incentivized price for RES producers in Germany (at 2014) 25;

Capital cost: In order to calculate the TCI is necessary define the PEC that is the sum of the capital cost of the each component of the plant (electrolyser, CCS system and methanol reactor). The capital costs depend on the size and operating parameters of the component, the cost functions used for this analysis are reported in Table 3 below.

Plant lifetime is assumed equal to 15 years to be conservative, considering the lifetime of the electrolysers, which is the most expensive plant component;

Methanol plant equivalent operating hours is assumed equal to 8640 hours per year, which represents a typical value for this kind of plants: in fact, due to the great inertia of chemical reactors, the methanol plant should operate at nominal conditions for the whole year, if possible:

Inflation is assumed equal to 0.4 %, which represents a typical value in Germany, Figure 4 [26].

Average income tax rate is assumed equal to 19%, which is a typical value in Germany 26.

Tab. 4 reports the main data assumed for the present thermo-economic analysis. All these data are inputs for the W-ECoMP software.

Table 3. Thermodynamic simulation main results

Plant component	Cost function	
Pressurized electrolyser	$C_{AEC} = 1.3 \cdot 10^6 \cdot P[kW]^{0.815}$	[€]
CCS plant (CO_2 separation)	$C_{CCS} = 75.45 \cdot 10^6 \left(\frac{M_{in}\left[\frac{kg}{h}\right]}{2.808 \cdot 10^6} \right)^{0.65}$	[€]
Methanol reactor	$C_{MeOH} = 14.2 \cdot 10^6 \left(\frac{M_{in}[kg/h]}{54000} \right)^{0.65}$	[€]
PV panels	$C_{PV} = 2000 \cdot P[kW]$	[€]
Wind generator	$C_{wind} = 1500 \cdot P[kW]$	[€]

Table 4. Economic data

Economic scenario parameters	
Economic data reference year	2015
Construction starting year	2015
Construction time	1 year
Plant lifetime	15 years
Depreciation time	10 years
Inflation rate	0.4%
Nominal escalation rates	2.5%
O&M factor	1.04
Average income tax rate	19%
Financing fraction (debts)	50%
Financing fraction (preferred stocks)	35%
Financing fraction (common equities)	15%
Annual cost rate (debts)	5%
Annual cost rate (preferred stocks)	5%
Annual cost rate (common equities)	5%
Discount rate	0.4%

Cases description

In this preliminary thermo-economic analysis, it is assumed to integrate the methanol plant with different RES (solar and wind). Considering the stochastic nature of RES, the renewable generators have been oversized in order to have an acceptable amount of energy supply. Three different plant configurations, based on the RES employed, are investigated keeping constant the size of the electrolyser (1 MW):

Case 1: 3MW of PV panels installed.

The PV panels are installed to generate the energy necessary to the hydrogen production by water electrolysis. When the renewable source is not available, the electrical energy is purchased from the grid in order to ensure the AEC

electrolyser to work at the nominal conditions. The system works at the rated condition imposed by the size of the electrolyser.

Case 2: 3MW of wind generator.

Wind turbines are installed to generate hydrogen by water electrolysis and to produce the required hydrogen, when the renewable source is not available the electricity is purchased by the national grid to help stabilize the hydrogen production. The system works at the rated condition imposed by the size of the electrolyser.

Case 3: 1.5MW of PV panels and 1.5MW of wind generator installed.

This case is similar to the previous configurations, but both PV field and wind farm are installed and interconnected to generate hydrogen by water electrolysis. The possibility to interconnect the two renewable sources is analyzed to increase the periods in which renewable energy is provided. Consequently, the percentage of green methanol (defined as the methanol produced employing only renewable energy) is increased. When renewable sources are not available the electricity is purchased from the national grid.

For each of the three Cases described above, two different energy options are taken into account:

A: The PtF is only fed by the renewable energy (production of "100%" green methanol)

B: The PtF is fed by the renewable energy, when available, and by grid energy in the other periods.

It is worth underling that this is a theoretical analysis that aims to investigate the possibility of coupling a renewable plant directly to the PtF plant from both the operating and economic point of view in order to identify any critical aspects that can be improved with further development.

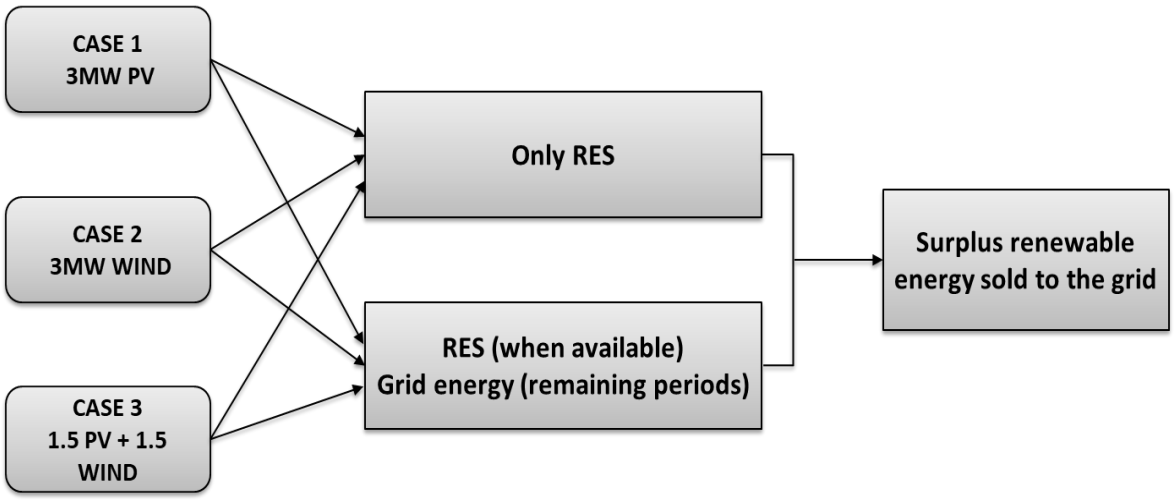

Fig. 4. Scheme of the different cases under analysis

MAIN RESULTS

In this thermo-economic analysis, the management option *A* for the three different plant configurations is investigated from an operating and economic point of view. It is assumed to feed the methanol plant employing only the renewable energy produced by 3MW renewable power plant that is represented by PV panels (case 1), wind generator (case 2), integration of both (case 3).

In Table 5 a comparison between the three cases from the operating point of view is reported: it is evident that the case 2A is the best solution because it presents the highest renewable energy production and the highest utilization factor as well. This entails a higher methanol production and therefore higher revenues as reported in Figure 6.

Figure 5 shows that the Case 2A results the best solution also from the economic point of view: although the system is not profitable due to the high costs value, it has the minimum difference between the cost and revenues due to the combined effect of higher revenues and lower TCI.

In the second part of the analysis, the management option B for three different plant configurations is investigated as well: it is assumed to feed the methanol plant employing, when available, the renewable energy produced by 3MW generators, represented by PV panels (case 1), wind generator (case 2) or integration of both (case 3). In the remaining periods, the electrical energy is purchased from the grid in order to keep the methanol plant at constant nominal conditions.

.

Table 5. Operating management comparison (case A)

		CASE-1A (3MW PV)	CASE-2A (3MW WIND)	CASE-3A WIND + PV
Total Energy production	[MWh]	4800	7004	5902
Equivalent hours	[h]	1600	2335	1203
RES energy to AEC	[MWh]	3026	5123	4699
AEC utilization factor	[%]	34	57	53
RES energy to the grid	[MWh]	1774	1881	1190
Methanol production	[ton]	295	494	458

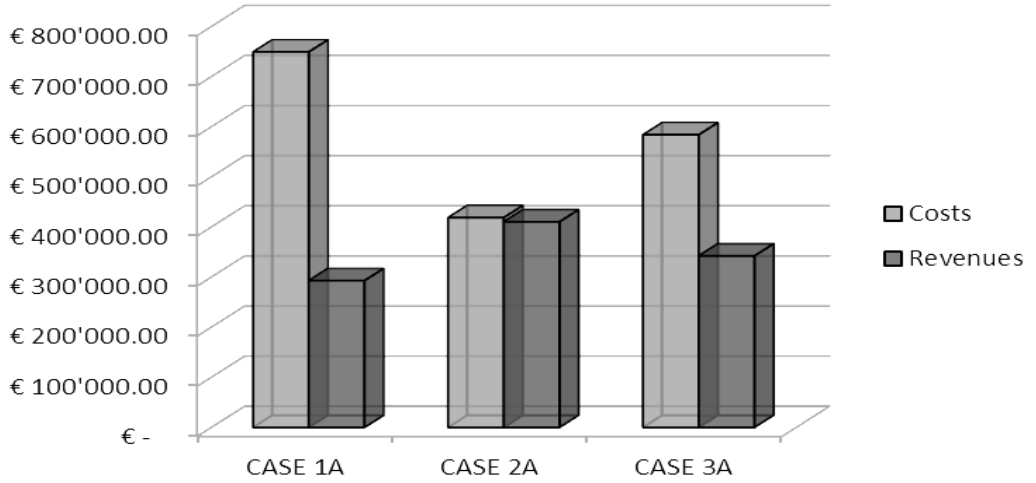

Fig. 5. Case comparison: costs and revenues

In Table 6 a comparison between the three cases from the operating point of view is reported: it is evident that the case 2B results again the best solution because of the highest amount of renewable energy utilized by the plant and consequently the lowest amount of purchased energy. Moreover, it presents also the highest amount of surplus renewable energy that can be sold to the grid. For these reasons, together with the lower TCI (due to the lower capital cost of the wind generator than the PV panels), the case 2B represents the best solution also from the economic point of view and the only one with a positive balance between costs and revenues, as shown in Figure 6.

Table 6. Operating management comparison (case B)

		CASE-1B (3MW PV)	CASE-2B (3MW WIND)	CASE-3B (1.5 PV + 1.5 WIND)
Tot. Energy production	[MWh]	4800	7004	5902
Equivalent hours	[h]	1600	2335	1967
Renewable energy to AEC	[MWh]	3026	5123	4699
AEC utilization factor	[%]	100	100	100
El. energy purchased from grid	[MWh]	5904	3807	4231
RES energy sold to the grid	[MWh]	1774	1881	1190
Methanol production	[ton]	866	866	866

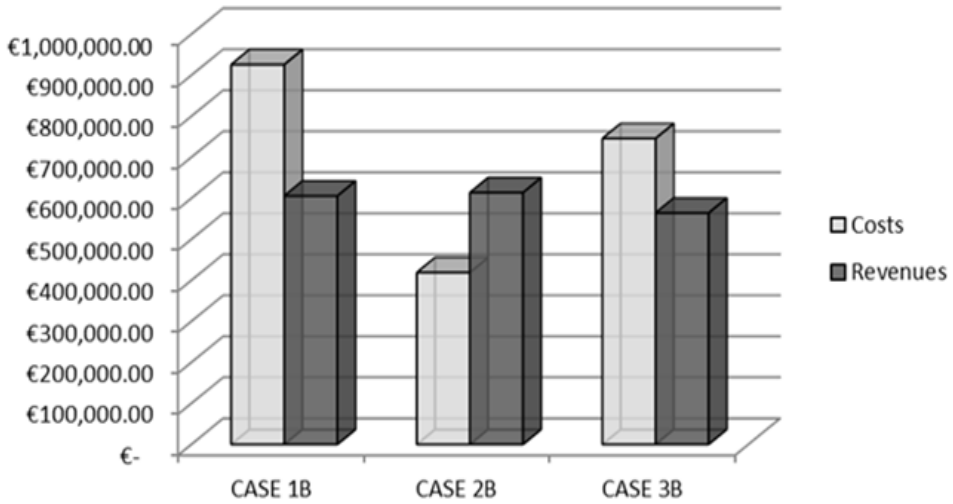

Fig.6. Costs and revenues comparison (case B)

CONCLUSION

In the paper, RES and methanol plant integration has been investigated. Three different plant configurations have been taken into account on the basis of the typology of RES coupled to the plant: in configuration 1 it was assumed to install 3MW of PV panels, in configuration 2 it was assumed to install 3MW of wind generators and, in configuration 3, the interaction between the two different energy sources was investigated: the 3MW of renewable power installed was distributed equally between PV panels (1.5MW) and wind generator (1.5MW).

Each configuration was analyzed considering two different energy options: (A) feeding the system with RES only; (B) powering the plant with RES, when possible, and purchasing the electrical energy from the grid in the remaining periods The following considerations can be drawn:

- Taking into account the energy option A, the system is forced to operate under discontinuous conditions: the utilization factor results significantly reduced; moreover this operating strategy would not be compatible with the methanol reactor.
- Taking into account the option B, the plant can operate continuously at nominal condition, the methanol production increase up to the 100% of the capacity plant; on the other side the electricity purchased increases the operating costs and the methanol produced is not "*100% green"*.
- The solar energy source presents a high rate of predictability that allows the system to operate in on-off modality with a regular profile; on the other hand, PV panels present a lower energy production compared to the wind generators.
- The best solution results to be the configuration 2B: since renewable energy production is higher, the green methanol produced results the highest as well as the amount of surplus energy sold to the grid. Moreover, wind generators capital cost are lower than the PV panels: thus, configuration 2B results the best one also from the economic standpoint.

Acknowledgments: *Authors gratefully acknowledge the financial support from the 'EU Framework Programme for Research and Innovation Horizon 2020' under the grant agreement No 637016 (MefCO$_2$).*

Nomenclature

AEC	Alkaline Electrolyser
CCS	Carbon Capture Sequestration
PEC	Purchased Equipment Cost
PtF	Power to fuel
RES	Renewable Energy Sources
TCI	Total Capital Investment
TPG	Thermochemical Power Group
WTEMP	Web-based Thermo-Economic Modular Program
W-ECoMP	Web-based Economic Cogeneration Modular Program

REFERENCES

1. Varone A., Ferrari M., Power to liquid and power to gas: An option for the German Energiewende, *Renewable and Sustainable Energy Reviews*, **45**, 207 (2015).
2. Liu H., Wang Z., Xiang S., Wang J., Wagnon S.W., Methanol-gasoline Dual-fuel Spark Ignition (DFSI) combustion with dual-injection for engine particle number (PN) reduction and fuel economy improvement, *Energy*, **89**, 1010 (2015).
3. Balki M.K., Sayin C., The effect of compression ratio on the performance, emissions and combustion of an SI (spark ignition) engine fueled with pure ethanol,

methanol and unleaded gasoline, *Energy*, **71**, 194 (2014).
4. Galindo Cifre P., Badr O., Renewable hydrogen utilisation for the production of methanol, *Energy Conversion and Management*, **48**, 519 (2007).
5. www.methanolfuels.org last access 10/10/2016
6. Pellegrini L., Soave G., Gamba S., Langè S., "Economic analysis of a combined energy–methanol production plant", *Applied Energy*, **88**, 4891 (2011).
7. Rivera-Tinoco R., Farran M., Bouallou C., Aupretre F., Valentin S., Millet P., Ngameni J.R., "Investigation of power-to-methanol processes coupling electrolytic hydrogen production and catalytic CO2 reduction", *International Journal of Hydrogen Energy*, **41**, 4546 (2016).
8. Jadhav S.G., Vaidya P.D., Bhanage B.M., Joshi J.B., Catalytic carbon dioxide hydrogenation to methanol: A review of recent studies, *Chemical engineering and Research and Design*, **92**, 2557 (2014).
9. Van-Dal ES, Bouallou C. Design and simulation of a methanol production plant from CO_2 hydrogenation. J *Clean Prod*, **57**, 38 (2013).
10. Impedance Spectroscopy Theory, Experiment, and Applications, ed. E. Barsoukov, J. Ross Macdonald, John Wiley & Sons, New Jersey, Second Edition, 2005.
11. G. Raikova, M. P. Carpanese, Z. Stoynov, D. Vladivkova, M. Viviani, A. Barbucci, *Bulg. Chem. Commun.*, **41**, 199 (2009).
12. Ivers-Tiffée, E., Weber, A. *Journal of the Ceramic Society of Japan*, **125 (4),** 193 (2017).
13. Viviani, M., Canu, G., Carpanese, M.P., Barbucci, A., Sanson, A., Mercadelli, E., Nicolella, C., Vladikova, D., Stoynov, Z., Chesnaud, A., Thorel, A., Ilhan, Z., Ansar, S.-A., *Energy Procedia*, **28**, 182 (2012).
14. Vladikova, D., Stoynov, Z., Chesnaud, A., Thorel, A., Viviani, M., Barbucci, A., Raikova, G., Carpanese, P., Krapchanska, M., Mladenova, E., *International Journal of Hydrogen Energy*, **39(36)**, 21561 (2014).
15. Carpanese, M.P., Barbucci, A., Canu, G., Viviani, M., *Solid State Ionics*, **269**, 80 (2015).
16. Giuliano, A., Carpanese, M.P., Panizza, M., Cerisola, G., Clematis, D., Barbucci, A., *Electrochimica Acta*, **240**, 258 (2017).
17. S. Presto, A. Barbucci, M. P. Carpanese, M. Viviani, R. Marazza, *J. Appl. Electrochem*., **39**, 2257 (2009).
18. www.tpg.unige.it, last access on 31/03/2018.
19. Rivarolo M., Bellotti D., Mendieta A., Massardo A.F., "Hydro-methane and methanol combined production from hydroelectricity and biomass: Thermo-economic analysis in Paraguay", *Energy Conversion and Management*, 79, 74 (2014).
20. Rivarolo M., Bogarin J., Magistri L., Massardo A.F., "Time-dependent optimization of a large hydrogen generation plant using "spilled" water at Itaipu 14 GW hydraulic plant", *International Journal of Hydrogen Energy*, **37**, 5434 (2012).
21. Bellotti D., Rivarolo M., Magistri L., Massardo A.F., "Thermo-economic comparison of hydrogen and hydro-methane produced from hydroelectric energy for land transportation", *International Journal of Hydrogen Energy*, **40**, 2433 (2015).
22. www.wettergefahren.de, last access on 31/03/2016.
23. www.dwd.de. last access on 31/03/2016
24. www.methanex.com last access on 31/03/2016.
25. http://scenarieconomici.it/prezzi-2013-nei-28-paesi-europei-del-gas-e-dellenergia-elettrica-italia-e-germania
26. www.tradingeconomics.com, last access on 31/05/2016.

Синтез на метанол от възобновяема електрическа енергия: Предпроектно проучване

М. Ривароло *, Д. Белоти, Л. Магистри

Група по термомеханика, Университет на Генуа, ул. Виа Монтенегро 1, 16145 Генуа, Италия

Постъпила на 07 юни 2018г.; приета на 01 септември 2018г.

(Резюме)

Тази статия представя предпроктно проучване на потенциала за осъществимост на инновативна инсталация за синтез на метанол от въглероден двуокисид и водород, произведен от електролизьор чрез възобновяема електрическа енергия. Анализът има за цел да представи инсталация за производство на метанол, базирана на инсталиран електролизьор с мощност от 1MB, както от гледна точка на управление, така и от икономическа гледна точка: мощността на инсталацията от 1MB е подбрана так, че да представлява модулна инсталация за разпределение на енергия произведена от възобновяеми енергиини източници.

Термо-икономическото изследване е осъществено като се прилагат два различни подхода: подробен анализ на проектните точки, осъществен с цел да се идентифицират оптималните размери на компонентите и оперативните параметри, последвани от оптимизация на управлението на инсталацията по време. И двете проучвания са осъществени с две методики на симулация, наречени ВТЕМП (уеб-базирана термо-икономична модулна програма) и В-ЕкоМП (уеб-базирана икономична поли-генеративна модулна програма) разработени от групата по термомеханика към Университета в Генуа.

Bulgarian Chemical Communications, Volume 50 Special Issue D (pp. 123 – 130) 2018

Rotating Fourier Transform - Engine for Non-Stationary Impedance Spectroscopy

Z. Stoynov †

Acad. E. Budevski Institute of Electrochemistry and Energy Systems- Bulgarian Academy of Sciences, 10 Acad. G. Bonchev Str., Sofia1113, Bulgaria

Received August 8, 2018 Revised August 18, 2018

Explanatory Notes: In the last year of his unwearied active scientific life Zdravko Stoynov was focused on intensive theoretical and experimental activities for effective illustration of his powerful advanced mathematical tool Rotating Fourier Transform (RFT). He would describe it as a "powerful engine for non-stationary impedance spectroscopy which opens up the exploration of the low and infra-low frequencies where many important and interesting phenomena, still hidden, can be measured precisely." He was expecting the development of a new "4th Generation" marketable impedance analyzers, applying RFT and MRFT (Multiple RFT) in the near future. In order to accelerate the coming of this "near future" and be able to see it, he was working both on the mathematical tool and on the experimental verification.

We are presenting his last manuscript, as written by him, expecting, that there will be an interest in his work on RFTs and support of his idea for the 4th Generation of impedance analyzers to fruition. We are open to collaboration for the continuation of Zdravko Stoynov's work.

Daria Vladikova,

Electrochemical Methods Department, Acad. E. Budevski Institute of Electrochemistry and Energy Systems – BAS

The conventional Impedance Spectroscopy is based on the original Fourier Transform (FT), which is the best estimator of periodic signals in stationary conditions. Many practical applications however require impedance measurements of typically non-stationary objects. This paper presents an advancement of the classical Fourier Transform which provides for precise measurements of sinusoidal signals in presence of non-stationary noise. The new mathematical tool was called Rotating Fourier Transform (RFT). Its architecture contains multiple integrals converting the time-domain phenomenon into its frequency domain complex image. The classical Fourier Transform is used as a kernel of the multiple integrals. The new transform filtrates orthogonally the derivatives of the drifting potential which is in this case an additive aperiodic noise. The paper reports the first practical application of the new mathematical instrument in a real laboratory experiment.

More complex is the case of measurements of impedance, which is changing with the time. In this case the changes can be defined as a multiplicative aperiodic noise. The derived analytical expressions are showing that every simple element which is changing with the time, produces methodical errors increasing with the frequency decrease. Those errors are changing the original structure of the model producing an artificial substructure, which is a product of the applied mathematical tool - the FT. When applied transform is the RFT, the artificial structure is eliminated. It was proven that the RFT filtrates orthogonally the first derivative of this noise and provides for the estimation of the proper Instantaneous Impedance. The paper presents also the first practical application of the new mathematical tool for measurement of battery impedance.

Key words: Non-stationary Impedance Spectroscopy, Fourier Transform, Rotating Fourier Transform, Instantaneous Impedance, Battery State of Health.

INTRODUCTION

The Fourier Transform [1] is the kernel of the electrochemical impedance spectroscopy (EIS) - one of the most powerful methods, widely used in all fields of the electrochemical research. The EIS is based on the Transfer Function analysis developed in technical cybernetics. It is proven theoretically that under the conditions of sufficiently large frequency range, the Transfer Function is a full description of the dynamic properties of a linear system [2, 3].

Electrochemical systems are however intrinsically non-linear. In order to overcome this problem, EIS follows the theory of Friedholm - Volterra, in accordance to which the nonlinear system is measured at selected different working points of the non-linear voltage-current characteristic of the object [4]. In electrochemistry, the working point is stabilized galvanostatically (or potentiostatically) and perturbed additionally by small sinusoidal signal of a given frequency.

To whom all correspondence should be sent:
E-mail: d.vladikova@bas.bg

The response signal measured at the output of the object - voltage (or current) is also sinusoidal, partially deformed by the object's non-linearity. This signal is periodic and contains the basic frequency and a sum of higher harmonics. When the perturbing signal is small enough the main frequency dominates the response and can be separated successfully. This operation is performed by the applied Fourier Transform. Thus the FT is used for coherent (iso-frequency) detection of the linear part of the response produced by the non-linear object. In addition, it is proven theoretically, that the Fourier Transform is the best estimator of the sinusoidal signal in the presence of Gaussian noise [3].

THEORY

Aperiodic noise and Fourier Transform errors

The Fourier Transform is efficient and best estimator (detector) of stationary periodic signal in the presence of noise. However when the signal is non-stationary or when the noise contains aperiodic component, the FT is not efficient. The analysis of the resulting errors is principally interesting and necessary for the evaluation of the acceptable low frequency limit for the application of the 4-dimensional approach.

By definition, the impedance is the ratio between the voltage and current, defined in the complex frequency space:

$$Z(\mathrm{i}\omega) = Z'(\omega) + \mathrm{i}\,Z''(\omega) = \{a_u(\omega) + \mathrm{i}b_u(\omega)\}.\{a_I\omega + \mathrm{i}b_I(\omega)\}^{-1}, \quad (1)$$

where Z' and Z'' are the real and the imaginary impedance components, a_u, b_u, a_I and b_I are the real and the imaginary components of the object's voltage and current correspondingly. The voltage and the current are measured by the instrument as functions of the time and the acquired data are converted into the frequency space by the FT:

$$a_u(\omega) + \mathrm{i}b_u(\omega) = \boldsymbol{FT}\{u(t)\}, \quad (2a)$$

$$a_I(\omega) + \mathrm{i}b_I(\omega) = \boldsymbol{FT}\{\mathrm{i}(t)\}, \quad (2b)$$

where $\boldsymbol{FT}$ is a symbolic notation for Fourier Transform operator. In accordance with the classical FT definition [1, 2] the coefficients a and b are calculated by the Euler equations:

$$a = w\int_0^{NT} x(t)\,sin(\omega t)dt, \quad (3a)$$

$$b = w\int_0^{NT} x(t)\,cos(\omega t)dt, \quad (3b)$$

where w is the weighting normalizing factor, N is the number of periods T of integration and $x(t)$ is the input function (measured voltage or current). In order to keep the ortho-normality of

the Fourier spectra, the weighting coefficient should have the value $w = 2\,(NT)^{-1}$.

Performing these operations the instrument is changing the selected frequency step by step, under given program. The full programmed range of frequencies is covered and the produced set of data forms a linearized (quasi-linear) impedance function, characterizing the object dynamics in the vicinity of the selected working point. In order to enlarge the observation of the object, the same set of measurements should be performed at others working points. It is worth to state here, that the available frequency range is never enough wide to observe the entire variety of processes taking place in the electrochemical objects. Thus the EIS can give only partial and local description of the object dynamics.

As a matter of fact the impedance analyzer performs the FT over both voltage and current signals. Assuming galvanostatic mode and perfect operation of the galvanostat, the full calculation at a given frequency ω is:

$$Z(i\omega) = [FT\{U_{DC} + u(t) + n(t)\}].[FT\{I_{DC} + I_{AC}(t)\}]^{-1}, \quad (4)$$

where $Z(\mathrm{i}\omega)$ is the measured impedance, t is the time, U_{DC} and I_{DC} are constant values characterizing the selected working point, I_{AC} is the perturbating small galvanostatic sinusoidal current, $u(t)$ is the object response and $n(t)$ is a noise, which could be present. This noise can contain components of different origin, nature and structure. In the general case

$$n(t) = n_{uobj} + n_{k\omega} + n_{ss} + n_{instr}, \quad (5)$$

where n_{uobj} is the noise produced by the object voltage, $n_{k\omega}$ is the cumulative noise of the frequency harmonics produced by the object's non-linearity, n_{ss} is a typical statistically sufficient noise and n_{instr} is a noise related to the power supply frequency and to other instrumental imperfections. As far as the FT is a linear operator [2], the components of the errors caused by the different noise components in Eq. 5 can be studied separately.

The errors produced by the statistical noise are very small – the FT is filtering this kind of noise very efficiently. The errors produced by $n_{k\omega}$ depend on the relative nonlinearity - for small

signal perturbation those errors are also small. They are separated by FT very efficiently and some instruments are evaluating those errors in a range of higher harmonics. The instrumental errors depend to a large degree on the construction of the instrument and on its environment. Their evaluation however is out of the scope of this paper.

The target of this investigation is the study of the errors, produced by the object's voltage. In the cases when this voltage is constant (the object is stationary) the Fourier Transform is filtering this constant orthogonally (unconditionally) and the precision of this operation depends only on the limited precision of the calculations. The application of the ABC (Automatic Bias Correction) by the modern impedance analyzers supports the perfection of this noise filtration. In the opposite case - when the object's voltage changes with time, the FT produces methodical errors [6]. The analysis is based on the presentation of the voltage-time dependence as a typical aperiodic signal, which could be approximated by a Taylor's series expansion:

$$U_{\mathrm{obj}}(t) = U_{\mathrm{DC}} + \alpha t + k_2\beta t_2 + k_3 y t_3 + \cdots, \quad (6)$$

where U_{DC} is a constant, $k_n = (n!)^{-1}$ are the Taylor's series coefficients, and $\alpha, \beta, \chi, \ldots$ are the derivatives of $U_{\mathrm{obj}}(t)$ for $t = 0$. All these derivatives form the Taylor Spectrum [7], the shape of which could play an important role in the analyses. When the noise corresponds to the presentation of Eq. 6 it can be called aperiodic noise.

As far as the FT is a linear operator, the errors produced by the individual terms of Eq. 6 can be studied separately. The analytical solution of FT (Eq. 3) of the linear aperiodic term given with Eq. 6 is a direct one [5] and it gives $a = -2\alpha\omega^{-1}$ and $b = 0$. As it can be seen, the error is present only in the real component (defined by Eq. 3) and is absent in the imaginary one. Thus the linear aperiodic noise corrupts the orthogonality between the real and imaginary impedance components. For high frequencies the error is small and could be neglected. For low frequencies however, this error could be large and increases quickly with the decrease of the frequency. This phenomenon can corrupt significantly the shape of the measured impedance.

Fig. 1 and Fig. 2 illustrate the significance of those errors on very simple examples of electrochemical impedances.

The analytical derivation of the errors caused by the second Taylor term shows that they are in both the real and imaginary components: $a = -2\pi\beta N\omega^{-2}$ and $b = 2\beta N\omega^{-2}$ [7]. The analytically derived expressions for the errors from the higher Taylor's terms of Eq. 6 are more complicated. They are with increasing complexity and show interesting properties of conversion after the fifth term under given conditions [8].

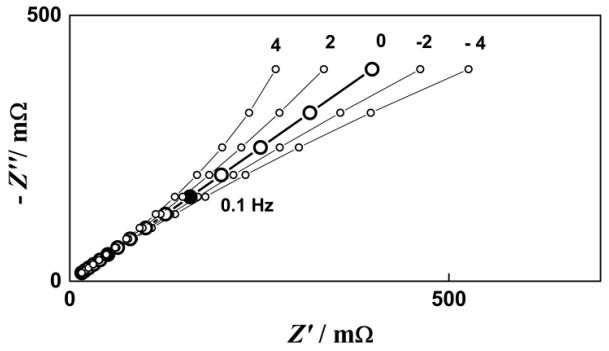

Fig. 1. Deformations of an ideal Warburg-type impedance diagrams from the errors of the Fourier Transform, caused by linear drift of the cell potential. Frequency range 10 Hz - 0.01 Hz, 5 points/decade, linear aperiodic noise with derivative values α = -4, -2, 0, 2, 4 mVsec^{-1}.

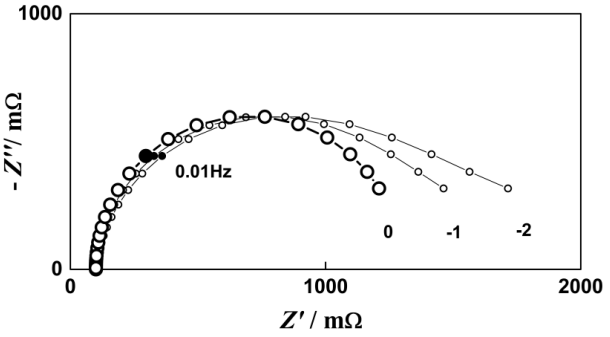

Fig. 2. Deformations of an ideal impedance diagram of Polarisable electrode from the errors of the Fourier Transform, caused by linear drift of the cell potential. Frequency range 100 Hz - 1.25 mHz, 5 points/decade, linear noise with derivative values α = -2, -1, 0 mVsec^{-1}.

Phase definite Fourier Transform

The initial phase of integration in Eq. 3 could not be zero. In the early definition of Eq. 3, Euler has used for initial limit of integration also π and $\pi/2$. As far as we are analyzing measurement of impedance which is defined as the ratio between two Fourier Transforms we can select any desired initial phase applied for both Transforms. Thus an additional definition the Fourier Transform can be constructed [8]. It was called Phase definite Fourier Transform and can be denoted by the symbol ***pFT*:**

$$a = w \int_{t_0}^{t_0+NT} x(t)\sin(\omega t)\mathrm{d}t, \quad (7a)$$

$$b = w \int_{t_0}^{t_0+NT} x(t)\cos(\omega t)\,\mathrm{d}t, \quad (7b)$$

where the only difference from the classical definition is the presence of one additional parameter - the initial time of integration, which corresponds to an initial phase $\varphi = t_0 T^{-1}$. In respect to stationary periodic signals the pFT is equivalent to the classical FT. However in respect to aperiodic noise pFT has different properties. The error produced by a linear noise term is a function of the initial phase φ. One remarkable property of this dependence is the equality of the errors correspondent to initial phase φ=0 and phase φ=2π. It corresponds to the analytical property of the space of the errors as functions of the initial phase. However the shape of the error produced by the second – quadratic term of the Taylor Spectrum of Eq. 6 is more complicated. This function is also complex, but it is non-linear and the correspondent space is not analytical.

Rotating Fourier Transform

On the base of the described analysis a novel transform was created. Using the analytical property of the pFT, the new transform has the following form [8]:

$$a = w_1 w_0 \int_{\Psi}^{\Psi+2\pi N_1} \int_{t_0}^{t_0+N_0T} x(t)\,sin(\omega t)dt\,d\varphi \quad (8a)$$

$$b = w_1 w_0 \int_{\Psi}^{\Psi+2\pi N_1} \int_{t_0}^{t_0+N_0T} x(t)\,cos(\,\omega t)dt\,d\varphi \quad (8b)$$

where the first (internal) integration is the classical phase definite Fourier Transform with initial phase $\varphi = t_0 T^{-1}$, the second (external) integration is in respect to this phase. It starts from the external initial phase ψ and is a full circulation. The coefficients w_1 and w_0 are normalizing coefficients, dependent on the numbers of the periods of integration N_1 and N_0 and on T. As far as the last integration is with respect to the phase φ, which symbolizes a rotation, the new transform can be called Rotating Fourier Transform (RFT). The operator symbol ***RFT*** has a number of parameters:

$$RFT\{x(t)\ |\ \omega, \varphi, \Psi, N_0\ and\ N_1\ |\}, \quad (9)$$

where $x(t)$ is the input signal, which is defined in the time domain and has to be converted into the frequency domain.

The kernel of this double integration is the classical Fourier Transform - as a result the RFT keeps the properties of the FT in respect to periodic signals and constant bias (zero term of the noise Taylor spectrum). The difference is with respect to the linear and higher terms of this spectrum - the RFT is orthogonal to the linear term (RFT filtrates it totally) and is suboptimal to the higher terms of the noise Taylor spectrum. This property is in correspondence with the classical FT, which is orthogonal to the zero term (constant bias) of the same Taylor spectrum. Thus the RFT is in continuity of the FT. This property of RFT was proved theoretically [8]. Fig. 3 is showing the described orthogonal property which keeps the precision of the FT.

Multiple Rotating Fourier Transform

The described continuity can be enlarged further. A second order and higher orders Rotating Fourier Transforms can be constructed also.

The general Multiple Rotating Fourier Transform (***MRFT***) of order ν has the form:

$$a = W_\nu \int_{\Psi_\nu}^{\Psi_\nu+2\pi N_\nu} \dots \int_{\Psi_1}^{\Psi_1+2\pi N_1} \int_{t_0}^{t_0+N_0T} x(t)\sin(\omega t)\mathrm{d}t\mathrm{d}\varphi\mathrm{d}\Psi_1 \dots \mathrm{d}\Psi_{\nu-1} \quad (10a)$$

$$b = W_\nu \int_{\Psi_\nu}^{\Psi_\nu+2\pi N_\nu} \dots \int_{\Psi_1}^{\Psi_\nu+2\pi N_1} \int_{t_0}^{t_0+N_0T} x(t)\cos(\omega t)\mathrm{d}t\mathrm{d}\varphi\mathrm{d}\Psi_1 \dots \mathrm{d}\Psi_{\nu-1} \quad (10b)$$

where the initial phase of the first integration is $\varphi = t_0 T^{-1}$, the normalizing coefficient W_ν is the product of all individual normalizing coefficients.

The MRFT keeps the property of the classical FT in respect to periodic signals. The MRFT of order ν is orthogonal to all ν terms of the noise Taylor spectrum - the MRFT filtrates unconditionally all ν derivatives of this noise (voltage drift).

Thus the RFT and MRFT are natural generalization of the Fourier Transform. They are keeping the continuity of its properties [9].

EXPERIMENTAL

The theory derived above was proven by multiple simulation studies as well as by real experimental measurements of battery under charge and discharge.

Simulation studies

The theoretically derived equations for FT and pFT errors, as well as the construction of RFT and MRFT were checked by series of simulations with varying structures and amplitudes of the additive aperiodic noise and varying periods of integrations. The influence on the final results of the calculations precision was also evaluated. The next examples are showing some of these simulation studies.

The property of the RFT for filtration of linear drift (orthogonality to the linear term of the noise Taylor spectrum) is shown in Fig. 3. The figure contains the equation used for synthesis of the input signal, having sinusoidal component and additive linear noise (drift). The resulting values of the produced transform into the frequency domain, together with the ratio signal to noise (S/N) are also given. It is clear that the RFT filtrates efficiently the linear noise.

The next Fig. 4 and Fig. 5 illustrate the property of the MRFT of second order for filtration of more complex additive noise. In this case the noise contains linear and quadratic terms. In Fig. 5 the amplitude of the sinusoidal signal is extremely low and un-visible. Nevertheless the final results are excellent.

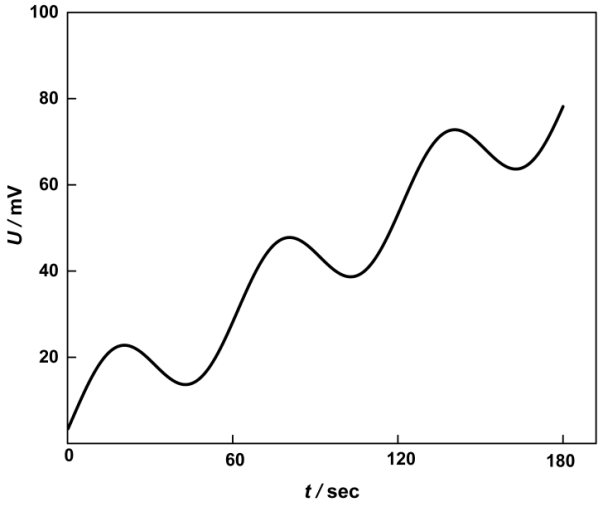

Fig. 3. Detection of sinusoidal signal in presence of linear aperiodic noise. Frequency 0.0156 Hz, A.C. amplitude 10 mV, derivative of the trend: α = 0.4 mVsec^{-1}. Input signal $x(t)$ = 10.01 sin (ωt) + 5 + 0.4t [mV], signal to noise ratio S/N = 0.1. RFT estimate: 10.01001 sin (ωt) + 3.52.10^{-6} cos (ωt).

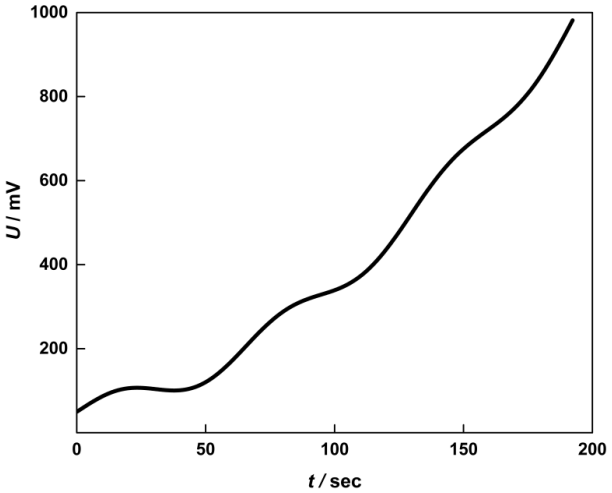

Fig. 4. Detection of sinusoidal signal in presence of complex aperiodic noise. Frequency 0.0156 Hz, A.C. amplitude 30 mV, derivatives of the noise: α = 1 mVsec^{-1}, β = 0.02 mVsec^{-2}. Input signal $x(t)$ = 30.01 sin (ωt) + 50 + t + 0.02 t^2 [mV]. Signal to noise ratio S/N = 0.06. R^{2}FT estimate: 30.01002 sin (ωt) – 6.78.10^{-6} cos (ωt).

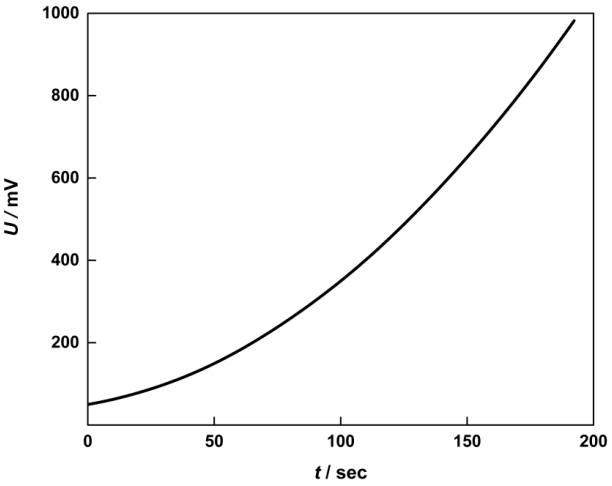

Fig. 5. Detection of very small (un-visible) sinusoidal signal in presence of complex aperiodic noise. Frequency 0.0156 Hz, A.C. amplitude 0.5 mV, derivatives of the noise: α = 1 mVsec^{-1}, β = 0.02 mVsec^{-2}. Input signal $x(t)$ = 0.505 sin (ωt) + 50 + t + 0.02 t^2 [mV], signal to noise ratio S/N = 0.001. R^{2}FT estimate: 0.505015 sin (ωt) – 9.83.10^{-6} cos (ωt).

Experimental measurements

In order to verify the theory, a series of real experimental measurements were recently carried out. The impedance measurements of a battery during charge, performed by a classical impedance analyzer and by the new mathematical instrument are compared.

The first measurement was conventional. It was performed in the frequency range 1 kHz down to 1 mHz during the charge of a battery (Li-ion, NiCo - type, 2000 mAh) using Solartron 1260 impedance

analyzer, controlled by an external computer. Fig. 6 shows the produced impedance diagram. As it is seen in the frequency range down to approximately 1 Hz the diagram is smooth and regular. However below 0.4 Hz irregularities appear and down to 1 mHz the diagram contains mainly increasing errors. In this range the measurements are totally non-usable.

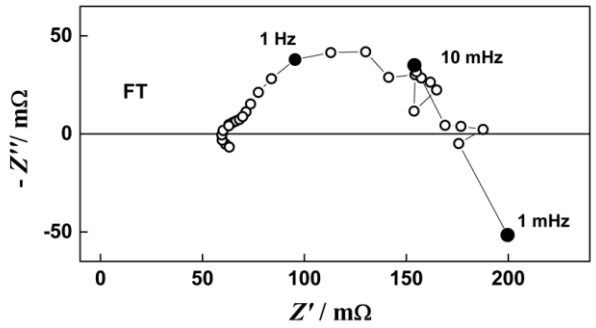

Fig. 6. Impedance diagrams of Li-ion battery 2000 mAh during charge with 100 mA produced by conventional Impedance Analyzer (Solartron 1260) using Fourier Transform. Frequency range 1 kHz – 1 mHz, 5 points/decade, A.C. current amplitude 11 mA.

The second series of impedance measurements are produced by using the Rotating Fourier Transforms. For this purpose a special laboratory set-up was assembled. In the frequency range 0.01 down to 0.001 Hz, the Solartron instrument is used only as a generator of the necessary frequencies with given amplitudes. This signal is mixed with the selected D.C. current via laboratory made galvanostat, connected to the measured battery. The current and the battery voltage are measured by two parallel AD converters (17 bits) with selectivity 0.002 mV and controllable acquisition time. The data are stored in the computer memory for post-experimental processing.

Fig. 7 shows the data record from the last decade (0.01 - 0.001 Hz) during the charge of the battery, measured immediately after the conventional measurements. The current signal shows a stationary DC component and a sinusoidal AC component with varying frequency and stationary amplitude (~ 10%). The battery response - the voltage signal, contains also sinusoidal components, however they are naturally mixed with the voltage drift during the battery charge.

The acquired data records are processed post-experimentally by FT, RFT and MRFT of second order. As it could be expected, the FT gives unreliable results with errors, which are frequency and phase dependent. The RFT and MRFT are producing similar estimates with very small differences - obviously the drift contains mainly linear term (un-known in advance). The RFT - produced diagram for the last decade of the measurement is given in Fig. 8. The impedance diagram is smooth, reliable and shows the real impedance of the battery in this very low frequency range, where the most interesting properties of the cathode intercalation are taking place.

The estimation of the impedance by using consecutive periods of the last frequency is showing the independence on time, which leads to the conclusion that the impedance is stationary during this measurement. This example shows again the property of RFT to filter efficiently a linear drift of the object voltage and confirms the applicability of the theory in real conditions.

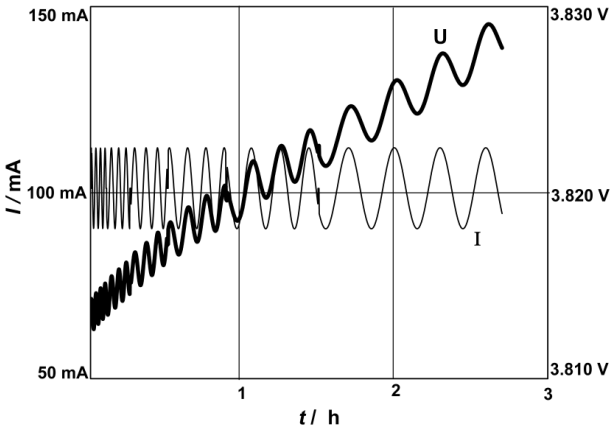

Fig. 7. Record of the current and voltage signals during the measurement of Li-ion battery 2000 mAh at charge with 100 mA. Frequency range 10 – 1 mHz, 5 points/decade, A.C. current amplitude 11 mA.

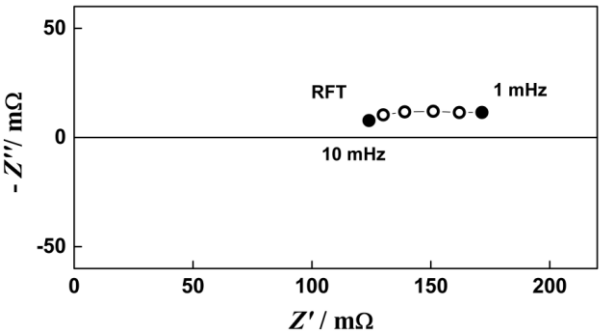

Fig. 8. Impedance diagrams produced by Rotating Fourier Transform of the data from Fig. 7. Frequency range 10 mHz to 1 mHz, 5 points/decade.

DISCUSSION

New types of Fourier Transforms are developed. The classical Fourier Transform, the Rotating Fourier Transform and the Multiple Rotating Fourier Transforms form a consistent and full set of transforms of evolving in the time domain phenomena into the frequency domain. The

general conclusion which can be derived is that the projection of time evolving phenomena into the frequency domain depends on the applied transform, which can have specific properties.

The RFT and MRFT keep the property of the classical FT in respect to periodic signals. The MRFT of order ν is orthogonal to all n terms ($n = \nu$) of the aperiodic noise Taylor spectrum - the MRFT filtrates unconditionally all n derivatives of this noise (voltage drift). Thus the RFT and MRFT are natural generalization of the Fourier Transform. They are keeping the continuity of its properties [10].

The newly developed transforms together with the classical FT are unidirectional operators. As the FT, the RFTs are filtrating unconditionally the zero term of the time-domain Taylor spectrum (constant value) of the signal under operation. The application of the back transforms can not restore the filtrated initial constant value and its time - derivatives. Other mathematical tools should be applied for that. The multiple integrals (8, 10) are of a specific type - every next integration is a circulation with respect to the parameter (initial phase) of the previous one, which is not conventional.

The first real experimental application of RFT, reported in this paper, shows the applicability of the new mathematical instrumentation and its robustness. The variations of the initial phase of the RFT of a single frequency record, produce impedance results with a very small phase differences ($\Delta < 0.25^{o}$), which confirms this robustness. The comparison between the estimates produced by RFT and MRFT (ν=2) shows the quasi-linear nature of the present aperiodic noise.

From practical point of view the RFT operators could be used in many scientific and applied areas. The typical example is the measurement of the battery impedance during its operation (charge or discharge), when large parts of the active materials volumes participate in the studied processes. However many electrochemical fields like corrosion, passivation, AC polarography and others can successfully apply the RFT for improvement of their precision and for enlargement of their applicability. Other scientific fields in physics, geophysics and material science could also gain from this novel mathematical tool. Areas of a special interest are the studies of non-stationary impedances - the situations when the impedance of the object is changing during the period of the single frequency measurements. In this case a multiplicative aperiodic noise can be defined [8]. In general, the amplitude and the phase can be also functions of time:

$$Z(\omega, t) = A_0 (1 + \alpha t + \beta t^2 + \cdots) e^{\{-i\omega t + \varphi(t)\}}, \quad (11)$$

where the terms $\alpha, \beta, \ldots$ form again a Taylor spectrum and can be treated by the RFT tools. Preliminary studies carried out on this subject have shown that the RFT filtrates orthogonally the linear multiplicative term. Thus the RFT can estimate the real Instantaneous Impedance for every point inside a single frequency period [9 - 11, 13]. This is a significant progress of the notion of Instantaneous Impedance, given by Harkevich [12], where it is defined as the limit of the mean value of the impedances of series of periods, when their number tends to 1; or that defined by the 4-D method where single period measurements are used [14, 15]. This subject however is out of the frame of this paper and will be discussed elsewhere.

Having these properties, the RFT mathematical instrumentation can serve as a powerful engine for non-stationary impedance spectroscopy. The implementation of this new transform tool opens the exploration of the low and infra-low frequencies in impedance spectroscopy. Many interesting phenomena, specially in Li-ion batteries, can be measured precisely, supporting the understanding of the processes under investigation. The acquired results will booster the further improvement of those objects. The efficient implantation of the RFT into the 4-Dimentional technology will provide for intensive application of this methodology for battery studies, State of Charge and State of Health diagnostics.

An important feature of the proposed new mathematical instrumentation is the possibility for separation of the real time data recording from the post-experimental data processing. In this second stage different algorithms can be applied, resulting in a set of frequency domain images. The comparison of the results produced by FT, RFT and high levels MRFTs can provide for precise impedance measurements and in addition can supply objective information about the structure and values of the noises, present in the analyzed signals.

The fine details concerning the robustness, noise immunity and other properties of the RFTs as well as the optimal design of MRFT are targets of next investigations. In any case the development of marketable impedance analyzers from a new "4-Generation" (applying RFT and MRFT) can be expected in the near future. They will perform the standard FT and also RFTs (as option), and could be of open architecture type, providing the recorded data sets to the user for customized processing.

REFERENCES

1. J. Fourier, Sur la propagation de la shaleure (1805 draft), Bibliotheque Nationale, Paris, MFF25252.
2. A. Papoulis, The Fourier Integral and its Applications, McGrow Hill Book Co. 1962.
3. R. B. Randall, Frequency Analysis, Bruel Kjaer, Naerum, 1977.
4. A. Oppenheim, Application of Digital Signal Processing, MIT, Mass.02139.
5. I. Gradshtein, I. Rizik, Tables of Integrals, Series and Products, ed. PM, Moskau, 1962.
6. Z. Stoynov, B. Savova-Stoynov, *J. Electroan. Chem.* **157**, 112 (1980).
7. Z. Stoynov, B. Savova-Stoynov, *J. Electroan. Chem.* **133.**183 (1985).
8. Z. Stoynov, Dissertation No7839, ETH Zurich, 1985.
9. B. Grafov, Z. Stoynov, V. Elkin, Electrochemistry, Moskau **25**, 1427(1989).
10. Z. Stoynov, B. Grafov, B. Savova-Stoynov, V. Elkin, Electrochemical Impedance, ed. Science, Moskau, 1991.
11. Z. Stoynov, Electrochimica Acta **37**, 2357 (1992).
12. A. Harkevich, Spectra and Analysis, ed. TTL, Moskau, 1957, 236.
13. Z. Stoynov, Electrochemistry, Moskau **29.1**, 43 (1993).
14. C.Julien, Z. Stoynov, Materials for Lithium-Ion Batteries, Kluver Academic Publishers, 1999.
15. Z. Stoynov, D. Vladikova, "Impedance Spectroscopy of Electrochemical Power Sources", Encyclopedia of Electrochemical Power Sources, ed. Juergen Garche, Elsevier Ltd., UK, 2008.

Ротираща Фурие трансформация - двигател на нестационарната импедансна спектроскопия

З. Стойнов†

Институт по електрохимия и енергийни системи „Акад. Евгени Будевски", Българска академия на науките, ул. Акад. Г. Бончев, бл.10, София 1113, България

Обяснителни бележки: През последната година от своя активен научен живот Здравко Стойнов работи интензивно както теоретично, така и експериментално, за да демонстрира нагледно мощния си математически инструмент "Ротираща Фурие Трансформация" (РФТ). Той го описваше като "мощен двигател за нестационарна импедансна спектроскопия, който осигурява нови информационни възможности в диапазона на ниските и свръх-ниски честоти, където много значими и интересни явления, все още неоткрити, могат да бъдат прецизно измерени". Той очакваше в близко бъдеще появата на ново, "четвърто поколение" импедансни анализатори, използващи РФТ и МРФТ (Многократна РФТ). За да ускори идването на това "близко бъдеще", което да може да види, той работеше както по математическия инструмент, така и по експерименталната му проверка.

Представяме последния му ръкопис, така както е написан от него. Очакваме, че работата му по РФТ ще предизвика интерес и неговата идея за 4-то поколение импедансни анализатори ще срещне необходимата за реализирането й подкрепа. Отворени сме за сътрудничество, което да продължи работата на Здравко Стойнов.

Д. Владикова
Секция „Електрохимични методи" на Института по електрохимия и енергийни системи „Акад. Евгени Будевски" - БАН

Bulgarian Chemical Communications, Volume 50 Special Issue D (pp. 131 – 134) 2018

Data Exchange Formats

Z. Stoynov †

Acad. E. Budevski Institute of Electrochemistry and Energy Systems- Bulgarian Academy of Sciences, 10 Acad. G. Bonchev Str., Sofia1113, Bulgaria

Explanatory Notes: With the increasing number of Electrochemical Impedance Applications, the problem of unified data exchange formats becomes important. In addition, the existing computerized experimental facilities produce automatically large sets of data files, which have to be stored, sorted, archived and possibly exchanged via Internet. The efficiency of the data banking and the speed of the virtual research depend notably on the selected Data Exchange Formats (DEF).

The material below describes the DEF for impedance measurements proposed by Zdravko Stoynov [1]. It will be nice if the equipment producers discuss this topic with the end users of their equipment and introduce common data banking as a convenient and appropriate tool, especially for friendly scientific communication in the big EU Framework programs projects.

We offer Zdravko Stoynov's approach since we use it for more than 15 years and find it extremely convenient. Our group is ready to develop and upload free of charge Data Convertor. We shall be thankful for every remark, correction, recommendation or suggestion.

The DEF description which we have included in this special issue of Bulgarian Chemical Communications can be also downloaded from the web site of the European Internet Centre for Impedance Spectroscopy www.accessimpedance.eu (in the Section Information Kit/News).

The web site of EICIS will be upgraded in September/October 2018 with its new name "Zdravko Stoynov Internet Centre for Impedance Spectroscopy

New ideas and approaches are welcome.

Daria Vladikova,

Electrochemical Methods Department, Acad. E. Budevski Institute of Electrochemistry and Energy Systems – BAS

.

INTRODUCTION

In accordance with the general IUPAC recommendations, the Electrochemical Impedance Spectroscopy's Data Exchange Formats (DEF) should be generic, economic and efficient. Following the practical experience, some other recommendations are useful: DEF should be self-explaining and easily readable by the user as well as by the computers. They should contain enough explanations and to a certain extent should be over-dimensioned by verbal information. The used symbols must be readable by computers of different versions and generations and should be selected only from the ASCII table.

For these reasons, the use of "text only" (xxxxx.txt) format is recommended for the storing and attachment format. The ".txt" format is not only universal, but it is also the most economic. The experimental comparison with ".rtf", ".doc" and other word processing formats shows an excessive enlargement of the file volumes, when stored in those formats. The inefficient enlargement for ".rtf" is about 5 times and for ".doc" extension – about 20 times. For a single file the enlargement can be neglected, but for a data bank, containing thousands of files, and for their exchange, the compactness becomes important.

The ".txt" files have the advantage to be readable by computers of all versions, independent of the type and version of its software and Internet instruments.

Another problem arises when a series of experiments are carried out with one and the same object with a varying parameter. One solution for the DEF efficiency is the application of the Large Structured Files (LSF), proven in our practice.

The LSF starts with a header. The header should contain all the information necessary for the understanding, sorting, exchange and banking of the data.

The LSF contains a certain number of pages. Each page starts with a symbol (#) and a number (1 to *N*) and has a verbal informative label, corresponding to the value of the varying

To whom all correspondence should be sent:
E-mail: d.vladikova@bas.bg

parameter. The label contains determination of the size (*n* x *m*) of the data matrix as well as the description of the type of the data (f, *Z´*, *Z´´*, t^o, or others).

After the label comes the data kernel. It contains a number of lines (*n*). Every value in the line is separated from the previous one by ";".

Every page finishes with a tag (@), which could be followed by the post–experimental observations.

The LSF finishes with a footer symbolizing the end of the file (@ EOF).

EXAMPLES

Examples for explanation of the DEF (Large Structured Files) with a code

#ftp:EISDEF205LSF.txt.

The file, stored as xxxxx.txt with this CONVENTION CODE is a Large Structured File (LSF).

The suggested EIS DEFs are illustrated in the following examples:

*Large Structure File – **Example LSF1**:*

```
File Name: BATI043.txt
#ftp:EISDEF205LSF.txt   #fnm:BATI043.txt   pages: 6
<BaTi  sample N.33  measured>
<No: 1243-49 author: X. Broun 29-01-2005   20:36:05>
<object: BaTi; sin.crystal [100] S=1.22 cm^2 d=0.2 cm>
<set-up: Sol 1256 + Pot. self-made; cell: planar>
<Udc=0; Uac=5 mV; down; variation: temper. 'C>
#p1      {f; Z`; Z``} [ SI ] (3*56)
<calibration short connected>
1000;1.356E-3;2.265E-3
…;       …;       …
…;       …;       …
…;       …;       …
0.001;1.222E-3;-0.005E-3
@p       <room temperature>
#p2      {f; Z`; Z``} [ SI ] (3*56)
<calibr. open>
…;       …;       …
@p
#p3      {f; Z`; Z``} [ SI ] (3*56)
<object row data    var: 20'C>
…;       …;       …
@p
#p4      {f; Z`; Z``} [ SI ] (3*56)
<object row   var:31'C>
…;       …;       …
@p
#p5      {f; Z`; Z``} [ SI ] (3*56)
<object row  var: 40'C>
…;       …;       …
@p
#p6      {f; Z`; Z``} [ SI ] (3*56)
<object row  var:51'C>
…;       …;       …
@p
@ EOF
```

Explanations:

File Name: BATI043.txt

#ftp:EISDEF205LSF.txt #fnm:BATI043.txt pages: 6
<BaTi sample N.33 measured>
<No: 1243-49 author: X. Broun 29-01-2005 20:36:05>
<object: BaTi; sin.crystal [100] S=1.22 cm^2 d=0.2 cm>
<set-up: Sol 1256 + Pot. self-made cell: planar >
<Udc=0; Uac=5 mV; down; variation: temper. 'C>
(this information forms the file's header)
#p1 {f; Z`; Z``} [SI] (3*56) = ***page 1 beginner & descriptor***
<calibration short connected> = ***free text***
1000;1.356E-3;2.265E-3 = ***data /example/***
…; …; …
…; …; …
…; …; …
0.001;1.222E-3;-0.005E-3 = ***last data***
@p <room temperature> = ***page footer & tag***

#p2 {f; Z`; Z``} [SI] (3*56) = ***page 2 beginner & descriptor***
<calibr. open>
…; …; …
@p
#p3 {f; Z`; Z``} [SI] (3*56) = ***page 3 beginner & descriptor***
<object row data. var: 20'C>
…; …; …
@p
#p4 {f; Z`; Z``} [SI] (3*56) = ***page 4 beginner & descriptor***
<object row var:31'C>
…; …; …
@p
#p6 {f; Z`; Z``} [SI] (3*56) = ***page 6 beginner & descriptor***
<object row var:51'C>
…; …; …
@p = ***last page footer***
@ EOF = ***file footer***

*Large Structure File – **Example LSF2**:*

```
File Name: BATI044.txt
#ftp:EISDEF205LSF.txt   #fnm:BATI044.txt  pages: 8
<BaTi recalculated from BATI043.txt corrected Z & Y >
<No: 1250-58 author: X.Balan       30-01-2005
21:36:05>
<object: BaTi; sin.crystal [100] S=1.22 cm2 d=0.2 cm>
<set-up: Sol 1256 + Pot. self-made cell:planar>
<Udc=0; Uac=5 mV; down; variation: temper. `C>
#p1      {f; Z`; Z``} [ SI ] (3*26)
<calibration short connection>
…;       …;       …
@p
#p2   {f; Z`; Z``} [ SI ] (3*56)
<calibr. open>
…;       …;       …
@p
#p3      {f; Z`; Z``} [ SI ] (3*56)
<object row data.   var: 20`C>
```

```
…;      …;      …
@p
#p4     {f; Z`; Z``} [ SI ] (3*56)
<object data corrected LCcell   var:20`C>
…;      …;      …
@p
#p5     {f; Y`; Y``} [ SI ] (3*56)
<object corrected;          Y     var:20`C>
…;      …;      …
@p
#p6     {f; lg |Y|; phi} [ SI ] (3*56)
<object corrected;   Bode       var:20`C>
…;      …;      …
@p
#p7     {f; Z`; Z``} [ SI ] (3*56)
<simulated M11= La: R C/R BW >
<par: 120; 1.23E-3; 1038; 30246\880 >
<identified by CNLS – Boukamp version "3/2000" for
20'C>
…;      …;      …
@p
#p8     {f; Z`; Z``} [ SI ] (3*56)
<residuals  f; dZ`/Z`; dZ``/Z``>
…;      …;      …
@p
@ EOF
```

Remarks:

1. The symbol "#ftp:EISDEF205LSF.txt" describes the file's type in accordance to this convention.
2. The symbols "(", ")", "\" and "var:" are for computer reading. They possess the dimensions of the data kernel matrix and the varying parameter's values.
3. The text within the symbols "<" and ">" is for the user's reading; its internal format is free.
4. The number of the text lines <……> is unlimited.
5. The value of the varying parameter should immediately follow the symbol "var:" ("var:" is for computer reading!).
6. The symbols "{","}", "[","]", "#ftp:" and "#fnm:" are for computer reading.
7. The data kernel may contain additional data for every frequency: time of measurement, quality of measurement, d.c. values and others.
8. The page footer is optional.
9. The file footer is optional.

Explanations:

#ftp:	= ***computer used symbol***
EISDEF205LSF.txt	= ***file type***
#fnm:	= ***computer used symbol***
BATI033.txt	= ***file name given by the operator***
<BaTi sample N.3 measured>	= ***text:object***
<No:1232 author: X.Green 29-01-2005 20:36:05>	= ***text:number***
<object: BaTi; single crystal[100] S=1.22cm2 d=0.2cm>	= ***object***
<set-up: Sol 1256 + Pot. self-made cell:planar>	= ***set-up***
<Udc=0; Uac=5 mV; down; temper. 22`C>	= ***meas.cond.***
# {f; Z`; Z``} [SI] (3*26)	= ***data descriptor***
…; …; …	= ***data***
…; …; …	= ***last data***
@p	= ***page footer = end page***

Additional Explanations:

file name:	- ***name of the file given by the author;***
file type:	- ***STANDARD, subject to this preliminary convention;***
<text>:	- ***free text, composed by the author, including information about the author, date/time, object, instrumentation, measurement conditions; other information.***
<text>	- ***a number of lines with*** <… …> ***is free.***
# {f; Z`; Z``} [SI] (3*26)	- ***descriptor of the following data:***
#	- ***computer used symbol (new page)***
{f; Z`; Z``}	- ***descriptor of data types***
[SI]	- ***descriptor of data units /in this case in SI/***
(3*26)	- ***data kernel format***
( )	- ***computer used symbol***
\	- ***computer used symbol***
3*26	- ***in this example: 3 columns, 26 lines***
# { } [ ] \: \ < > #ftp #fnm @p	- ***computer used symbols***

Additional Explanations of the file type descriptor:

#ftp:EISDEF205LSF.txt	- ***file type code***
#ftp:	- ***computer used record of file type***
EIS	- ***Electrochemical Impedance Spectroscopy***
DEF	- ***Data Exchange Format***
205LSF	- ***2005 year, Convention LSFile***
.txt	- ***type in which the file must be saved / attached***

REFERENCES

1. Z. Stoynov, D. Vladikova, Differential Impedance Analysis, Marin Drinov Academic Publishing House, 2005, pp, 207-213.

Формати за обмен на данни

З. Стойнов†

Институт по електрохимия и енергийни системи „Акад. Евгени Будевски“, Българска академия на науките, ул. Акад. Г. Бончев, бл.10, София 1113, България

Обяснителни бележки: С нарастване приложенията на електрохимичната импедансна спектроскопия, проблемът с унифициране на форматите за обмен на данни става все по-съществен. Успоредно с това съществуващите компютризирани измервателни системи автоматично генерират огромен брой файлове с данни, които трябва да бъдат съхранявани, сортирани, архивирани и обменяни чрез интернет. Ефективното съхранение на данни и разрастването на виртуалната колаборация зависят силно от избраните формати за обмен на данни (ФОД).

Предлаганият материал описва ФОД за импедансни измервания, предложени от Здравко Стойнов [1]. Би било полезно, ако производителите на оборудване дискутират тази тема с крайните си потребители и въведат общоприета форма за съхранение и обмен на данни като удобен и подходящ инструмент, особено полезен за научна комуникация в големи проекти по рамковите програми на ЕС.

Ние предлагаме подходът на Здравко Стойнов, който използваме повече от 15 години и който намираме за изключително удобен. Нашата група е готова да разработи и да качи безплатно *Конвертор на данни*. Ще бъдем благодарни за всяка забележка, корекция, препоръка или предложение.

Описанието на ФОД което включваме в това специално издание на Bulgarian Chemical Communications, може да бъде изтеглено и от уеб сайта на Европейския интернет център по импедансна спектроскопия (EICIS): www.accessimpedance.eu (в секция Информация / Новини).

Уеб сайтът на EICIS ще бъде актуализиран скоро с новото си име ”Интернет център за импедансна спектроскопия „Здравко Стойнов”.

Ще се радваме на нови идеи и подходи.

Д. Владикова
Секция „Електрохимични методи” на Института по електрохимия и енергийни системи „Акад. Евгени Будевски“ - БАН

CONTENTS

СЪДЪРЖАНИЕ